# INFORMATION TO USERS

This manuscript has been reproduced from the microfilm master. UMI films the text directly from the original or copy submitted. Thus, some thesis and dissertation copies are in typewriter face, while others may be from any type of computer printer.

The quality of this reproduction is dependent upon the quality of the copy submitted. Broken or indistinct print, colored or poor quality illustrations and photographs, print bleedthrough, substandard margins, and improper alignment can adversely affect reproduction.

In the unlikely event that the author did not send UMI a complete manuscript and there are missing pages, these will be noted. Also, if unauthorized copyright material had to be removed, a note will indicate the deletion.

Oversize materials (e.g., maps, drawings, charts) are reproduced by sectioning the original, beginning at the upper left-hand corner and continuing from left to right in equal sections with small overlaps.

Photographs included in the original manuscript have been reproduced xerographically in this copy. Higher quality 6" x 9" black and white photographic prints are available for any photographs or illustrations appearing in this copy for an additional charge. Contact UMI directly to order.

Bell & Howell Information and Learning
300 North Zeeb Road, Ann Arbor, MI 48106-1346 USA
800-521-0600

UMI®

# Cloud and Surface Properties and the Solar Radiation Budget Derived from Satellite Data over the Arctic Ocean: Comparisons with Surface Measurements and In Situ Aircraft Data

A

THESIS

Presented to the Faculty

of the University of Alaska Fairbanks

in Partial Fulfillment of the Requirements

for the Degree of

DOCTOR OF PHILOSOPHY

By

Xiaozhen Xiong, B.S., M.S.

Fairbanks, Alaska

December 2000

Bell & Howell Information and Learning Company
300 North Zeeb Road
P.O. Box 1346
Ann Arbor, MI 48106-1346

CLOUD AND SURFACE PROPERTIES AND THE SOLAR RADIATION BUDGET DERIVED FROM SATELLITE DATA OVER THE ARCTIC OCEAN: COMPARISONS WITH SURFACE MEASUREMENTS AND IN SITU AIRCRAFT DATA

By

Xiaozhen Xiong

RECOMMENDED:

Advisory Committee Chair

Department Head

APPROVED:

Dean, College of Science, Engineering and Mathematics

Dean of the Graduate School

12-1-00

Date

## Abstract

Use of satellite data to study the surface and cloud properties and the solar radiation budget (SRB) is very important for improving our understanding of cloud and sea-ice albedo feedback in the Arctic. Based on an accurate and comprehensive Radiative Transfer Model (RTM), algorithms were developed for using the National Oceanic and Atmospheric Administration (NOAA) Advanced Very High Resolution Radiometer (AVHRR) data for the discrimination of cloud from snow/ice surfaces, retrieval of snow surface properties and surface albedo, and retrieval of cloud optical depth ($\tau$) and effective droplet size ($r_e$).

Through the improved estimation of solar reflectance in AVHRR channel 3 (3.75 $\mu$m) and atmospheric anisotropic correction, a threshold function was found and used for developing an automatic cloud discrimination algorithm over snow/ice surfaces. Thin cirrus was discriminated using the brightness temperature difference between AVHRR channels 4 and 5 and brightness temperature in channel 4.

Retrieval of snow grain size and mass-fraction of soot from AVHRR is difficult because of the effects of aerosol in channel 1 and the strong water vapor absorption in channel 2. Retrieval of surface albedo is more promising, but, with the melt of snow/ice, different narrow-to-broadband conversion relations should be used to derive broadband albedo.

AVHRR channels 2, 3 and 4 are used to retrieve $\tau$, $r_e$ and cloud top temperature simultaneously. Validation of these algorithms with in-situ aircraft measurements by the NCAR C-130 and the NASA ER-2 and with surface measurements obtained during the Surface Heat Budget of the Arctic Ocean (SHEBA) experiment indicates that the retrieved $r_e$ is close to the "true" value of $r_e$, but the retrieved $\tau$ tends to be overestimated. Uncertainties of cloud retrievals with regard to cloud cover fraction, vertical inhomogeneity, multi-layer stratification and cloud phase were

examined. Inter comparison of different satellite data demonstrates that NOAA-14 AVHRR data for SHEBA is overestimated by 10-20% using the calibration by Rao and Chen (1996).

Finally, seasonal variation of surface albedo, cloud properties and SRB over SHEBA was derived based on 1 or 2 AVHRR overpasses per day from April to August, 1998.

# Contents

# List of Figures

# List of Tables

## Acknowledgments

I would like to give my sincere thanks to Professor Knut Stamnes, chairman of my graduate advisory committee, for his constant support, encouragement and excellent guidance through the entire graduate studies. Without his help, it is not possible for me to finish this thesis. My sincere thanks also go to other members of my graduate advisory committee: Dr. Ataur R. Chowdhury, Dr. Shusun Li, Dr. Antonius Otto and Dr. Brenton Watkins. The improvement on my thesis benefits from lots of comments and helpful suggestions from them. Thanks are also due to Dr. Dan Lubin for stimulating discussion and cooperation.

Thanks are extended to Dr. Jerry Harrington, Dr. John Olson, Dr. Gleen Shaw and Dr. Peter Olson for their extremely valuable insights into the physics, mathematics and philosophy during the course of my graduate education: Thanks to Gus Lindquist, Dr. Bingquan Chen, Wei Li and fellow graduate students, Rune Storvold, Hans Eide, North Larsen, Jennifer Delamere, Banghua Yan, Michael Kahnert and Qiuqing Zhang, and many other friends for their help.

I am especially grateful to my dear wife, Fang Zhou, and our lovable son, Yuzhou Xiong, for bringing me joy after the work. Thanks to my parents-in-law for their support in the past year. Without their support, the thesis could not have been finished so quickly. Finally, to express my love to my dear parents and sincere thanks to their support in my life, I would like to dedicate this thesis to them who never have chance to receive education in school.

# Chapter 1

# Introduction

In the context of global change, the Arctic is considered to be of particular importance because it is vulnerable to global change (e.g. IPCC, 1990). The ocean-ice-atmosphere processes that control the surface albedo and cloud-radiation feedback are poorly understood as current Global Climate Models (GCMs) produce widely different simulations of the present Arctic climate and predictions of high-latitude response to a $CO_2$ doubling (e.g. Moritz et al., 1993; Moritz and Perovich, 1996). Poor performance of GCMs in the Arctic and the need for better understanding of Arctic climate and climate change require improved treatment of cloud and sea-ice albedo feedback in regional and global climate models. This in turn requires: (1) better understanding of cloud properties and cloud radiative interactions, (2) better methods to estimate the SRB in the Arctic from satellite data because satellites provide a large coverage. Questions that must be addressed include: (1) what are the cloud properties in the Arctic and how do they vary with the season? and (2) how do clouds influence the radiative energy budget in the Arctic? and (3) how does the SRB vary during the melting season from May to August in the Arctic?

## 1.1 Characteristics of Clouds and Solar Radiation Budget in the Arctic

Solar radiation in the Arctic (similar to the Antarctic) exhibits much greater seasonal change than at temperate and tropical latitudes on the earth. Because the relative movement of the sun and earth, the Arctic experiences no insolation during winter and an overall maximum during summer. The long solar illumination in summer results in the largest and most significant temporal and spatial change of surface optical properties, e.g. albedo, due to the melting of snow/ice. This melting season is from May to August in the central Arctic Ocean but varies with latitude. In general, snow covers the Arctic sea ice for 8-9 months of the year, and it evolves from dry snow in April-May to wet, melting snow in June, and the melt water soaks the remaining snow and collects in ponds. As the melting season progresses, the snow cover disappears, the bare ice develops a melting surface granular layer, and the ponds grow deeper and wider (Perovich et al., 1999).

Albedo, a quantity to describe the reflectivity of the surface, is a critical component of the surface heat balance. Very high albedo of snow/ice surface and the significant change in albedo during the melting season in the Arctic are of primary importance to the energy budget in the Arctic (Stamnes et al., 1999). For snow-covered first-year ice in April, wavelength-integrated albedos were high (0.8) and spatially uniform. At the onset of melt in June, the ice surface rapidly evolved into a variegated mixture of melting snow, bare ice, and melt ponds. Albedos were lower and exhibited considerable spatial variability, ranging from 0.2 to 0.5 over distances of a few meters concomitant with the variation in the surface characteristics (Perovich et al., 1998). In September, water begins to freeze which increases albedo and, as winter comes, precipitation of snow further increase the surface

albedo.

Clouds are one of the most important factors modulating the radiation budget. The Arctic atmosphere is characterized by persistent and prevalent low-level stratus clouds comprising of two or more separate, well-defined layers (for example, Herman, 1977; Tsay and Jayaweera, 1984). The highest amounts of low-level clouds were observed in autumn and summer with the smallest amount occurring in winter and spring. Annually, 10/10 cloud cover is the most frequent category (about 15%) with stratus the most frequently observed cloud type (Curtis et al., 1998). The annual cycle of mean monthly fractional cloud cover in the central Arctic shows a summertime maximum as high as 90% and a minimum of 40% to 68% during the winter (Hahn et al., 1995).

The dominant effects of clouds on the solar radiation budget for the atmosphere-surface system in the Arctic is especially significant during the late spring and summer when the mean cloudiness exceeds 85% and the incident shortwave radiation is large (Moritz and Perovich, 1996). From the Arctic Stratus Experiment, Herman and Curry (1984) found the values of broadband shortwave optical depth for the summertime Arctic stratus is 2-24 for low-level clouds and 2-5 for midlevel clouds. Liquid water path (LWP) in Arctic stratus is normally less than 20 $gm^{-2}$. Arctic cloud optical depth determined from satellite by the International Satellite Cloud Climatology Project (ISCCP) analysis is about 10-15 at 0.6 $\mu$m wavelength in summertime, and much larger (about 40-60) in spring and autumn (Rossow and Garder, 1993a,b), but it may be significantly overestimated due to the use of spherical particle scattering phase function for ice crystals (Minnis et al., 1993).

## 1.2 Radiation Budget Study from Satellite

The radiation budget represents the balance between incoming energy from the sun and outgoing thermal (longwave) and reflected (shortwave) energy from the Earth. Energy from solar radiation is the driver of the movement of the atmosphere and ocean, and of the incoming solar flux (342 $Wm^{-2}$ averaged over the entire planet), 31% is reflected back to space through the complex radiative interactions with the atmosphere-earth system, and the reminder is absorbed by the atmosphere and the Earth's surface.

With the development of satellite techniques, observations of the global radiation budget became possible. To improve our understanding of the radiation budget and its effects on the Earth's climate, the first attempt to make accurate regional and global measurements of the components of the radiation budget from satellite, Earth Radiation Budget Satellite (ERBS), Earth Radiation Budget Experiment (ERBE) was carried out in 1985 and 1986, in which ERBE instruments were launched on two National Oceanic and Atmospheric Administration (NOAA) weather monitoring satellites, NOAA-9 and NOAA-10 in 1984 and 1986 (Hartmann et al., 1986).

The Clouds and the Earth's Radiant Energy System (CERES) experiment is expected to improve the understanding of the role of clouds and the energy cycle in global climate change. The first CERES instrument was successfully launched aboard the Tropical Rainfall Measuring Mission (TRMM) satellite in November 1997. CERES also flew on the EOS satellites starting in 1999. Multiple satellites are needed to provide adequate temporal sampling since clouds and radiative fluxes vary throughout the day. The initial data from CERES on TRMM suggest that the CERES instruments are substantially improved over the ERBE instruments. The CERES data show lower noise, improved ties to the ground calibration in absolute

terms, and smaller fields of view. The CERES instrument calibration stability on TRMM is better than 0.2% and calibration consistency from ground to space is better than 0.25%. Such levels of accuracy have never before been achieved for radiation budget instruments (Wielicki et al., 1996). CERES was developed for EOS (Earth Observing System), and its products include both solar-reflected and Earth-emitted radiation from the top of the atmosphere. Cloud properties are determined using simultaneous measurements by other EOS instruments such as the Moderate Resolution Imaging Spectroradiometer (MODIS).

Due to the complex physical and chemical processes involved in radiative transfer in the earth-atmosphere system, large uncertainties with respect to the estimation of the radiation budget and its influence on climate change still exist, especially the radiation at the surface in the polar regions. Normally, two kinds of methods: empirical/statistical and theoretical/physical are used to derive the incoming short wave radiation or net shortwave radiation at the surface (Pinker et al., 1995). Empirical/statistical methods just compare satellite and surface measurements of radiation and find an empirical relation between them, so they are site specific and difficult to use. Theoretical/physical methods use a radiative transfer model with input variables derived from satellite data to compute the radiation budget. So, theoretical/physical methods can treat, at least in principle, all kinds of realistic atmospheric and surface situations once all the input variables are available. Two most important variables controlling the downwelling surface solar radiation are cloud properties and surface albedo or, more accurately, surface BRDF (Bidirectional Reflectance Distribution Function), which is a function of surface properties, viewing geometry and wavelength. However, large uncertainties in the input parameters, like cloud optical properties and surface albedo, are the essential problems. With improved derivations of the cloud properties and surface properties from satellite measurements, theoretical/physical methods will

be applicable to estimate the radiation budget, i.e. the downwelling solar radiation, net solar radiation at surface, net radiation in the column of atmosphere, or shortwave forcing at the top of atmosphere in the Arctic regions. In this thesis, we will only investigate the use of theoretical/physical methods to estimate the solar radiation budget in the Arctic.

As the spatial coverage of ground-based radiation measurements in the Arctic is sparse as compared with mid- and low-latitudes, and due to the large spatial and temporal variability of cloud and surface properties during the transition seasons in the Arctic regions, satellite observations became a powerful and economical technique in the past decades, especially in the polar regions where in-situ long-term measurements are difficult and expensive.

## 1.3 AVHRR, its Calibration and Applications

The Advanced Very High Resolution Radiometer (AVHRR) was designed in the mid-70s as an instrument to be flown on the NOAA polar-orbiting satellite for meteorological purposes (Cracknell, 1997). AVHRR is a broad-band, four or five channel (depending on the model) scanner, sensing in the visible, near-infrared, and thermal infrared portions of the electromagnetic spectrum. The AVHRR sensor provides global (pole-to-pole) on-board collection of data from all spectral channels. Each pass of the satellite provides a 2,399 km wide swath. The orbital period of a polar orbiting satellite is about 102 minutes which produces 14.1 orbits per day from 833 km above the surface. In the polar regions, overlap of satellite passes provides enhanced opportunity for AVHRR to observe the polar earth surface, so AVHRR coverage is especially good in the Arctic.

The first version of AVHRR was a four-channel version flown on TIROS-N; a slightly different four-channel version flown on NOAA-6, -8, and -10; and a five-

**Table 1.1** AVHRR Spectral Features ($\mu$m).

| Channel | Satellites: NOAA-6.8.10 | Satellites: NOAA-7.9.11.12.14.15 | IFOV(mr) |
|---|---|---|---|
| 1 | 0.58-0.68 | 0.58-0.68 | 1.39 |
| 2 | 0.725-1.00 | 0.725-1.00 | 1.41 |
| 3 | 3.55-3.93 | 3.55-3.93 | 1.51 |
| 4 | 10.50-11.50 | 10.3-11.3 | 1.41 |
| 5 | band 4 repeated | 11.5-12.5 | 1.30 |

channel version flew on NOAA-7, -9, -12 and -14. NOAA-15 became available in May, 1998. In NOAA-15, a new channel at 1.6 $\mu$m is used alternately in daytime instead of 3.7 $\mu$m channel in night time. A list of AVHRR spectral features and related information is shown in Table 1.1.

Channels 1 and 2 were calibrated before and after launch, to provide direct quasi-linear conversion between the 10-bit digital numbers and the albedo. In the laboratory, twelve matched quartz-iodide lamps, which emit known radiance, are used. By turning on combinations of the lamps, a plot of radiance versus output digital counts is constructed for each channel. The slope $S_i$ and intercept $L_i$ of the straight line that best fits this plot is used to convert digital counts $C$ returned by the satellite to albedo (percent) $A_i$ at the Top Of Atmosphere (TOA):

$$A_i = a * C + b \tag{1.1}$$

Due to sensor degradation, pre-launch calibration coefficients $a, b$ for channel 1 and channel 2 changes during the in flight. As there are no on-board calibration devices, post-launch calibration to estimate the degradation rate has to be made against surface calibration targets, for example, ocean glint, desert reflection (see for example, Kaufman and Holben, 1993; Rao and Chen, 1995, 1996; Teillet et al.,

Table 1.2 Calibration Coefficients for NOAA-14 AVHRR (after Rao and Chen, 1996).

| Year | Julian Day | $Ch_1$ a | $Ch_1$ b | $Ch_2$ a | $Ch_2$ b |
|---|---|---|---|---|---|
| 1998 | 286 | -5.7845 | 0.1411 | -7.4040 | 0.1806 |
| 1998 | 267 | -5.7512 | 0.1403 | -7.3505 | 0.1793 |
| 1998 | 224 | -5.7246 | 0.1396 | -7.3077 | 0.1782 |
| 1998 | 163 | -5.6647 | 0.1382 | -7.2113 | 0.1759 |
| 1998 | 138 | -5.6380 | 0.1375 | -7.1685 | 0.1748 |
| 1998 | 104 | -5.6114 | 0.1369 | -7.1257 | 0.1738 |

1990), or using simultaneous aircraft or satellite measurements (see for example Leob, 1997; Marshall et al., 1999). The reflected solar radiation in channels 1 and 2 are in albedo units and are calculated using the pre-launch channel characteristics, and are stored as short integers in units of albedo (%)*100, and for NOAA-14, time dependent coefficients are used as listed in Table 1.2 based on the post-launch calibration by Rao and Chen (1996). In our study, we found independently the calibration error of Rao and Chen (1996), as described in Section 5.4.2.

Based on Rao and Chen (1999), their last post-launch calibration (Rao and Chen, 1996) overestimated the in-orbit degradation of the channel 1 and 2, resulting in spurious upward trends in the albedo time series. From Rao and Chen (1999), the more accurate AVHRR radiance/albedo is obtained by multiplying the last derived values (Rao and Chen, 1996) by correction factors as follow (Rao and Chen, 1999):

$$Channel\ 1 : CF_1 = 1.015 - 8.8 * 10^{-5} d + 1.3 * 10^{-8} d^2 \qquad (1.2)$$

$$Channel\ 2 : CF_2 = 1.037 - 1.8 * 10^{-4} d + 3.2 * 10^{-8} d^2 \qquad (1.3)$$

where $d$ is the number of days after the launch of NOAA-14 in December, 30, 1994. Channels 3, 4 and 5 can be calibrated in flight. More details on AVHRR instrumentation is provided by Kidwell (1995).

There are three formats for AVHRR data: High Resolution Picture Transmission (HRPT) data are full resolution image data transmitted to a ground station as they are collected. Local Area Coverage (LAC) are full resolution data that are recorded on an on-board tape for subsequent transmission during a station overpass. The average instantaneous field-of-view for both HRPT and LAC is 1.4 milliradians which yields a LAC ground resolution of approximately 1.1 km at the satellite nadir. Global Area Coverage (GAC) data are derived from a sample averaging of the full resolution AVHRR data. Four out of every five samples along the scan line are used to compute one average value and the data from only every third scan line are processed, yielding 1.1 km by 4 km resolution at the subpoint.

The data gathered by AVHRR have come to be widely used in many areas in addition to meteorology and oceanography. There are many other environmental applications which was never envisaged when the AVHRR was originally designed. Detailed description of the non-meteorological applications of AVHRR is provided by Cracknell (1997). The most successful example are vegetation indices (Cracknell, 1997). Other applications include, for example, ocean surface temperature, snow and ice cover, snow depth, volcano, forest fire, precipitation and water resources. In order to use AVHRR data for studies of the polar cloud properties and radiation budget, one needs to make cloud and surface discrimination at first, then one may proceed to retrieve surface optical properties, such as albedo, and cloud properties, including cloud optical depth, effective cloud particle size and cloud top temperature.

## 1.4 Atmospheric Attenuation in AVHRR Channels

While electromagnetic waves propagate through the atmosphere-earth system, they will be scattered or absorbed. The scattering by particles which are small compared to the wavelength of the light is called Rayleigh scattering. Rayleigh scattering by molecules depends inversely on the forth power of the wavelength, so Rayleigh scattering is very important in AVHRR channel 1, and its effect in channel 2 is much weaker than channel 1. Similarly, scattering by aerosol is significant in channel 1. Absorption by aerosol strongly depends on its composition. As channel 2 is broad and covers the strong water absorption band centered at 0.94 $\mu$m, the absorption of water vapor in channel 2 is significant. For channel 3 water vapor line absorption is the principal mechanism but several minor constituents, notably $CO_2$ as well as water vapor continum, also have a significant effect on the attenuation of solar radiation. As channel 3 includes the thermal radiation from the atmosphere, cloud and surface in addition to reflected solar radiation, channel 3 was seldom used before. AVHRR channels 4 and 5 are located in an atmospheric window region where the atmospheric transmittance is high. The water vapor continum absorption is the main absorption mechanism. $CO_2$ has a significant absorption band in channel 4.

Reflectivity over surface in different channels is different. AVHRR channel 1 is sensitive to both snow grain size and mass-fraction of soot while channel 2 is primarily sensitive to snow grain size and relatively insensitive to the mass-fraction of soot. Albedo in channel 2 decreases significantly over water or ponds on the ice. Over clouds, both channels 1 and 2 are sensitive to cloud droplet size and cloud optical depth, but solar reflectance in channel 3 is primarily sensitive to cloud

**Table 1.3** The Most Sensitive Physical Parameters in AVHRR Channels 1, 2 and 3.

| Channel | Atmosphere | Surface | Cloud |
|---|---|---|---|
| 1 | Rayleigh scattering<br>Haze | Snow $r_s$ and $s_t$<br>Surface albedo | $\tau$ and $r_e$ |
| 2 | Water vapor absorption<br>Rayleigh scattering | Snow $r_s$<br>Surface albedo | $\tau$ and $r_e$ |
| 3 (solar) | Absorption by water vapor, $CO_2$ | | $r_e$ |

droplet size. Thermal emissivities of clouds in AVHRR channels 3, 4 and 5 are different, which will be discussed in Section 2.2.5. A summary of the most sensitive physical processes in AVHRR channels 1, 2 and the solar reflectance in channel 3 is listed in Table 1.3. This is the basis for us to design the retrieval algorithms.

## 1.5 Radiative Transfer Model (RTM)

It is possible to carry out forward calculations to solve the radiative transfer equation for the radiance in any specified direction. Radiance sensors like AVHRR can be used to measure the upward radiance in specific channels, which include information about the complex atmosphere-cloud-surface system. To make use of satellite measurements to get the information "embedded" in this system is obviously an inverse problem. This approach is normally referred as "retrieval" or inversion problem. Radiative transfer theory provides a theoretical basis for the retrieval of information about parameters in the atmosphere-earth system that give rise to the measured radiances.

The radiative transfer method used for solution of the radiative transfer equation in this research is the DIScrete Ordinate Radiative Transfer model (DISORT) (Stamnes et al., 1988). In this model, the atmosphere is assumed to consist of multiple adjacent plane-parallel homogeneous layers in which the single-scattering

properties are constant within each layer but may vary from layer to layer. The physical processes considered include the absorption by atmospheric gases, such as $CO_2, O_3, O_2$ and $H_2O$, absorption/scattering/emission by stratospheric aerosols, Arctic haze particles, tropospheric aerosols and cloud droplets, and multiple scattering. Molecular scattering is computed from Rayleigh scattering theory (Penndorf, 1957). Parameterization of water cloud properties is taken from Hu and Stamnes (1993), and parameterization of ice cloud properties is from Fu and Liou (1993). The solar spectrum from 0.28-4 $\mu$m is divided into 24 bands with unequal spectral widths varying from 240 to 3040 $cm^{-1}$. In the thermal spectral region for wavenumbers less than 2500 $cm^{-1}$ the bandwidth is 20 $cm^{-1}$, and the exponential-sum fitting of transmissions (ESFT) method is adopted to simulate the gaseous absorption (Tsay et al., 1989, 1990) while calculating the thermal radiation in channel 4 and channel 5 of AVHRR.

Since the channel response function and the channel width of satellite sensors are not exactly consistent with that used in the radiative transfer model, MODTRAN (Moderate Resolution Model) is used to compute the clear sky optical depth profile for the atmospheric absorbers such as $H_2O, CH_4, O_3, N_2O, CO$ and $CO_2$ at the specified levels in the atmosphere. The tropospheric background aerosol model is used in the Arctic since the volume extinction coefficient of Arctic haze is similar to that of tropospheric aerosol (Blanchet and List, 1983).

A subarctic model atmosphere (McClatchey et al., 1971) is employed but the atmospheric temperature distribution and water vapor profile is taken from in-situ sounding data. The lower boundary is treated as follows: For snow-free conditions, the surface is treated as a Lambert reflector with an assigned albedo, and under snow covered conditions, an additional layer of snow is added at the bottom of the atmosphere to represent snow overlying tundra (or sea ice). Optical properties of snow is from Warren and Wiscombe (1980). The snow grains are assumed to be

spherical particles which allows the optical properties to be computed with Mie theory.

## 1.6 Cloud Discrimination from Satellite

The polar regions are characterized by low surface temperatures and solar insolation. The current satellite radiometers are therefore operating near the limit of their performance range, and the effects of instrument noise, calibration uncertainties, and digitization on radiance accuracy lead to a reduction in the sensitivity of satellite radiometers in the polar regions (Curry et al., 1996). Since the reflectance in the visible channel over a cloud and a snow surface is almost the same, and the temperature difference between the cloud and the surface is small in the Arctic, cloud discrimination is much more difficult in the polar regions than at mid- and low-latitude regions. Current data analysis demonstrates that there are significant differences between surface and satellite climatologies in the Arctic clouds (e.g. Rossow et al., 1993; Curry et al., 1996). For example, ISCCP analyses underestimate cloud amounts at both poles by about 10% in the winter (Schweiger and Key, 1992) and at least 25% in the summer (Rossow et al., 1993).

A single spectral feature, or a combination of 2 or 3 channels has been widely adopted for cloud discrimination using a simple threshold test, a ratio test, or the difference of brightness temperature between two channels. Much more complicated cloud discrimination and classification techniques tend to use both the spectral and the textural features, in combinations with the fuzzy logic and/or the neural network approaches for determination of feature clusters and classifiers (see for example, Konvalin et al., 1998). Use of textural information (see for example Ebert, 1987, 1989, 1992; Welch et al., 1988, 1992) and temporal coherence may improve cloud detection in the Arctic, but further algorithm validation, which was

hampered by lack of observational data before (Curry et al., 1996) is urgently required.

## 1.7 Cloud Retrievals

Cloud amount or cloud cover fraction, a bulk cloud property, has become a general product of many meteorology satellites. Two other important parameters characterizing the microphysics of warm clouds are the cloud effective droplet size ($r_e$) and the LWP because the single scattering albedo $\omega$, the extinction coefficient $k$, and the asymmetry factor $g$ can be accurately parameterized in terms of $r_e$ and LWP (Hu and Stamnes, 1993). Extensive measurements of cloud amount, cloud-top temperature and cloud optical thickness ($\tau$) are being made by the ISCCP (Rossow and Schiffer, 1991), in which visible radiance is used to infer the cloud optical thickness assuming that the effective droplet size of all clouds is 10 $\mu$m. Such an assumption makes the retrieved values of $\tau$ uncertain by 15-25% for warm clouds (Rossow et al., 1989; Nakajima and King, 1990) and by 30-50% for thin ice clouds due to the uncertainty in the ice particle scattering phase function (Minnis et al., 1993). Retrieval of cloud effective droplet radius, cloud optical depth and, sometimes cloud top temperature has been investigated in recent years (e.g. Key, 1999; Han et al., 1999; Nakajama and Nakajima, 1994; Nakajima and King, 1990). The major sources of uncertainty are in the observed radiance (Han et al., 1999), detection of cloud pixel, and the forward RTM as multiple solutions may exist for retrieval of cloud optical depth using visible reflectance at very low solar zenith angle or very thin cloud (Nakajima and King, 1990). Agreement of retrieved effective droplet size from satellite with in situ measurement is relatively good (Han et al., 1994; Nakajima and Nakajima, 1994), but the cloud optical depth retrieved from satellite is consistent with that determined from surface measurements only when

the cloud optical depth is less than 10 as indicated by Min and Harrison (1996). Barker et al. (1998) pointed out that the cloud optical depth from the ISCCP data is 1.6-2.25 times smaller than that derived from surface data. ISCCP analysis of cloud properties is most reliable in the summertime when liquid water clouds are most prevalent and the surface reflectivity is lower, but it is still somewhat uncertain, and the spring and autumn values are significantly overestimated (see for example, Curry et al., 1996). Due to the large spatial and temporal variation of cloud properties, comparison of satellite-derived cloud properties over a large spatial domain with measurements taken at a specific location at the surface is very difficult. So, further validation with more data is very important. The SHEBA (Surface Heat Budget of the Arctic Ocean) and ARM (Atmospheric Radiation Measurement) data sets provide this opportunity.

## 1.8 Retrievals of Surface Albedo or Snow Grain Size and Soot

The polar regions are covered by snow or ice surface most of the year. The surface albedo may be underestimated as much as 30% if the Lambert assumption is used as compared to a snow surface with bidirectional reflectance properties (Han et al., 1999). So, in order to account for the surface bidirectional reflectance accurately, snow or ice surfaces have to be treated in a way different from the Lambert approximation. From the parameterization of Warren (1982), two variables, snow grain size and mass fraction of soot, can be used to simulate accurately the snow optical properties. The radiation in the sea ice is controlled by the absorption of pure ice, as well as scattering and absorption of inclusions, such as brine pockets, air bubbles, solid salts and other impurities (Jin et al., 1994). Surfaces other

than snow and ice will be treated as Lambert reflectors and AVHRR channels 1 and 2 will be used to retrieve the narrowband albedos individually. Then a NTB conversion will be used to get the broadband albedo.

## 1.9 Validation Data from SHEBA, ARM/NSA and FIRE-ACE

Lack of in-situ measurement data in polar regions constitutes a major obstacle for improving algorithms for satellite retrieval of cloud and surface properties. Evaluation of satellite retrieval results assessing their precision and uncertainty is required for improvement of the retrieval algorithms. In this study, in-situ measurements are available from three programs. The SHEBA was conducted between October, 1997, and October, 1998. The First ISCCP Regional Experiment-Arctic Cloud Experiment (FIRE-ACE) was conducted between April and July, 1998. The Atmospheric Radiation Measurement at North Slope of Alaska site (ARM/NSA) started in April, 1998, and it is still on-going.

SHEBA is a coordinated program aimed at addressing the interaction of surface energy balance, atmospheric radiation and clouds over the Arctic Ocean. The SHEBA project is focused on enhancing understanding of the key processes that determine ice albedo feedback in the Arctic pack ice and on applying this knowledge to improve climate modeling. The Canadian Coastguard icebreaker *Des Groseilliers* was used as a floating station deployed in the Arctic Ocean at 75°16.3′N, 142°41.2′W. The icebreaker was frozen into the pack ice in October, 1997, and left to drift for a year. The SHEBA Ice Camp drifted considerably northwestward, and it was at 78.5°N and 166°W by the end of July, 1998. One-year-around composite measurements at the Ice Camp station from October 1997

to October 1998 were made, including radiation measurements at the surface, atmospheric profiling by balloon-borne sounding systems, Radar and Lidar systems. Clouds were observed by several instruments. One crucial element of SHEBA was to extend the process-oriented observations and models to larger-scales. Collocated AVHRR and surface data over SHEBA Ice Camp during April-August, 1998 is the main data source for the satellite retrieval efforts investigated in this research. The retrieved results will be compared with surface observations of clouds, surface albedo measurements and surface radiation measurements. Sounding profiles over SHEBA are also used.

ARM is a long term measurement program. The ARM Program has established and operates field research sites, called Cloud and Radiation Testbeds (CARTs), to study the effects of clouds on global climate change. Three primary locations, the Southern Great Plains (SGP), the Tropical Western Pacific (TWP), and North Slope of Alaska (NSA), were identified as representing the range of climate conditions that should be studied. Each CART site has been heavily instrumented to gather massive amounts of climate data. Using these data, scientists hope to better understand the effects and interactions of sunlight, radiant energy, and clouds on temperatures, weather, and climate. Most instruments deployed by ARM at SHEBA are similar to those deployed at ARM/NSA in Barrow. The data set with a long-term measurement at ARM/NSA in Barrow will be useful for future validation and improvement of the algorithms developed in this thesis.

FIRE-ACE interacted closely with SHEBA and ARM. The main goal of FIRE-ACE was to examine the effects of Arctic clouds on radiation exchange between the surface, the atmosphere, and space; as well as the influence of surface characteristics of sea ice, leads, and ice melt ponds on the evolution of boundary layer clouds. Observations collected will be used to improve current climate model simulations of the Arctic climate, especially with respect to clouds and their effects on the

surface energy budget, satellite remote sensing of cloud and surface characteristics and understanding of cloud-radiation feedbacks in the Arctic (Curry et al., 2000). FIRE-ACE used research aircraft to obtain remote and in-situ measurements of the properties of clouds and the sea ice/ocean surface. The NASA ER-2 flew at an altitude of 20 km with a suite of remote sensors that can be used to infer the characteristics of the surface and cloud. Cloud retrieval from the MODIS Airborne Simulator (MAS) will be used to evaluate AVHRR cloud retrieval as discussed in Chapter 5. Cloud effective droplet size data from the medium-altitude aircraft, the NCAR C-130 will also be used to evaluate the AVHRR retrieval of cloud effective droplet size.

## 1.10 Research Emphases

In Chapter 2 of this thesis, an automatic cloud mask technique is presented, which is specifically developed for cloud discrimination over snow/ice surface in the Arctic Ocean. Spectral features in the five channels of AVHRR are used for the cloud mask. In particular, we use the solar reflectance in channel 3. Normalized reflectance in channel 3 of AVHRR is used after removing the thermal radiation emitted from the lower atmosphere and the underlying cloud and surface with the help of channel 4. Correction of the anisotropic effects in channel 3 was made by invoking the Anisotropic Reflectance Factor (ARF) based on model simulations. After anisotropic correction, the albedo at the TOA is obtained. A threshold function is obtained for automatic cloud discrimination. A cloudy pixel is identified as low water cloud, cirrus, cirrus over water cloud or partly cloudy cover. Variation of cloud amounts and frequency of occurrence for different cloud types over SHEBA are examined.

In Chapter 3, snow grain size and mass fraction soot were retrieved from

AVHRR channels 1 and 2 for snow surface, and broadband surface albedo was retrieved based on the reflectance in channels 1 and 2 and through the NTB conversion. The retrieved broadband albedo is compared with the SHEBA surface measurements of Perovich et al. (1999).

In Chapter 4, the cloud optical depth is retrieved from the downwelling solar irradiance measured by the Precision Spectral Pyranometer (PSP) installed at the surface. Seasonal variations of cloud optical depth over the SHEBA Ice Camp during April to August, 1998 are presented.

In Chapter 5, a cloud retrieval algorithm was developed and used to retrieve cloud effective particle size, cloud optical depth and cloud top temperature from AVHRR measurements. Uncertainty analyses were conducted to investigate the accuracy of cloud properties in the Arctic retrieved from AVHRR data. The effects of vertically inhomogeneous stratification of the cloud, as well as cloud phase on the retrieval is discussed. MAS data taken on the platform of the NASA ER-2 and in-situ measurements of cloud effective radius from the NCAR C-130 aircraft, and cloud optical depth derived from surface PSP measurements are used for validation. We found that the effective cloud droplet size retrieved from AVHRR channel 3 is close to the true value. However, cloud optical depth tends to be overestimated, especially during April-May.

In Chapter 6, the solar radiation budget at the surface, in the column of the atmosphere and at the TOA was estimated using a RTM with the inputs of surface albedo and cloud properties derived from the AVHRR measurements. Uncertainties of SRB estimated from satellite are evaluated. This method was applied to estimate the SRB during the melt season in 1998 in the Arctic and the results are compared with SHEBA surface measurements.

A summary discussion and conclusion of the thesis are presented in Chapter 7.

# Chapter 2

# Discrimination of Clouds and Snow Cover over the Arctic Ocean from Daytime AVHRR Data

Understanding of polar clouds and their interaction with radiation is of particular importance to the study of regional and global change, but there are large uncertainties (IPCC, 1990; Moritz et al., 1993; Moritz and Perovich, 1996; Curry et al., 1996). Use of satellites for this study is economic and has a promising future. Discrimination of cloudy pixels from the clear pixels is a necessary first step. Monitoring of cloud movements from satellites has been one of the basic tool for weather forecasting. However, satellite remote sensing of clouds encounters significant obstacles in the Arctic because there is little contrast in the visible channels and small contrast in infrared channels between the clouds and the underlying snow or ice surface. The frequent isothermal conditions or temperature inversions in the lower troposphere and significant bidirectional reflectance effects at the low

solar illumination angle in the polar regions make it even more difficult (Garand and Nadon, 1998; Lubin and Morrow, 1998; Curry et al., 1996). So, discrimination of clouds from snow/ice surfaces is much more difficult than from other surfaces on the earth. The largest discrepancies in cloud fraction among different satellite climatology studies were found in the polar region (Key and Barry, 1989; Curry and Ebert, 1992; Rassow et al., 1993; Garand and Nadon, 1998), so validation and improvement of current cloud discrimination algorithms in the polar region is of particular importance. The SHEBA, NSA/ARM and FIRE/ACE programs provide unique data sets with measurements relevant for validation of the current algorithms.

## 2.1 Background

Considerable efforts on cloud detection, for example ISCCP (International Satellite Cloud Climatology Project) (Rossow et al., 1993) and APOLLO (AVHRR Processing scheme Over Land, cLoud and Ocean) (Arking, 1985; Kriebel and Saunders, 1988; Kriebel et al., 1989; Gesell, 1989), have led to reliable cloud masks applicable at low and mid latitudes. The most common technique is the threshold test based on visible and infrared data. In the ISCCP cloud masking algorithm, as described by Rossow (1989) and Rossow and Garder (1993b), the observed radiance in two channels (0.6 $\mu m$ and 11 $\mu m$) are compared with their corresponding clear-sky values. Rossow and Garder (1993b) summarized the five steps for ISCCP cloud detection as follows: (i) space contrast test on a single infrared image; (ii) time contrast test on three consecutive visible images; (iii) cumulation of space/time statistics for infrared and visible images; (iv) construction of clear-sky composites for infrared and visible images every 5 days at each diurnal phase and location; and (v) radiance threshold for infrared and visible radiance for each pixel.

The AVHRR Processing scheme Over cLoud Land and Ocean (APOLLO) (Kriebel and Saunders, 1988; Kriebel et al., 1989; Gesell, 1989) uses AVHRR channels 1 through 5 based on a series of threshold tests, i.e. brightness temperature threshold test, reflectance ratio of channels 2 to 1, temperature difference between channels 4 and 5, and spatial uniformity over ocean (Kriebel et al., 1989). A pixel is defined as cloud contaminated if it fails in any single test for a clear pixel, so in that sense it is cloud conservative.

The NOAA Cloud Advanced Very High Resolution Radiometer (CLAVR) algorithm (Phase I) relies on multispectral decision, channel differences, and spatial differences, and then employs a series of sequential decision tree tests based on all five channels of AVHRR (Stowe et al., 1994). A 2×2 global area coverage (GAC) pixel array is used to identify the regions, that is, if all four pixels satisfied just one of the cloud tests, then the array is labeled as 100% cloudy, otherwise, it is labeled as mixed or 50% cloudy. Subsequent phases of CLAVR used dynamic thresholds and pixel by pixel classification. Cloud-contaminated pixels are radiatively typed as belonging to low stratus, thin cirrus or deep convective cloud systems.

A modification of the ISCCP cloud detection procedure for polar application was made by Key and Barry (1989), who used Arctic AVHRR and SMMR (Scanning Multichannel Microwave Radiometer) data. Composites of 5-day periods were used to find the clear sky for the final multispectral thresholding of the daily data. However, lack of "ground truth" makes testing and validation difficult (Key and Barry, 1989). The long insolation in summer leads to significant change of surface physical conditions due to the rapid melting of snow and ice in the melting season, June to August. The high cloud coverage in the autumn makes it difficult to use 5-day-period data to get clear sky surface information. An algorithm suitable to derive cloud amounts at night from the brightness temperature difference in infrared channels of AVHRR was applied in the Antarctic by Yamanouchi et al. (1987).

Comparison of cloud fraction obtained by the brightness temperature difference between channels 3 and 4 (BTD34) in summer agreed approximately with manual cloud amounts from analysis of two months data in the Antarctic (Yamanouchi and Kawaguchi, 1992), but use of an uniform threshold of BTD34 is almost impossible. An effort to employ the threshold functions was made by Hutchson and Locke (1995) for automatic bi-spectral cloud analysis. Garand and Nadon (1998) used the 3.7 $\mu$m channel of AVHRR and available information on atmospheric and ground temperature, for example from atmospheric sounding profiles, in the Arctic for cloud discrimination, but validation is lacking.

From all the above work, we see that most cloud mask algorithms rely on threshold tests in the visible and infrared channels, or features derived from simple relationships between channels, for example, the brightness temperature difference test or the ratio test based on two channels. The thresholds are normally predetermined or are decided dynamically. The advantage of this method is its simplicity and also that it can be used easily for pixel-by-pixel processing. However, it is almost impossible to use a uniform threshold. More complicated methods use both the textural and spectral features, such as pattern recognization, Fuzzy Logic or neutral network approaches for groups of pixels in the image (Ebert, 1987, 1989, 1992; Welch et al., 1988, 1992; Simpson and Keller, 1995; Baum et al., 1997; Konvalin et al., 1998; Lubin and Morrow, 1998). Texture extracted in regions of $16 \times 16$ pixel or higher is preferred because too small regions lead to unstable textural measures (Steffen et al., 1993). Accuracy greater than 80% was reported with this approach (Steffen et al., 1993; Lubin and Morrow, 1998). However, all these methods depend on a set of pre-chosen images (called "Training Data", for which the clouds have been discriminated by experienced meteorological observers or by other methods) to select the spectral or textural features, so further validation is no doubt required in the Arctic (Dan and Morrow, 1998; Curry et al., 1996). An

evaluation of cloud detection and classification based on the maximum likelihood method (Ebert, 1987) was made by Lubin and Morrow (1998) using AVHRR data over the Arctic Ocean. They found that 81% of the classifications are consistent with surface measurements. However, only one month of data from July to August has been tested in the maritime Arctic.

## 2.2 Automatic Cloud Discrimination over High Arctic Ocean

For nomenclature, we shall denote the satellite measured radiance as $L_\lambda$, normalized reflectance as $R_\lambda$, and refer to the infrared radiance as brightness temperature denoted as $BT_\lambda$. Subscripts refer to the wavelength in $\mu$m at which the measurement is made. The normalized isotropic reflectance at the TOA is:

$$R_\lambda = \frac{\pi L_\lambda}{S_\lambda \cos\theta_0} \tag{2.1}$$

where $S_\lambda$ is the extraterrestrial solar irradiance, and $\theta_0$ is the solar zenith angle.

The brightness temperature in channels 3, 4, and 5 is the equivalent blackbody temperature determined from the Planck function:

$$B_\nu(T) = \frac{C_1 \nu^3}{exp(C_2 \nu / T) - 1} \tag{2.2}$$

Here $C_1 = 2hc^2 = 1.191066 \times 1.0^{-5} mW\, m^{-2} sr^{-1} (cm^{-1})^{-4}$, $C_2 = hc/k = 1.438833$ cm-deg, $\nu$ = wavenumber in $cm^{-1}$, and $T$ is the brightness temperature in Kelvins. The measured spectral radiance is calculated as:

$$L_\nu = \frac{\int B_\nu \phi_\nu d\nu}{\int \phi_\nu d\nu} \tag{2.3}$$

where $\phi_\nu$ is the spectral response function. The radiance measured by AVHRR channels 3, 4 and 5 is assumed to arise from blackbody sources as described by the Planck function. Thus, by replacing the blackbody spectral radiance in the Planck function with $L_\nu$, we get the brightness temperature $T_B$ as:

$$T_B = \frac{C_2 \upsilon_c}{ln[(C_1 \upsilon_c^3 / L_\nu) + 1]} \tag{2.4}$$

where $\upsilon_c$ is the effective wavenumber, which is a weak function of the response function and the measured radiance, as shown by Davis (1993). We will denote the brightness temperature in AVHRR channels 3, 4 and 5 as BT3, BT4 and BT5, and the reflectance in channels 1, 2 and 3 as $R_1$, $R_2$ and $R_3$.

In this chapter, an automatic cloud discrimination method is developed for cloud discrimination and surface classifications using multispectral AVHRR information and it is applied to daytime AVHRR data between April and August, 1998 in the high Arctic. In this algorithm, normalized isotropic reflectance in channel 3 ($R_3$) is used after removal of the thermal component. An improvement to estimate $R_3$ approximately is achieved. Due to the strong bidirectional reflectance, a method to derive the anisotropy-corrected albedo ($r_3$) at the TOA is developed by dividing the isotropic reflectance by the Anisotropic Reflectance Factor (ARF). The ARF is obtained from model simulations. Cloud discrimination based on the anisotropy-corrected albedo, $r_3$, is preferable because the threshold is a function of solar zenith angle only, and can be expressed as a 2nd-order polynomial in $sec(\theta_0)$. However, this method is difficult to use to discriminate thin ice clouds from snow/ice surface due to the error in the calculation of $r_3$. The brightness temperature difference between channels 4 and 5 will be used for thin ice cloud discrimination.

The following threshold tests are used for cloud discrimination:

- Solar reflectance of channels 1 ($R_1$ ) and 2 ($R_2$ ):
- Ratio test between channels 1 and 2, i.e. $R_{21} = R_2/R_1$ :
- Brightness temperature of channels 4 (BT4):
- Brightness temperature difference between channels 4 and 5, i.e. BTD45 = BT4-BT5:
- Albedo in channel 3 ($r_3$), where the thermal component has been removed from the measured radiance and an anisotropic correction had been made.

The choice of thresholds was based on radiative transfer simulations and examination of dozens of images. For application of this algorithm over the Arctic Ocean, more than 100 images from April to August, 1998 over SHEBA have been used to validate the choice of thresholds and to compare with composite surface meteorological observations, as well as radar and lidar data from SHEBA. This method is expected to be very useful for further studying the Arctic cloud properties by reprocessing the AVHRR data in the past 20 years. It also could be extended for use over any snow/ice surfaces at middle and high latitudes.

The cloud detection scheme is composed of the cloudy/clear discriminator, the snow/sea-ice discriminator, and a simple cloud classification. It starts with single-pixel (1 $km$ FOV) tests, and we first discriminate the clear pixels from cloudy pixels. For cloudy pixels, five types of clouds including cirrus, cirrus over liquid water cloud, mixed phase cloud, low water cloud and partly cloudy coverage are discriminated. For clear pixels, snow pixels were identified in order to retrieve snow grain size and mass fraction of soot (see next chapter).

### 2.2.1 Estimation of Reflectance in 3.7$\mu$m Channel ($R_3$)

AVHRR channel 3 data historically have been contaminated by highly variable sensor noise which generally has hampered its use in the classification of polar scenes (Simpson and Keller. 1995). However. as the reflectivity at 3.7 $\mu$m for liquid water clouds is much higher than for snow/ice. reflectance of channel 3 ($R_3$) becomes useful for discriminating clouds from the underlying snow/ice surface (see for example. Gesell. 1989: Steffen et al.. 1993). and particularly for discriminating between water and ice surface features and between water and ice clouds (Steffen et al.. 1993: Hutchison and Locke. 1997). Reflectance of solar radiation in channel 3 over clouds also results in significant increase of the brightness temperature of channel 3. so the difference of brightness temperature between AVHRR channels 3 and 4 (BTD34=BT3-BT4) over clouds becomes much larger than for clear sky. This is why BTD34 has also been used directly to detect cloud over snow and ice surface (see for example. Yamanouchi and Kawaguchi. 1992: Simpson and Keller. 1995). However. BTD34 strongly depends on the solar zenith angle. which makes the choice of threshold difficult. The normalized reflectance in channel 3 obtained by dividing by the cosine of solar zenith angle can be used to compare scenes (Steffen et al. 1993). However. even over ice and ocean. the normalized reflectance values were observed to vary substantially across a single line (Steffen et al. 1993). so the bidirectional reflectance function may have to be used to normalize this spectral signature.

The measured daytime radiance in channel 3 includes reflection from solar radiation as well as the thermal radiance emitted from the earth surface. atmosphere and clouds. Therefore to obtain the reflected component in AVHRR channel 3. the undesired thermal component. which has the same magnitude as the solar reflectance. has to be removed from the weak signal in channel 3. However. accu-

rate estimation of $R_3$ is almost impossible before we know the cloud microphysical properties, like effective particle size, optical depth, cloud phase, cloud top temperature and underlying surface temperature. An approximate estimation of the thermal radiation in channel 3 can be made by way of the brightness temperature in channel 4. Kaufman and Nakajima (1993) used the effective temperature derived from channel 4 and the optical thickness guessed from channel 1 to estimate thermal radiation in channel 3 and thus get the solar reflectance of the cloud. Here, the emissivity in channels 3 and 4 are assumed to be approximately the same. However, the emissivity for thick clouds at 3.7 $\mu$m is lower than that at 11 $\mu$m (Yamanouchi and Kawaguchi, 1992). For cirrus, the difference in emissivity between channels 3 and 4 is more significant according to the analysis of measurements obtained by instruments deployed on the ER-2 platform (Ackerman et al., 1995). The emissivity also varies with view angle, which can produce differences between thermodynamic temperature and brightness temperature as large as 3 K at wavelengths 12 to 14 $\mu$m (Dozier and Warren, 1982). This view angle dependence makes BTD34 work incomplete as a cloud discriminator (Yamanouchi and Kawaguchi, 1992). Following the methodology to estimate the surface temperature from channels 4 and 5 in clear sky, we used the night AVHRR data over SHEBA during March and April to get the following equation:

$$T_{3t} = 0.79 + 1.004 * BT4 + 0.3 * BTD45 + 0.103 * BTD45^2 \qquad (2.5)$$

where $T_{3t}$ is the equivalent brightness temperature for the thermal component in channel 3.

This expression is obtained from statistical analysis of dozens of images at night. This is an approximate relation because for cirrus, satellite measured BT3 could be higher than that estimated from the above equation. In the Arctic summer, it may

be possible for BT3<BT4 over low cloud or fog (Saunders and Kriebel, 1988). We are certain that this approximation to the equivalent brightness temperature for the channel 3 thermal radiance is better than just using BT4. As we do not have night in the Arctic during the summer, this relation is used to get an approximate equivalent brightness temperature for channel 3 thermal emission in the summer time.

From the Planck function, an error of ±2 K in brightness temperature in channel 3 (assuming the cloud top temperature as 270 K) leads to an error in the calculated radiance of 10%, and an error of ±1 K leads to an error in the calculated radiance of 5% as shown in Figure 2.1. This error increases as the temperature decreases.

The normalized reflectance $R_3$ at the TOA which can be calculated as follows:

$$R_3 = \frac{L_3 - \varepsilon_3 \int o_3(\lambda) B_\lambda(T_{3t}) d\lambda}{\mu_0 F_{03}/\pi} \tag{2.6}$$

where $L_3$ is the measured radiance in channel 3, $o_3(\lambda)$ is the sensor spectral response function in channel 3, and $B_\lambda$ is the Planck function, $\lambda$ is the wavelength, $F_{03}$ is the extraterrestrial solar irradiance, and $\varepsilon_3$ is the emissivity in channel 3.

Since $0 \leq \varepsilon_3 \leq 1$, we get:

$$R_3 \geq \frac{L_3 - \int o_3(\lambda) B_\lambda(T_{3t}) d\lambda}{\mu_0 F_{03}/\pi} \equiv R_3' \tag{2.7}$$

For optically thick clouds where the transmittance can be assumed to be negligible, $\varepsilon_3 = 1 - R_3$, and we obtain:

$$R_3 = \frac{L_3 - \int o_3(\lambda) B_\lambda(T_{3t}) d\lambda}{\mu_0 F_{03}/\pi - \int o_3(\lambda) B_\lambda(T_{3t}) d\lambda} \equiv R_3'' \tag{2.8}$$

Physically, for the same type of cloud, $R_3$ for a thin cloud can not be larger than for a thick cloud. So we have:

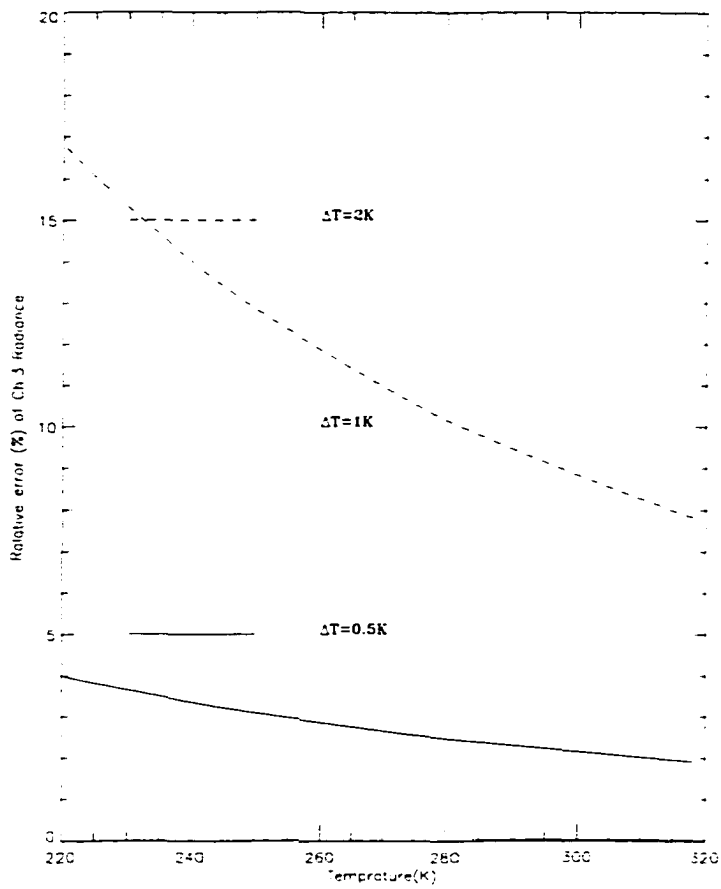


**Figure 2.1** Error of radiance in channel 3 versus temperature.

$$R_3' \leq R_3 \leq R_3'' \tag{2.9}$$

and.

$$R_3'' - R_3' = \frac{L_3 - \int o_3(\lambda) B_\lambda(T_{3t}) d\lambda}{\mu_0 F_{03}/\pi - \int o_3(\lambda) B_\lambda(T_{3t}) d\lambda} - \frac{L_3 - \int o_3(\lambda) B_\lambda(T_{3t}) d\lambda}{\mu_0 F_{03}/\pi}$$

$$= (L_3 - \int o_3(\lambda) B_\lambda(T_{3t}) d\lambda)(\frac{1}{\mu_0 F_{03}/\pi - \int o_3(\lambda) B_\lambda(T_{3t}) d\lambda} - \frac{1}{\mu_0 F_{03}/\pi})$$

$$= (L_3 - \int o_3(\lambda) B_\lambda(T_{3t}) d\lambda) \frac{\int o_3(\lambda) B_\lambda(T_{3t}) d\lambda}{[\mu_0 F_{03}/\pi - \int o_3(\lambda) B_\lambda(T_{3t}) d\lambda] * \mu_0 F_{03}/\pi}$$

For cloud temperature at 273 K, thermal emission radiance in channel 3 is no more than 0.07 $W/m^2$. For solar zenith angle $\theta_0 = 60^\circ$, $\mu_0 = 0.5$, and for extraterrestrial solar irradiance in channel 3 $F_{03} = 6.98$ $W/m^2$, $\mu_0 F_{03}/\pi$ is 15 times larger than the thermal radiance in channel 3, so we can assume

$$\mu_0 F_{03}/\pi \gg \int o_3(\lambda) B_\lambda(T_{3t}) d\lambda.$$

Since the thermal and solar component of channel 3 are about the same magnitude, that is:

$$L_3 - \int o_3(\lambda) B_\lambda(T_{3t}) d\lambda \sim \int o_3(\lambda) B_\lambda(T_{3t}) d\lambda.$$

so we get,

$$R_3'' - R_3' \sim \frac{(L_3 - \int o_3(\lambda) B_\lambda(T_{3t}) d\lambda)^2}{(\mu_0 F_{03}/\pi - \int o_3(\lambda) B_\lambda(T_{3t}) d\lambda)^2} = (R_3'')^2. \tag{2.10}$$

$$R_3'' - R_3' \sim (R_3'')^2 \sim (R_3')^2 \tag{2.11}$$

So, the error in the estimation of $R_3$ is about $(R_3'')^2$. $R_3''$ is smaller than 1, and for a typical value $R_3'' = 0.3$, the error in $R_3$ is less than 0.01. Thus, we can get a very good approximate value for $R_3$ from the above calculation. From our calculations to $R_3''$, $R_3'$ for dozens images over SHEBA Ice Camp during May, 1998, the average for cloudy pixels, identified by simple threshold $R_3' > 0.08$ (Gesell, 1989), is shown in Figure 2.2. The difference is less than 5% between $R_3''$ and $R_3'$. As the difference between $R_3''$ and $R_3'$ also represents the uncertainty of $R_3$, we can say the uncertainty of $R_3$ estimation is about 5%.

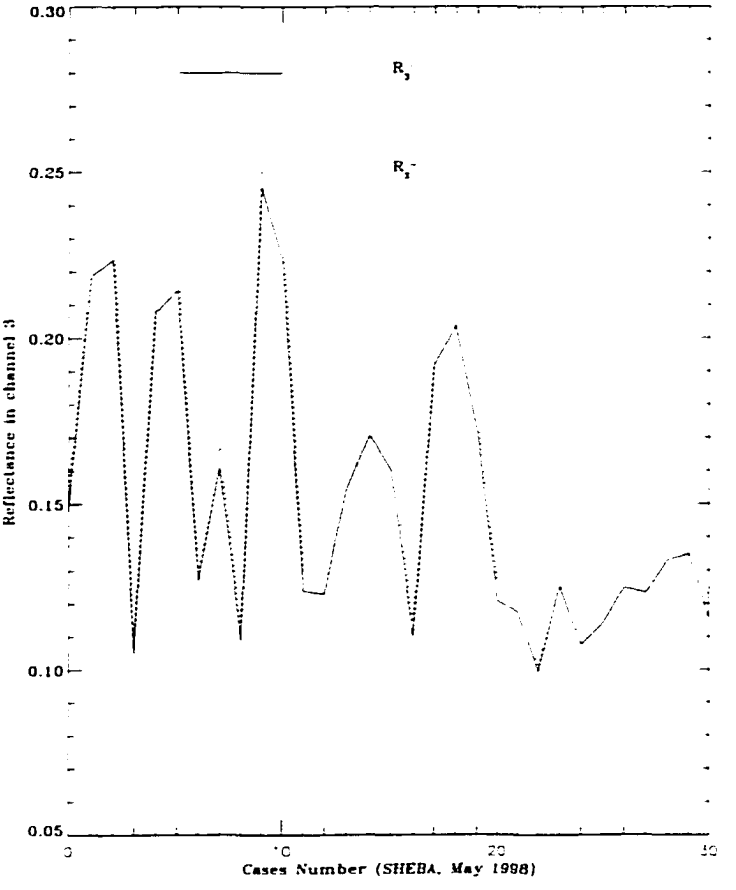


Figure 2.2 Comparison of the averaged $R_3'$ and $R_3''$ for cloudy pixels using AVHRR data over SHEBA Ice Camp during May, 1998 .

### 2.2.2 Anisotropic Correction

Due to effects of bidirectional reflectance over snow/ice surface, $R_3$ varies significantly with the viewing geometry. Model simulations show that $R_3$ increases significantly with solar zenith angle, view angle and relative azimuthal angle. $R_3$ is also very sensitive to the cloud droplet effective radius but almost insensitive to the optical depth (or liquid water content) when optical depth is larger than 10. Only for thin clouds is $R_3$ sensitive to the optical depth (or liquid water path).

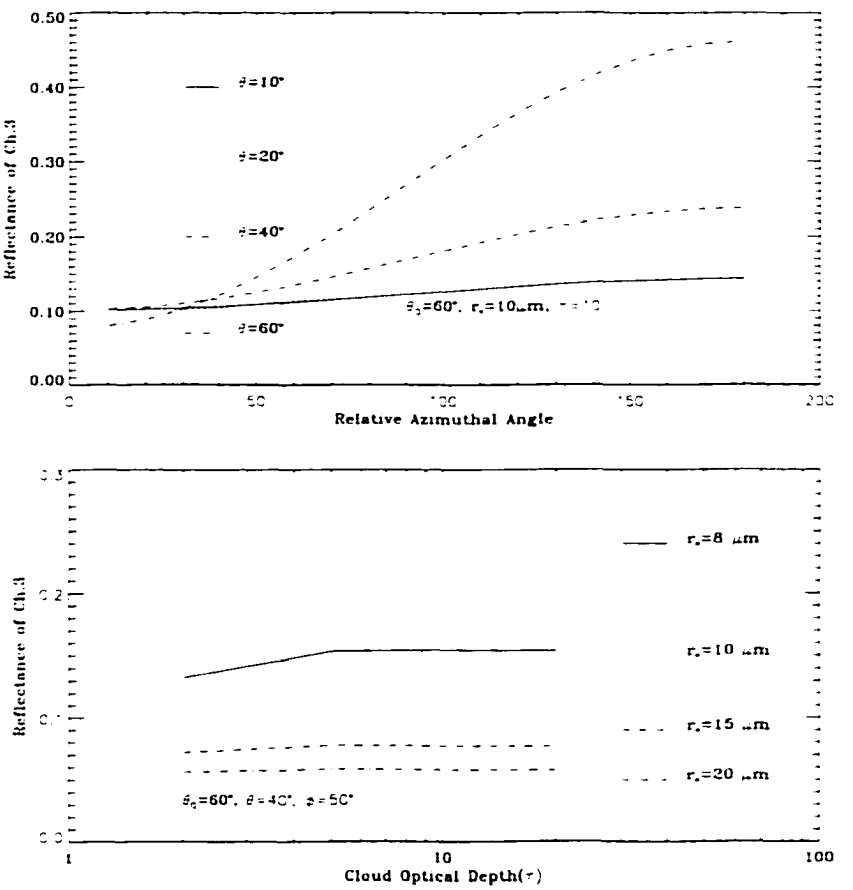


**Figure 2.3** $R_3$ as a function of $\theta$ and $\phi$ for $\theta_0 = 60°$, $r_e = 10$ $\mu$m and $\tau = 10$ (upper panel), and as a function of $r_e$ and $\tau$ under the condition of $\theta_0 = 60°$, $\theta = 40°$ and $\phi = 50°$ (lower panel) for water clouds

.

When cloud droplet effective radius is smaller than 15 $\mu$m, $R_3$ is normally larger than 0.08. For water clouds, cloud droplet effective radius is normally less than 15 $\mu$m (Han et al., 1994), so setting $R_3 = 0.08$ as a threshold for liquid water cloud (Gesell, 1989) looks fine in mid-latitudes, but at very high latitudes, this threshold is too low. For cloud droplet effective radius larger than 20 $\mu$m or for ice cloud, $R_3$ can be smaller than 0.08, so this threshold may be too high. A better way to improve cloud detection using channel 3 reflectance is to do bidirectional

correction to isotropic reflectance to get albedo at the TOA.

The Anisotropic Reflectance Factor (ARF) is the ratio of the Bidirectional Reflectance Distribution Function (BRDF) and the TOA albedo. The ARF is also equivalent to the ratio of the isotropic albedo to the actual albedo:

$$ARF(\theta_0, \theta, \phi) = \frac{\pi I(\theta_0, \theta, \phi)}{F_u(\theta_0)} = \frac{R_\lambda(\theta_0, \theta, \phi)}{\alpha(\theta_0)}$$

so,

$$\alpha(\theta_0) = \frac{R_\lambda(\theta_0, \theta, \phi)}{ARF(\theta_0, \theta, \phi)} \tag{2.12}$$

where $F_u(\theta_0)$ is the upward flux, $R_\lambda(\theta_0, \theta, \phi)$ is the reflectance and $\alpha(\theta_0)$ is the actual albedo, which is independent of view angle and the relative azimuthal angle. Thus, the ARF represents the departure of the reflected radiation field from an isotropic distribution and is unity if the reflected radiation is isotropic. Using the ARF to correct the satellite-derived reflectance, we can get the albedo at TOA ($r_3$) by dividing $R_3$ by the ARF. However, ARF is not only a function of viewing geometry, it also depends on cloud effective radius. If the cloud layer is assumed to be a homogeneous layer in our plane parallel RTM, the reflectance field over the cloud may be similar to that over the surface, and the difference of cloud effective radius corresponds to the difference of surface albedo. From this similarity we borrow the concept of anisotropic correction. Model simulations prove this possibility, as shown in Figure 2.4, the distribution of ARF over cloud with $r_e = 10$ $\mu$m as a function of view angle and azimuthal angle is almost similar to that over cloud with $r_e = 20$ $\mu$m, except that the values of ARF at $r_e = 10$ $\mu$m is a bit larger than that at $r_e = 20$ $\mu$m.

Broadband ARF has been compiled by Taylor and Stowe (1984) for a variety of different surfaces using Nimbus 7 Earth Radiation Budget data. Because correction

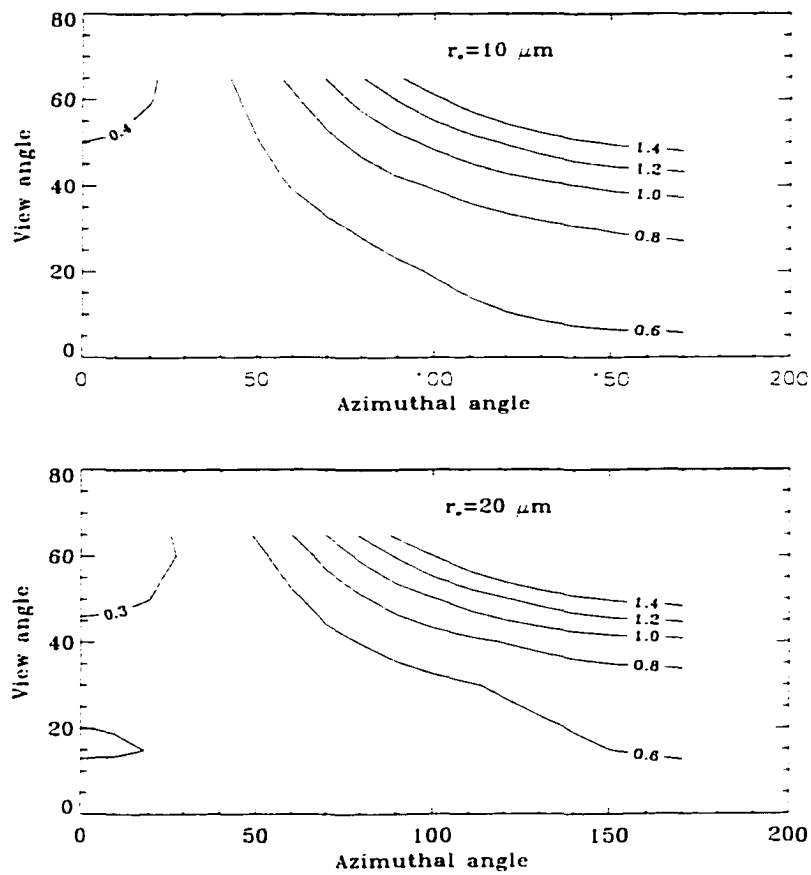


**Figure 2.4** Contour plots of ARF over water clouds with $r_e = 10$ $\mu$m (upper panel) and $r_e = 20$ $\mu$m (lower panel). $\theta_0 = 60^0$ .

of $R_3$ requires the ARF in the narrow band of channel 3, we use a RTM for the coupled atmosphere-snow surface system to calculate the ARF. In this model, we need not make any assumption about the surface reflectance. As shown in Figure 2.4, for a liquid water cloud with smaller effective droplet radius, ARF is larger, but the pattern of the scattering field is similar for $r_e = 10$ $\mu$m and $r_e = 20$ $\mu$m. Given a satellite scene without any information of cloud microphysics, we do not know the cloud droplet effective radius. We assume $r_e = 20$ $\mu$m to calculate the ARF as a function of view angle and azimuthal angle for water clouds, and for ice

clouds, we assume $D_e = 80$ $\mu$m.

These values of ARF are used for the anisotropic correction (see eq. (2.12)). Obviously, this method will amplify the calculated $r_3$ for $r_e < 20$ $\mu$m, and for $r_e > 20$ $\mu$m $r_3$ will be underestimated because a larger ARF is used in eq. (2.12). However the decrease of ARF with $r_e$ is much smaller after $r_e > 20$ $\mu$m, and for $r_e = 30$ $\mu$m, the calculated $r_3$ is underestimated by less than 10%. As discussed later, this underestimate will result in some cloudy pixels with $r_e > 20$ $\mu$m to be identified as ice cloud or partly cloudy pixels, but these pixels are only a small portion because the representative value of cloud effective radius was observed to be 3.3-11.4 $\mu$m (Herman and Curry, 1984), and the effective radius is seldom lager than 20 $\mu$m from Han et al. (1994). Overestimation of $r_3$ for cloudy pixel with $r_e < 20$ $\mu$m will not influence its identification as cloudy pixels.

Model simulation shows albedo at TOA ($r_3$) is not sensitive to $\tau$ but very sensitive to $r_e$ and solar zenith angle for both the ice and water clouds, as shown in Figure 2.5 and 2.6. For both the water and ice clouds, $r_3$ increases with the solar zenith angle. For smaller effective cloud droplet size, the $r_3$ is larger due to the strong backscattering for smaller droplet size. $r_3$ increases with optical depth for $\tau < 2$, and reachs a constant value for $\tau > 6$. We also examined the sensitivity of $r_3$ to the atmospheric profile, and the difference in $r_3$ for the sub-Arctic summer and the winter profile is less than 5%.

### 2.2.3 A Threshold Function

Using a second order polynomial in $sec(\theta_0)$, we can fit $r_3$ as a function of solar zenith angle with good precision. This dependence of $r_3$ on solar zenith angle will play an important in our design of an automatic cloud discrimination algorithm based on $r_3$. As an example, the fitted $r_3$ with a second order polynomial of $sec(\theta_0)$

for $r_e$ = 20 $\mu$m (water cloud) and $D_e$ = 80 $\mu$m is also shown in Figures 2.5 and 2.6 (rhomboidal), respectively. The threshold function is as follows:

$$r_3 = b0 + b1 * sec(\theta_0) + b2 * sec^2(\theta_0) \tag{2.13}$$

where the coefficients are a weak function of cloud effective radius as shown in Table 2.1.

**Table 2.1** Coefficients of the Threshold Function $r_3$ for Different $r_e$ (or $D_e$) for Water and Ice clouds.

| water cloud | $r_e$ = 8 $\mu$m | $r_e$ = 10 $\mu$m | $r_e$ = 15 $\mu$m | $r_e$ = 20 $\mu$m |
|---|---|---|---|---|
| b0 | -0.036 | -0.047 | -0.055 | -0.051 |
| b1 | 0.185 | 0.168 | 0.128 | 0.105 |
| b2 | -0.021 | -0.018 | -0.01 | -0.006 |

| Ice cloud | $D_e$ = 40 $\mu$m | $D_e$ = 60 $\mu$m | $D_e$ = 80 $\mu$m |
|---|---|---|---|
| b0 | -0.056 | -0.054 | -0.052 |
| b1 | 0.084 | 0.077 | 0.073 |
| b2 | -0.0039 | -0.0032 | -0.0028 |

From Figure 2.6, $r_3$ for $\theta_0$ = 70° and $\tau$ = 0 (clear sky) is larger than $r_3$ for $\theta_0$ = 55° and $\tau$ = 6 for ice clouds, so the threshold of cloud detection must be adjusted according to the solar zenith angle. This threshold function is the basis of our automatic cloud discrimination.

The thresholds to detect water or ice cloud are calculated from eq. (2.13). For water clouds, the threshold function, *thre* , is calculated for $r_e$ = 20 $\mu$m, and for ice clouds, the threshold function, *threi*, is calculated for De = 80 $\mu$m. For a liquid water cloud $r_3$ is much larger than for a snow/ice covered surface, so $r_3$ can be used to discriminate water cloud from snow/ice surface. However, for an ice cloud (Figure 2.6), the difference in $r_3$ between clear and ice cloud is small (about 0.015

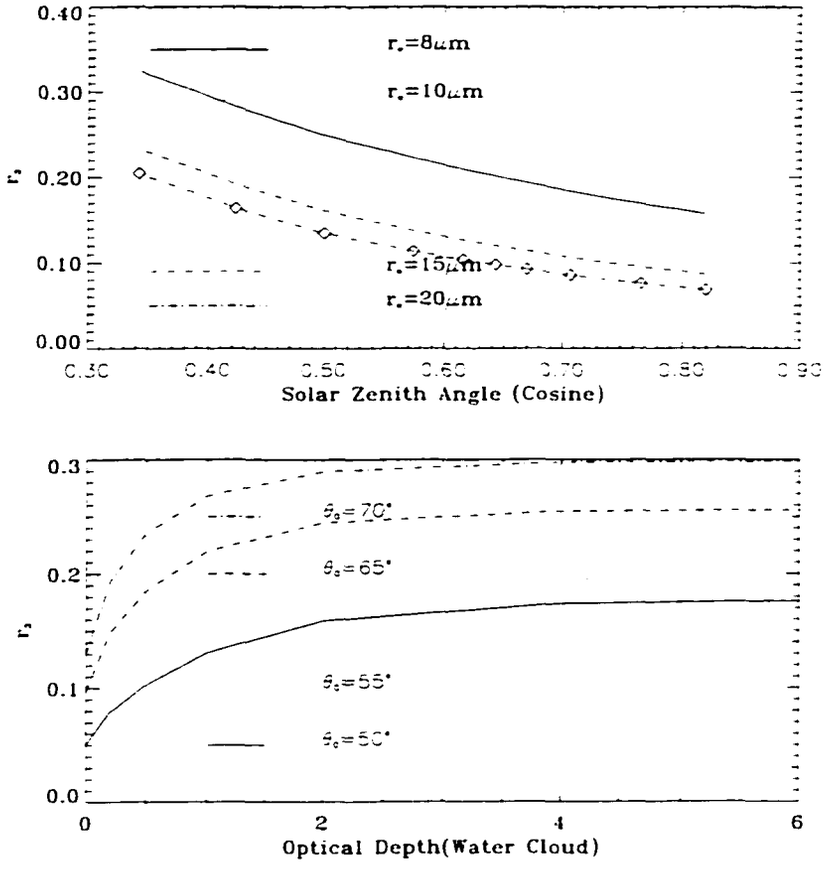


**Figure 2.5** $r_3$ at the TOA as a function of $\theta_0$ and $r_e$ (upper panel); and as a function of $\theta_0$ and $\tau$ (lower panel) for water clouds. The fitting of threshold function is shown in rhomboidal .

- 0.02). Considering the error in the calculation of $R_3$ and $r_3$ associated with the anisotropic correction and the removal of thermal component in channel 3, and the small difference of $r_3$ over ice clouds and snow/ice surfaces, ice cloud discrimination will be based on the difference in brightness temperature between channels 4 and 5.

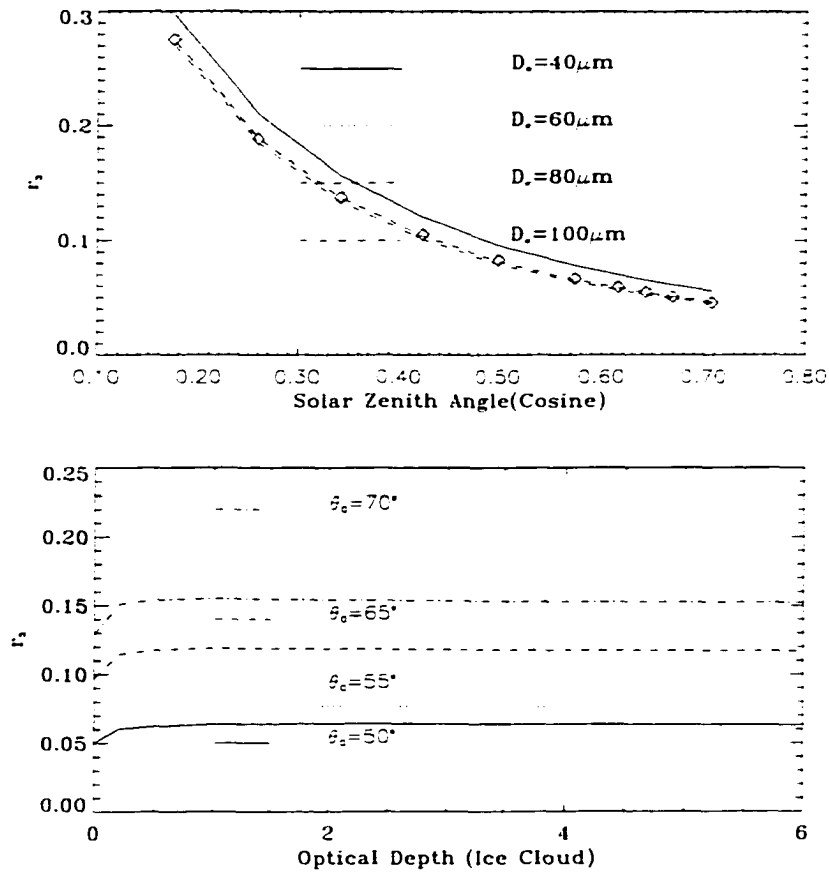


**Figure 2.6** As in Figure 2.5, but for ice clouds.

### 2.2.4 Clear/Cloudy Discrimination Scheme

Figure 2.7 is a flow chart of the cloudy/clear discrimination algorithm. It includes two main parts. One is the detection of clear sky, in which a clear pixel will be identified for a small $r_3$ and small BTD45, and further identified if it passes the following tests and belongs to one of the known possible surfaces. This approach decreases the possibility of missing any partly cloudy pixels or thin clouds, so we normally say it is a cloud conservative approach. Another part in the flow chart

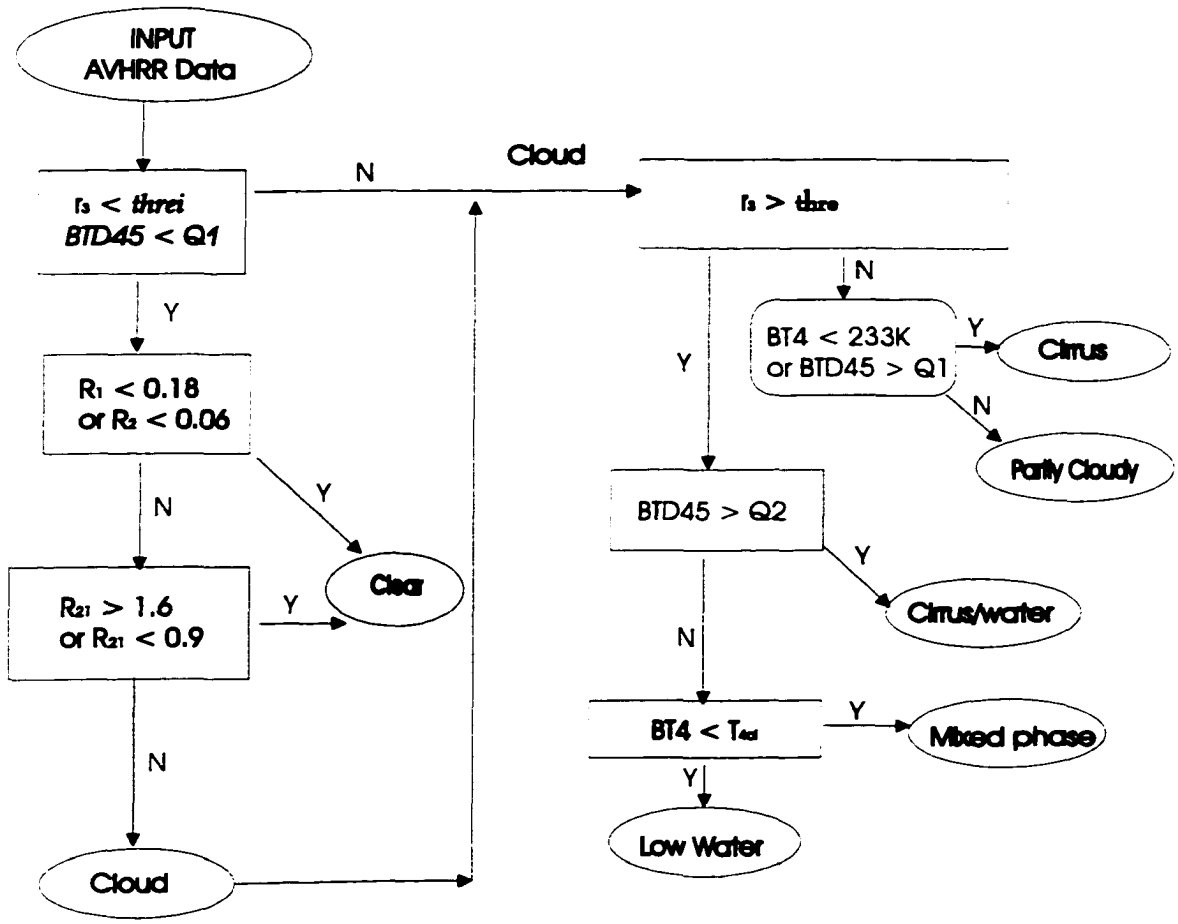


**Figure 2.7** The Flow Chart of Clear/Cloudy Discriminator.

illustrates a simple cloud classification scheme to detect low water clouds, cirrus, cirrus over low clouds or mixed phase clouds. If a pixel has not yet been identified as any of the above types, it is grouped as a partly cloudy pixel automatically.

If a pixel passes the following three tests, it is identified as a clear pixel.

1. Solar albedo in channel 3 ($r_3$):

   If the normalized reflectance of channel 3 after anisotropic correction is smaller than *threi* ($r_3 < threi$), this pixel is designated as clear with a very

low possibility for this pixel to be contaminated by clouds because the reflectance of channel 3 increases significantly over clouds. However, as the precision of $R_3$ and $r_3$ is limited for a cirrus or a partly cloudy situation, more tests are required. If BTD45 < Q1, this pixel will not be a thin cloud or cirrus.

2. Single threshold test: $R_1$ or $R_2$

   As $R_1$ and $R_2$ is high over clouds and snow/ice surfaces, low values of $R_1$ or $R_2$ will be indicative of open ocean or melt pond. However, $R_1$ over a pond is influenced by the ice below the water in the pond, so the decrease of $R_1$ is not so significant as the decrease of $R_2$ because the absorption by water in near infrared or infrared is much stronger.

3. Ratio test: $R_{21} = R_2/R_1$

   The spectral reflectance of snow, ice and cloud is different, especially in the near infrared (channel 2 of AVHRR). Snow reflects visible radiation more strongly than it reflects radiation in the near infrared, while cloud reflectance remains high in these two spectral regions. Thus, a high value of the ratio will be indicative of cloud, a relatively lower value will be indicative of snow cover, and for ice this value is much lower. Both $R_1$ and $R_2$ are low over land, but $R_{21}$ over land is larger than over cloud. Normally $R_{21} > 1.6$ is indicative of land (Saunders and Kriebel, 1988). For ice $R_{21}$ is between 0.6 and 0.85, and for clouds $R_{21}$ is between 0.85 and 1.1. Use of $R_{21}$ to discriminate ice from snow is relatively easy, but it is sometimes difficult to use $R_{21}$ to discriminate cloud from snow surface.

In the flow chart, $R_1 < 0.18$ and $R_{21} > 1.6$ are used to identify the land. $R_{21} < 0.9$ is used to identify snow/ice or pond, and $R_2 < 0.06$ is used to identify open

water. If a pixel passes these tests, it is identified as a clear pixel. Otherwise, it is identified as a cloudy pixel. For the cloud retrieval (see Chapter 5), we need to know the cloud phase, such as ice cloud or water cloud, for the choice of an appropriate cloud retrieval algorithm.

A simple cloud classification algorithm is developed using the multiple spectral information. Five types of clouds, such as cirrus, cirrus over low clouds, low water cloud, and partly cloudy situation are identified. Here, as the spatial resolution for AVHRR is 1.1 km at satellite subpoint and is larger for large viewing angles, some pixels will be partly clear and partly cloudy. A pixel that is not completely filled with cloud is called as partly cloudy pixel. Partly cloudy pixels will not be further classified.

The cloud top temperature, $T$, has been used to classify the cloud as low clouds for $T > 265K$, middle clouds for $265K > T > 245K$ and high cloud for $T < 245K$ (Key and Barry, 1989). Thresholds of cloud top temperature used to identify supercool liquid water from satellites are set as $-17 \sim -30°C$ (Thompson et al., 1997, Ellrod and Nelson, 1997). If $T$ is smaller than 253 K, it is cirrus over low cloud because above this temperature, the cloud is most likely composed only of water cloud (Matveev, 1984, Ou et al., 1993). From field observations during April 1983 and 1986 in the Arctic, Curry et al. (1990) reported that significant ice crystal nucleation routinely occurs at temperatures as high as $-15 \sim -20°C$, and in October completely crystalline clouds occur at temperature as high as $\sim -14°$ C (Curry et al., 1996). As BT4 is close to the cloud top temperature, from these observations, we set BT4 > 258 K as a condition for pure water clouds.

1. Cirrus: while $BT4 < 233$ K, it is identified as cirrus since 233 K is the spontaneous freezing point for water droplets (Rogers and Yau, 1989). Because of the influence of thermal emission from surface or lower warmer clouds below

cirrus. $BT4 < 233$ K is indicative of thick ice clouds.

A large BTD45. for example BTD45 > Q1. is widely used to detect cirrus (see for example. Inoue. 1985. 1987: Saunders and Kriebel. 1988: Ou et al.. 1993). However. not only for the cirrus. but other types of cloud also have large BTD45 in some range of thickness. As BTD45 also depends on the viewing angle (Saunders and Kriebel. 1988: Yamanouchi et al.. 1987). use of BTD45 to identify cirrus needs to be further evaluated. To avoid the thin low water cloud or partly cloudy pixel to be classified as cirrus. we set BT4 $< T_{4ci}$ and $r_3 < thr\epsilon$. together with BTD45 > Q1 to detect cirrus.

2. Water cloud and ice-contaminated mixed phase cloud: $r_3 > thr\epsilon$ is indicative of water clouds. If $r_3 > thr\epsilon$ and BTD45 > Q2 it is identified as cirrus over low clouds. and if If $r_3 > thr\epsilon$ and BT4 $> T_{4ci}$ K it is identified as a mixed phase cloud. Otherwise it is identified as a low water cloud. As we will see in Section 2.2.5. the threshold of Q2 is smaller than Q1. and both of them will be determined in Section 2.3.2.

3. If a pixel has not been identified after the above tests. it is identified as a partly cloudy pixel automatically.

### 2.2.5 Rationale of the Choice of Thresholds

In this section. a RTM for the coupled atmosphere-snow system is used to calculate the reflectance in channels 1 and 2 under clear and cloudy conditions. and the brightness temperature in channels 3. 4 and 5 as well. Water cloud parameterization is taken from Hu and Stamnes (1993). and ice cloud parameterization is taken from Fu and Liou (1993). The background tropospheric and stratospheric aerosol model from MODTRAN is used. The cloud top height is set where the

cloud top temperature equals the temperature of environmental air following the temperature profile. This is very important for the calculation of thermal radiation and brightness temperature. Only Atmospheric profile in the sub-arctic summer is used.

As we will see in the next chapter, the reflectance in channel 1 is sensitive to atmospheric aerosol or haze, but channel 2 is sensitive to water vapor in clear sky because the effects of Rayleigh scattering and aerosol scattering are significant in channel 1 but small in channel 2. Therefore, under clear sky conditions, $R_{21}$ is smaller in summertime as compared to wintertime as there is more water vapor in the atmosphere in the summer. For different atmospheric profiles, the simulated brightness temperatures in channels 3, 4 and 5 are different for these channels but the brightness temperature difference, BTD34 and BTD45, is not sensitive to the atmospheric profile. BTD45 in summer is a little higher than that in winter as there is more water vapor in the summer in the Arctic.

1. **Ratio test $R_{21}$**

   To account for the bidirectional effects of snow or ice on the ratio $R_{21}$ , the reflectance in AVHRR channels 1 and 2 for a series of snow grain sizes, mass-fractions of soot and viewing geometry are computed. Model simulations show that the dependence of $R_{21}$ on solar zenith angle and view angle is weak. The variation of $R_{21}$ for solar zenith angle $\theta_0 = 60^0$, view angle $\theta = 40^o$, and two different azimuthal angles, $\phi = 30^o$ and $\phi = 175^o$ under clear sky condition is shown in Figure 2.8. Due to the strong bidirectional reflectance over snow, $R_{21}$ increases significantly with azimuthal angle. $R_{21}$ over new snow with small grain size is larger than that over old snow because the decrease of $R_2$ with snow grain size is more significant for channel 2 than for channel 1. $R_{21}$ is larger over dirty snow than over clean snow because

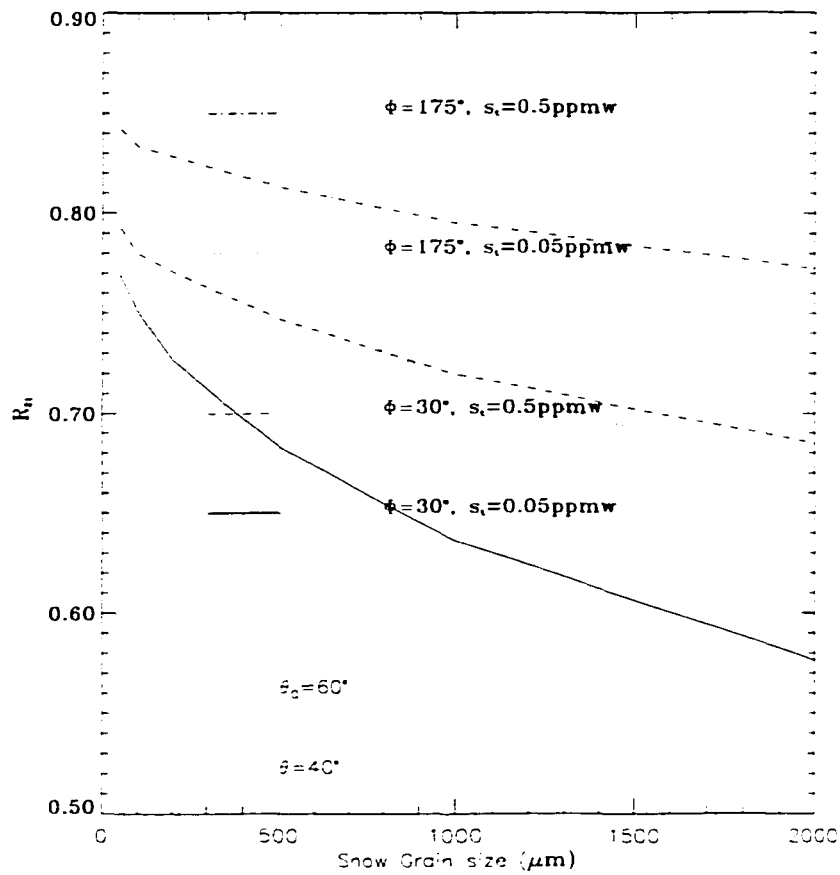


**Figure 2.8** $R_{21}$ as a function of $r_e$, $s_t$ and $\phi$ over snow surfaces.

$R_1$ is more sensitive than $R_2$ to soot "embedded" in the snow. From our simulations, values of $R_{21}$ over snow surface lie between 0.52 and 0.92.

Under cloudy conditions, $R_{21}$ is higher than under clear sky conditions over snow/ice surfaces. $R_{21}$ increases with the cloud optical depth but decreases with the effective droplet size, implying that $R_{21}$ over water cloud is larger than over ice cloud. As shown in Figure 2.9, $R_{21}$ increases with the relative azimuthal angle due to the strong bidirectional reflectance over a snow sur-

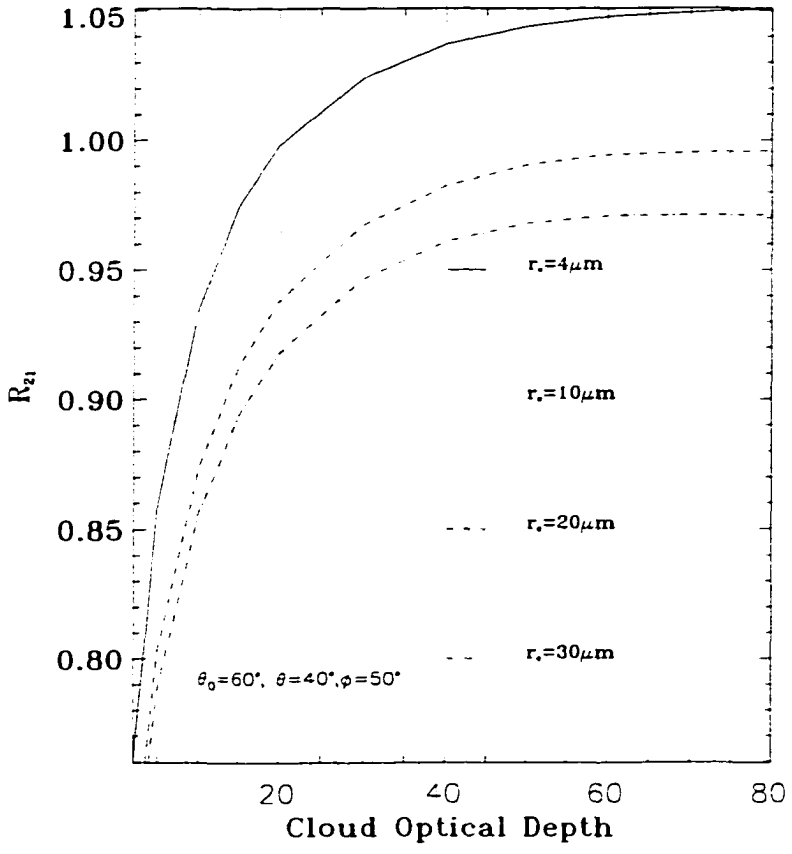


**Figure 2.9** $R_{21}$ as a function of $\tau$ and $r_e$ over warm clouds.

face. So, for a small azimuthal angle $R_{21}$ over a thin cloud may be lower than over snow for large relative azimuthal angles, so setting a uniform threshold of $R_{21}$ to discriminate snow from cloud is difficult. From model simulations, $R_{21}$ over clouds is between 0.6 and 1.4.

## 2. Brightness temperature difference BTD45

As we mentioned before, brightness temperature is obtained by inverting the Planck function while the radiance is given as the measured one from satel-

lite. However, due to the the non-linear relationship of the Planck function with wavenumber and temperature, errors in the response function and the effective wavenumber will lead to errors in the calculated brightness temperature. Assuming the emissivity of surface is 1 and no atmosphere, if the response function and effective wavenumber used are accurate, the brightness temperatures in channels 3, 4 and 5 should equal to the physical temperature. As shown in the upper left panel of Figure 2.10, the difference of brightness temperature with the physical temperature in channels 3, 4 and 5 is less than 0.5 K for a surface temperature between 230 K and 290 K. Brightness temperature difference between different channels is much less. BTD45 (upper right of Figure 2.10) is in a range of -0.1 K $\sim$ 0.15 K, and BTD34 (lower left) is in range -0.15 K $\sim$ 0.1 K. This model is used to examine the variation in BTD34 and BTD45 for different clouds and surfaces.

Figures 2.11 and 2.12 show the simulated BTD45 for liquid water and ice clouds, respectively. Water vapor absorption in channels 4 and 5 causes the radiative temperature to be less than the surface temperature. As the absorption of water vapor in channel 5 is stronger than in channel 4, BTD45 is always positive over clouds. For both water and ice clouds, BTD45 decreases with the increase of effective cloud droplet size. For clear sky or for thick clouds that are thermally black, the channel 4 brightness temperature is about the same as that of channel 5, so BTD45 is small. For thin clouds, whether the cloud consists of liquid water or ice, BTD45 increases significantly with a maximum value of BTD45 occurring at an optical depth of approximately 2-3. Because the transmittance of a thin cloud is high, BTD45 is almost insensitive to cloud top temperature, the measured radiance by satellite is mostly the thermal radiance emitted from the underlying atmosphere and surface. As the emissivity of cirrus is channel 4 is usually

less than that in channel 5, more transmission of clouds radiation from below leads to a larger values of BTD45.

BTD45 is smaller for cirrus overlying water cloud than for cirrus over a surface because most water vapor is in the lower troposphere. This is the reason that $Q2 < Q1$. Similarly, as water vapor is much less in the polar regions than that in mid-to-low latitude regions on Earth, the threshold for BTD45 is expected to be smaller in polar regions than that in mid-to-low latitude regions.

3. **Brightness temperature difference BTD34**

The brightness temperature in channel 3 over cloud is much larger than over snow/ice surface due to the reflection of solar radiation in channel 3 by cloud, so BTD34 has been used for cloud detection, especially water clouds. Figure 2.13 shows BTD34 as a function of solar zenith and effective droplet radius for liquid water and ice clouds at specific cloud top temperature. The smaller the cloud effective radius, the larger BTD34. For a water cloud with an effective droplet radius of 10 $\mu$m, BTD34 is 20~30 K depending on the solar zenith angle, and for effective droplet size 20 $\mu$m, it decreases to around 15 K, as shown in upper panel of Figure 2.13. For ice clouds, BTD34 is about 16~18 K under the condition of surface temperature 283 K and cloud top temperature 220 K. As BTD34 depends on the cloud microphysical properties and solar zenith angle, a dynamic threshold is normally required. This is the reason we used $r_3$ instead of BTD34 in our cloud discrimination algorithm.

### 2.2.6 Identification of Snow Cover

As the high albedo of snow cover presents a good contrast with most other natural surfaces, snow cover has been observed since the first image obtained from the

TIROS-1 weather satellite following its launch in April 1960 (Singer and Popham, 1963). Snow cover has been mapped in the Northern Hemisphere on a weekly basis since 1966 by NOAA using a variety of sensors, including AVHRR and passive-microwave sensors. A lot of snow cover mapping techniques, ranging from visual interpretation, multispectral image classification, decision trees, change detection, and ratios (Kyle et al., 1978; Bunting and d'Entremont, 1982) have been developed. Spectral-mixture modeling is also used for subpixel classification of snow in a scene (Nolin et al., 1993; Rosenthal, 1993).

Snow is easy to map with the 1.6 $\mu$m channel, which is available instead of 3.75 $\mu$m during the day time on NOAA-15 and on MODIS (Hall et al., 1995). As there was no 1.6 $\mu$m channel for AVHRR before, snow mapping is normally based on the difference of reflectance in channels 2 to 1. As discussed in the previous section, a high value of $R_{21}$ will be indicative of clouds, and a relatively higher value of snow cover, and a low value is indicative of ice, pond or open water. In Chapter 3 and the following chapters, snow surface is identified when $0.6 < R_{21} < 0.9$ for clear pixels. A limitation of this test is that $R_{21}$ over thin clouds is close to that over snow surfaces.

### 2.2.7 Estimation of Cloud Cover

Cloud cover inferred from satellite data is an effective cloud cover which is related to the wavelength, cloud optical properties and the underlying surface. So, it may be quite different from the conventional cloud cover reported by a surface observer (Saunders and Kriebel, 1989). The biggest difficulty in estimating the cloud cover is related with the partly cloudy pixels. For simplicity, the cloud cover calculated in this chapter is just the ratio of the number of cloudy pixels to the total pixels on a specific domain without further identification of cloud cover for partly cloudy

pixel. This will no doubt overestimate the cloud cover if there are many partly cloudy pixels.

## 2.3 Application and Results

### 2.3.1 Data

One or two NOAA-14 AVHRR overhead passes every day collocated over the SHEBA Ice Camp for 100 by 100 pixels, from April to September, 1998, are used for cloud discrimination from satellite. Cloud fraction from surface weather reports are used for validation. The surface weather reports were prepared at six-hour intervals (00, 06, 12, 18 GMT) by the SHEBA Project Office weather observers aboard the Canadian Coast Guard icebreaker *"Des Groseilliers"*, who recorded the current, 10-minute average values of temperature, dew point temperature, sea level pressure, wind speed, and wind direction. The observers also made visual estimates of cloud fraction, cloud base height, visibility, and current and past weather from the deck and bridge of the ship.

In the surface weather report, cloud observation includes:

1. Fraction of the sky covered by clouds of all types (eights: number 9 implies sky obscured and / implies cloud cover indiscernible for other reasons)

2. Fraction of the sky covered by all low clouds present (or if no low clouds, the fraction covered by medium clouds present) (eights: number 9 implies sky obscured and / implies cloud cover indiscernible for other reasons)

3. Cloud types, including types of low cloud (coded categories 0-9 and /), types of medium cloud (coded categories 0-9 and /), and types of high cloud (coded categories 0-9 and /)

In order to assess the cloud phase detected from AVHRR, the Depolarization and Backscatter-Unattended Lidar (DABUL) data over SHEBA are used. DABUL is a pulsed laser-radar operating at 523 nm wavelength, that was operated during the SHEBA, except for February 1998 (Intrieri et al., 2000). The range resolution of DABUL is 30 m, and the time resolution is 5s. This Lidar system uses a low energy laser with high repetition rates for good sensitivity while being completely eye-safe. Data are collected in four channels according to receiver field of view and polarization detected: far parallel, far perpendicular, near parallel, and near perpendicular. The far channel returns were used to determine the cloud layers due to their high sensitivity. Linear polarization is transmitted, and parallel and perpendicular refer to the polarization detected. The depolarization ratios are obtained by taking the ratio of the perpendicular to the parallel channels in either the near or far channels (Sassen, 1991). Nearly spherically symmetrical and optically homogeneous scatterers, such as cloud and drizzle drops, generate near-zero depolarization of the incident energy in the exact backscattering direction, while nonspherical scatterers such as ice particles, on the other hand, generate values which are typically in the range $\delta \simeq 0.4$ - 0.5 (Sassen, 1991), and typically $\delta \leq 0.1$ is used as a threshold to distinguish clouds with liquid water dominated optical properties (Intrieri et al., 2000), even though they may contain small concentrations of ice crystals (Bretherton et al., 2000). Intermediate values of $\delta$ may indicate mixed-phase clouds. The cloud boundary determination was obtained by simply thresholding the intensity and depolarization values for cloud base and top height. After each cloud layer is determined (base and top heights) the average returned power and the depolarization values are assigned for as many layers as are detected.

### 2.3.2 Choice of Thresholds

The average of $R_3$ versus $r_3$ (upper panel) and $R_3$ versus BTD34 (lower panel) for cloudy pixels for the AVHRR images over SHEBA from April to August, 1998 are shown in Figure 2.14. There are good correlations between $R_3$ and $r_3$, and between $R_3$ and BTD34. The large variation range of BTD34 demonstrates that to set a uniform threshold of BTD34 to detect water clouds is difficult because of its variation solar zenith angle. With the northwestward movement of SHEBA Ice Camp and the seasonal variation, the solar zenith angle changes a lot. Figure 2.14 also shows that the use of $R_3$ greater 0.08 to detect water clouds (Gesell, 1989) is inappropriate because many cloudy pixels will be mis-identified as clear pixels and the cloud cover will be underestimated.

Because BTD45 tends to be large for both cirrus and thin warm clouds, it is inappropriate to use only BTD45 to detect the cirrus, as widely used in current cloud detection algorithms. Figure 2.15 shows the seasonal variation of the number of pixels under the condition of BTD45 $>$ 1.8 K, BTD45 $>$ 2 K with or without BTD4 $<$ 258 K during the melt season. The comparison of pixel numbers in the lower panel of Figure 2.15 demonstrates that the number of cirrus is much less if setting the threshold BTD4 $<$ 258 K. Although the accuracy of this threshold may need to be further evaluated, it implies that in most situations, cirrus co-exists with lower warm clouds. As the total number of cloudy pixels during June-August is much larger in April-May, Figure 2.15 does not indicate that the ice cloud cover fraction during June-August is larger than that during April-May.

To determine the thresholds, we have examined dozens of images from May, 1998. Here we present only one case for the choice of thresholds. Figures 2.16-2.18 show the histogram of BTD34, BTD45, BT4 and $r_3$, and the corresponding color images for the NOAA-14 overpass on May 16, 1998 at 23:59 UTC over the

SHEBA. The SHEBA Ice Camp is in the middle of the image. There are two distinct peaks from the histogram of BTD34 and $r_3$ (Figure 2.16). The threshold of *thre* calculated from eq. (2.13) is about 0.12. *threi* is 0.054 and the corresponding threshold for BTD34 from histogram is about 20 K and 15 K. The total cloud area determined from BTD34 > 15 K is in good agreement with $r_3 > 0.054$. which is obvious from Figure 2.17. The water cloud area determined from BTD34 > 20 K is also in agreement with that determined from $r_3 > 0.12$. For $0.054 < r_3 < 0.12$. it is the partly cloudy cover. which is visible from BTD34 and BTD45. From Figure 2.18. the lower bright part is cirrus over lower water clouds because the $BTD45 > 1.8K$ and $r_3 > thre$.

As discussed before. BTD45 is widely used for detection of cirrus. but BTD45 depends on view angle and water vapor content in the atmosphere (Saunders and Kriebel. 1988). In our following analysis. one or two NOAA-14 passes close to the local noon time of SHEBA are chosen. so the view angle is small. As the water vapor content over snow/ice surface in the polar regions is much less than that over land or ocean at mid- and low- latitude. the threshold of BTD45 is expected to be less in the Arctic. BTD45 = 2.0 K is chosen as a threshold without considering its variation with viewing angle.

Based on the analysis of dozens of images. we got the thresholds which will be used in this chapter as listed in Table 2.2.

**Table 2.2** Thresholds for SHEBA.

| Q1 | Q2 | $T_{4ci}$ |
|---|---|---|
| 2.0 K | 1.8 K | 258 K |

### 2.3.3 Seasonal Variation of Cloud Fraction over SHEBA

Figure 2.19 shows the seasonal variation of cloud fraction derived from AVHRR on NOAA-14. Cloud fraction is calculated as the ratio of the cloudy pixels to the total pixels for AVHRR overpass of 100 by 100 pixels. One or two overpasses per day close the local noon time over SHEBA were used. In these images, the view angles are small, so the effects of bidirectional reflectance are small. For comparison, the cloud cover fraction from surface weather reports is used if the time difference between satellite overpass and the surface weather observation is less than 1 hour. For this comparison, the cloud fraction from surface weather reports needs to be multiplied by 1/8 because in the surface weather reports the cloud cover is represented in eighths.

Averaged cloud fraction from AVHRR between April and August, 1998, is 74%, with a mean cloud fraction of 45% in April, 72% in May, 69% in June, 83% in July and 87% in August. The mean cloud fraction from surface observations is 75% during the season, and the monthly average is 49%, 70%, 75%, 81% and 90% from April to August, respectively. The difference between AVHRR derived cloud cover with surface observation is about 2%~8%, and the largest difference is in June. One possible reason is that there are not enough NOAA-14 AVHRR images available over SHEBA in June, 1998. On average, cloud cover derived from AVHRR is 2% less than from surface observation. Historical data of observation at Barrow from 1949-1995 shows the average cloud cover is 50% in April, 80% in May, 80% in June, 80% in July and 90% in August. Obviously, they agree very well. Maykut and Church (1973) found that completely overcast skies exist about 50% of the year, and that cloud cover is maximum between May and November (70%~90%). The cloud fraction from AVHRR is in good consistency with the surface weather observations if we take into account the difference of coverage

from AVHRR and surface observations. However, the water cloud amount from AVHRR in the season is 56% while the low cloud amount from surface observer is 70% (Figure 2.20). Here water clouds from AVHRR refer to the cloudy pixels with $r_3 > thre$.

## 2.4 Summary and Discussion

In this chapter, a relatively simple cloud discrimination algorithm was designed and applied over the Arctic Ocean. The "simplicity" arises from the fact that only spectral features are used for detection so as to avoid complicated calculation of textural features and complicated decision strategy.

Solar reflectance in channel 3 is used for cloud discrimination from snow/ice surface in the Arctic. After making an improved estimation of $R_3$ and anisotropic correction, we get the albedo in channel 3 at TOA. A threshold function is obtained for automatic cloud discrimination. The main disadvantage of this technique is its difficulty in detecting cirrus, so the brightness temperature difference between channel 4 and 5 is used. The physical soundness of the choice of thresholds is examined from model simulations.

This cloud discrimination algorithm is employed for AVHRR overpasses over SHEBA Ice Camp during April-August, 1998. A good consistency of cloud cover fraction from AVHRR with that from the surface weather observations over SHEBA is obtained. This algorithm proves to be effective, and can be applied to study the long-term cloud properties and their relation to the climate change using the AVHRR data during the past 20 years.

Around the thick clouds, there may be shadows. The detection of cloud shadows is a big problem in cloudy/clear discrimination. Theoretically, it can be computed with the given view angle, solar angle, distribution of cloud edges, and cloud

altitude, but it is impractical. Cloud shadow detection over snow is still under development. Because of the large spatial coverage observed by AVHRR, the underlying surface during the melting season is not homogeneous, and some pixels could be composed of partial cloud cover, snow, ice, lead and pond. No efforts have been made to achieve sub-pixel discrimination from the satellite measurements. More detail about cloud phase detection can be found in the work of Menzel and Strabala (1997). Improvement in the detection of cirrus is possible using channel in 1.38 $\mu$m (Gao et al., 1993), which is available on MODIS and some other new sensors to be launched in the future.

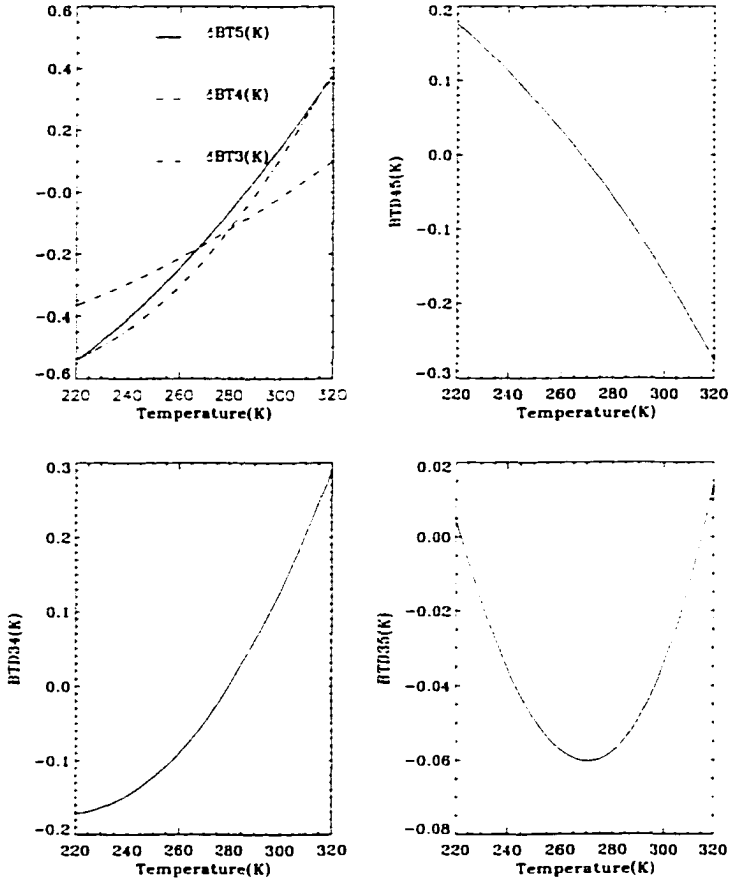


**Figure 2.10** Difference between brightness temperature and physical temperature in channels 3, 4 and 5 (upper left) and BTD45, BTD34 and BTD35 versus with physical temperature, assuming surface emissivity equals to 1 without atmosphere.

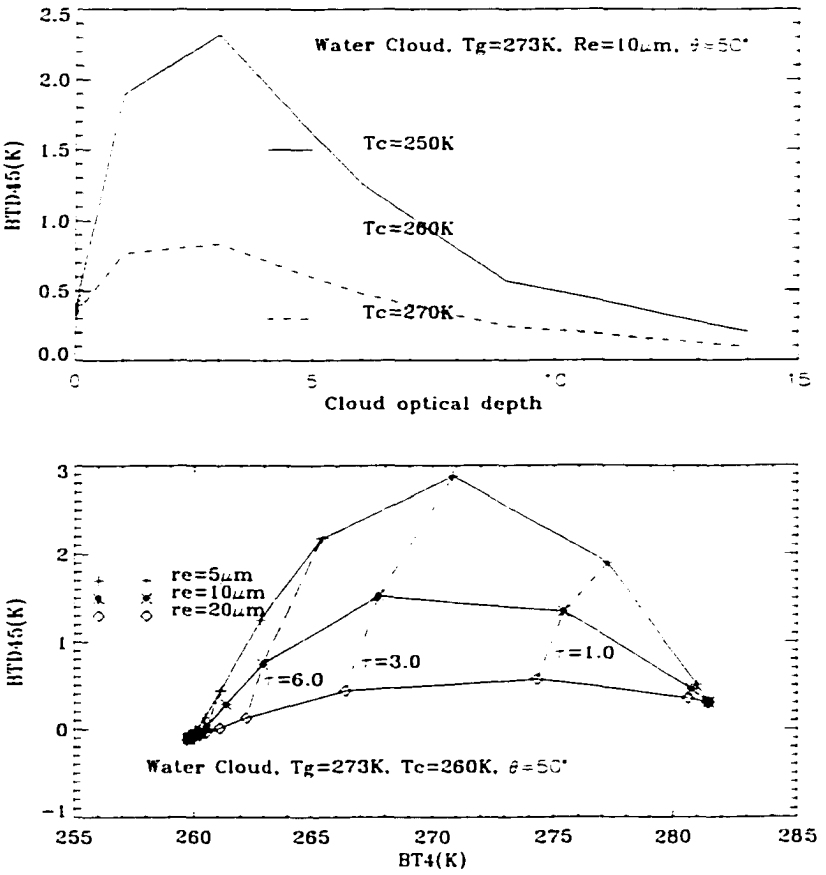


**Figure 2.11** BTD45 as a function of $\tau$, $r_e$, $T_c$ and $T_g$ for water clouds.

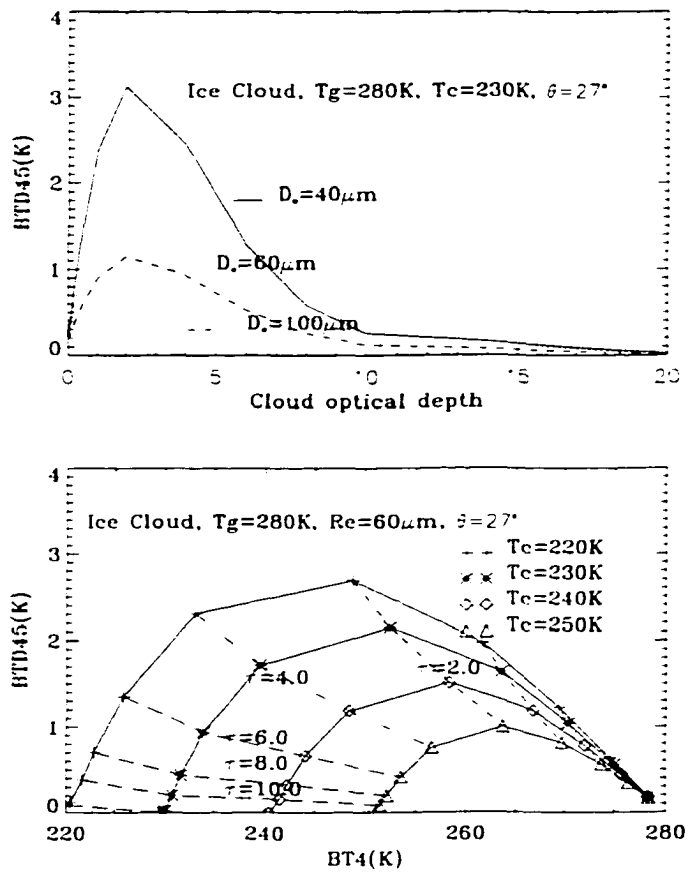


**Figure 2.12** Similar to Figure 2.11 but for ice clouds .

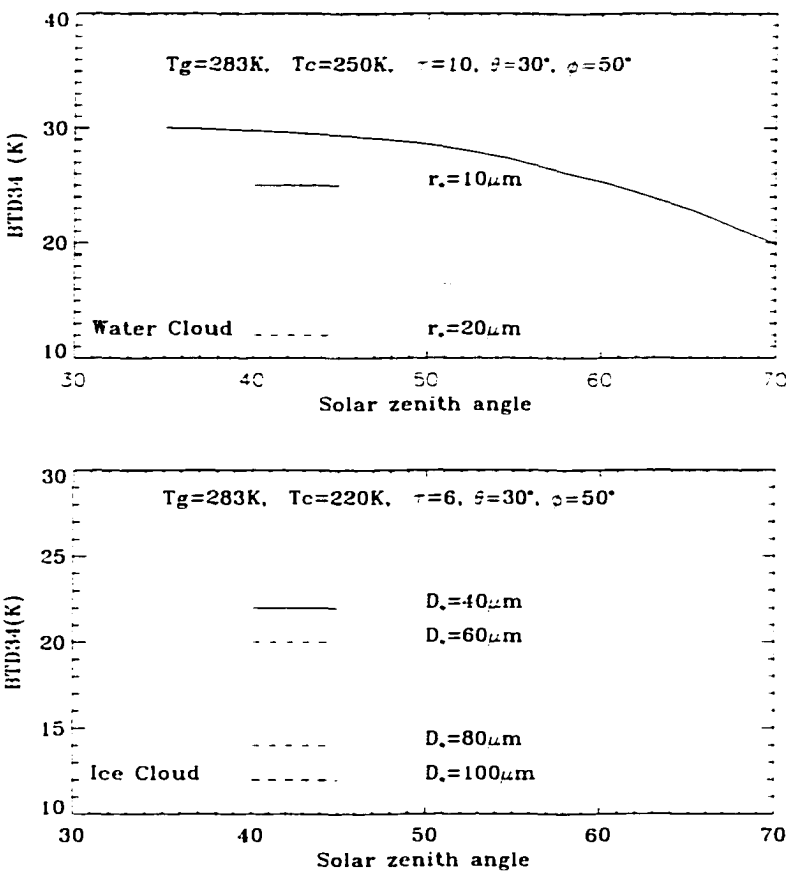


**Figure 2.13** BTD34 versus $\theta_0$ for water and ice clouds under the condition of $T_g = 283$ K and $T_c = 250$ K for water clouds; and $T_g = 283$ K and $T_c = 220$ K for ice clouds. $\theta = 30°$ and $\phi = 50°$ .

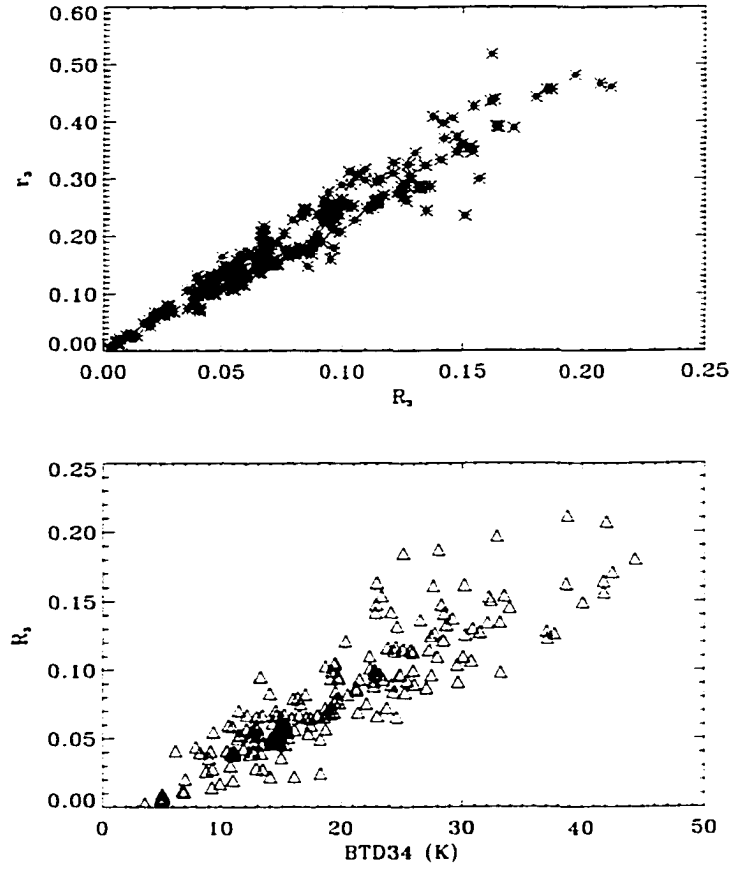


Figure 2.14 Mean $R_3$ versus $r_3$ (upper panel) and BTD34 versus $R_3$ (lower panel) for cloudy pixels during April to August, 1998 over SHEBA .

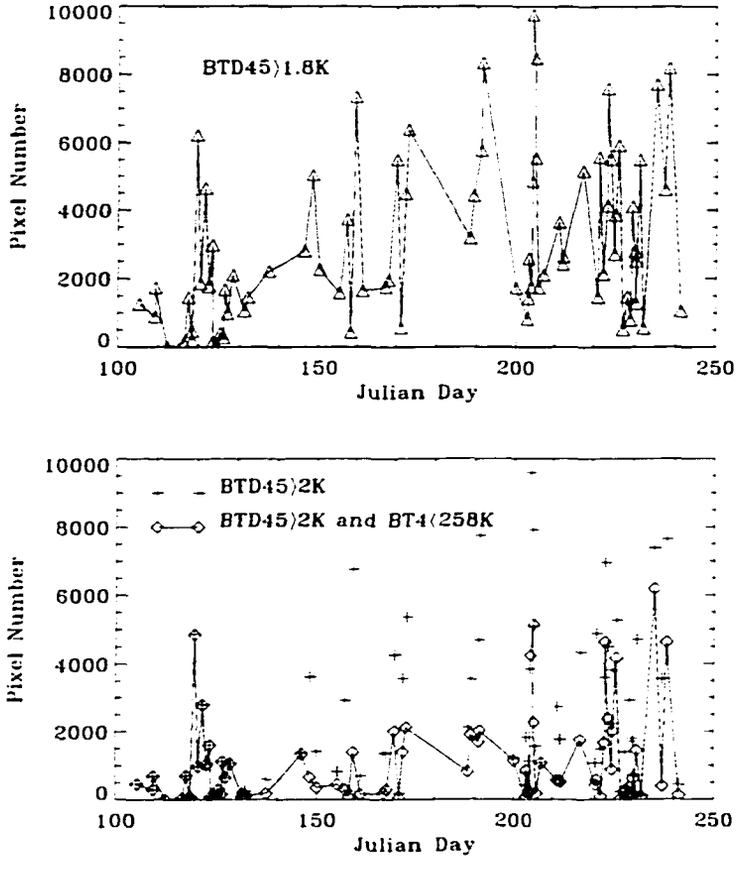


**Figure 2.15** Pixel numbers under the conditions of BTD45 > 1.8 K (upper panel); and BTD45 > 2 K with and without BT4 < 258 K. Total number of pixels are 100 by 100 .

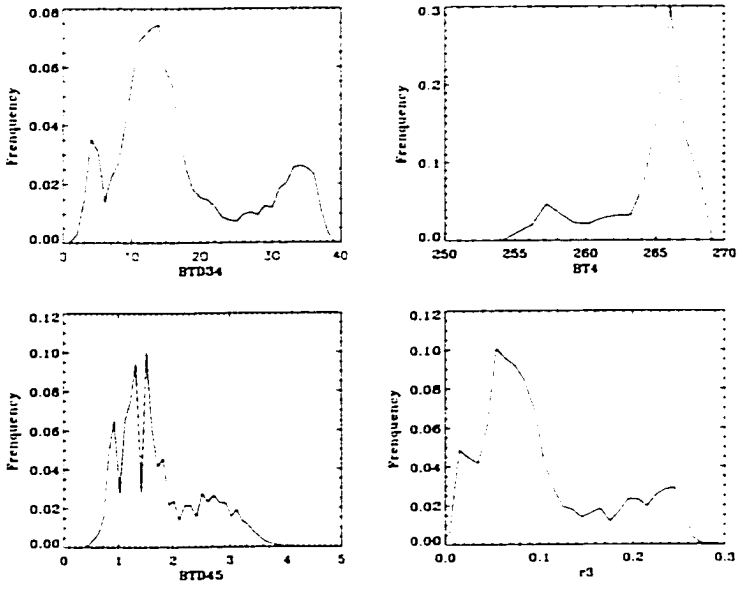


**Figure 2.16** Histogram of BTD34, BTD45, BT4 and $r_3$ for NOAA-14 AVHRR pass on May 16, 1998 at 23:59 UTC .

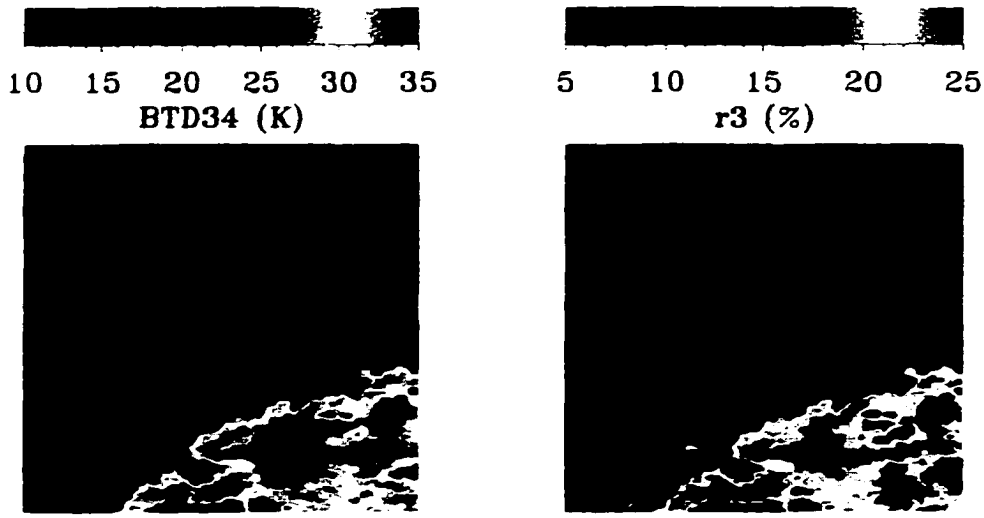


Figure 2.17 Color image of BTD34 and $r_3$ for NOAA-14 AVHRR pass on May 16, 1998 at 23:59 UTC

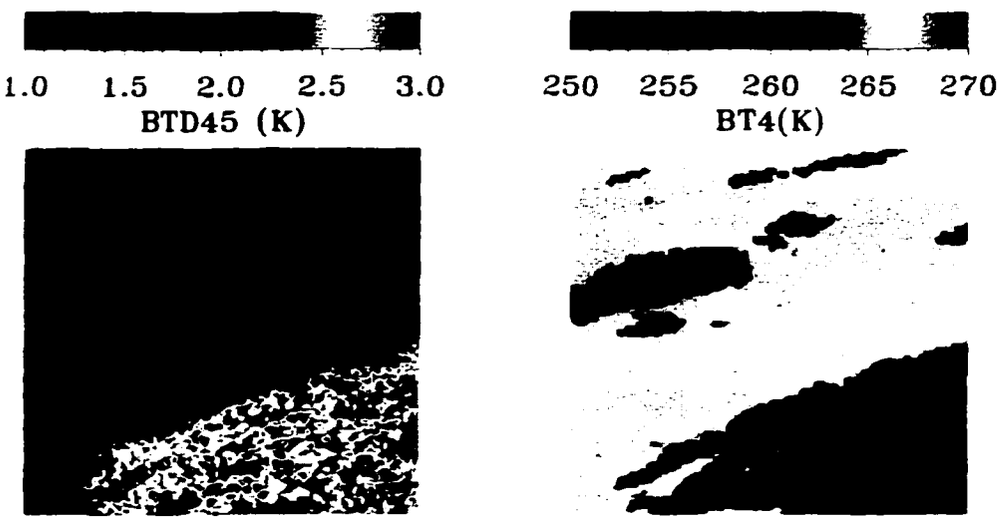


**Figure 2.18** As in Figure 2.17, but for BTD45 and BT4 .

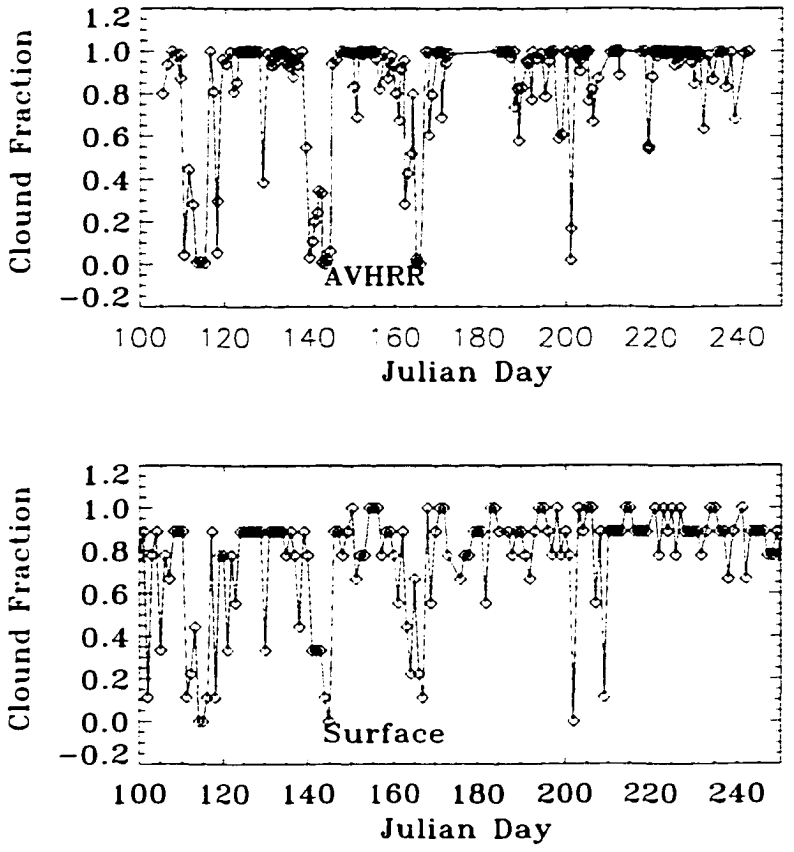


**Figure 2.19** Cloud fraction derived from AVHRR (upper panel) and surface weather observer (lower panel) over SHEBA during April-August, 1998 .

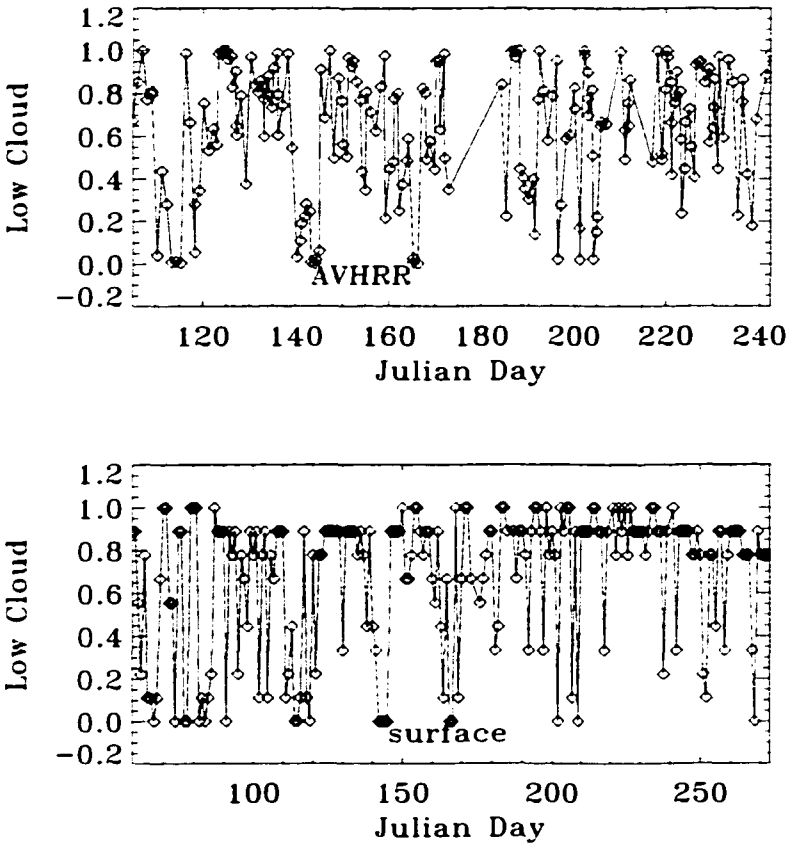


**Figure 2.20** As in Figure 2.19, but for water cloud cover fraction from AVHRR (upper panel) and low cloud cover fraction from surface weather observer (lower panel) .

# Chapter 3

# Retrieval of Snow Grain Size, Soot and Surface Albedo from AVHRR Data: Validation with SHEBA Measurements

Surface albedo is one of the most important factors influencing the radiation budget of the earth-atmosphere system. Of all the surface types on Earth, snow and ice surfaces have the highest albedo. The bidirectional reflectance over snow or ice surface is pronounced for the large solar zenith angles in the Arctic (Curry et al., 1996). Thus, accurate determination of the albedo and the BRDF (Bidirectional Reflectance Distribution Function) is essential for reliable estimation of the radiation budget in the Arctic. As surface reflective properties also have significant effects on the upward radiance at the top of atmosphere (see Chapter 5), accurate determination of the surface albedo and BRDF is also important for cloud retrieval (see Chapters 4 and 5). However, the continuous solar illumination during the summer results in a rapid change of the surface physical conditions.

such as the melting of snow and ice, and the formation of ponds and leads. This season between May and August in the Arctic, characterized by rapid change of surface physical conditions, is called "Transition Season". The rapid change of surface albedo due to the fast change of surface conditions, and the paucity of field measurements of albedo make it difficult to get the real-time albedo which is necessary for improving the performance of regional climate models in the Arctic. Measurements over large spatial areas from satellite and the multiple overpasses of the polar-orbiting satellites in the polar regions make it feasible to monitor the change of the surface albedo and BRDF from space.

The snow/ice albedo generally depends on the wavelength of the incident solar radiation, snow/ice age and depth, air bubble distribution in ice, sun angle, cloud cover and impurities such as dust, ash, soot and salt (Clarke and Noone, 1985; Warren 1982; Tsay et al., 1989). Due to the pronounced bidirectional reflectance over snow/ice surfaces, anisotropic correction is required for accurate retrieval of surface albedo from satellite data. The anisotropic correction is usually done by multiplying the TOA albedo, obtained by assuming that the TOA reflected radiation is isotropic, with an empirical anisotropic correction factor, which is normally based on results from the ERBE (Earth Radiation Budget Experiment) studies of anisotropic reflectance over various surfaces (e.g., Taylor and Stowe, 1984; Suttles *et al.*, 1988). However, since ERBE is a broadband instrument, these correction factors are not appropriate for narrowband channels. If we can retrieve the physical parameters of the surface, from which it is possible to derive the surface albedo and BRDF directly, we can avoid any further anisotropic correction and any assumption about surface reflectance characteristics. This is true for snow surfaces because their optical properties can be parameterized in terms of the effective snow grain size ($r_s$) and the mass fraction of soot ($s_t$), as shown by Warren and Wiscombe (1980). Moreover, $r_s$ and $s_t$ can be retrieved from AVHRR

channels 1 and 2 (see for example Han et al., 1999; Key, 1996). In this chapter, an algorithm for simultaneous retrieval of $r_s$ and mass-fraction of soot is developed using the reflectance in AVHRR channels 1 and 2. The basis of this algorithm is a RTM which includes snow as an additional layer at the bottom of the atmosphere.

Non-snow covered surfaces are assumed to be Lambertian. This is a simple but widely used approximation to the reflectance for most types of Earth surfaces. An algorithm to retrieve the narrowband albedo in channels 1 and 2 using AVHRR data is developed. The broadband albedo of the surface can be obtained through NTB conversion.

In this chapter, we will first introduce the algorithm and discuss the uncertainty associated with the use of AVHRR channels 1 and 2 to retrieve $r_s$ and $s_t$. Next, the algorithm for albedo retrieval is presented with emphasis on the NTB conversion. The effect of snow bidirectional reflectance on the albedo retrieval is discussed. Finally, this algorithm is applied to get the seasonal variation of albedo over the Arctic Ocean.

## 3.1 Retrieval of Snow Grain Size and Mass-Fraction of Soot

### 3.1.1 Retrieval Method

The snow/ice discrimination algorithms of Chapter 2 can be used to identify surface pixels covered by snow. Now, we will investigate the possibility of retrieving the $r_s$ and $r_t$ for snow pixels.

The retrieval of $r_s$ and $s_t$ is possible because the snow reflectance in the near infrared depends primarily on the $r_s$, while in the visible it depends on both $r_s$ and $s_t$. Nolin and Dozier (1993) estimated snow grain size using the reflectance at 1.04

$\mu$m. Bourdelles and Fily (1993) used the Thematic Mapper band 4 (TM4, 0.84 $\mu m$) to retrieve $r_s$, and found that the retrieved $r_s$ from TM4 is much larger than that retrieved using TM5 (1.65 $\mu$m) and TM7 (2.2 $\mu$m). Further investigation of the relationship of $r_s$ with the wavelength used for retrieval was made by Li et al. (2000). Li et al. (2000) concluded that the difference in retrieved $r_s$ is related to the difference in penetration depth, which was 5.0 cm for 0.86 $\mu$m channel, 1.0-2.0 cm for 1.24 $\mu$m channel and 0.1-0.2 cm in wavelength 1.73 $\mu$m. Because the retrieved $r_s$ from satellite measurements is a depth-weighted-averaged value, and the snow grain size normally increases with the snow depth, it is easy to understand that the snow grain size is larger for shorter wavelengths that penetrate deeper into the snow and thus lead to larger retrieved grain size. It should be noted that the retrieved effective snow grain size may be different from the measured geometric grain size because the effect of snow grain shape cannot be neglected. Aoki et al. (1998) found that for wavelengths larger than 1.5 $\mu$m, the fine structure of snow was measured instead of the crystal radius, so extreme care must be exercised if one desires to retrieve snow grain size using the 1.73 $\mu$m channel (Li et al., 2000).

Based on the radiative transfer theory, we can write one equation for each channel. Under clear sky condition, the variables influencing the radiative transfer in the atmosphere are the optical properties of aerosols, Rayleigh scattering, absorption by water vapor and other trace gases. As the in-situ measurement of aerosol in AVHRR channel 1 and 2 is unavailable, we use climatological data for aerosol and $O_3$. The profile of water vapor can be obtained from sounding profiles. As the snow surface reflectivity properties can be represented accurately with $r_s$ and $s_t$ as provided by Wiscombe and Warren (1980), in which Mie theory was used to get the extinction coefficient and the phase function assuming the snow grains to be spherical particles, the satellite measured radiances in channels 1 and 2 will depend only on the surface $r_s$ and $s_t$. As shown in Figure 3.1, the reflectances

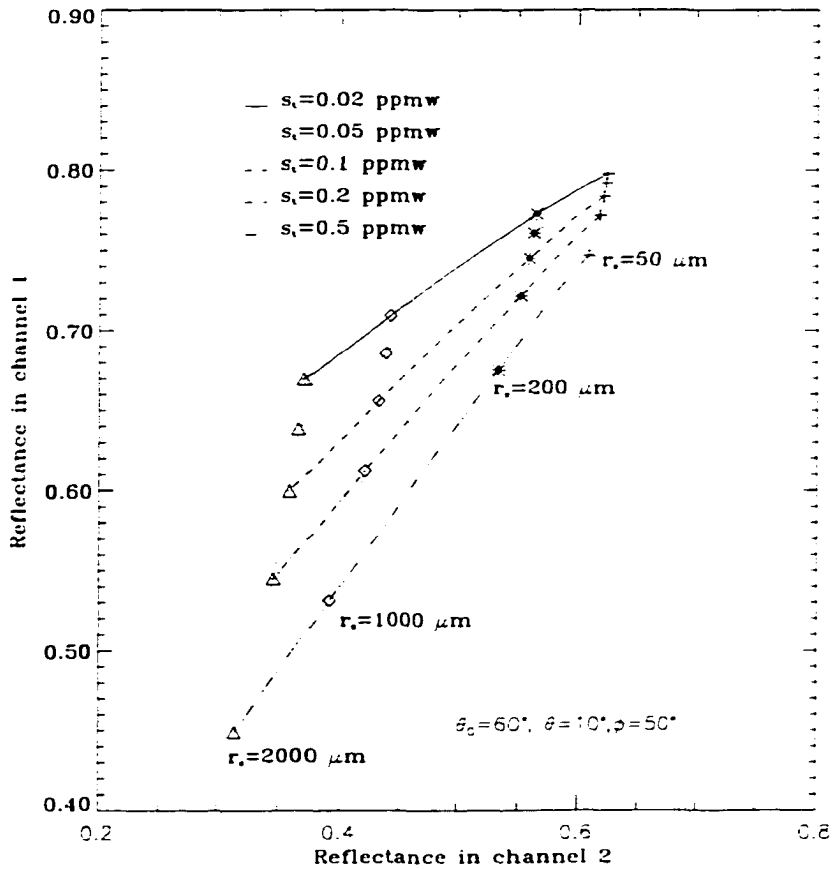


**Figure 3.1** Simulation of reflectances in AVHRR channels 1 and 2 as a function of snow grain size ($r_e$) and mass-fraction of soot ($s_t$) under the condition of $\theta_0 = 60°$, $\theta = 10°$, $\phi = 50°$ .

in channels 1 and 2 decrease monotonically with the increase of snow grain size and the amount of soot "embedded" in the snow, but the reflectance in channel 2 is not so sensitive to $s_t$ as channel 1. Using these two channels, we have two equations with two unknown variables: $r_s$ and $s_t$, which normally can be solved. The solutions are unique as shown in Figure 3.1.

Using the RTM in which snow is treated as an additional layer at the lower boundary we generated, two look-up tables for channels 1 and 2 for a series of $r_s$ and mass-fractions of soot. The viewing geometry is also considered. For a given

viewing geometry, the dimension of the look-up tables can be decreased to 2-D tables of reflectance in channels 1 and 2 as functions of $r_s$ and $s_t$. Next, by searching for a set of simulated radiances which coincide with the measured radiances within a predefined error margin, then standard extrapolation and interpolation techniques can be used to find the corresponding values of $r_s$ and $s_t$.

Since reflectance in channel 1 is sensitive to both snow grain and amount of soot embedded in the snow, and channel 2 is primarily sensitive to grain size and insensitive to soot amounts, the steps of retrieval can be designed as follows:

1. Set an initial value of mass fraction ($st_0$) of soot as 0.05 ppmw, and adjust the $r_s$ until the simulated reflectance in channel 2 is matched with the satellite measurement. As channel 2 is not sensitive to soot fraction, this $r_s$ ($r_{s0}$) tends to be a good approximation to the true value.

2. Set the $r_s$ to the value $r_{s0}$ determined in step 1, adjust the soot fraction until the simulated reflectance in channel 1 is matched with the satellite measurement. This value is an approximate value of the soot fraction $st_1$:

3. If the difference between $st_1$ and $st_0$ is larger than 0.001 ppmw, we set $st_2 = (st_1+st_0)/2$, and return to step 1. Continue this loop until both the simulated reflectances in channels 1 and 2 are matched with the satellite measurements within the prescribed error range.

Normally a few iterations are enough to get a converged numerical solution. From our experience, the error between the model simulated reflectance and satellite-measured reflectance is set as 1%. If a solution cannot be obtained, this pixel may be cloud contaminated (partly cloudy pixel), and we abandon it.

This algorithm for the retrieval of $r_s$ and $s_t$ is similar to that developed by Han et al. (1999). The differences are:

- In this chapter, the normalized reflectance is used instead of the absolute value of radiance. Thus, we can decrease the error between the model simulated reflectance and the real satellite measurement because the channel width and response function in the band model does not exactly fit the real satellite channel.

- Fourier expansion in azimuthal angle with 9 terms is used (Dan and Weber, 1995), so interpolation in azimuthal angle is not necessary. In this way, we can increase the computational precision and decrease the size of the look-up tables by 1 dimension.

In the look-up tables, we used $r_s$ ranging from 50 to 2000 $\mu$m, and $s_t$ ranging from 0.02 ppmw to 0.5 ppmw (parts per million by weight). For soot we used a 5.74 cross-sectional area per unit mass, which is a typical value for a mixture of graphite and amorphous carbon (Warren and Wiscombe, 1980; Han et al., 1999). A comprehensive RTM based on the DISORT code (Stamnes et al., 1988) was used for generating the look-up tables.

### 3.1.2 Uncertainty Analysis

Possible error sources in the retrieval of $r_s$ and $s_t$ include use of an inappropriate atmospheric profile and aerosol model, uncertainties in the satellite measurements and uncertainties associated with the retrieval method itself due to interpolation and/or extrapolation in the look-up tables. The contamination by partly cloud cover or mis-identified ice as snow due to error in the cloud mask is another important source or error. Other error sources include the deviation of the assumed spherical shape of snow grain size from their true shape and surface roughness.

Because the absorption of $H_2O$ in the visible is weak, the influence of atmospheric humidity on channel 1 is very small. As shown in Figure 3.2, $R_1$ calculated

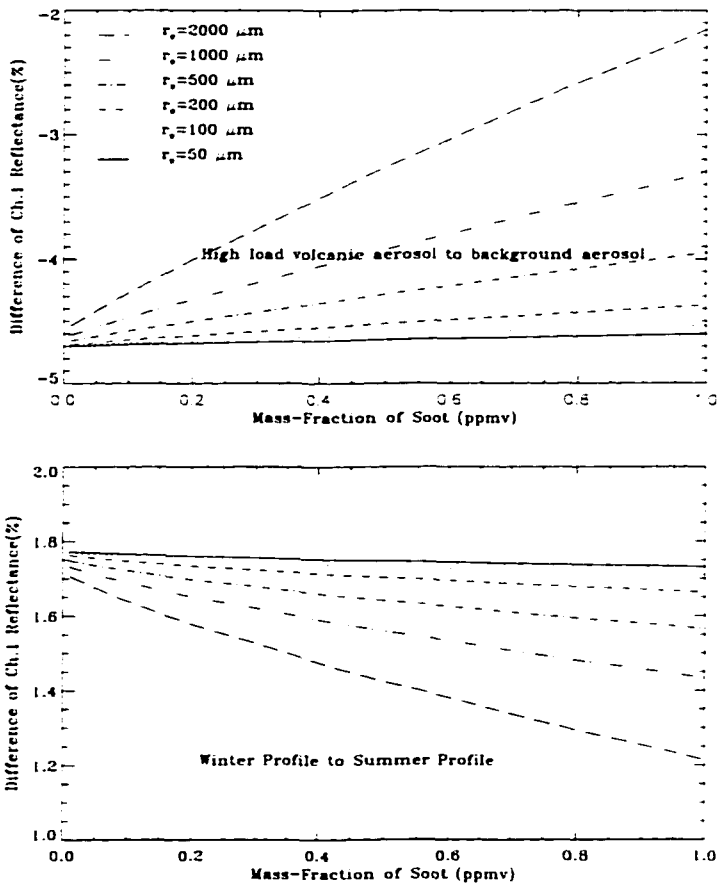


**Figure 3.2** Difference of reflectance in AVHRR channel 1 for different aerosol models (upper panel) and different atmospheric profiles (lower panel) under the condition of $\theta_0 = 60°$, $\theta = 10°$, $\phi = 50°$.

from a subarctic winter atmospheric profile is a little larger than that from the summer atmospheric profile, but the difference is less than 2%. However, AVHRR channel 2 (0.72-1.10 $\mu$m) cover the strong water absorption band at 0.94 $\mu$m, so water vapor absorption is significant in channel 2. The calculated $R_2$ from the winter atmospheric profile is more than 40% larger than from the summer profile because the optical depth of lower atmosphere water vapor absorption is almost two times larger in summer than in winter.

The effect of aerosol may be important in channel 1, but not in channel 2.

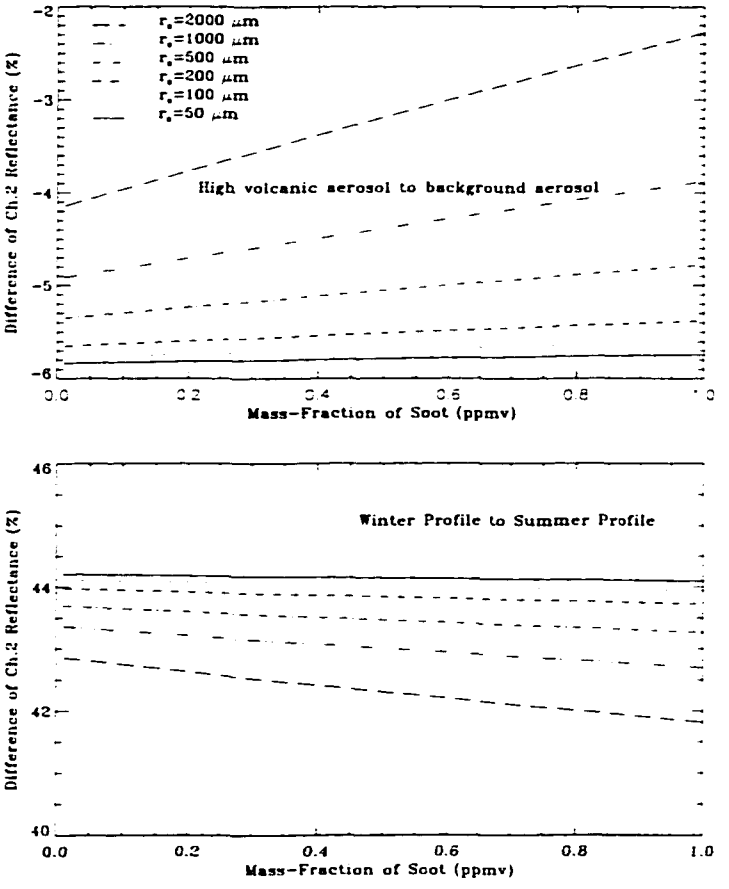


**Figure 3.3** As in Figure 3.2, but for AVHRR channel 2.

To examine the effect of aerosol, two different aerosol models were chosen. One represents very clean air conditions assuming the boundary layer tropospheric extinction with default visibility of 50 km and a background stratospheric aerosol. The other model represents boundary layer maritime aerosol extinction with visibility of 23 km, and a stratospheric aerosol with high volcanic profile and fresh volcanic extinction. Both $R_1$ and $R_2$ from the high volcanic aerosol model is lower than from the background stratospheric model, but the difference is about 5%. As the scattering by aerosol is larger in the visible than in the near infrared, the

influence of aerosol in channel 1 should be larger than in channel 2. This seems inconsistent with the above calculation. However, the atmospheric profile used in this comparison is the subarctic summer profile, so the value of $R_2$ is much smaller than $R_1$, leading to the relative error in $R_2$ being a little larger than in $R_1$, but not the absolute error. The difference in $R_2$ resulting from different aerosol models that is about 5%.

From the above discussion, use of instantaneous water content, ozone amount and aerosol optical depth of the atmosphere is required to improve the accuracy for snow retrieval. From the SHEBA sounding profile data over snow and ice surface in April and May, we found that the subarctic winter profile is close to most of the real atmospheric sounding profiles, so in the following snow retrievals between April and May, we use the subarctic winter profile instead of the subarctic summer profile.

In order to examine the error of the retrieval method itself due to the interpolation and extrapolation in the look-up tables, we generated the reflectance in channels 1 and 2 from accurate radiative transfer simulations for a series of $r_s$, $s_t$ and viewing geometries, covering the range of grain size 50~2000 $\mu$m, mass-fraction of soot 0.02~1.0 ppmw and a large range of viewing geometry. With these simulated data as inputs to the snow retrieval algorithm, we got the "retrieved" $r_s$ and $s_t$. Comparison of the "retrieved" $r_s$ and $s_t$ with the "real" values used to calculate the reflectances (Figure 3.4) shows the error in the retrieved $r_s$ is less than 20 $\mu$m (1%), and the error in the retrieved $s_t$ is less than 5~10%.

The estimated absolute error of satellite measured radiance is 5%~10% (Han et al., 1994). In order to examine the uncertainty of satellite measurements on the snow retrievals, we assumed ±5% error in the reflectances in channels 1 and 2. The uncertainties in the retrieved snow $r_s$ and $s_t$ are shown in Figure 3.5. For $r_s < 50\mu$m, the relative error of $r_s$ can be as high as 200%, and for $r_s > 500$ $\mu$m,

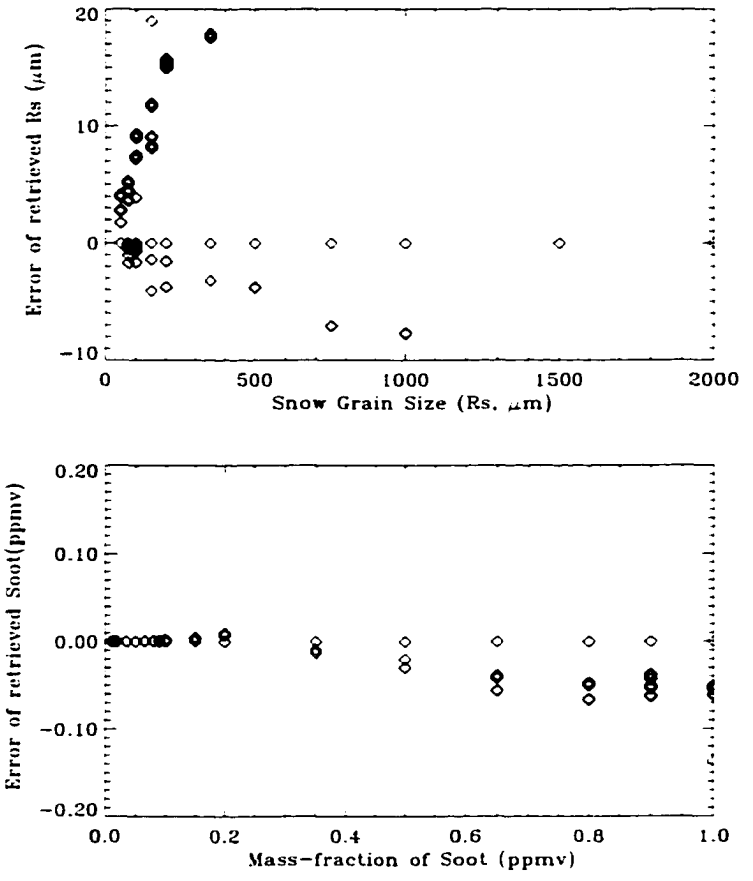


**Figure 3.4** Error of the retrieved snow grain size (upper panel) and soot (lower panel) due to the retrieval procedure.

the error is about 30%. For clean snow with mass-fraction of soot less than 0.05 ppmw. the error in the $s_t$ can be as high as 200%. for $s_t > 0.1$ ppmw. the average error is about 50%. It can be concluded that errors in the satellite measurements in AVHRR channels 1 and 2 can lead to quite significant errors in the retrieved $r_s$ and $s_t$. Due to the poor calibration of AVHRR in channels 1 and 2. use of the retrieved $r_s$ and $s_t$ in the radiation budget estimates is subject to large uncertainties.

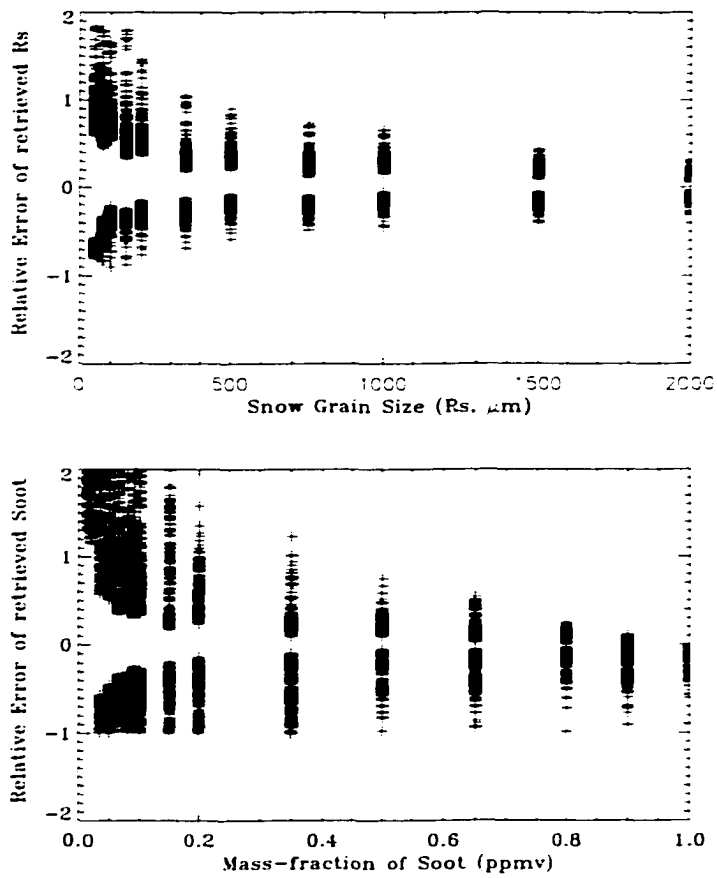


**Figure 3.5** Error of the retrieved snow grain size (upper panel) and soot (lower panel) for an uncertainty of $\pm$ 5% in satellite-measured reflectances in channels 1 and 2.

# 3.2 Retrieval of Surface Albedo

## 3.2.1 Retrieval Principle

Retrieval of surface albedo from the satellite-measured radiances has been attempted for many years, but most attempts were made over non-snow covered land surface (see for example Langleben, 1971; Briegleb et al., 1986; Saunders, 1990; De Abreu et al., 1994; Li and Leighton, 1992; Toll et al., 1997; Csiszar and

Gutman, 1999; Song and Gao, 1999). A retrieval of surface albedo of the Arctic sea ice was made by Lindsay and Rothrock (1994). However, surface measurement data used for validation were limited in the Arctic, and the cloud masking techniques used in the past to identify the clear pixels were unreliable. So, improvement and validation for surface albedo retrieval over high albedo surfaces in the Arctic are required.

For each channel, we have one equation based on radiative transfer theory. If the surface is assumed to be a Lambert reflector, which assumes the reflectance is uniform independent of angle, and the optical properties of aerosol and the amount for the trace gases are taken from the climatological data, this equation is simplified as an equation with one unknown variable because the measured reflectance at the TOA depends only on surface albedo. As the reflectance at the TOA increases with the increase of surface albedo, the solution is unique. Because the satellites measure only the narrowband directional radiance in specific channels, we can only derive the spectral albedo from the satellite-measured radiance. However, GCMs and/or regional climate models use, in general, the broadband albedo, so it is desirable to derive the surface broadband albedo from satellite data. Derivation of surface broadband albedo from satellite data requires (i) conversion of directional reflectance to hemispherically integrated reflectance or albedo, (ii) removal of atmospheric effects, and (iii) conversion from narrowband albedo to broadband albedo. Distinct characteristics of albedo in the red (visible) and near-infrared regions for different snow/ice surface conditions may require different narrow-to-broad conversions.

Anisotropic correction is required when retrieving surface albedo from satellite measured radiance, especially in the polar regions due to strong bidirectional reflectance over snow or ice surface. An "anisotropic correction" to the albedo at the TOA has generally been made to account for the bidirectional reflectance using

the correction factors from ERBE (Taylor and Stowe, 1984). However, ERBE is a broadband instrument, the correction factors from ERBE can only be used if we assume that they are the same for AVHRR channels 1 and 2 (De Abreu et al., 1994). This assumption is not appropriate. Saunders (1990) found that when the Taylor and Stowe factors were applied to the case with $\theta > 65°$, large discontinuities in the resultant surface albedo were obtained. As the solar zenith angle in the Arctic is large most of the time throughout the year, the traditional way of using the Taylor and Stowe factor for anisotropic correction is not appropriate.

Instead of multiplying the TOA albedo with an empirical anisotropic correction factor, another method is employed based on the accurate RTM described previously. The methodology is to adjust the narrowband surface albedo in the model until the model simulated reflectance (forward calculation) in this band at the TOA is matched with the satellite measurement. Obviously, in this method, we can avoid any attempts to make anisotropical correction and atmospheric correction, but have to assign the unknown atmospheric variables in the RTM, such as aerosol optical depth, the amount of ozone and water vapor. Narrowband albedos in AVHRR channels 1 and 2 are retrived individually, and the broadband albedo is obtained through NTB conversion, which normally consists of a linear regression of the spectral surface albedos in AVHRR channels 1 and 2.

For the retrieval of narrowband albedo, we first used the RTM to generate two look-up tables via forward calculations in channels 1 and 2. Each of the table saves the reflectance at the TOA for a variety of albedo values and viewing geometries. For a given viewing geometry, the tables can be decreased to an array of reflectance versus albedo, then for a given satellite reflectance, the narrowband albedo can be easily obtained ("retrieved") by spline interpolation.

### 3.2.2 Narrow-to-broadband (NTB) Conversion

Surface broadband albedo represents the fraction of solar radiation reflected back to the sky, and from the definition it can be expressed as follows:

$$\alpha = \frac{\sum_i \alpha_i F_i}{\sum_i F_i} = \alpha_{VIS}\frac{F_{VIS}}{\sum_i F_i} + \alpha_{NIR}\frac{F_{NIR}}{\sum_i F_i} + \frac{Others}{\sum_i F_i} = B_1 * \alpha_{VIS} + B_2 * \alpha_{NIR} + B_0$$

Here,

$$B_1 = \frac{F_{VIS}}{\sum_i F_i};\ B_2 = \frac{F_{NIR}}{\sum_i F_i};\ B_0 = \frac{Others}{\sum_i F_i} \tag{3.1}$$

where $F_i$ is the downward radiation in band $i$, $F_{VIS}$ and $F_{NIR}$ are the downward radiation in visible and near infrared (NIR), $\alpha$ is the broadband albedo, and $\alpha_{VIS}$ and $\alpha_{NIR}$ are the narrowband albedo in the visible and near infrared, respectively. As the albedo over snow/ice surfaces decreases significantly for wavelengths larger than 1.10 $\mu$m, the last term $B_0$ is small and can be assumed as a constant.

If we assume the albedo in the visible is close to the albedo in AVHRR channel 1 (0.58-0.68 $\mu$m), and the albedo in the near infrared is close to the albedo in AVHRR channel 2 (0.725-1.10 $\mu$m), we can write:

$$\alpha = C_1 * \alpha_1 + C_2 * \alpha_2 + C_0 \tag{3.2}$$

Here,

$$C_1 = \frac{F_{VIS}^{up}}{F_1^{up}} * \frac{F_1}{\sum_i F_i} = \frac{\alpha_{VIS}}{\alpha_1} * B_1$$

$$C_2 = \frac{F_{NIR}^{up}}{F_2^{up}} * \frac{F_2}{\sum_i F_i} = \frac{\alpha_{NIR}}{\alpha_2} * B_2$$

$$C_0 = B_0$$

where $F_1$ and $F_2$ are the downward surface irradiance in AVHRR channels 1 and 2. $F_1^{up}$ and $F_2^{up}$ are the corresponding upward surface irradiance, and $\alpha_1$ and $\alpha_2$ are the narrowband albedo values in channels 1 and 2, respectively.

Although $C_1$ and $C_2$ are complicate non-linear functions, as an approximation it can be assumed as a constant for a specific atmosphere-surface condition. Then, the broadband albedo is represented approximately as a linear function of spectral albedo in channels 1 and 2. The physical meaning is clear. For example, the coefficients $C_1$ is the ratio of downwelling solar irradiance in channel 1 to the total downwelling solar irradiance multiplied by the ratio of upward irradiance in the visible to that in channel 1. Obviously, $C_1$ and $C_2$ are functions of real atmospheric conditions and surface optical properties, e.g. scattering and absorption in the atmosphere by aerosol, water vapor and other trace gases, and the reflection and absorption at the surface. From this derivation, we can see that $C_1$ and $C_2$ represents the degree of the representativeness of the narrowband reflectance to the broadband reflectance. Use of two AVHRR channels should give an overall higher accuracy than using one of them to estimate the broadband albedo.

From the measurements made on the Greenland ice sheet, Key (1996) obtained the following NTB relation:

$$\alpha = 0.04228 + 0.661\alpha_1 + 0.208\alpha_2. \tag{3.3}$$

Based on measurements for snow-covered ice in the east Antarctic by Allison et al. (1993), Lindsay and Rothrock (1994) obtained:

$$\alpha = 0.43\alpha_1 + 0.47\alpha_2. \tag{3.4}$$

Obviously, there are large differences between NTB conversion coefficients derived from these two different experiments over snow/ice surfaces. The difference

between the above two NTB conversions should be due to the difference in surface conditions and the different airmass. If we ignore the variation of airmass, the increase of surface albedo leads to the increase of the downwelling shortwave radiation because the multiple scattering between the surface and atmosphere increases with the albedo. This can be seen from eq. (4.14) because the denominator decreases as albedo increases while the numerator keeps the same. With the melt of snow/ice surface, spectral albedo in channel 2 decreases much more significantly than in channel 1, so change of $F_1$ is very small, whereas $F_2$ decrease significantly, and the decrease rate of $\sum F_i$ is smaller than $F_2$ but larger than $F_1$. As the ratio of the upward irradiance in the visible to that in channel 1 and the upward irradiance in the NIR to that in channel 2 is almost a constant, so $C_1$ will increase and $C_2$ will decrease according to eq. (3.2).

This expectation can be tested using the SHEBA surface measurements. Over SHEBA, Perovich et al. (1999) measured albedo along a survey line of 200 m covering snow/ice and its melting progress. We took the average of the albedo along the survey line, which is expected to represent the average condition of the surface viewed by the satellite. Using the measurements of Perovich et al. (1999), we performed a linear regression between the broadband albedo and spectral albedos centered at 0.63 $\mu$m and 0.86 $\mu$m during May-August, 1998 over SHEBA to obtain:

$$\alpha = 0.501\alpha_1 + 0.405\alpha_2. \tag{3.5}$$

To examine the dependence of the coefficients after the onset of snow melting, we made linear regressions using the surface measurements during June 20 - August 30, and obtained:

$$\alpha = 0.007 + 0.542\alpha_1 + 0.340\alpha_2. \tag{3.6}$$

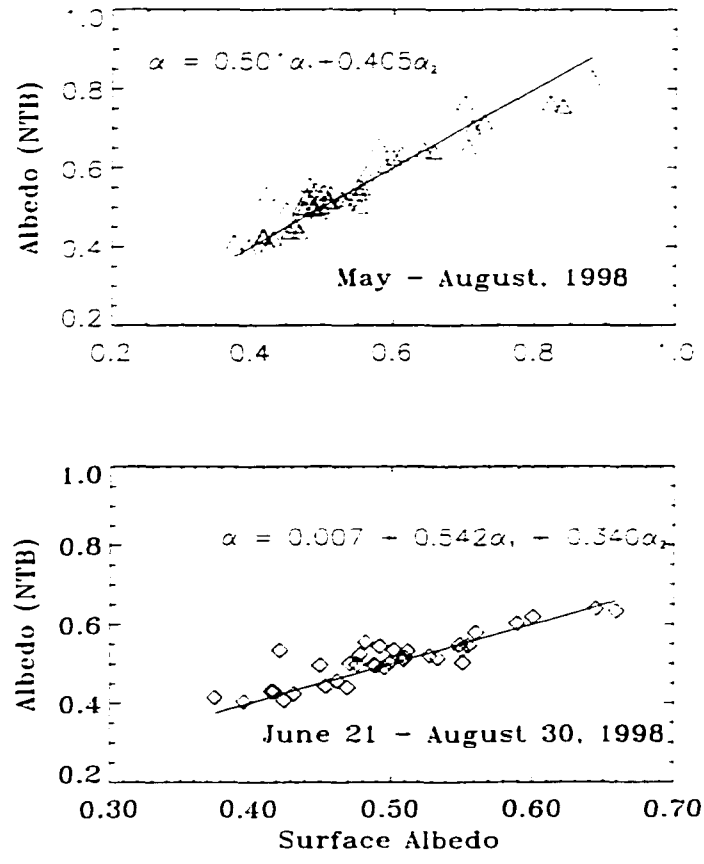


**Figure 3.6** NTB conversion derived from SHEBA data (Perovich et al., 1999) in the period from May to August (upper panel) and from June 20 to August (lower panel) .

where the coefficient $C_1$ is larger and $C_2$ is smaller than in eq. (3.5).

Comparison of surface measurement of albedo by Perovich et al. (1999) with the albedo estimated by NTB conversion is shown in Figure 3.6. A good fit is obtained for the whole melting season with a relative error of 5% and a standard deviation of 0.04. As surface conditions evolved from dry snow (April-May) to melting snow (June 3) to early melt ponds (mid-late June) to fully developed melt ponds (July-August), the albedo in channel 2 decreases significantly after July 20, so the contribution of channel 2 to the broadband albedo becomes smaller.

resulting in a smaller value of $C_2$ for the NTB conversion. As there is only a few measurements by Perovich et al. (1999) over the snow surface before the melt of snow in June, we used the RTM to simulate the spectral albedos in channels 1 and 2 and the corresponding broadband albedo for a series of $r_s$, $s_t$ and solar zenith angle in the Arctic. Using a linear regression we found the following relation between the narrowband and broadband albedo over the snow surface:

$$\alpha = 0.007 + 0.434\alpha_1 + 0.464\alpha_2. \tag{3.7}$$

At the top of atmosphere (TOA), the NTB conversion is as follows:

$$\alpha = 0.045 + 0.304\alpha_1 + 0.486\alpha_2. \tag{3.8}$$

Figure 3.7 shows the difference between the broadband albedo obtained directly from the model simulations and that derived through the NTB conversion using the model simulated narrowband albedos in AVHRR channels 1 and 2 over snow surfaces. The error between the model simulated broadband albedo with that derived by NTB is about 2%. The NTB relationship derived over snow surface from model is close to that over Antarctic snow (Lindsay and Rothrock, 1994). Model simulations also demonstrate that with increase of $s_t$ in snow, $C_1$ increases and $C_2$ decreases.

Using ERBE broadband and AVHRR narrowband data over snow/ice, Li and Leighton (1992) got the NTB conversion at the TOA as follows:

$$\alpha = 0.0453 + 0.389\alpha_1 + 0.452\alpha_2. \tag{3.9}$$

The NTB coefficients at the TOA derived from our model simulations are different from those obtained by Li and Leighton (1992). The disagreement between the

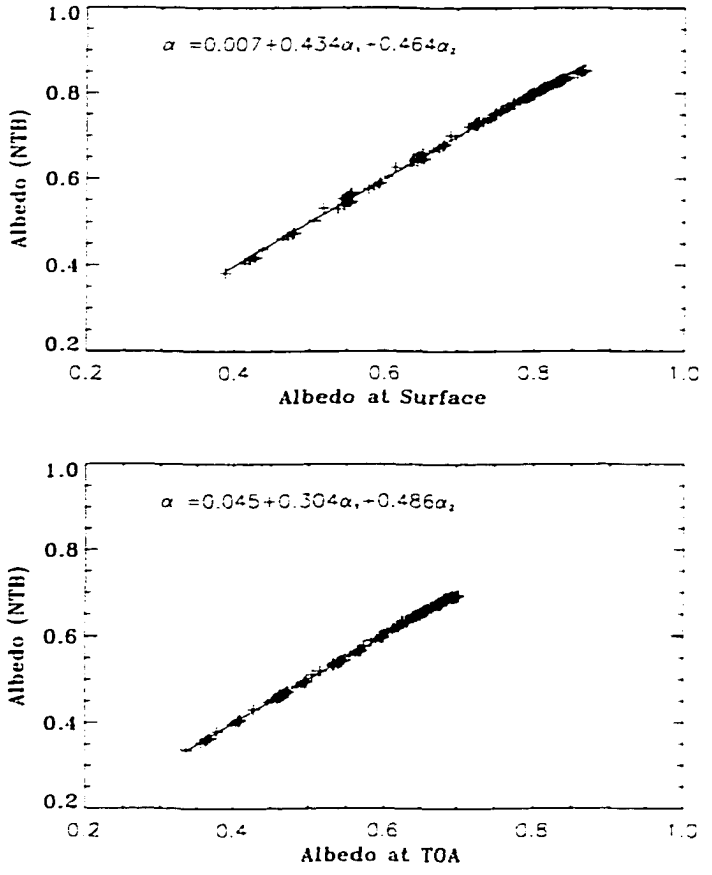


**Figure 3.7** Broadband albedo and the NTB relations over snow surfaces (upper panel) and at the TOA (lower panel).

various NTB conversion coefficients implies that current products of broadband albedo from satellite data based on the use of a uniform NTB conversion coefficients in the polar regions may result in large uncertainties.

### 3.2.3 Uncertainty and Sensitivity Analysis

Lindsay and Rothrock (1994) pointed out that sparse data on aerosols, ozone, and water vapor in the atmospheric column contributed uncertainty in the albedo

of 0.13, 0.04 and 0.08 respectively, but uncertainties in monthly average albedos were not this large. Contemporaneous estimation of these variables could reduce the uncertainty in the estimated albedo considerably, but retrieval of aerosol over snow/ice surface from AVHRR is very difficult. Only water vapor data are available from the sounding profile, so we examined the effects of using such profile on the retrieval of albedo from the RTM. Figure 3.8 shows the reflectance of channels 1 and 2 as a function of surface albedos for two different atmospheric profiles. The higher the albedo, the larger the difference using summer and winter profiles. The influence of using different atmospheric water vapor profiles is much smaller in channel 1 than channel 2, and for surface albedo values between 0.5 and 0.8, the difference in channel 1 is less than 5%, but for channel 2, the difference is about 15-25%. So, use of real sounding profiles helps improve the precision of albedo retrieval for channel 2. Comparison of the retrieved spectral albedo in channels 1 and 2 with the albedo used to calculate the reflectance in these two channels is shown in Figure 3.9. The retrieved albedo error for an assumed $\pm$ 5% error in the reflectance in channels 1 and 2 is also shown in this figure. For $\pm$ 5% error in the reflectance in channels 1 and 2, the error in the retrieved albedo is about 10% and 7% for channels 1 and 2 correspondingly, and only when the albedo is smaller than 0.1, does the error become a little larger.

### 3.2.4 Effects of Snow Bidirectional Reflectance

To examine the effect of bidirectional snow reflectance on the retrieval of albedo, we compared the model simulated narrowband albedo over a snow surface with that retrieved from our albedo retrieval algorithm, in which a Lambert surface is used.

Reflectance in channels 1 and 2 are computed via forward computations using

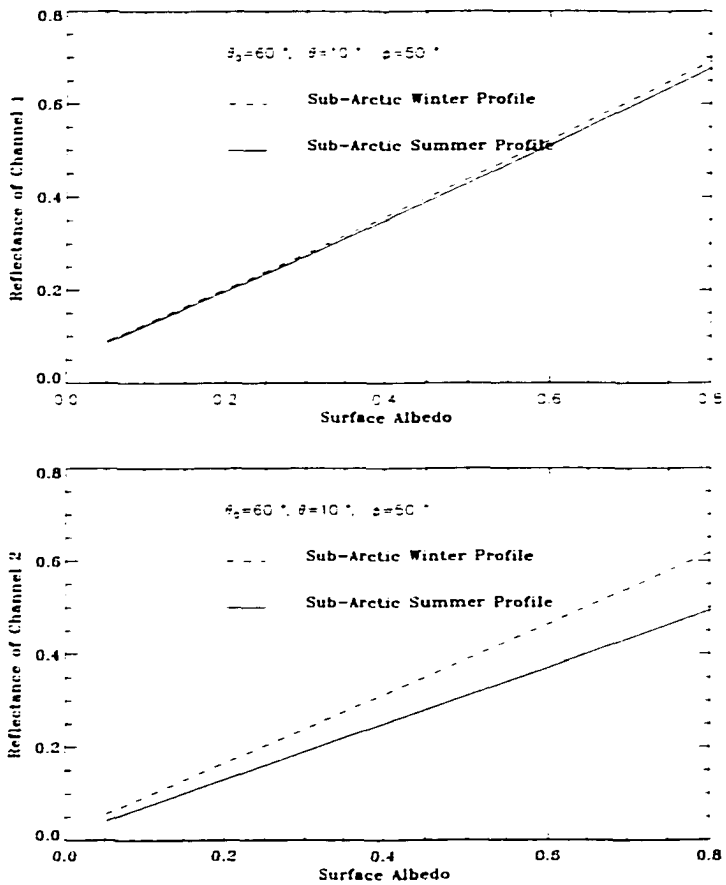


**Figure 3.8** Simulated reflectance for AVHRR channels 1 (upper panel) and 2 (lower panel) as a function of surface albedo for different atmospheric profiles, for $\theta_0 = 60°$, $\theta = 10°$ and $o = 50°$ .

the RTM for the coupled snow-atmosphere system for a series of $r_s$ and $s_t$. With these reflectances as inputs to our albedo retrieval algorithm, we obtained the retrieved albedo over the snow surface. The corresponding "true albedo" values of the snow surfaces were calculated directly from the forward snow-atmosphere radiative transfer model as the ratio of upward irradiance to downward irradiance at the snow surface. Comparison of the narrowband retrieved albedos with the "true" albedos are shown in Figure 3.10. On average, the narrowband albedo in channels 1 (upper panel) is overestimated by 6% when $\theta = 10°$, $o = 50°$.

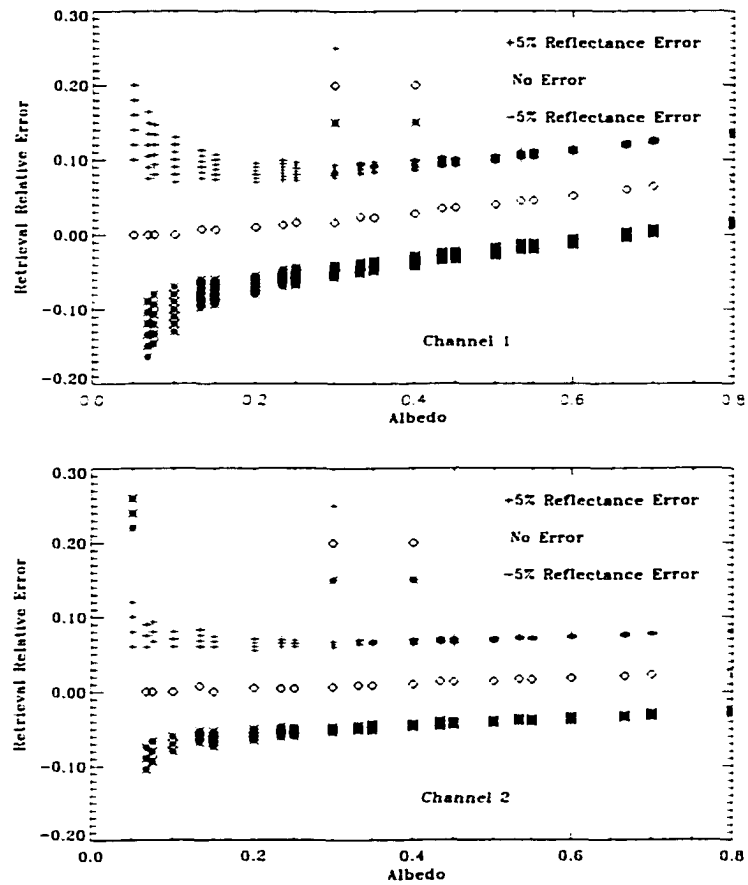


**Figure 3.9** Error of the retrieved narrowband albedo for AVHRR channels 1 (upper panel) and 2 (lower panel) for an uncertainty of ± 5% in satellite-measured radiance.

and overestimated by 18% when $\theta = 30°$, $\phi = 150°$. On the other hand, when $\theta = 10°$, $\phi = 50°$, the narrowband albedo in channels 2 (lower panel) is only a little overestimated for low albedo but a little underestimated for high albedo. When $\theta = 30°$, $\phi = 150°$, the albedo in channel 2 is overestimated by 14%. As the anisotropic factor becomes larger for larger view and azimuthal angles (see Figure 1, Han et al., 1999), the effect of snow bidirectional reflectance leads to the reflectance in channels 1 and 2 to be larger for snow surface than for Lambert reflector. Thus the retrieved albedo in channels 1 and 2 will be overestimated. From our

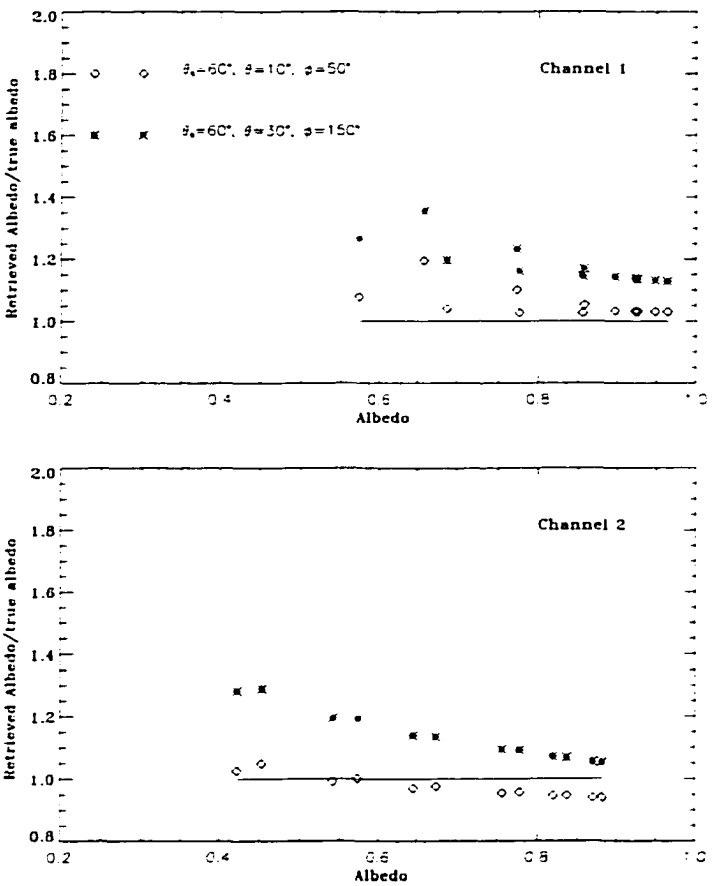


**Figure 3.10** Comparison of the retrieved narrowband albedo in channels 1 (upper panel) and 2 (lower panel) with the actual snow surface albedo for $\theta = 10°$, $\phi = 50°$, and for $\theta = 30°$, $\phi = 150°$ .

calculations, we also have found that the albedo in channels 1 is overestimated by 9% when $\theta = 10°$, $\phi = 150°$, whereas the albedo in channels 2 is overestimated by 3%. From these calculations, it can be concluded that when the view angle is small ($\theta < 10°$), the uncertainty in the retrieved broadband albedo is about 5% if the effect of bidirectional reflectance is not considered, but it can be as high as 15~20% for $\theta = 30°$. In our analysis of SHEBA data, only the near overhead passes with small view angles are chosen, so our albedo retrieval errors due to ignoring the snow bidirectional reflectance effects are less than 5~10%.

## 3.3 Application and Results

### 3.3.1 Seasonal Variation of Surface Albedo over SHEBA and its Comparison with Surface Measurements

For validation purposes, we use the surface albedo measured at SHEBA (Perovich et al., 1999). As part of the ice-albedo feedback studies during SHEBA, spectral and wavelength-integrated albedos were measured at least weekly every 2.5 m along a 200-m survey line from April through October. From June through August, albedo measurements were made every other day. Albedos integrated from 300 to 3000 nm were measured using a Kipp & Zonen albedometer. Spectral albedos from 300 to 2000 nm were measured using a Spectron Engineering SE-590 spectroradiometer. Albedos were accurate to within $\pm$ 0.01 (Perovich et al., 1999). In the beginning of the measurements, the survey line was completely snow-covered, but with the onset of melting surface conditions evolved from dry snow (before May) to melting snow (early June) to early melt ponds (late June) to fully developed melt ponds (middle of July).

Figure 3.11 shows the variation of observed albedo along the line for May 11, May 25, June 25 and July 23, 1998 over SHEBA. On May 11 and May 25, the surface along the line is still snow covered, so albedo is stable along the line. With the occurrence of melt ponds along the line (June 25), the albedo became smaller and also varied along the line, but the amplitude of the variation is small. By July 23, the ponds had fully developed, and the albedo decreased further with large variation along the line. Generally, the albedo shows a gradual evolution due to seasonal transitions and abrupt shifts resulting from synoptic weather events. A pronounced decrease of spectral albedo in melt ponds during summer was observed by Perovich et al. (1999). The pond albedo is dominated by the scattering prop-

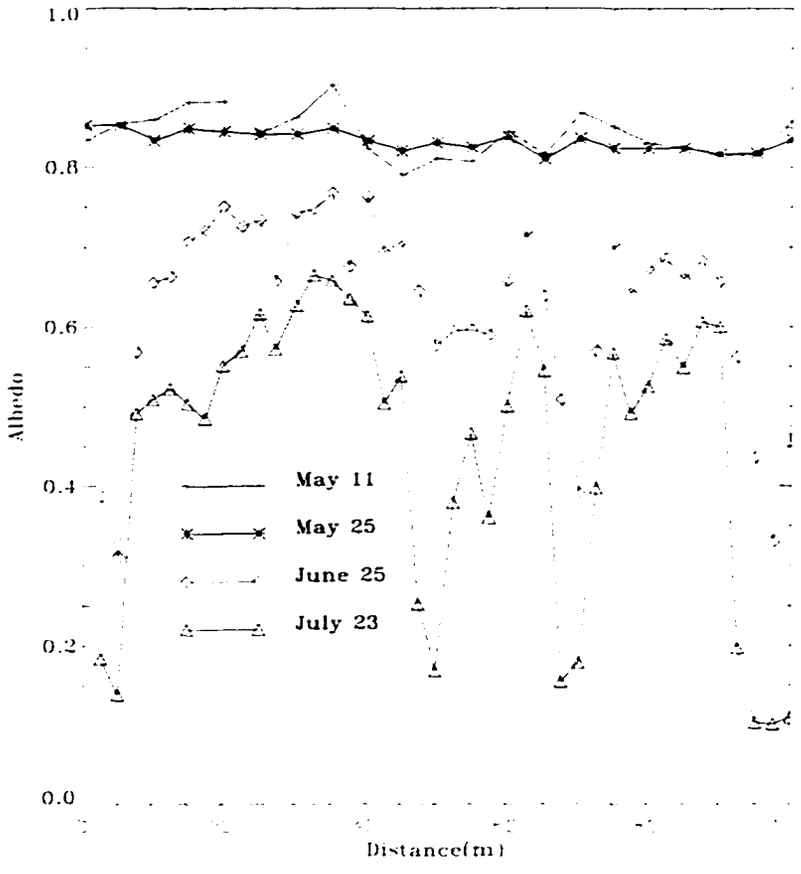


**Figure 3.11** Variation of measured surface albedo along the scan line in different date (data is taken from Perovich et al. (1999)) .

erties of the underlying ice because the scattering of the underlying ice has the greatest influence on the albedo from 400 nm to 600 nm, where the pond water is most transparent. From 400 nm to 600 nm light pond albedos were 0.2 to 0.25 larger than dark pond values, despite no appreciable difference in the pond water depth between the light and dark pond. Spectral albedos measured at the bare ice site on 12 days between 7 July and 12 August shows that over white ice the albedo at a particular wavelength never varied by more than 0.1 during this five-week period, and the albedo over bare ice fluctuated, rather than showing a systematic

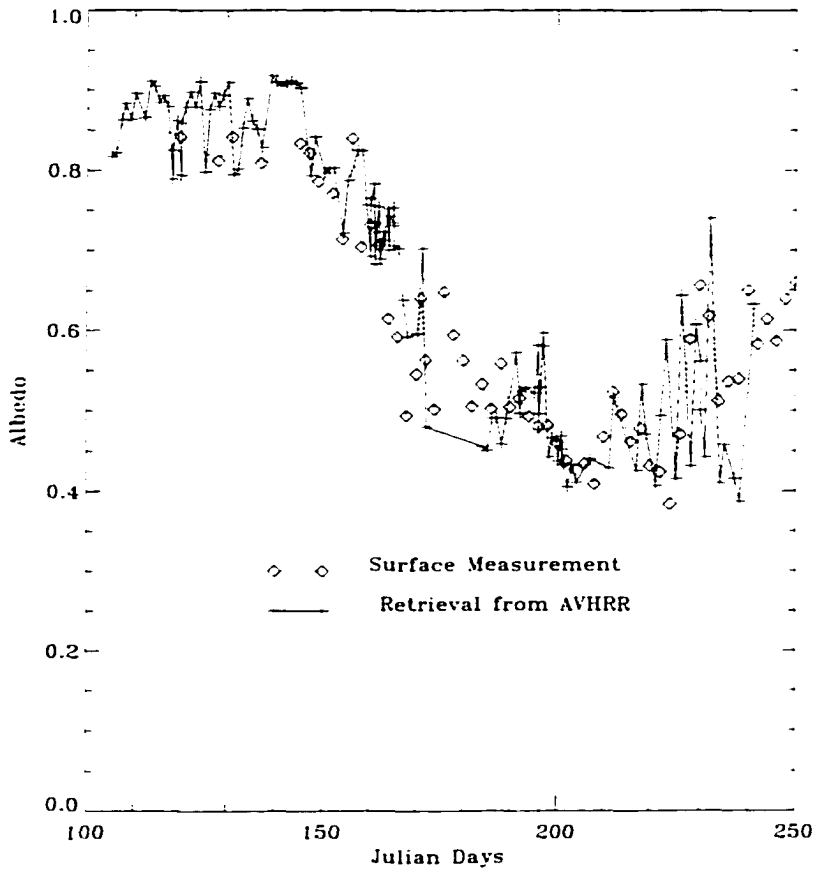


Figure 3.12 Comparison of surface albedo retrieved from AVHRR with the SHEBA surface measurements.

downward trend as it does over the melt pond. There was approximately 60-70 cm of surface ablation in the summer.

AVHRR data for retrieval of albedo is chosen from one or two passes of NOAA-14 per day over SHEBA during April to August, 1998. Because no post-launch calibration of AVHRR channels 1 and 2 on NOAA-12 is available, AVHRR on NOAA-14 is used. Revised calibration to NOAA-14 AVHRR in 1999 (Rao and Chen, 1999) is used instead of the calibration in 1996. Our independent study found the error on the post-launch calibration in 1996, which will be discussed

in Chapter 5. Observed surface albedo from Perovich et al. (1999) is used to evaluate the satellite retrieval of albedo. The results are shown in Figure 3.12. Obviously, satellite retrieval has captured the seasonal variation of the albedo, but it has missed some of the abrupt shifts in albedo due to synoptic weather events, for example snow precipitation, which leads to the increase of albedo, and rain precipitation, which leads to the decrease of albedo when dry snow becomes wet. These albedo differences when the spikes occurred are understandable because of the much larger spatial coverage of the satellite, and because the synoptic process is always of limited temporal and spatial coverage. Also albedo retrieval is not available while the surface is obscured by clouds, and mis-identification of clear sky will lead to some error in the albedo retrieval. In view of the large variation of albedo in the survey line (100 m), the difference between satellite-retrieved and surface-measurement albedo is quite reasonable. The agreement is relatively worse in August. Large variation of albedo in August, due to developed ponds and leads, resulting in a very inhomogeneous surface, is the reason for the disagreement.

### 3.3.2 Correlation of Surface Albedo and Surface Temperature

To examine the correlation between the surface temperature and the albedo, the technique of Key et al. (1997) based on the thermal channels of AVHRR is used to estimate the surface temperature. The average temperature versus the albedo during the season is shown in Figure 3.13. With the increase of surface temperature, albedo tends to decrease, but there is little correlation during the whole melting season. Lindsay and Rothrock (1994) found that surface albedo and surface temperature are correlated most strongly in March with little correlation in the summer.

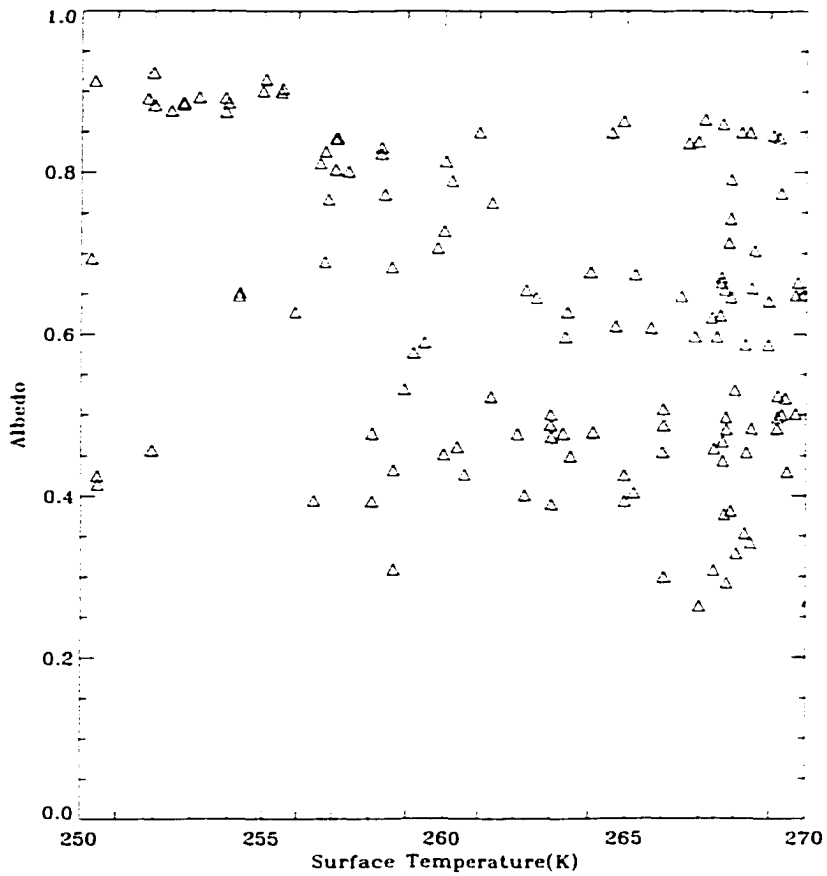


**Figure 3.13** Relation of satellite retrieved albedo versus surface temperature .

## 3.4 Discussion and Summary

Two algorithms to retrieve the $r_s$ and its mass fraction of soot, and the broadband albedo were developed and applied to AVHRR data obtained between April and August, 1998 over the SHEBA Ice Camp.

In these algorithms, channels 1 and 2 were used together to retrieve snow gain size and soot, or broadband albedo. The error stems mainly from the satellite measurements. A $\pm$ 5% uncertainty in the satellite measured reflectance in channel

1 and 2 result in an uncertainty in the retrieved $r_s$ and $s_t$ of about 200% for new snow whose $r_s$ is small. For old snow with large $r_s$, the error is more than 50%. Retrieval of albedo is not so sensitive to the error in the satellite measurement. A $\pm$ 5% uncertainty in the satellite measurement results in an albedo uncertainty of about 10%.

The effect of water vapor on the satellite-measured radiance in channel 2 is significant. Use of the subarctic summer atmospheric profile instead of the winter profile could lead to a 40% difference in reflectance over snow surface. So use of instantaneous sounding profiles is important for retrieval of snow properties or the retrieval of narrowband albedo in channel 2. The uncertainty resulting from the lack of knowledge of aerosol is about 5% in the Arctic.

For different surface conditions the NTB coefficients are quite different. With the melt of snow, the channel 1 coefficient increases while the channel 2 coefficient decreases. Use of different NTB conversions may result in a broadband albedo uncertainty of about 10-15%. The conversion coefficients depend on both the atmosphere and surface physical conditions, so different NTB conversion coefficients should be used under different circumstances. These coefficients can be obtained from surface measurements.

For the retrieval of albedo over snow surface, the use of the Lambert assumption is not appropriate. For $\theta < 10°$, the error in the albedo is less than 5-10%, but for $\theta > 30°$ and large azimuthal angles, the error in the albedo is significant due to the large bidirectional reflectance. This is the reason that we chose the near-overhead passes of AVHRR for analysis.

Comparison of the AVHRR-retrieved surface albedo from April to August, 1998 over SHEBA with SHEBA surface measurements shows that the satellite retrieval is in good agreement with surface measurements. Minor differences between them are due to the difference in spatial coverage, and the large variation in surface

albedo due to the development of melt ponds and leads. Failure to discriminate thin/cirrus cloud from snow surface may lead to a significant error in albedo retrieval. With the deployment of new sensors, such as MODIS and GLI, much more channels become available. New channels, such as the 1.38 $\mu$m channel of MODIS are expected to improve the discrimination of ice clouds and to improve the albedo retrieval over snow surface.

# Chapter 4

# Retrieval of Cloud Optical Thickness from SHEBA Ground-Based Irradiance Measurements

## 4.1 Introduction of Cloud Parameterization

Clouds have a major impact on weather and climate by influencing the radiative properties such as shortwave albedo, infrared emission, and absorption. High clouds are generally thought to warm the earth-atmosphere system while low clouds cool it. However, the effect of clouds on the climate is still one of the biggest uncertainties in the study of climate change (see for example IPCC, 1990). One reason is the large temporal and spatial variation of cloud microphysical and radiative properties.

Of all cloud variables, cloud optical depth and effective cloud particle size are the most important ones determining the radiative properties (see for example,

Nakajima and King, 1990; Slingo, 1989; Hu and Stamnes, 1993; Hu and Stamnes, 2000). The cloud optical properties needed for radiative transfer calculations are the volume extinction coefficient $\beta_{ext}$, the single scattering albedo $\omega$ and the asymmetry factor g. For warm clouds consisting of spherical cloud droplets, the liquid water content and the equivalent radius ($r_e$) are the two most important cloud microphysical parameters influencing the radiative properties (Slingo, 1989). Also, it was found that the cloud optical properties depend almost exclusively on equivalent radius and liquid water content, and are insensitive to the details of the drop size distribution (Hu and Stamnes, 1993; Slingo, 1989).

The cloud effective radius, or equivalent radius ($r_e$, in $\mu m$) is defined as:

$$r_e = \frac{\int_0^\infty n(r) r^3 dr}{\int_0^\infty n(r) r^2 dr}. \tag{4.1}$$

where $n(r)$ is the cloud droplet size distribution, and $r$ is the radius.

The liquid water content ($LWC$, in $g \cdot cm^{-3}$) is defined as:

$$LWC = \frac{4\pi\rho_w}{3} \int_0^\infty n(r) r^3 dr. \tag{4.2}$$

where $\rho_w$ ($g \cdot cm^{-3}$) is the density of water.

The volume extinction coefficients is:

$$\beta_{ext} = \pi \int_0^\infty n(r) r^2 Q_{ext}(r) dr, \tag{4.3}$$

where $Q_{ext}$ is the extinction efficiency factor. For shortwave radiation, the droplet size is much larger than the wavelength ($\frac{2\pi r}{\lambda} \gg 1$), so we can take $Q_{ext} \approx 2$ as a good approximation. Combining the above three equations, we find:

$$\beta_{ext} \approx \frac{3LWC}{2\rho_w r_e}. \tag{4.4}$$

Cloud optical depth ($\tau$) is the optical path in the vertical direction.

$$\tau = \int_{z_1}^{z_2} \beta_{ext} dz, \tag{4.5}$$

where $z_1$ is the height of cloud base and $z_2$ is the height of cloud top. The liquid water path (LWP) is simply $LWP = LWC(z_2 - z_1)$ if the $LWC$ is assumed to be independent of $z$. Combining the above two equations, we get:

$$\tau \approx \frac{3LWP}{2\rho_w r_e}. \tag{4.6}$$

From this simple relation, $\tau$ is proportional to LWP and inversely proportional to $r_e$. Thus we can estimate $r_e$ if $\tau$ is retrieved and $LWP$ can be measured using, for example, Microwave Radiometer (MWR) data.

In this thesis we used a more general and accurate parameterization relationship for water clouds. Hu and Stamnes (1993) showed that the single scattering albedo $\omega$, the extinction coefficient $\beta_{ext}$, and the asymmetry factor $g$ can be described in terms of the cloud droplet effective radius $r_e$ and the liquid water content $LWC$ as follows:

$$\frac{\beta_{ext}}{LWC} = a_1 r_e^{b_1} + c_1. \tag{4.7}$$

$$1 - \omega = a_2 r_e^{b_2} + c_2. \tag{4.8}$$

$$g = a_3 r_e^{b_3} + c_3. \tag{4.9}$$

The coefficients, $a_i, b_i$ and $c_i$ are wavelength-dependent. For the table of coefficients, see Hu and Stamnes (1993).

As ice clouds contain almost exclusively nonspherical ice crystals of various shapes, such as bullet rosettes, plates, and columns, the parameterization relationship is quite different. From the parameterization of Fu and Liou (1993), a mean effective size $D_e$ representing an area-weighted mean crystal width is used to account for the ice crystal size distribution with respect to radiative calculations, as follows:

$$D_e = \frac{\int_{L_{min}}^{L_{max}} D * DLn(L)dL}{\int_{L_{min}}^{L_{max}} D * Ln(L)dL} \tag{4.10}$$

where $D$ is the width of an ice crystal, and $n(L)$ denotes the ice crystal size distribution.

For ice clouds, the extinction coefficient divided by ice water content (IWC) and the single-scattering albedo can be parameterized using polynomials in terms of the mean effective size (Fu and Liou, 1993) as follows:

$$\beta_{ext} = IWC \sum_{n=0}^{N} a_n / D_e^n. \tag{4.11}$$

$$1 - \omega = \sum_{n=0}^{N} b_n / D_e^n. \tag{4.12}$$

Finally, the moments of the phase function may be determined in a similar fashion:

$$g = \sum_{n=0}^{N} c_n / D_e^n. \tag{4.13}$$

where $a_n$, $b_n$ and $c_n$ are certain coefficients, which must be determined from numerical fitting. $N$ is the total number of terms required to achieve a prescribed accuracy. The coefficients are provided by Fu and Liou (1993).

Generally, global distribution of cloud optical thickness $\tau$ comes largely from the International Satellite Climatology Project (ISCCP) (Rossow 1989; Rossow and Schiffer, 1991). In the ISCCP analysis, visible radiances are used to infer cloud optical thickness assuming the effective radius to be 10 $\mu$m (Rossow et al., 1991). Such an assumption leads to 15% - 25% error in optical thickness for water clouds (Rossow et al., 1991; Nakajima and King, 1990; Han et al., 1994), and the error is larger for ice clouds and over the polar regions. Long-record ground-based measurements of incoming solar irradiance provide another opportunity to

derive the cloud optical thickness from the downwelling shortwave solar radiation (DSSR). This method, which uses the transmittance of radiation to derive the optical thickness, was developed by Leontyeva and Stamnes (1994; 1996), and successfully used by Min and Harrison (1996) and Barker et al. (1998).

In this chapter, an algorithm to infer cloud optical depth from ground-based measurements is briefly described and applied to get the seasonal variation of cloud optical depth using the SHEBA Precision Spectral Pyranometer (PSP) measurements.

## 4.2 Retrieval Method

A method similar to that used by Leontyeva and Stamnes (1994) and Barker et al. (1998) was employed to derive cloud optical thickness from ground-based measurements of the irradiance of the DSSR. To avoid time-consuming root-finding iterations of the radiative transfer equation for each spectral interval and admissible observation to solve for $\tau$, an approach developed by Stamnes (1982) was employed in this method. With this efficient computational algorithm, look-up tables were generated of spectral transmittance $T_j(\tau_j, \mu_0, \alpha_s = 0)$, one for each of the 24 bands in the solar spectrum (0.25-4.0 $\mu$m) at several values of $\mu_0$, for clouds over a nonreflecting surface ($\alpha_s = 0$). Spectral atmospheric spherical albedos $\overline{\alpha_j}$ for upwelling radiation were also computed and stored in the look-up tables.

The spectral atmospheric transmittance for a specific albedo $\alpha_s$ were calculated as:

$$T_j(\tau_j, \mu_0, \alpha_s) = \frac{T_j(\tau_j, \mu_0, \alpha_s = 0)}{1 - \alpha_s \overline{\alpha_j}} \quad (j = 1, 24). \tag{4.14}$$

This expression is exact for a Lambert surface with albedo $\alpha_s$.

Using the same atmospheric model and the radiative transfer model DISORT as discussed in Section 1.5, we computed the spectral transmittance over a "black"

surface $T_j(\tau_j, \mu_0, \alpha_s = 0)$ for 165 cosines of the solar zenith angle $\mu_0$ with equal intervals (in the range of 0-80°) and 52 values of $\tau$ of unequal intervals in range of 0 to 100 for each of the 24 bands. The band transmittance is approximated as a weighted sum of the "monochromatic" transmittance in all the sub-bands used to approximate the gaseous absorption in each of the 24 bands as explained in Section 1.5. As the spectral distribution of solar irradiance at the TOA is known, the transmittance of solar radiation can be weighted and summed to produce a two-dimensional table of the broadband solar irradiance at the surface as a function of $\tau$ and $\mu_0$ for a given albedo. Given the $\mu_0$ and the surface measurement of irradiances, it is easy to retrieve $\tau$ through interpolation in the 2-D table.

Model simulations show that transmitted solar irradiance is not very sensitive to cloud effective radius, but the DSSR for a low albedo surface is more sensitive to equivalent radius than for a bright snow/ice surface (Leontyeva and Stamnes, 1994). As the albedo is large over snow/ice surface, the retrieval of $\tau$ from the downwelling solar radiation is accurate in the polar regions. The cloud effective radius used in our retrieval is 7 $\mu$m, the same as that used by Leontyeva and Stamnes (1994).

## 4.3 Uncertainty Analysis

According to the analysis of Leontyeva and Stamnes (1994), the retrieval method itself leads to uncertainty in the estimated $\tau$ that is smaller than 1 for $\tau < 10$, and smaller than 3 for $\tau \leq 20$. Lack of instantaneous measurements of aerosol optical depth and precipitable water could result in uncertainty of 10% in the retrieved $\tau$.

Model simulations show that for a 5% error in the pyranometer measurement, the uncertainty in the estimation of $\tau$ is smaller than 2 for a small surface albedo. The uncertainty is about 3-4 under the condition of high albedo, large solar zenith

angle and large optical thickness. By comparison, cloud optical depth retrieval from satellite data is also uncertain. For a 5% error in satellite-measured reflectance at 0.75 $\mu$m, the error in the retrieved $\tau$ monotonically increases as $\tau$ increases, from about 10% at $\tau = 5$ to more than 50% at $\tau = 50$ (Nakajima and King, 1990; Leontyeva and Stamnes, 1994). So $\tau$ retrieved from ground-based measurements may be more reliable than that derived from satellite data.

As the DSSR depends on the surface albedo, uncertainty in the albedo is another source of uncertainty for the retrieval of $\tau$. Figure 4.1 shows the uncertainty of the retrieved $\tau$ as a function of cloud optical depth and the surface albedo for +5% uncertainty of albedo at solar zenith angle 50°. For a high albedo of 0.7, the error in $\tau$ is less than 10%, and for an albedo of 0.45, the error is about 5%.

## 4.4 Application and Results

### 4.4.1 Data

DSSR measured at SHEBA will be used to retrieve $\tau$ if the solar zenith angle is smaller than 76° because at solar zenith larger than this value, the signal is too small and therefore unreliable. Hourly mean values of DSSR were used to retrieve the average cloud optical depth for this hour in order to avoid the presence of broken clouds, cloud development and/or dissipation. When the measured DSSR is larger than the model-simulated DSSR under clear sky condition, or the retrieved $\tau$ is smaller than 1, we do not attempt a retrieval because then either the sky may be clear or the uncertainty in the retrieved $\tau$ will be very large.

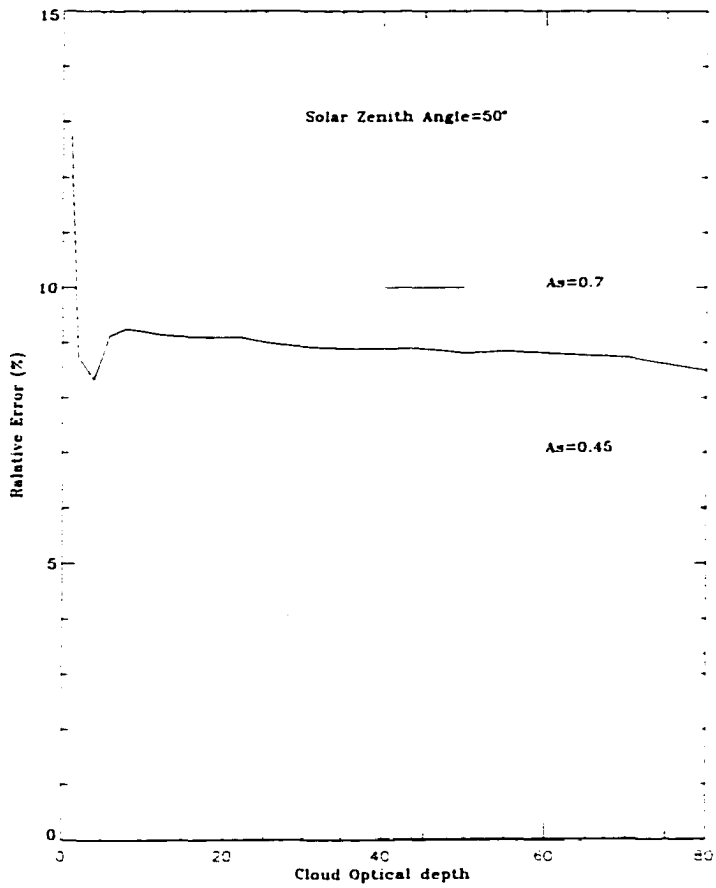


Figure 4.1 Uncertainty of retrieved $\tau$ for a +5% error in surface albedo (As) of 0.45 and 0.7 under the condition of $\theta_0 = 50°$. .

### 4.4.2 Characteristics of $\tau$ over SHEBA

With the increase of effective radius, both the absorption and forward scattering by cloud drop increase (decrease of $\omega$ and increase of g). Increase of the cloud absorption results in a decrease of the downwelling irradiance, whereas an increase of forward scattering by cloud droplet results in an increase of the downwelling irradiance. Due to these two opposite effects, the downwelling radiation is not sensitive to changes in cloud effective radius. Equivalent radius in Arctic stratus

clouds was observed to lie in the range between $r_e = 3.3$ $\mu$m and 11.4 $\mu$m (Herman and Curry, 1984), so while generating the look-up tables of transmittance, the cloud layer was assumed to reside between 1 and 2 km above the ground, and consist of liquid water droplets with effective radius 7 $\mu$m. Neglect of ice and mixed phase clouds may lead to only a slight overestimation of $\tau$ because g for ice clouds is roughly equal to that for liquid clouds, and the difference in $\omega$ between ice and liquid water clouds has a relatively minor impact on the transmittance (Barker et al., 1998).

Although Leontyeva and Stamnes (1994) demonstrated that the use of a spectrally invariant surface albedo $\alpha_s$ is not a problem for snow surface, for a better approach, we will allow the spectral albedo to vary of snow surface in 24 bands while the snow grain size and mass fraction of soot are retrieved (Chapter 2). For other types of surface, $\alpha_s$ is simply calculated as the upwelling to incoming irradiance measured at SHEBA, and it is kept constant across the spectrum (Barker et al., 1998). The subarctic summer atmosphere profile (McClatchey et al., 1971) with 33 layers up to 100 km was used. Background tropospheric aerosol optical properties taken from MODTRAN were used.

Cloud optical depth is retrieved from April to August, 1998 over SHEBA. In March and September, most solar zenith angle is larger than 76°, so the number of admissible data points is limited. Figure 4.2 shows the mean hourly optical depth for April to August, 1998 as a function of the GMT time over SHEBA. The mean $\tau$ is about 10 without distinct daily variation. To see the cloud distribution, Figures 4.3 show the histogram of hourly mean cloud optical depth for each month. Figure 4.4 shows the seasonal variation of mean cloud optical thickness and its standard deviation at SHEBA. A comparison with the cloud optical depth derived from surface radiation measurements in Barrow in 1988 by Leontyeva and Stamnes (1994) is also shown. There is a tendency for $\tau$ to increase during the

melting season. There are several factors influencing the development of clouds. With regard to radiation, we note that with the melting of surface snow and ice during the summer, the surface albedo decreases, and the net radiation absorbed at the surface increases, so more energy is available to heat the surface and lower atmosphere and thereby influence the development of clouds. The retrieved $\tau$ at SHEBA is smaller than at Barrow. From the analysis of cloud optical depth derived from Pyranometer measurements at 21 Canadian stations over more than 20 years, Barker et al. (1998) concluded that the mean values of $\tau$ decrease from about 35 at a latitude of 50°N to about 22 near the Arctic Circle. This poleward trend of decreasing $\tau$ is consistent with our results because SHEBA was at a higher latitude than Barrow, if we disregard the possible change in cloud optical depth between 1988 and 1998 due to climate change.

## 4.5 Summary and Discussion

In this chapter, an approach to derive the cloud optical thickness from DSSR at the ground was applied to SHEBA data obtained between April and August, 1998. This approach to infer the cloud optical depth from transmittance of solar radiation passing through the cloud/atmosphere could be used to evaluate the satellite retrieval of cloud optical depth using the reflectance at the TOA.

As the DSSR is not sensitive to cloud effective radius and cloud phase, it is possible for us to set a constant value for the effective radius as $r_e = 7.0\ \mu m$ and assume the cloud to be a water cloud while deriving the cloud optical depth. A fast algorithm based on a method described by Stamnes (1982) is used for this retrieval which has an error of about 10%. Model simulations indicate that uncertainty in the measured irradiance of 5% results in the uncertainty in $\tau$ to be 3-4 for a high surface albedo. The error in the cloud retrieval between April and May is expected

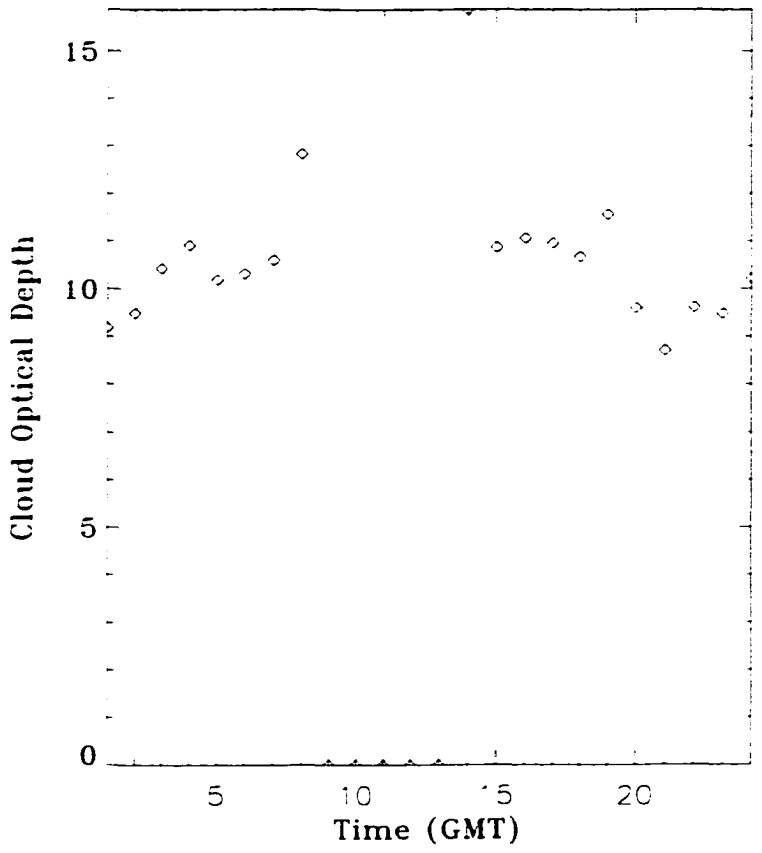


**Figure 4.2** Daily variation of $\tau$ from April to August, 1998 over SHEBA .

to be larger than in June - August.

We derived the cloud optical depth between April and August, 1998 using ground-based radiation measurements at SHEBA. The results show that the mean optical depth is about 10 over the high Arctic Ocean, and it tends to increase with the melting of the snow/ice surface. In the next step, we will use this technique to study the variation of $\tau$ in the Arctic using the measured DSSR at the NSA/ARM site in Barrow.

In addition to the errors associated with the retrieval method and the mea-

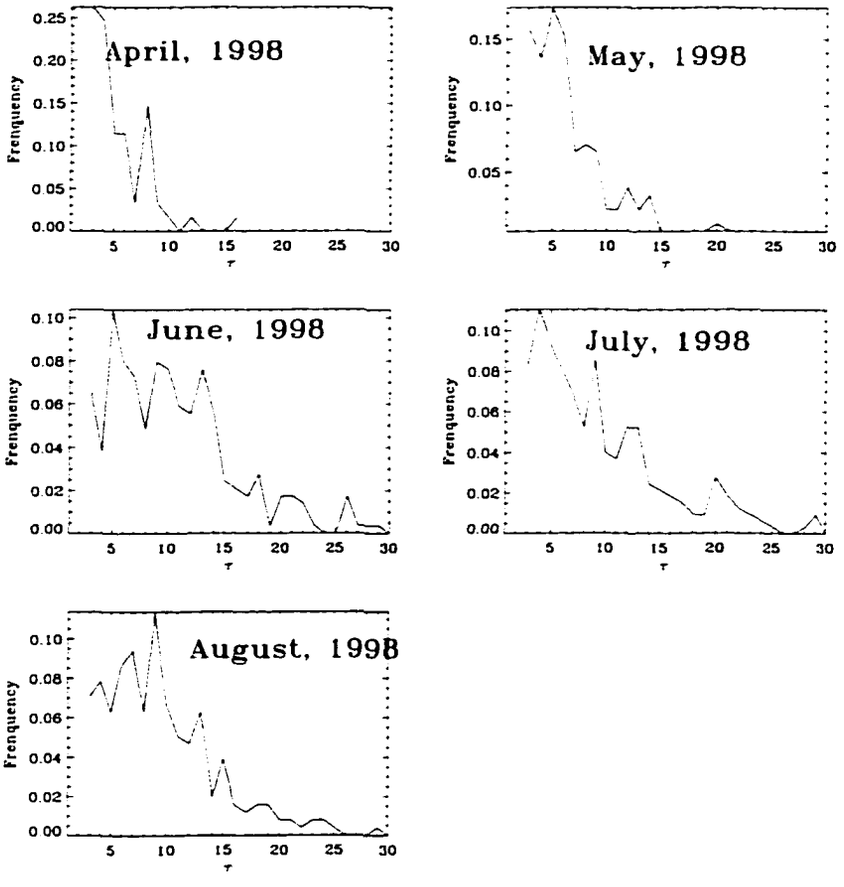


**Figure 4.3** Histogram of optical depth from April to August, 1998 over SHEBA .

sured irradiance, the most important source of error is the surface albedo because of its rapid change during the melting season (see Chapter 3). In our RTM, the cloud is assumed to be a plane-parallel slab. The low-level stratiform clouds that are a prevalent feature in the Arctic (Tsay and Jayaweera, 1984) seem to be good candidates for the theoretical study of radiative transfer in a plane-parallel atmosphere with multiple scattering. However, the influence of cloud variation in the horizontal direction on the retrieval of cloud optical depth may be large. Use of a 3-D radiative transfer model may provide better results. In recent years, it is

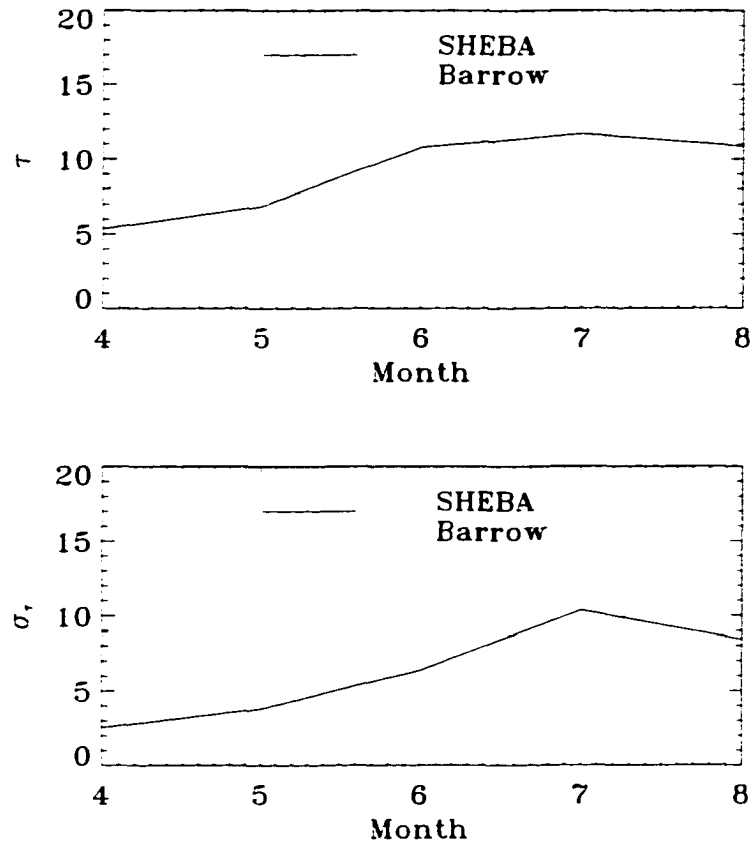


**Figure 4.4** Comparison of monthly mean cloud optical depth (upper panel) and the standard deviation over SHEBA in 1998 and Barrow in 1988 (from Leontyeva and Stamnes, 1994) .

found that theoretical model computation overestimates the downward shortwave irradiance at the surface compared with observations (see for example, Kato et al., 1997). This uncertainty is not considered in this chapter.

# Chapter 5

# Cloud Properties Retrieved from AVHRR over the Arctic Ocean

## 5.1 Background

As mentioned in Chapter 4, of all the cloud variables, cloud optical depth and cloud effective radius are the most important ones for the cloud radiative properties (see for example, Nakajima and King, 1990; Slingo, 1989; Hu and Stamnes, 1993, 2000). The use of satellite data to derive some of the cloud properties, such as cloud cover, optical depth, cloud droplet effective radius and liquid water path (LWP) has proven to be a possible and economic way to establish a global data base of cloud properties (see for example Nakajima and King, 1990; Nakajima et al., 1991; Key, 1997; Han et al., 1994; Han et al., 1999).

Many studies have been conducted to determine cloud optical depth ($\tau$) and effective particle radius ($r_e$) over low albedo surfaces at low- and mid-latitudes using the reflected solar radiation in the visible and near-infrared (NIR) spectral range (Curran and Wu, 1982; King, 1987; Foot, 1988; Rossow *et al.*, 1989; Twomey and Cocks, 1982, 1989; Nakajima and King, 1990; Rawlins and Foot, 1990; King et

al., 1997). These algorithms rely on the fact that the reflection function of clouds at a nonabsorbing channel in the visible wavelength region is primarily a function of cloud optical depth, whereas the reflection function at a water absorbing channel in the NIR is primarily a function of cloud droplet size. However, in the polar regions, the surface is covered by snow/ice most of the time throughout the year. Visible solar radiation reflected by clouds over a bright snow/ice surface is not as sensitive to the cloud optical depth as over a dark surface. This is due to the low contrast between the cloud and the bright surface, and the multiple reflections between the cloud base and the underlying snow/ice surface. However, the reflection function at a water-absorbing channel in the NIR is sensitive to the cloud optical depth, so channel 2 is better than channel 1 for the retrieval of cloud optical depth over a snow/ice surface.

Retrievals of cloud $\tau$ and $r_e$ in the polar regions have been attempted in recent years (see for example, Key, 1997; King *et al.*, 1987); Lubin et al., 1994; Han *et al.*, 1999). Key used AVHRR channel 2 to infer water cloud optical depth over snow/ice. Han *et al.* (1999) also used AVHRR channel 2 for the retrieval of water clouds in the Arctic, but instead of using the Lambert approximation to the surface reflection as Key (1997) did, the bidirectional reflection of the snow surface was accounted for. Lubin *et al.* (1994) proposed an empirical parameterization of cloud optical depth as a function of the brightness temperature difference between AVHRR channels 3 and 4 over the Antarctic. In all these works, there are no direct validations due to lack of in-situ measurements, and indirect comparisons of the derived downward solar irradiance with surface measurements are scarce. So, more theoretical and experimental studies are required in order to assess the soundness and the accuracy of these methods when applied to AVHRR measurements in the polar regions. Observations of clouds using surface radar, lidar and airborne observations in the Arctic have been carried out by the SHEBA, ARM/NSA and

FIRE-ACE projects. These observational data sets provide a good opportunity to evaluate cloud retrieval algorithms.

In this chapter, two retrieval algorithms are developed that are suitable for inferring cloud $\tau$, $r_e$ and cloud top temperature ($T_c$) under polar conditions from the reflectance in channel 2, and the brightness temperatures in channels 3 and 4. Similar to Han et al. (1999) the BRDF of the snow surface is considered using a RTM for the coupled atmosphere-snow system. This Cloud Retrieval Algorithm over Snow surface (CRAS) is used for data acquired in April and May. After the melting season begins in June, the surface bidirectional reflectance is much less pronounced because the surface is composed of leads, ponds or water-soaked melting snow. Thus the Lambertian approximation will be used. This Cloud Retrieval Algorithm over a Lambert surface is called CRAL. The AVHRR retrieved results from these two algorithms are compared with the in-situ aircraft measurements. MAS retrieval results from FIRE-ACE data and surface-retrieved cloud optical depths (see Chapter 4) derived from SHEBA and ARM (Xiong et al., 2000a, c).

## 5.2 Description of the Retrieval Algorithms

### 5.2.1 Radiative Transfer Model (RTM)

Cloud liquid water content (LWC) or ice water content (IWC), effective droplet radius $r_e$ or effective width $D_e$, and cloud-top temperature $T_c$ are the most important parameters for water or ice clouds because the single scatter albedo $\omega$, the extinction coefficient $\beta$, and the asymmetry factor $g$ can be expressed in terms of $r_e$ ( or $D_e$ ) and $LWC$ (or IWC) for water or ice clouds. A parameterization of water clouds is provided by Hu and Stamnes (1993) and of ice clouds by Fu

and Liou (1993) as described previously. Cloud top temperature is an important variable for the estimation of thermal radiation. The snow surface can be treated as an independent layer coupled to the atmosphere in the RTM to avoid making assumptions about the surface BRDF. Parameterization of snow properties is taken from Warren and Wiscombe (1982). This RTM has been used for rigorous theoretical studies of both the troposphere and stratosphere (e.g. Tsay et al. 1989; Stamnes and Tsay, 1990) as discussed before.

### 5.2.2 Principle of Cloud Retrieval Using AVHRR

Use of an RTM to make sensitivity analyses of satellite measurements in different channels constitute the basis for choosing satellite channels for any specific remote sensing purpose.

Sensitivity of channel 2 to the cloud optical depth and effective radius can be seen from Figures 5.1 and 5.2, which show the reflectance of channel 2 for water clouds and ice clouds, respectively, as a function of cloud droplet effective radius $r_e$ (or $D_e$) and cloud optical depth $\tau$ over both snow surfaces and Lambert surfaces. Snow grain size and soot are assumed to be 200 $\mu$m and 0.3 ppmw respectively, and the albedo for the Lambert surface is assumed to be 0.577. For both the snow surface and the Lambertian one, the reflectance in channel 2 ($R_2$) for water clouds increases with cloud optical depth and decreases with the effective cloud droplet radius, so over thicker clouds or clouds of smaller cloud droplets, the radiance reflected back to space is larger. For an ice cloud over a snow surface and $D_e > 40\mu$m, $R_2$ decreases with cloud optical depth when $\tau < 20$, but for a mean crystal width $D_e = 20$ $\mu$m, $R_2$ increases with cloud optical depth when $\tau < 20$ (Figure 5.2). As cirrus is normally very thin, the variation of $R_2$ with the optical depth can be used to retrieve the cirrus optical depth. Because a correction for

Rayleigh scattering effects is required when 0.66 $\mu$m channel is used to retrieve cloud optical thickness (Wang and King, 1997), and AVHRR channel 2 is more sensitive than channel 1 to cloud optical depth over snow/ice surface, channel 2 is used instead of channel 1 for the retrieval of cloud optical depth in this thesis.

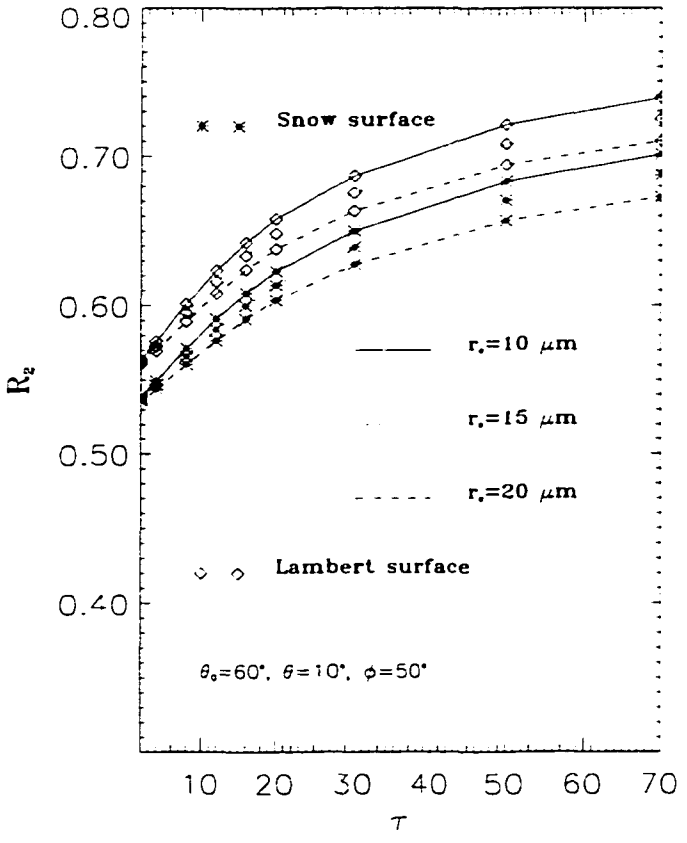


Figure 5.1 Simulation of reflectance in AVHRR channel 2 as a function of $r_e$ and $\tau$ under the condition of $\theta_0 = 60°$, $\theta = 10°$ and $\phi = 50°$ for water clouds. Two different surfaces are used (1) snow surface with grain size 200 $\mu$m, mass-fraction of soot 0.3 ppmw, and (2) Lambert surface with an albedo of 0.577 (0.86 $\mu$m).

The sensitivities of the reflectance in channel 3 ($R_3$) with $\tau$ and $r_e$ for liquid water clouds are shown in Figure 2.3. For liquid water clouds $R_3$ is larger for smaller effective droplet radius because the backscattering is larger for a smaller

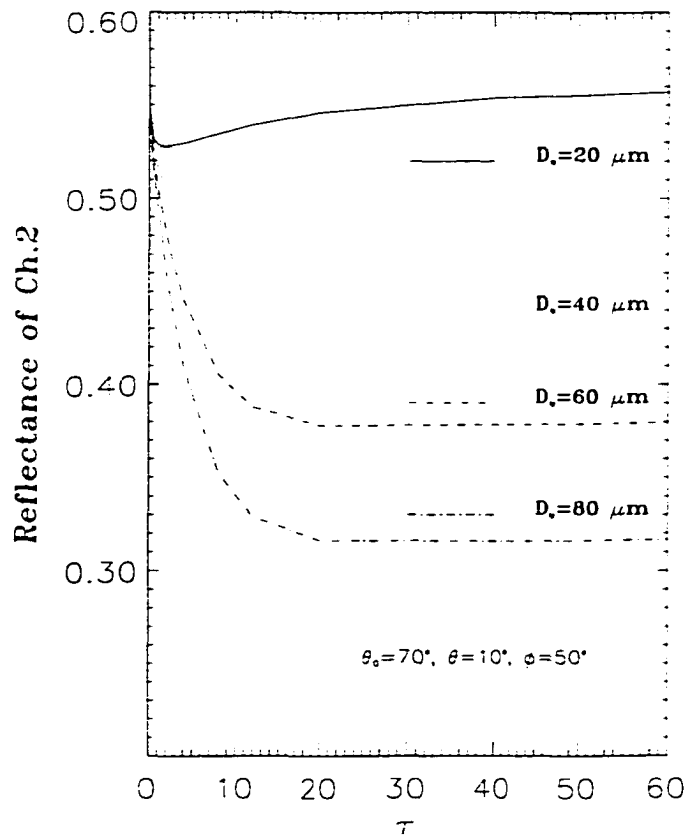


**Figure 5.2** As in Figure 5.1, but for ice clouds over a snow surface.

drop size. $R_3$ increases for $\tau$ but in a very limited optical depth region, and after $\tau > 10$, it is almost a constant. Due to the strong absorption by cloud water in channel 3, the "penetration depth" (which could be thought as the maximum optical depth beyond which $R_3$ will not change) of channel 3 is limited to a shallow layer of the cloud. A further increase of $\tau$ does not have any influence on $R_3$. This behavior can be used to simplify the cloud retrieval algorithm, as discussed below. The variation of $R_3$ for ice clouds as a function of $D_e$ and $\tau$ is shown in Figure 5.3. Similar to water clouds, $R_3$ decreases with $D_e$ for $D_e > 40$ $\mu$m, but the magnitude

of $R_3$ for ice clouds is much smaller than for water clouds. So, use of $R_3$ for the retrieval of $D_e$ for ice clouds is much more difficult.

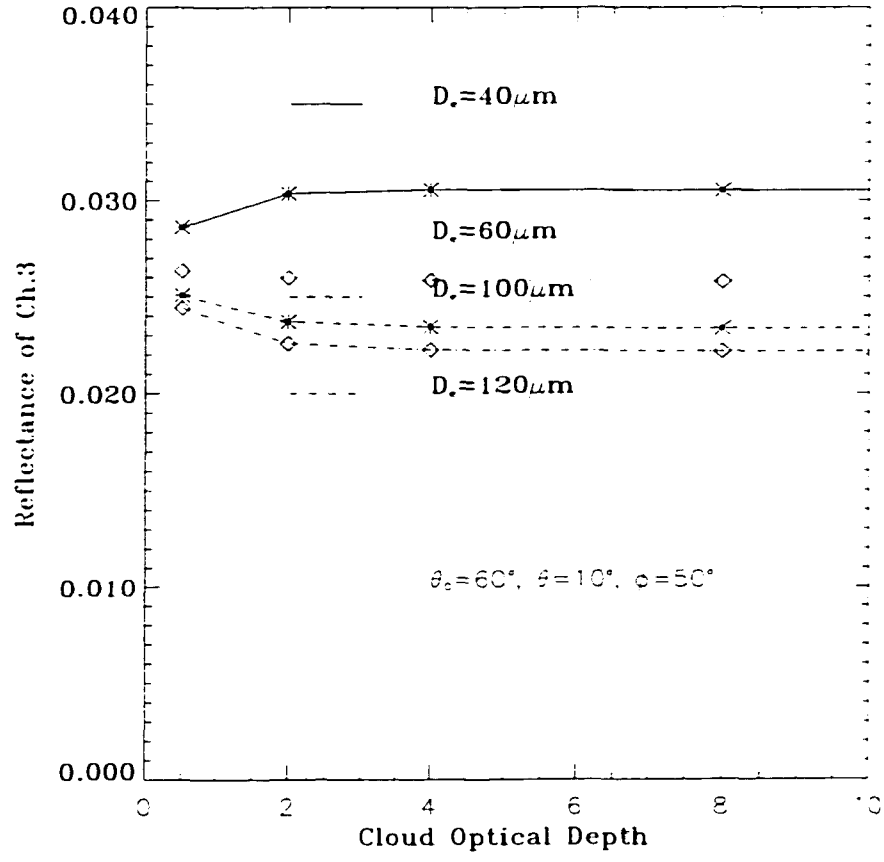


**Figure 5.3** As in Figure 5.2, but for reflectance in channel 3.

From Figures 5.1-5.3, $R_2$ is primarily sensitive to cloud $\tau$ and not very sensitive to $r_e$, and $R_3$ is primarily sensitive to cloud $r_e$ and not very sensitive to $\tau$ when $\tau > 10$. Thus, we can use channels 2 and 3 to retrieve the cloud $r_e$ and $\tau$ simultaneously, and for thick clouds ($\tau > 10$), it is possible to use channel 3 independently to retrieve $r_e$. Except for very thin clouds with $\tau < 2$, for which there are multiple solutions over Lambert surface as pointed out by King and Nakajima (1990), the

solutions are unique for $\tau > 2$. Using the snow surface, multiple solutions are not a problem even for $\tau < 2$ (Han et al., 1999).

As the measured radiance in channel 3 includes the thermal component emitted from the cloud and atmosphere as well as the solar reflectance, accurate removal of the thermal component is necessary for the retrieval of $r_e$. The method we used for the removal of thermal radiation in channel 3 is based on radiative transfer modelling. The thermal radiation in channel 3 and 4 depend on cloud $r_e$, $\tau$, cloud top temperature $T_c$ and surface temperature $T_g$. As shown in Figure 5.4, for a thick cloud with $\tau > 15$, BT4 is almost equal to the cloud top temperature $T_c$ and does not depend on the $r_e$. For clear sky, BT4 is almost equal to $T_g$. When $0 < \tau < 15$, BT4 depends on $T_g$, $T_c$, $r_e$ and $\tau$. The smaller the cloud drop $r_e$, the larger BT4. A similar relationship is found for ice clouds, and as $\tau > 10$, BT4 for ice clouds almost equals $T_c$. The dependence of BT4 with $D_e$ is weak. The dependence of brightness temperature for thermal component in channel 3 on $r_e$, $\tau$, $T_c$ and $T_g$ is similar to BT4.

As the surface temperature can be estimated based on clear pixels using AVHRR channels 4 and 5 (Key, 1997), we can generate two look-up tables of thermal radiance in channels 3 and 4 corresponding to a series of $T_g$, $\tau$, $r_e$ and $T_c$ using RTM. If $T_g$, $\tau$, $r_e$ and BT4 are given, we can use the look-up table to derive $T_c$, and then derive the thermal radiance in channel 3. However, cloud $\tau$ and $r_e$ are unknown, so simultaneous retrieval of $\tau$, $r_e$ and $T_c$ is required using the measurements in AVHRR channels 2, 3 and 4. Obviously, we have three unknown variables and three equations for these three channels, and numerical solutions can be obtained.

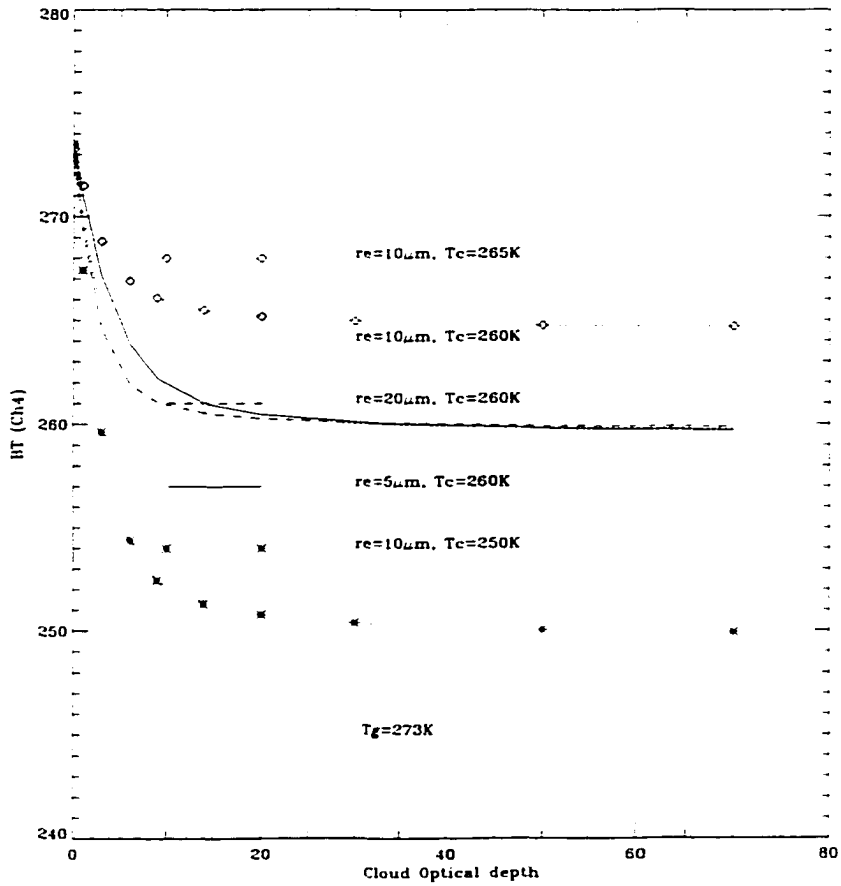


Figure 5.4 Simulation of brightness temperature in AVHRR channel 4 (BT4) as a function of $r_e$, $\tau$ and $T_c$ for water clouds. $T_g$=273 K .

### 5.2.3 Retrieval Procedure

From the above sensitivity analyses, the retrieval procedure for $\tau > 15$ can be simplified as follows:

1. As BT4 equals the cloud top temperature $T_c$ for a thick cloud, we can use $T_c$=BT4 and the Planck function to calculate the thermal radiation in channel 3, and get the solar reflectance in channel 3 ($R_3$) via eq. (2.7) accurately;

2. Assume $\tau = 20$, using $R_3$ to retrieve the effective radius $r_e$;

3. Using $r_e$ and channel 2 we can retrieve the cloud optical depth. If $\tau$ is indeed larger than 15. these values of $r_e$ and $\tau$ will be what we need. If the errors between the model simulations and the measurements in channels 2 and 3 are smaller than a prescribed accuracy. iteration will be required in the procedure as that for $\tau < 15$.

For $\tau < 15$.

1. Assume $r_e^{(0)} = 8$ $\mu$m. and retrieve $\tau^{(0)}$ from $R_2$:

2. Given surface temperature $T_g$ (can be retrieved from clear pixels using the algorithm of Key et al. (1997)) and BT4. using $r_e^{(0)} = 8$ $\mu$m and $\tau^{(0)}$. we can retrieve the cloud top temperature $T_c$:

3. Estimate thermal emission in channel 3 from $T_c$. $r_e^{(0)}$. $\tau^{(0)}$ and $T_g$:

4. Estimate the reflectance $R_3$ after removing the thermal component in channel 3. and use the $\tau^{(0)}$ and $R_3$ to retrieve $r_e^{(1)}$:

5. If the $r_e^{(0)} - r_e^{(1)} > \delta$. we set $r_e = (r_e^{(0)} + re^{(1)})/2$ and repeat the procedure until $|r_e^{(0)} - r_e^{(1)}| < 0.1$ $\mu$m and the error between the model simulation and the measurement in channel 2 and 3 is smaller than a prescribed accuracy.

Look-up tables are used for the retrievals in CRAS and CRAL. which are generated from RTM. There are six look-up tables: (1) Two look-up tables of reflectances in channel 2 as a function of cloud $\tau$ and $r_e$ for snow surface and Lambert surface. respectively: (2) Like for channel 2. there are two look-up tables of solar reflectances in channel 3. but the albedo in channel 3 is much less than in channel 2: (3) One look-up table of brightness temperature in channel 4 as a function of surface temperature. cloud top temperature. cloud $\tau$ and $r_e$: (4) Similar to channel 4. there is a look-up table for the thermal component in channel 3.

Retrieval of the ice clouds is much more difficult in the polar regions because (i) ice clouds often co-exist with underlying liquid water clouds, (ii) there is low contrast in channel 2 between ice clouds and snow/ice surfaces, and (iii) there is low contrast in channels 3 and 4 between ice clouds and snow/ice surfaces. Considering the large uncertainty in the retrieval of ice cloud over snow/ice surface, the retrieval of ice cloud is not presented in this thesis.

## 5.3 Uncertainty Analysis

A series of numerical experiments are designed to examine the uncertainties of the cloud retrieval with regard to cloud cover fraction, overlap of cirrus over low water clouds, inhomogeneous cloud stratification, and poor calibration of AVHRR channels 1 and 2. Uncertainties resulting from surface albedos and surface temperature is also discussed. In these experiments, the lower boundary is usually assumed to be a snow surface. Similar tests can be applied to the retrievals over a Lambert surface, and the uncertainties are expected to be smaller than for a snow surface due to the bidirectional reflectance of the snow surface.

1. **Surface Albedo and/or BRDF**

   For thin clouds, an error in the albedo may result in a large error in the retrieved cloud optical depth. If the albedo is underestimated, the reflectance at the TOA from the model will be underestimated. To match the model simulated $R_2$ with the satellite measurement, we have to increase $\tau$, so the retrieved $\tau$ will be overestimated. Figure 5.5 shows the error of the retrieved cloud optical depth for a surface albedo 0.2 with an error of $\pm 5\%$ and $\pm 20\%$. For thick clouds with $\tau = 10$, a $\pm 20\%$ error of albedo results in an error in $\tau$ of about 5%, and a $\pm 5\%$ error results in the error in $\tau$ of about 2%. With

the increase of $\tau$, the error is much less. For $\tau < 2$, the error in $\tau$ is as large as 8% and 28% for errors in albedo ±5% and ±20%, respectively.

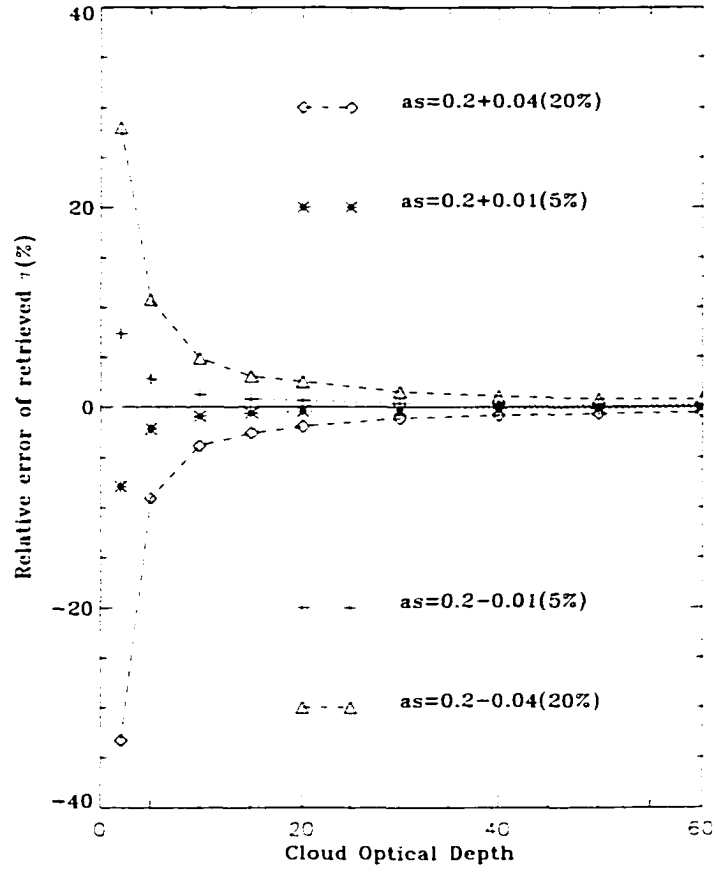


**Figure 5.5** Uncertainty of the retrieved $\tau$ for errors of ±5% and ±20% in surface albedo 0.2 (0.86 $\mu m$) under the condition of $\theta_0 = 60°$, $\theta = 10°$ and $\phi = 50°$ for water clouds .

Model simulations of BRDF over a snow surface (see Figure 1 of Han et al., 1999) in channel 1 indicate that the radiation reflected from the snow surface is highly anisotropic. The radiation field at the TOA under a clear sky is less anisotropic, and the addition of haze further reduces the degree of anisotropy at the TOA. Han et al. (1999) concluded that using the snow surface as an additional layer of the coupled snow-atmosphere model results

in a greater overall accuracy in retrieved surface properties as compared with a simplied approach that uses a Lambertian approximation for the surface albedo. To quantify this difference, a test was therefore performed to examine the discrepancy of cloud retrieval using CRAS and CRAL. As we discussed in Chapter 3, the effects of BRDF is small when the view angle is small, we just show this difference under the condition of $\theta = 10^{o}$.

For a snow grain size $r_s = 1000$ $\mu$m, mass fraction of soot $s_t = 0.3$ ppmw, and under the conditions of solar zenith angle $60^{o}$, view angle $10^{o}$, and two relative azimuthal angles, $50^{o}$ and $150^{o}$, respectively, we used the RTM for the coupled system to compute the reflectance in channels 2 and 3 for a series of cloud $\tau$ and $r_e$ values. The albedo corresponding to $r_s = 1000$ $\mu$m, $s_t = 0.3$ ppmw and solar zenith angle $60^{o}$ in channel 2 is 0.54. Several points for a value of $\tau$ in upper panel correspond to different $r_e$ in range of 4-20 $\mu$m, and several points for a value of $r_e$ in lower panel correspond to different $\tau$ in range of 2-70. Using these reflectances and viewing geometry for clouds over snow surface as the inputs to the CRAL, the retrieved $\tau$ and $r_e$ as compared to those used to simulate the satellite reflectance over the snow surface show that (Figure 5.6): (1) for $\tau > 4$, the disparity in both $\tau$ and $r_e$ is less than 5%; (2) for $\tau < 2$, the disparity in $\tau$ is large, but it is less than 5% in $r_e$; (3) for $o = 50^{o}$, $\tau$ is overestimated by 1%, and for $o = 150^{o}$, $\tau$ is underestimated by 5%. An exact opposite test is made, in which the reflectance in channels 2 and 3 are calculated for a Lambert surface and used as inputs to CRAS for retrieval. Comparison of the retrieved $r_e$ and $\tau$ from CRAS with that used to simulate the satellite reflectance over the Lambert surface shows that for $o = 50^{o}$, $\tau$ is underestimated by -6%; and for $o = 150^{o}$, $\tau$ is overestimated by 2%.

From these experiments, it can be concluded for $\tau > 4$, use of the Lambert assumption results in an error of about 5% for the retrieved $\tau$ and $r_e$ when the view angle is less than 10°. This is the reason we only choose the near overhead overpasses of AVHRR in our analysis.

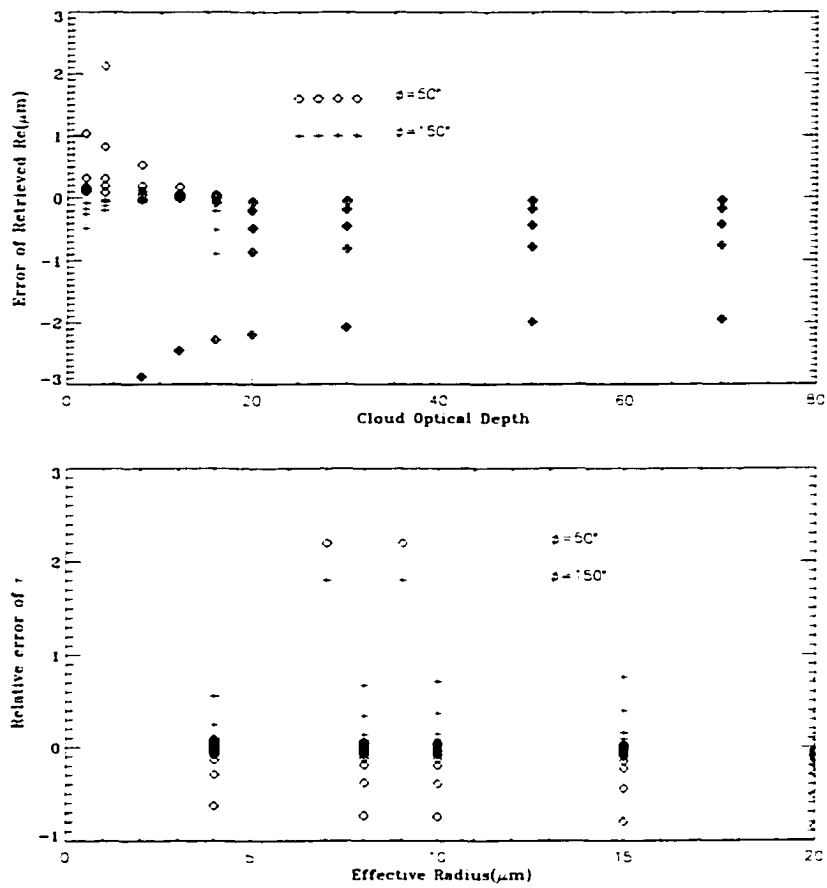


**Figure 5.6** Error of the retrieved $r_e$ (upper panel) and $\tau$ (lower panel) using CRAL for snow surface ($r_e$ = 1000 $\mu$m, $s_t$ = 0.3 ppmw). The corresponding albedo is 0.54 (0.86 $\mu$m). $\theta_0 = 60°$, $\theta = 10°$ and $\phi$ at 50° and 150° .

## 2. Satellite measurements

There is no onboard calibration for AVHRR channels 1 and 2, so uncertainty of the reflectance in channels 1 and 2 may be very large due to poor cali-

bration. As is shown later there are large disparities among the collocated NOAA-10, NOAA-12 and NOAA-14 data. Through the comparison of these collocated data from NOAA-10, NOAA-12 and NOAA-14 and the model simulation over the snow surface, we estimated that the NOAA-14 AVHRR channel 1 and 2 data obtained from the ARM Archive for SHEBA is over-estimated by 10-15%. This estimate is very close to the revised calibration to NOAA-14 AVHRR by Rao and Chen (1999), which was made three years after their first publication of calibration (see Rao and Chen, 1996).

To examine the sensitivity of cloud retrieval to the uncertainty in satellite-measured radiances, we assumed a ±5% error in the reflectance in both channels 2 and 3. The error in the retrieved $r_e$ for different $\tau$ and $r_e$ is shown in Figure 5.7 (upper panel). The different points for one $\tau$ represent different $r_e$ (in a range of 4 - 20 $\mu$m). The error in $r_e$ is about 1 $\mu$m in most cases, but a little larger for $r_e = 20$ $\mu$m. The error in the retrieved $r_e$ for different $r_e$ and $\tau$ (in a range of 2-70) is shown in the lower panel. It is concluded from Figure 5.7 that for a ±5% error in the reflectance in both channels 2 and 3, the error in $r_e$ is typically less than 2 $\mu$m, but the error in the retrieved $\tau$ is large. For $\tau = 20$, the error is about 40-50%. For a thin cloud such as $\tau = 2$, the error can be as large as 80-90%.

### 3. Cloud fraction

To test the error in cloud fraction on the retrieval of cloud optical depth and droplet effective radius, we consider the cloud over a snow surface, and the reflectance of channel 2 is:

$$R_2 = R_{2cld} * r + R_{2clr} * (1 - r) \tag{5.1}$$

where $R_{2cld}$ and $R_{2clr}$ is the TOA reflectance for a cloudy and a clear situation, respectively, $r$ is the cloud cover fraction. Similarly, reflectance in channel 3

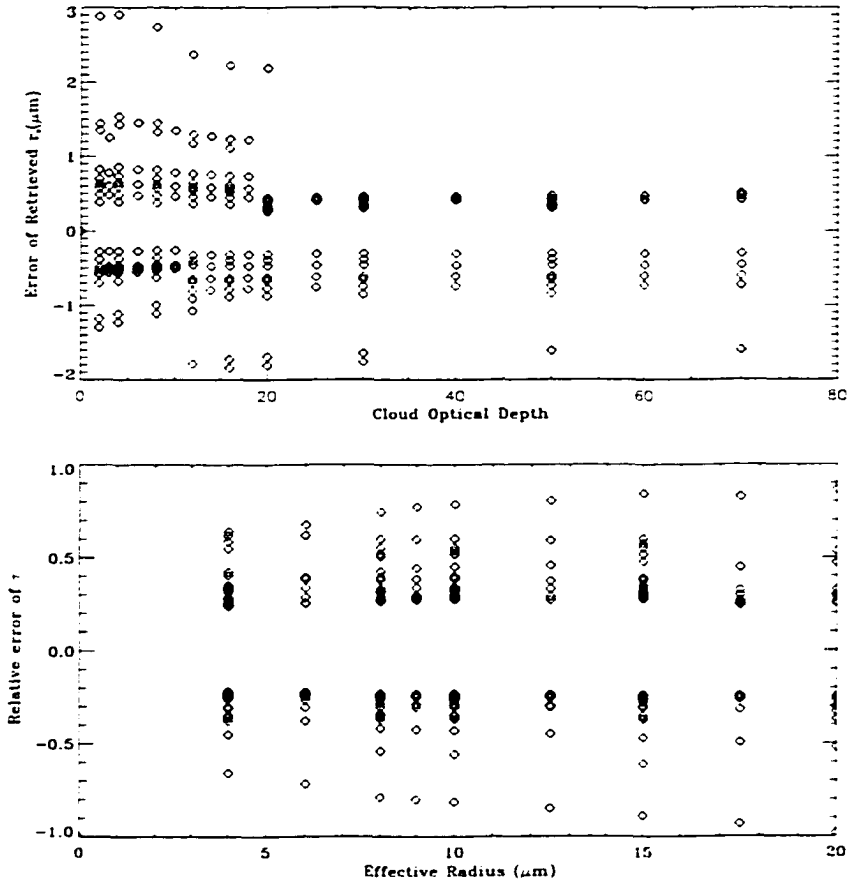


**Figure 5.7** Uncertainty of the retrieved $r_e$ (upper panel) and $\tau$ (lower panel) for $\pm 5\%$ error on both $R_2$ and $R_3$ for different $r_e$ and $\tau$ .

is:

$$R_3 = R_{3cld} * r + R_{3clr} * (1 - r) \tag{5.2}$$

where $R_{3cld}$ and $R_{3clr}$ is the reflectance for a cloudy and clear situation, respectively. For cloud cover $r$ varying from 0.1 to 1.0, the retrieved cloud optical depth and the droplet effective radius for water clouds with $r_e = 10\mu$m and $\tau = 30$ under the condition of $\theta_0 = 50°$, $\theta = 10°$, $\phi = 50°$, surface snow grain size 1000 $\mu$m and mass-fraction of soot 0.3 ppmw is shown in Figure

5.8. For a partly cloud pixel, $r_e$ is overestimated and $\tau$ is underestimated. When a cloud cover fraction is 0.8, $r_e$ is overestimated by 25%, and $\tau$ is underestimated by 26%.

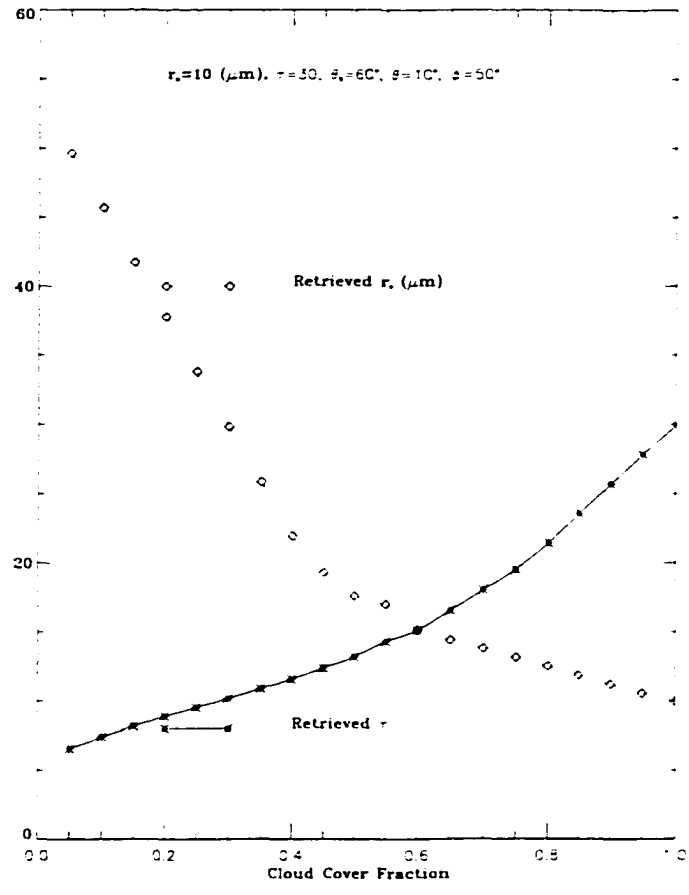


**Figure 5.8** Variation of retrieved $r_e$ and $\tau$ versus cloud cover fraction for water clouds with $r_e = 10$ $\mu$m and $\tau = 30$ under the condition of $\theta_0 = 50°$, $\theta = 10°$, $\phi = 50°$, surface snow grain size 1000 $\mu$m and mass-fraction of soot 0.3 ppmw.

## 4. Inhomogeneous vertical stratification of the cloud

In all the previous cloud retrieval analyses, the cloud is always assumed to be a homogeneous layer. This assumption is common for satellite retrievals. However, both model simulations and field observations show that terrestrial

water clouds contain significant vertical inhomogeneity, with cloud effective radius increasing linearly from the cloud bottom to the cloud top except in the uppermost optically thin entrainment region (Nakajima and King, 1990, Olsson et al., 1998, Harrington et al., 1999). In-situ measurements by Slingo et al. (1982), Stephens and Platt (1987), Albrecht et al. (1988), and Spinhirne et al. (1989) showed that the effective radius at the bottom of the cloud is about 0.49-0.58 of the effective radius at the cloud top. Profiles of normalized effective radius as a function of normalized optical depth is shown in Figure 5.9.

In order to examine the effect of vertical stratification of a cloud on the satellite remote sensing results, the vertically inhomogeneous cloud stratification is considered by dividing the clouds into 5 layers with $r_e$ changing according to the profile of Stephens and Platt (1987). The computed reflectance in channels 2 and 3 over a snow surface for different cloud top effective radii and cloud optical depths are shown in Figure 5.10. For comparison, the reflectance in channels 2 and 3 for homogeneous clouds are also shown. For inhomogeneous clouds, the reflectance in both channel 2 and 3 is higher than that for homogeneous clouds with the same cloud top $r_e$. As reflectance in channel 3 is very sensitive to cloud effective radius, $R_3$ is much larger for an inhomogeneous cloud than over a homogeneous cloud with the same cloud top effective radius. However, the difference is small in channel 2. Using these simulated reflectances as input to our cloud retrieval algorithm, as described before, we retrieved the $\tau$ and $r_e$. Figure 5.11 shows the ratio of the AVHRR derived cloud optical depth to the true optical depth and the AVHRR derived effective radius to the effective radius at cloud top as a function of $r_e$ and $\tau$ for inhomogeneous clouds. These results demonstrate that the error associated with the inhomogeneous cloud stratification results in

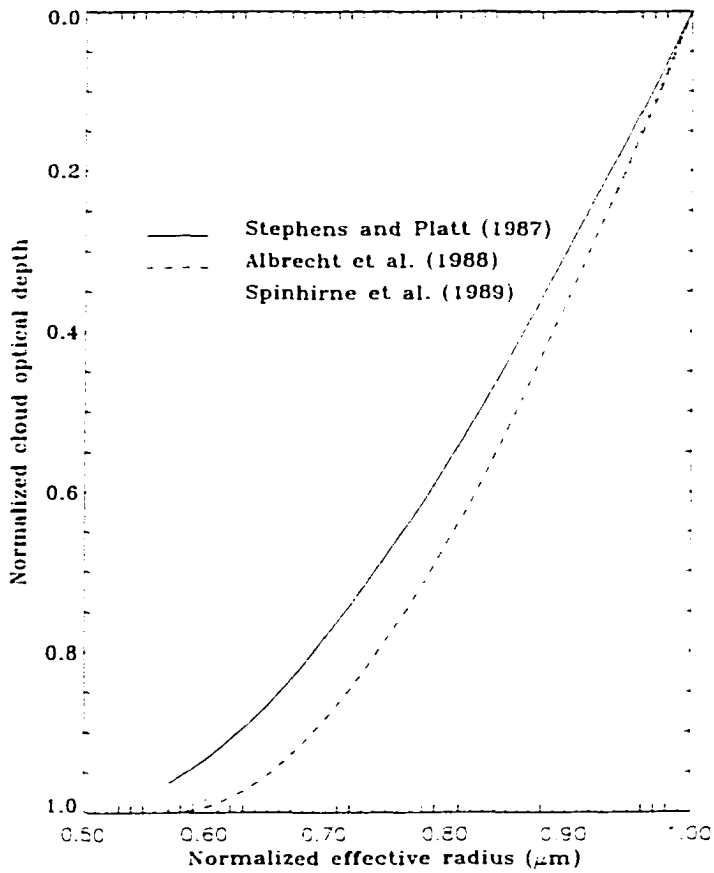


Figure 5.9 Normalized effective radius to the effective radius at cloud top as a function of normalized optical depth.

an error in the retrieved cloud optical depth of only 5-10%, but the effect on the cloud effective radius is significant. The satellite retrieved cloud droplet effective radius ($r_e$(retrieved)) is 80-85% of $r_e$ (true) at the cloud top, for which the $\tau$ is about 45-55% of the cloud optical depth according to Figure 5.9.

### 5. Overlap of cirrus over low water cloud

Summertime Arctic stratus clouds are believed to form as relatively warm and moist continental air flows over the pack ice, and the radiative and diffusive cooling at the colder surface and longwave emission to space initiates the condensation (Herman and Goody, 1976; Curry et al., 1988). The Arctic clouds are frequently observed to have a multiple-layer stratification structure, and the formation mechanisms are still not very clear although several mechanisms have been proposed by many researchers, for example, Herman and Goody (1978), Tsay and Jayaweera (1984), McInnes and Curry (1995), Olsson et al. (1998), Harrington et al. (1999). Discussion of these formation mechanisms is beyond the scope of the current research. From the SHEBA DABUL lidar observations and the AVHRR observations, multi-layer clouds are also frequently found.

In order to examine the impact of cirrus over water cloud on the satellite remote sensing of cloud optical depth, we performed simple model simulations for a two-layered cloud system. The cirrus layer is assumed to be located between 7 and 8 km, to have a particle size $D_e = 60$ $\mu$m, and an optical depth of 0.2 or 0.5. The water cloud is assumed to be located between 1 and 2 km, and its cloud droplet effective radius and optical depth are allowed to vary. Reflectances in channels 2 and 3 for a series of lower water cloud optical depths and effective radii are computed as inputs to the cloud retrieval algorithm (water cloud). Comparison of the retrieved cloud optical depth and the droplet effective radius with the lower water cloud $\tau$ and $r_e$ (Figure 5.12) shows that for $\tau_{ci} > 0.5$, the water cloud retrieval algorithm has difficulty in retrieving the water cloud effective radius and optical depth. This is because the strong absorption in channel 2 and 3 by ice particles

results in a significant decrease in the reflectance. For $\tau_{cl} = 0.2$ and when the lower water cloud optical depth is larger than 6, the retrieved effective droplet radius is larger than the lower water cloud effective radius by 20-30 %, whereas the retrieved cloud optical depth is underestimated by 50% or more, as shown in Figure 5.12.

6. **Other sources of error**

Uncertainty of the surface temperature results in an uncertainty of the estimation of thermal radiation in channel 3 if the cloud is not very thick, which influences the retrieval of $r_e$ and cloud top temperature $T_c$. Overestimation of surface temperature will obviously overestimate the thermal emission in channel 3 and channel 4 from the ground. Thus, $T_c$ and thermal emission from the cloud in channel 3 will be underestimated, the solar reflectance in channel 3 will be overestimated correspondingly. $r_e$ will be underestimated as $R_3$ is overestimated. Over a thick cloud, BT4 is close to cloud top temperature, so its influence on cloud retrieval can be neglected.

There are some errors in the retrieval method itself due to the interpolation or extrapolation in the look-up tables. The error in $\tau$ is less than 1, and for $r_e$ it is less than 0.5 $\mu$m, but may be larger when $\tau < 2$ due to multiple solutions over Lambert surface as pointed out by Nakajima and King (1990).

## 5.4 Validation Study

The validation of our cloud retrieval algorithm is made through direct comparisons of satellite retrieved cloud effective droplet radius with in-situ aircraft measurements by NCAR C-130, and indirect comparisons of cloud retrievals inferred

from AVHRR with those inferred from MODIS Airborne Simulator (MAS) data obtained on the NASA ER-2.

### 5.4.1 Comparison with C-130 in-situ Measurements

In order to create an integrated data set of the physical and radiation characteristics of the surface and clouds in the vicinity of the SHEBA Ice Camp on a horizontal scale that is useful for numerical climate models, and support satellite remote sensing efforts of SHEBA, FIRE, and ARM investigators, the NCAR-130 was used to "map" the surface and characteristics on a horizontal scale of up to $(50\ \mathrm{km})^2$ with a resolution of 10-100 m. Eight research flights in May and July, 1998, respectively, were conducted. The NCAR C-130Q is a four-engine medium-altitude research aircraft. Horizontal traverses of 20-200 km were made at various altitudes above, below and within the clouds, and in the boundary layer to map the surface using aircraft remote sensing instruments. Slow ascents and descents speed were maintained to obtain high-resolution vertical profiles using in-situ instruments. The timing of the flights was coordinated with satellite overpasses of NOAA-12 and -14. The cloud effective radius was measured by Particle Measuring Systems Inc. (PMS) cloud physics probes, which measure the cloud drop size distribution between 1.4 and 2.250 $\mu$m in radius. One of these probes, FSSP (Forward Scattering Spectrometer Probe), was used to measure the cloud droplet spectrum, mean particle diameter and water/ice content. Calibration was confirmed on the FSSP by injection at flight speeds of spherical beads of known size. More complete description of these instruments can be found in Knollenberg (1981).

**Case 1: May 4, 1998**

Radar and lidar images show that a water droplet-dominated layer occurred between two ice crystal layers (Curry et al., 2000; Dong et al., 2000). The ice

crystals from the dissipating altostratus fell through the liquid phase cloud layer to the surface. Ceilometer-measured cloud base height is about 0.6 km. and radar-derived cloud top height is near the top of the ice crystal layer (4 km). From the histogram of FSSP-derived $r_e$ (Figure 5.13). there are two peaks: one is at 7-8 $\mu$m. another is at about 18 $\mu$m. From the $r_e$ versus height (not shown). it is clear that the first peak corresponds to the water cloud located between the two ice cloud layers. and the second peak corresponds to the ice cloud. From 21:00 until 24:00 UTC. the mean effective radius is 13.9 $\mu$m and the standard deviation is 5.6 $\mu$m.

Overpass of NOAA-14 AVHRR at 22:50UTC on May 4. 1998 available in ARM Archive is used for cloud retrieval. In this data set. AVHRR channels 1 and 2 was calibrated based on the calibration results of Rao and Chen (1996). As it was overcast. surface albedo or snow grain size is not from retrieval (as discussed in Chapter 3). For CRAL. the albedo in channel 2 is set at 0.85. consistent with the measurement of Perovich et al. (1999). For CRAS. snow grain size is set at 50 $\mu$m and mass-fraction of soot is 0.02 ppmw. Solar zenith angle in this scene is about 59.5° - 60.5°. and the albedo over snow surface from the model is consistent with that from the measurements of Perovich et al. (1999). For comparison. we take an average of the retrieved $\tau$ and $r_e$ over 10 by 10 pixels centered on the SHEBA Ice Camp.

From CRAS. the mean retrieved cloud droplet effective radius and the cloud optical depth are 10.8 $\mu$m and 60.9. respectively. The AVHRR derived cloud effective radius is close to the in-situ measurement by the NCAR C-130 but the AVHRR derived cloud optical depth is highly overestimated and unrealistic. Similar results were found by Dong et al. (2000). who used NOAA-14 AVHRR data taken at 21:21UTC on May 4. 1998. Using AVHRR channels 1. 3 and 4 and the algorithms of Minnis et al. (1995). Dong et al. obtained $r_e = 9.5$ $\mu$m and $\tau = 56$. The improved algorithm of Minnis et al. (1998) with a clear sky reflectance of 0.72

gave the same values for $T_c$ and $r_e$, but $\tau = 26.7$.

Use of the 1.6 $\mu$m channel instead of a visible channel was expected to produce a more accurate value of $\tau$ over the snow surface. The Along Track Scanning Radiometer (ATSR) has a channel at wavelengths of 1.6 $\mu$m and three thermal bands at 3.7 $\mu$m, 11 $\mu$m, and 12 $\mu$m, and the spatial resolution is 1 km. The first ATSR instrument, ATSR-1, was launched on board the European Space Agency's (ESA) European Remote Sensing Satellite (ERS-1) in July 1991, and an enhanced version of ATSR, ATSR-2, was successfully launched on board ESA's ERS-2 spacecraft on 21st April 1995. Dong et al. (2000) used the ATSR-2 1.6 $\mu$m channel for a 10*10 pixel box centered at 175 km northwest of the ship to derive the cloud optical depth and droplet effective radius as $r_e = 11.1$ and $\tau = 8.5$, while the other two algorithms (Minnis et al., 1995, 1998) gave $r_e = 9.5$, $\tau = 57$, $T_c = 248$K and $r_e = 9.5$, $\tau = 32.5$, respectively.

The difference of our results from Dong et al. (2000) may be due to the different calibration, the setting of surface albedo and the different retrieval algorithms. The calibration of NOAA-12 and NOAA-14 by Minnis et al. (1999) was used by Dong et al. (2000), and in their retrieval algorithms channel 1 is used for the retrieval of cloud optical depth, which is not appropriate over snow or ice surface as we discussed before.

Before the revised calibration to NOAA-14 AVHRR by Rao and Chen (1999), we found that the unrealistic retrieval of $\tau$ might be due to the error resulting from calibration. Through the comparison of collocated NOAA-10, 12 and 14 (see section 5.3.2), we estimated that the reflectances in channels 1 and 2 were overestimated by 10-20%. This result was proven by Rao and Chen (1999). From Rao and Chen (1999), NOAA-14 data from the ARM archive is overestimated by 14%. After multiplying $R_2$ by (1 - 14%), the retrieved $r_e$ is 9.9 $\mu$m and $\tau$ from CRAS is 15.8 (Figure 5.14). As compared to Dong et al. (2000) using the improved

algorithm of Minnis et al. (1998), the retrieved $\tau$ from our algorithm is closer to that derived from the surface $\tau$=5.7 and that inferred from the 1.6 $\mu$m channel at ATSR-2, but it is still overestimated.

**Case 2: May 27/28, 1998**

The DABUL lidar image shows that there are two layers of liquid cloud with the top of the upper layer at 1.5 km during the overpass of NOAA-14 around 23:30 UTC. In-situ aircraft measured $r_e$ from FSSP during May 27 22:00 - May 28 1:00 as is shown in Figure 5.15. The histogram shows that there is only one peak at 7-8 $\mu$m, and the mean $r_e$ inferred from the aircraft measurements is 8.8 $\mu$m with a standard deviation of 2.7 $\mu$m. Using the algorithm of Minnis et al. (1998), Dong et al. (2000) found $r_e$ = 13.5 $\mu$m with $T_c$ = 250 K and $\tau$ = 37.4 using NOAA-14 AVHRR overpass at 23:49 UTC on 27 May 1998. The reason for this difference was due to two distinct types of cloud in the vicinity of the ship. As shown in Figure 5.16, higher BTD34 indicated clouds with a small effective radius and vice versa. Dong et al. used the 1.6 $\mu$m channel from the ATSR-2 instrument to retrieve $r_e$ = 8.6 $\mu$m, $\tau$ = 7.4 north of the SHEBA Ice Camp, and $r_e$ = 21.6, $\tau$ = 10.4 south of the ship . The aircraft flew mostly over the north of the ship (Dong et al., 2000).

The NOAA-14 AVHRR overpass on May 27 at 23:38 UTC was used in our retrieval, and the retrieved mean cloud effective radius $r_e$ is 13.9 $\mu$m with a standard deviation of 0.7 $\mu$m. The mean cloud optical depth is 39.5 using the ARM Archive AVHRR data. This result is similar to that of Dong et al. (2000). Using the calibration of Rao and Chen (1999) and the CRAS (snow grain size is taken as 1000 $\mu$m and mass-fraction of soot is taken as 0.1 ppmw, we obtained $r_e$ = 11.7 $\mu$m and $\tau$ = 13.6. The $\tau$ retrieved from surface PSP is 6.5 at 22:00 UTC.

From the above two cases, we found that AVHRR can be used to retrieve cloud effective radius accurately over snow surface, but may yield unrealistic cloud optical depth over snow surface as is evident from both our retrieval and Dong et

al. (2000). However, use of the new calibration of Rao and Chen (1999) yields retrieved $\tau$ close to the retrieval from the surface. Comparison of the retrieval results is summerized in Table 5.1.

**Table 5.1** Comparison of Cloud Retrieval with C-130 Aircraft Measurements.

| Date | C-130 | CRAS | Dong et al. (2000) | 1.6 $\mu$m (ATSR-2) | Surface PSP |
|---|---|---|---|---|---|
| | $r_e$ ($\mu$m) | $\tau$ $r_e$($\mu$m) | $\tau$ $r_e$ ($\mu$m) | $\tau$ $r_e$ ($\mu$m) | $\tau$ |
| May 4 | 13.9±5.6 | 15.8 9.9 | 27.0 9.5 | 8.5 11.1 | 5.7 |
| May 27/28 | 8.8±2.7 | 13.6 11.7 | 37.4 13.5 | 7.4 8.6 | 6.5 |

### 5.4.2 Calibration of NOAA-14 AVHRR Channels 1 and 2

From our study, we found both the retrieved cloud optical depth and surface albedo using NOAA-14 AVHRR data obtained from the ARM Archive, which is calibrated based on Rao and Chen (1996) for AVHRR channels 1 and 2, do not compare well with the surface measurements and in-situ aircraft measurements. After a great deal of effort checking all the algorithms and making sensitivity/uncertainty analyses, we concluded that there are some error in the calibration of Rao and Chen (1996) although it is widely used in applications or used as standard for the calibration of other satellite sensors. To examine the possible error in the calibration of NOAA-14 from Rao and Chen (1996), we performed comparisons of model simulated reflectances with satellite measurements from NOAA-10, 12 and 14 for clear sky conditions. In these comparisons, the measured surface albedo is taken from Perovich et al. (1999). Reflectance in channel 2 for different pixels with different viewing geometries in the whole images under clear sky can be calculated from an accurate RTM. The difference between model-simulated and satellite-measured reflectance is shown as the ratio of the simulated and measured values.

This ratio represents the departure of the satellite measurement from the model simulation. If one neglects the error in the model simulation and there is no error in the satellite measurement, this ratio should be unity. This ratio is comparable for all satellites and can be used for in-flight calibration.

We have investigated the clear sky reflectances between April and August, 1998, and two cases are shown in Figure 5.17. Case 1 is the comparison with NOAA-10 and NOAA-14 reflectances on June 15, 1998, over SHEBA, where surface albedo is set at 0.67 (at 0.86$\mu$m) from the measured averaged albedo along a scan line of 200 m by Perovich et al. (1999). NOAA-10 data are obtained from the ARM Archive. The satellite overpass includes 100 by 100 pixels. The lower panel of Figure 5.17 shows the comparison of NOAA-12 with NOAA-14 on May 24, 1998, over SHEBA, where the surface albedo is 0.76 at 0.86 $\mu$m from Perovich et al. (1999). This albedo corresponds to a snow surface with grain size of 200 $\mu$m and mass-fraction of soot 0.05 ppmw. From the comparisons of these two cases, we found the reflectance in channel 2 of NOAA-14 AVHRR is 10-20 % higher than model simulations and the measurements by NOAA-10 and NOAA-12. Figure 5.17 also shows that the reflectance of NOAA-10 AVHRR channel 1 is lower than the model simulations by about 10%. For NOAA-12, no post-launch radiometric calibration over time is available, so we make an estimate of the sensor degradation over time by running regressions over several AVHRR channel degradation rates provided by ISCCP. The average of these regressions suggests that we correct the channel 2 radiances by a factor of 1.38. On average, this calibrated reflectance in channel 2 of NOAA-12 is about 5% lower than model simulation.

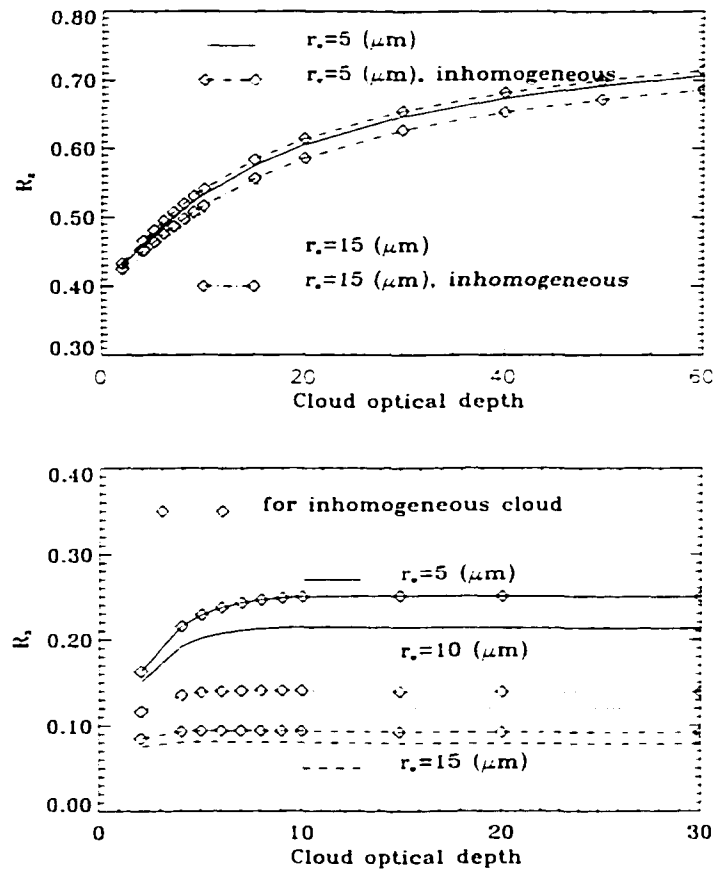


**Figure 5.10** Simulated $R_2$ (upper panel) and $R_3$ (lower panel) as a function of $\tau$ and $r_e$ for inhomogeneous water clouds. Under the condition of $\theta_0 = 50°$, $\theta = 10°$, $\phi = 50°$, surface snow grain size 1000 $\mu$m and mass-fraction of soot 0.3 ppmw.

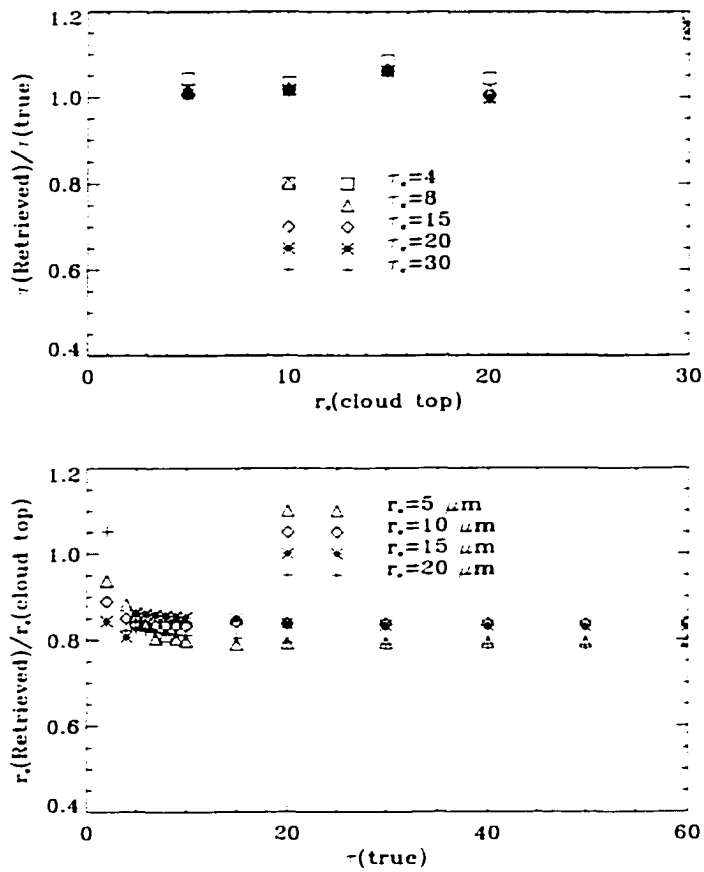


Figure 5.11 Ratio of the AVHRR derived cloud optical depth to the true optical depth (upper panel) and the AVHRR derived effective radius to the effective radius at cloud top for inhomogeneous clouds (lower panel) .

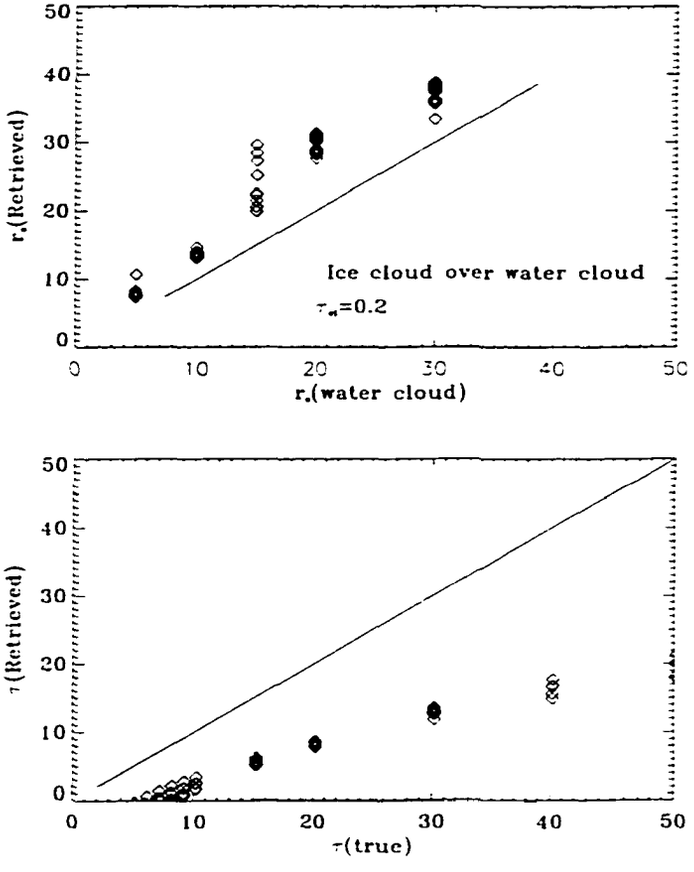


**Figure 5.12** Relation of AVHRR derived $r_e$ to the lower water cloud $r_e$ (upper panel) and cloud optical depth (lower panel). Cirrus properties are held constant with $D_e = 60$ $\mu$m, $\tau_{ci} = 0.2$ (0.86 $\mu$m) located at 7-8 km.

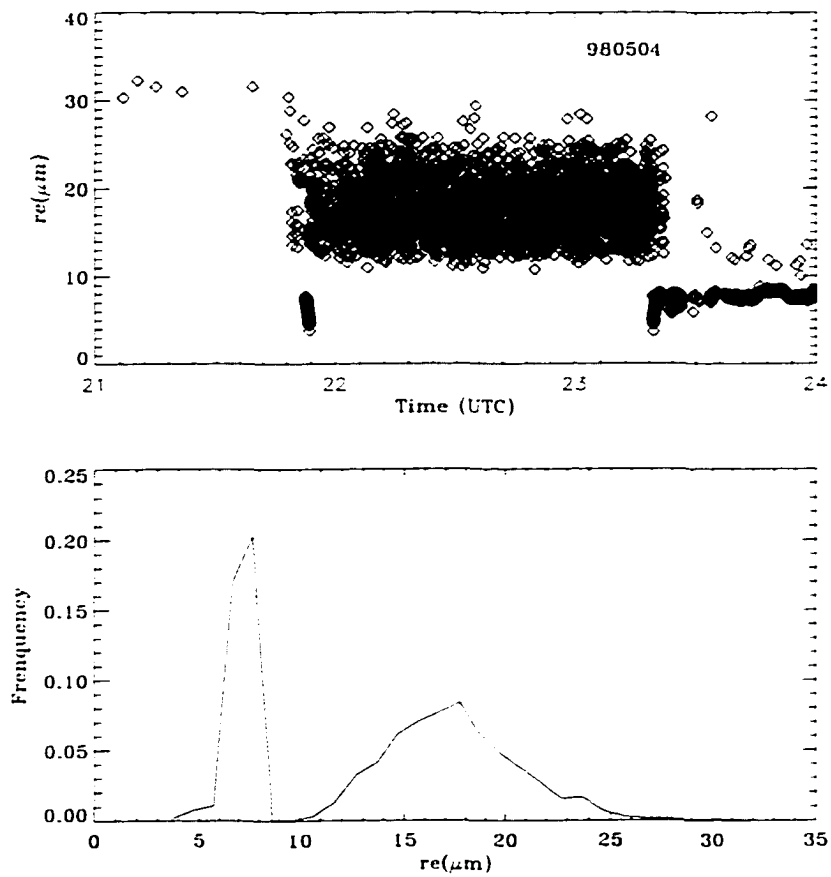


Figure 5.13 Variation of in-situ cloud effective droplet size measured by FSSP on C-130 at May 4, 1998 and the histogram .

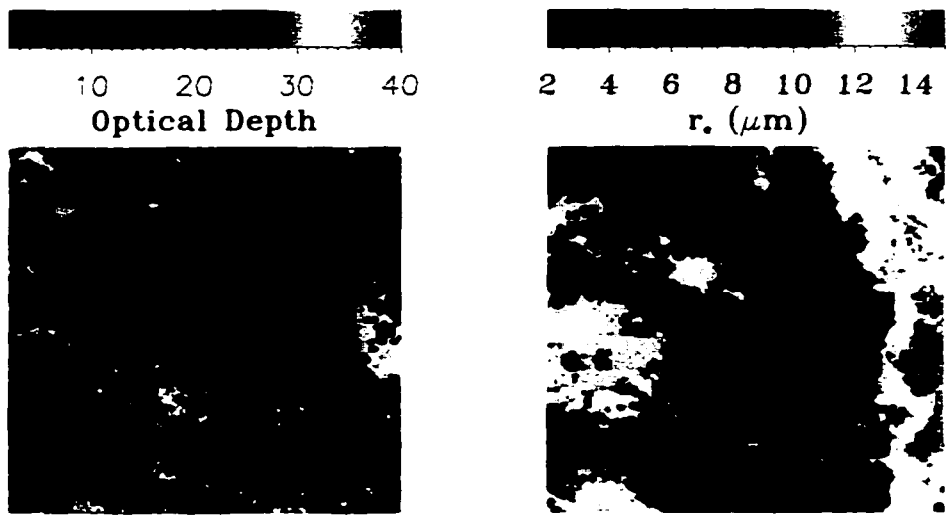


Figure 5.14 Color images of $\tau$ and $r_e$ derived from NOAA-14 AVHRR overpass on May 4 at 22:50 UTC over SHEBA (100 *100) .

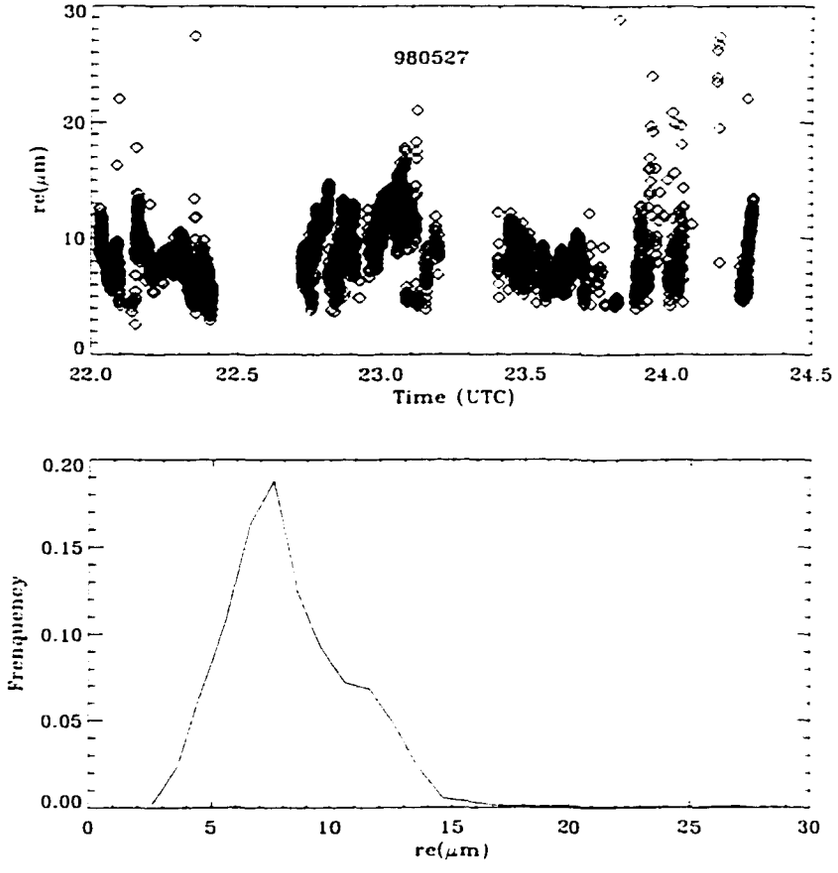


**Figure 5.15** As in Figure 5.13, but at May 27/28, 1998.

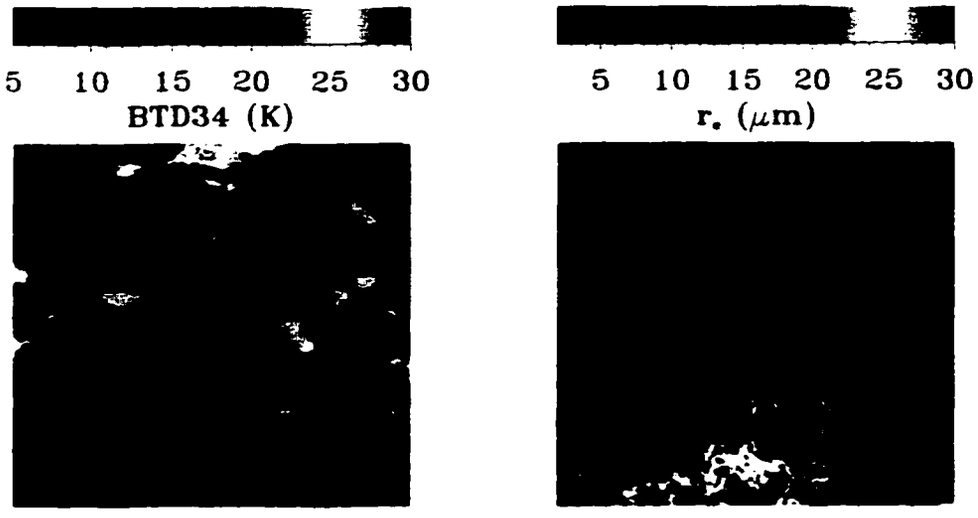


**Figure 5.16** Color images of BTD34 and the retrieved $r_e$ for AVHRR overpass on May 27 at 23:38 UTC over SHEBA (100 *100) .

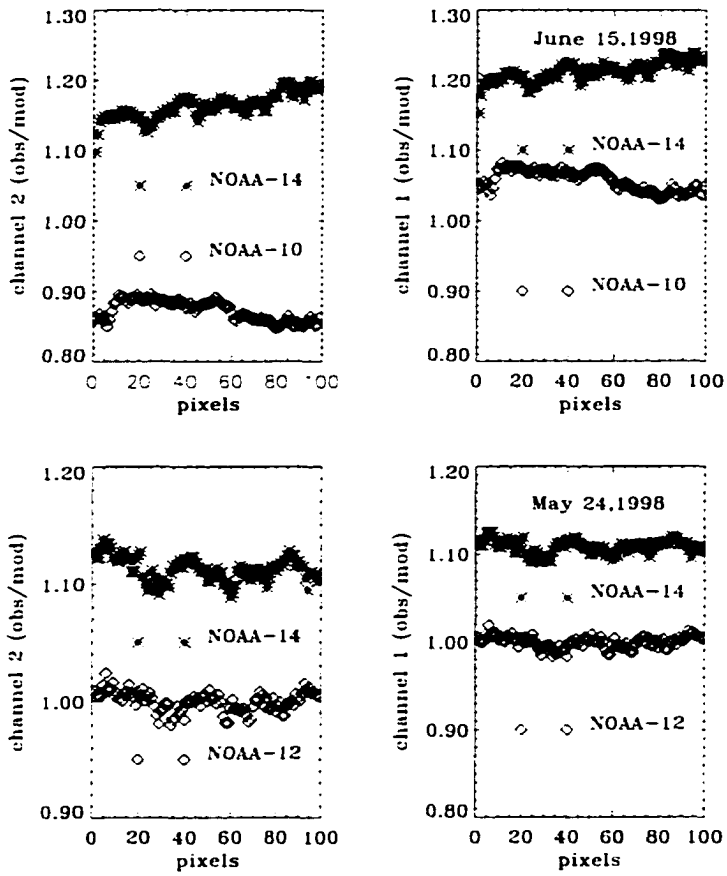


Figure 5.17 Ratio of satellite-measured reflectance at the TOA to model simulations in channels 1 and 2 for the comparison of NOAA-10 with -14 on June 15, 1998 (surface albedo is set as 0.67 at 0.86 $\mu$m) (upper panel), and the comparison of NOAA-12 with -14 on May 24, 1998 (surface is set as snow with $r_e$=200 $\mu$m and $s_t$=0.05 ppmw) (lower panel).

### 5.4.3 Comparison of Cloud Retrieval from AVHRR and MAS

The SHEBA and FIRE data sets give us an opportunity to validate AVHRR retrieval principles and methods through comparison with cloud retrieval from the

MODIS Airborne Simulator (MAS) data. MAS is a modified Daedalus Wildfire scanning spectrometer which flies on a NASA ER-2 high altitude research aircraft and provides spectral information similar to that provided by the Moderate Resolution Imaging Spectroradiometer (MODIS) launched on the EOS-AM platform. MAS acquires high spatial resolution imagery with a spatial resolution of about 40-50 m. and has 50 channels in the range between 0.55 and 14.3 $\mu$m. Therefore, it is expected that MAS will yield better retrievals of cloud optical depth and droplet effective radius because: (1) the sensor has direct radiometric calibration in all channels; (2) the 1.62 $\mu$m channel allows for cloud phase and particle size retrieval without error associated with a thermal radiation component; and (3) the high spatial resolution (50 m) should make MAS retrievals less susceptible than AVHRR to errors associated with the single-pixel approximation for a given geographic area.

Cloud retrieval algorithms for MAS are in principal similar to AVHRR as described before, but simple because the 1.62 $\mu$m channel is used instead of the AVHRR 3.7 $\mu$m channel, so no efforts are required for the calculation of the thermal component.

For validation, two overpasses of AVHRR and collocated MAS flight tracks over SHEBA are considered. One is the NOAA-14 overpass occurred at 22:34 UTC on June 2, 1998, and another one is the NOAA-12 overpass at 20:40 UTC on June 3, 1998. The MAS overflight tracks that best match these satellite overpasses in time and space are track 9 on June 2 (20:24 - 20:37 UTC) and track 6 on June 3 (20:34 - 20:49 UTC). Both AVHRR images with overlaid MAS flight tracks are shown in Figure 5.18.

Figures 5.19 and 5.20 depict AVHRR-based retrievals of cloud optical depth and effective droplet radius for the June 2 and June 3 case, respectively. What is immediately apparent in these images is the large variability in cloud optical

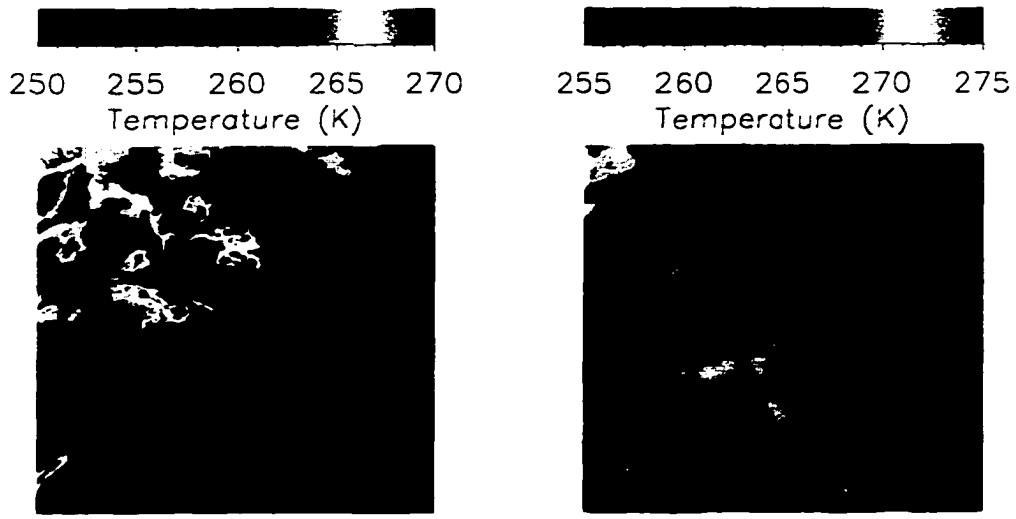


Figure 5.18 AVHRR channel 4 color images with overlaid MAS flight tracks (thin solid line), for 22:34 UTC on June 2 (left panel), and 20:40 UTC on June 3, 1998 (right panel) .

depth, and hence cloud liquid water path, over spatial scales of the order of 10 km, in typical Arctic stratus cloud decks. In the June 2 case, the cloud optical depth sometimes varies between 25 and 60 within a few pixels. In the June 3 case, the overall range in cloud optical depth is not as large, but the cloud optical depth often varies by a factor of two (20 - 40) within a few pixels. Both cases show a similar range of variability in effective droplet radius (approximately 6 - 14 microns). The corresponding retrievals from the MAS flight tracks on June 2 and June 3 (figures not shown) show a similar range of variability in both cloud optical

depth and effective radius over only a few pixels (spatial scales smaller than 1 km).

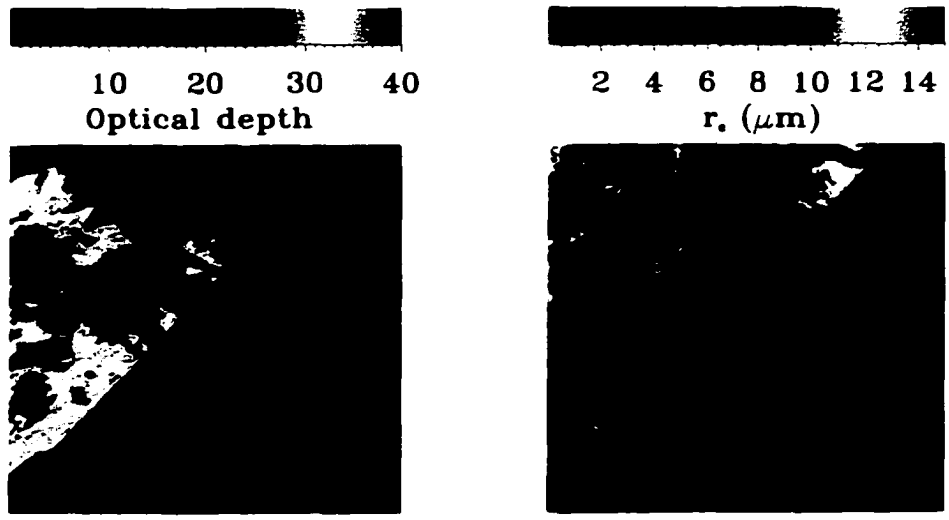


**Figure 5.19** Color images of retrieved $\tau$ (left panel) and $r_e$ (right panel) from the NOAA-14 AVHRR pass on June 2, 1998 at 22:34 UTC .

In Figures 5.21-5.24, for the June 2 and June 3 cases respectively, the MAS retrievals of cloud optical depth and effective droplet radius are averaged to the resolution of the AVHRR data, and averaged across the flight track, are plotted with the AVHRR retrievals along the flight track. In both cases, the MAS and AVHRR retrievals of effective radius correlate well throughout most of the flight tracks. At the beginning and end in the June 3 case we see a larger variability and largest discrepancies between effective radius retrievals, but there is no obvious

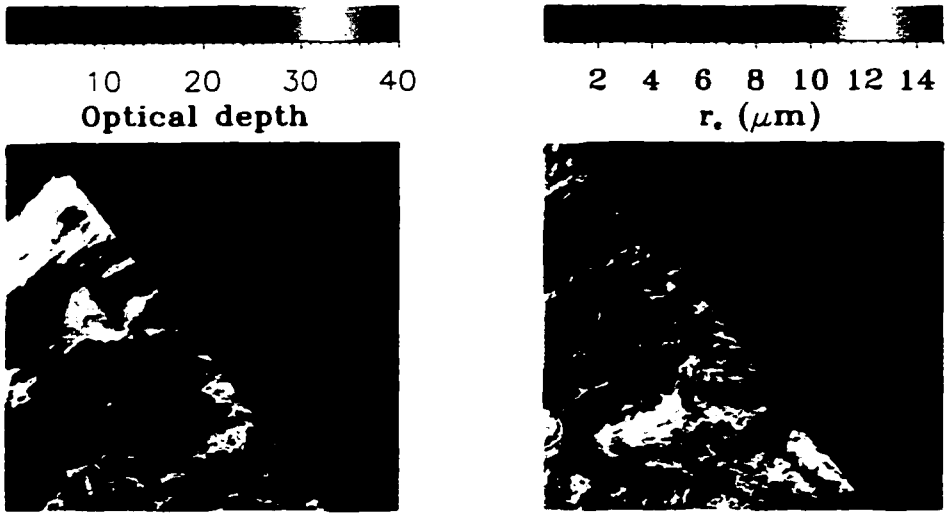


**Figure 5.20** As in Figure 5.19, but for the NOAA-12 AVHRR pass on June 3,1998 at 20:40 UTC .

overall bias in the AVHRR retrievals as compared to MAS and the difference is about 2 $\mu$m.

In the June 3 case, we see that the AVHRR retrievals of optical depth are larger than MAS retrievals by about 50% on average. In the June 2 case, the AVHRR retrieved optical depth are smaller than MAS retrievals by about 40% on average. One possible reason for this disagreement may be due to the calibration error because there is not post calibration for NOAA-12. The larger variability (a factor of 3) in cloud optical depth along the flight track on June 3 is less surprising; Figure

5.18 shows that the cloud top brightness temperature varies between 260~270 K along this flight track. The MAS and AVHRR retrievals of cloud optical depth correlate very well, but with an apparent bias in the AVHRR retrieval. Figure 5.18 shows that along the final 1/5 of the flight track, the scene brightness temperature is uniform at 270 K. In the AVHRR data at 1 km resolution, this is ambiguous, and the AVHRR cloud masking technique identified all of these pixels as cloudy. However, Figure 5.18 shows that most of the MAS pixels in the final 1/5 of the flight track (toward the top of the figure) are identified as cloud-free. Thus, the AVHRR pixels in this part of the flight track probably contain broken cloud cover, and the AVHRR retrievals of optical depth should be considered inaccurate. Similarly, Figure 5.18 suggests that many of the AVHRR pixels near the end of the flight track on June 2 may also be partially cloudy, and in Figure 5.23 we see that the high bias in the AVHRR optical depth retrievals is largest (a factor of two) at the end of the flight track. The high bias in cloud optical depth retrieved from the AVHRR data on June 3 is significant, because it is the likely the result of only a small error in channel 2 radiance calibration.

If we use the retrievals to estimate the cloud liquid water path using eq. (4.6), we find that the discrepancies between the AVHRR and MAS estimates are consistently of the order 100 g $m^{-2}$ (figure omitted). Thus small errors in radiometric calibration can lead to unacceptably large errors in microphysical parameters retrieved from the AVHRR data. If one examines closely and intercompares the time-dependent post-launch radiometric correction functions given by ISCCP (Brest and Rossow, 1991), NOAA (Rao and Chen, 1996), and others, one will routinely notice radiance discrepancies of order 5% between them. There is also additional uncertainty implied by the scatter within the empirical functions of radiance versus time that form the basis for these post-launch corrections. This underscores the value of the FIRE MAS data set as a calibration standard for the AVHRR solar

backscatter channels during SHEBA.

## 5.5 Application and Results

To further validate our cloud retrieval algorithm and to study the seasonal variation of cloud properties in the Arctic, the current algorithms are applied to 1 or 2 NOAA-14 near overhead passes per day with the center on the SHEBA Ice Camp. There are multiple overpasses everyday, but only the near overhead passes, in which the view angle is close to zero, are chosen. Calibration of NOAA-14 AVHRR channel 2 is applied using the data provided by Rao and Chen (1999).

The cloud retrieval procedure consists of the following steps:

1. Cloud Mask: discrimination of cloudy/clear sky and identification of snow surface.

2. Surface property retrieval:

   - snow grain size and mass fraction of soot for each snow pixel:
   - surface albedo in channel 2 and the broadband albedo for clear pixels other than the snow surface:
   - surface temperature using the procedure of Key et al. (1997).

3. Setting surface variables:

   When the fraction of clear pixels is larger than 10%, we will retrieve the surface albedo, temperature, snow grain size and soot in the whole scene. The averaged values will be used to set the lower boundary for cloud retrieval. If the fraction of clear pixels is less than 10%, their representativity of the whole image is suspect, so default values are used. The default albedo is from

Perovich et al. (1999), and the default surface temperature is from SHEBA measurements. In April and May, the change in surface conditions is small, so the snow grain size and soot from the most recent day are used as the default values.

4. Cloud property retrieval:

   Simultaneous retrievals of cloud effective radius, cloud optical depth and cloud top temperature are carried out using CRAS during April - May, and CRAL during June - August. An average for 30 by 30 pixels over SHEBA is made.

### 5.5.1 Seasonal Variation of Cloud $r_e$ and $\tau$

Our algorithms were applied to retrieve the cloud properties for 1 or 2 NOAA-14 overpasses per day over the SHEBA Ice Camp. The retrieved cloud optical depth, effective radius and cloud top temperature (averaged for 30 by 30 pixels over the SHEBA Ice Camp) are shown in Figures 5.25 and 5.26. For comparison, the cloud optical depth retrieved from downwelling solar radiation measured at SHEBA is also plotted (upper panel of Figure 5.25). It is very interesting to note that for April and May before the onset of snow melt, satellite retrieved cloud optical depth is overestimated by a factor of 2-3 on average. One possible reason is the presence of ice crystals over water clouds, as was pointed out by Curry et al. (1996). In our retrieval, only the cirrus or partly cloud pixels are not retrieved, and for other pixels, like cirrus over water or mixed phase clouds, we treated it as one homogeneous water clouds and and retrieved its properties. After snow begins to melt in June, AVHRR retrieval is in good agreement with surface retrieval. These results are consistent with results from ISCCP (Curry et al., 1996).

The histogram of cloud effective radius shows that $r_e$ of the highest frequency

is 11.6 $\mu$m. The cloud top temperature lies between 250-270 K, and it tends to increase with the progress of the melt season until the melting is fully developed at the end of June.

## 5.6 Summary and Discussion

In this chapter, two algorithms using AVHRR channel 2, 3 and 4 are developed for simultaneous retrieval of the cloud optical depth, effective droplet radius and cloud top temperature for clouds overlying a snow surface and a Lambert surface, respectively.

Since satellite remote sensing normally assumes the cloud to be one homogeneous layer and relies on plane parallel RTMs, broken cloud cover and/or the inhomogeneous vertical structure of cloud are not considered. To account for the influence of cloud cover, cloud vertical inhomogeneity, cloud phase, satellite measurement and snow surface BRDF on the cloud retrievals, a series of numerical experiments are carried out to examine the uncertainty of cloud retrieval from AVHRR. Validation of the cloud retrievals was made against the aircraft measurements and other retrieval results. These two algorithms, together with the algorithms for cloud mask and surface retrievals, are employed to study the seasonal variation of cloud properties in the high Arctic Ocean. From these studies, we make the following conclusions:

1. Uncertainty in satellite measurements related to calibration issues is the biggest source of uncertainty in the satellite remote sensing of clouds and the surface as well. For a 5% error in satellite measurement of $R_2$, the error in the retrieved $\tau$ is 20-30% for thick clouds, and about 40-50% for $\tau = 20$, whereas for a thin cloud such as $\tau = 2$, it can be as large as 80-90%. The strong sensitivity of cloud optical depth to the satellite-measured radiances

requires a re-evaluation of the previous research results in which NOAA-14 AVHRR channel 1 and 2 with calibration from Rao and Chen (1996) were used in the past several years, at least from 1996-1999. The reflectance in channels 1 and 2 is overestimated by 10 - 20% from our examination of NOAA-10, 12 and 14. A revised calibration of NOAA-14 AVHRR by Rao and Chen (1999) is close to our estimation, and is recommended to be used. The method we developed for the calibration of AVHRR can also be used for real time cross-calibration of other satellite sensors.

2. Cloud discrimination from snow/ice surface is much more difficult than from other low albedo surfaces. Improvement in the cloud mask, especially the identification of partly clouds and cloud phase, in the polar regions is required because partly cloudy situations with a certain cloud cover fraction results in an overestimate of $r_e$ and an underestimate of $\tau$. Our analysis shows that for a cloud cover fraction of 0.8, $r_e$ is overestimated by 25%, and $\tau$ is underestimated by as much as 26%.

3. Uncertainties associated with inhomogeneous cloud stratification, multilayered cloud structure and cloud phase have large influences on the retrieval results. The increase of $r_e$ from cloud bottom to top results in an error in the retrieved $\tau$ of 5-10%. Satellite-retrieved $r_e$ is 80-90% of $r_e$ at the cloud top. The contamination of cirrus influenced the cloud retrieval more significantly. If there is cirrus with $\tau_{ci} > 0.5$ over low water clouds, it is almost impossible to use AVHRR to get reliable information about the underlying water clouds. For $\tau_{ci} = 0.2$ and when the lower water cloud optical depth is larger than 6, the retrieved cloud droplet effective radius is overestimated by 20-30%, and the retrieved $\tau$ is underestimated by 50% or more. Moreover, its effects on the estimation of cloud radiative forcing is significant, as we will see in

Chapter 6.

4. The effects of snow bidirectional reflectance on the retrieval of $\tau$ is small when the view angle is smaller than 10°. For $\tau > 4$. the use of a Lambert approximation to surface reflectance will result in 5% error in the retrieved $\tau$ and $r_e$.

5. Validations of the retrieved cloud optical depth and the effective droplet radius with in-situ aircraft NCAR C-130 measurements and remote sensing results from MAS on NASA ER-2 show that the retrieved effective radius from AVHRR is close to the true value. but an unrealistic cloud optical depth is obtained if there is an ice cloud. For pure water clouds. the retrieved $\tau$ is consistent with surface retrievals.

6. Comparison of the AVHRR retrieved effective droplet radius and optical depth with that retrieved from collocated MAS data. shows that the effective droplet radius derived from the AVHRR 3.75 $\mu$m channel generally agrees well with the retrieval from the MAS 1.62 $\mu$m channel. But the retrieved optical depth tends to be larger than that retrieved from the MAS data.

7. The seasonal variation of cloud optical depth and effective droplet radius from 1 or 2 near overhead satellite passes between April and August. 1998. is derived. Comparison of cloud optical depth inferred from AVHRR with surface retrieval from downward solar radiation measurements demonstrates that in April and May before the onset of snow melt. AVHRR retrieved cloud optical depth is 2-3 times larger than the surface retrieval. but from late June to August. the optical depths derived from these two methods are relatively consistent.

A large difference in spatial resolution. the use of different channels and cali-

bration error are the main reasons for the discrepancy between AVHRR-retrieved $r_e$ and C-130 FSSP in-situ measurements, and between AVHRR-retrieved values of $\tau$ and those inferred from several other remote sensing techniques. Another reason for the difference between optical depth inferred from AVHRR $\tau$ and surface retrievals may be the methods themselves as the satellite remote sensing is based on the reflectance while the surface retrieval is based on the transmittance. However, even after considering all the uncertainties discussed before, it is still difficult to explain the large overestimation of $\tau$ in April - May over the central Arctic Ocean.

In these algorithms, use of plane-parallel RTMs for retrievals of cloud optical depth and effective radius may not immediately appear to be unreasonable. The identification of partially cloudy pixels in high latitude AVHRR data may be one of the most important challenges. Another challenge is the set of surface reflection properties and its temperature because the surface becomes very inhomogeneous after the onset of snow melt. As the number of AVHRR channels is limited and the channels are broad, the availability of more channels from new sensors will improve our ability to monitor the cloud microphysical properties from space. For example, the 1.38 $\mu$m channel in MODIS is good for cirrus detection, and use of the 1.6 $\mu$m channel available on NOAA-15 could improve the estimate of cloud $\tau$ over snow/ice surface, but we have difficulties retrieving $r_e$ due to the lack of a 3.75 $\mu$m channel on NOAA-15 during the daytime. More validations will be required to improve cloud retrievals using these new sensors.

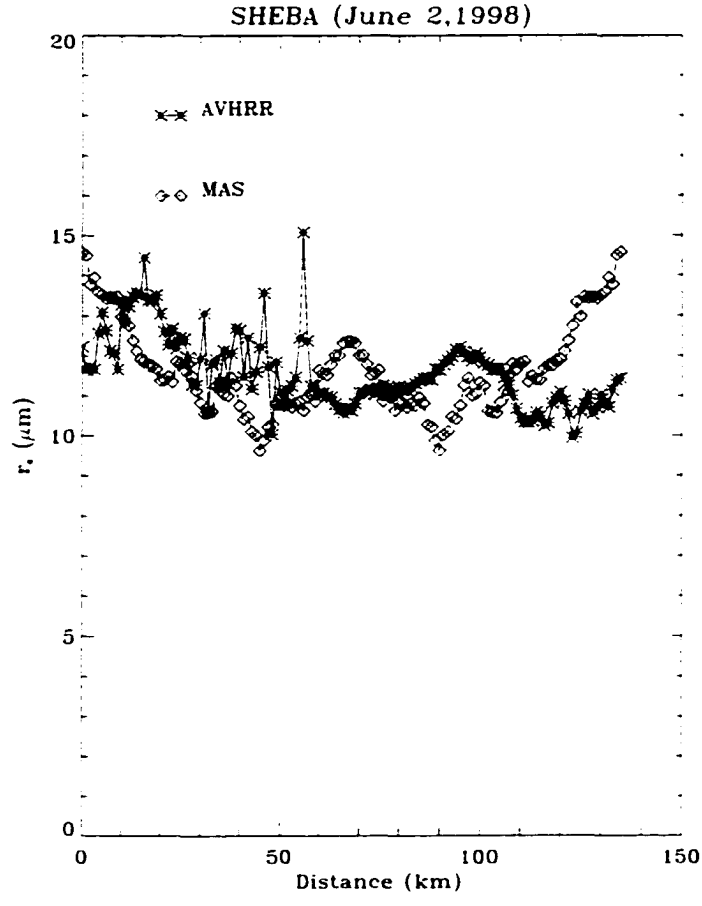


**Figure 5.21** Retrieved $r_e$ for the collocated MAS and AVHRR along the MAS flight track in the afternoon of June 2, 1998. The MAS retrievals have been averaged to the resolution of the AVHRR. The distance scale on the horizontal axis refers to increasing distance inward from the edge of the AVHRR image shown in Figure 5.18 .

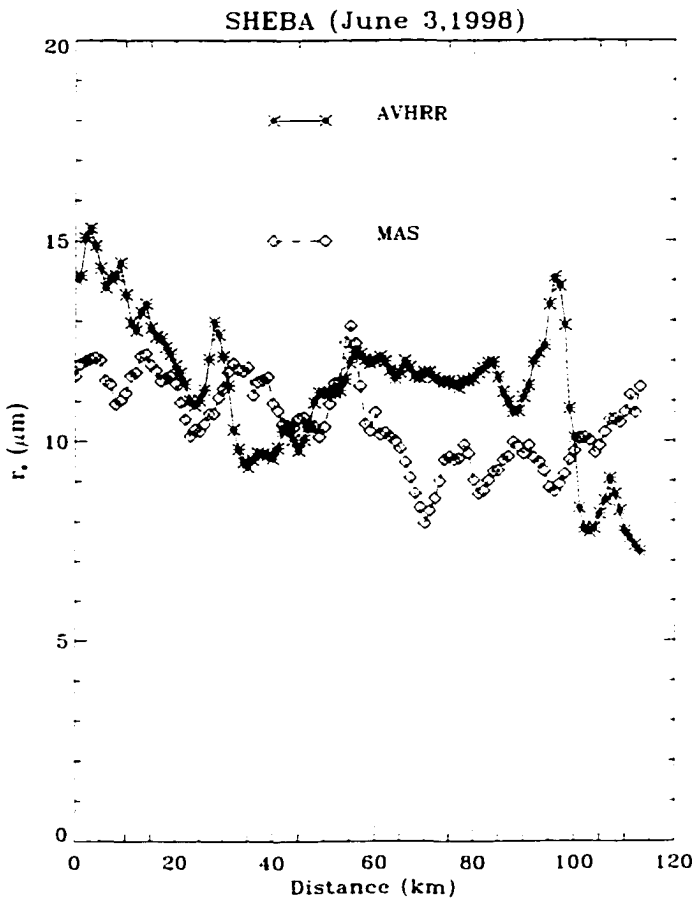


**Figure 5.22** As in Figure 5.21, but for $r_e$ for the collocated MAS and AVHRR images from the afternoon of June 3, 1998.

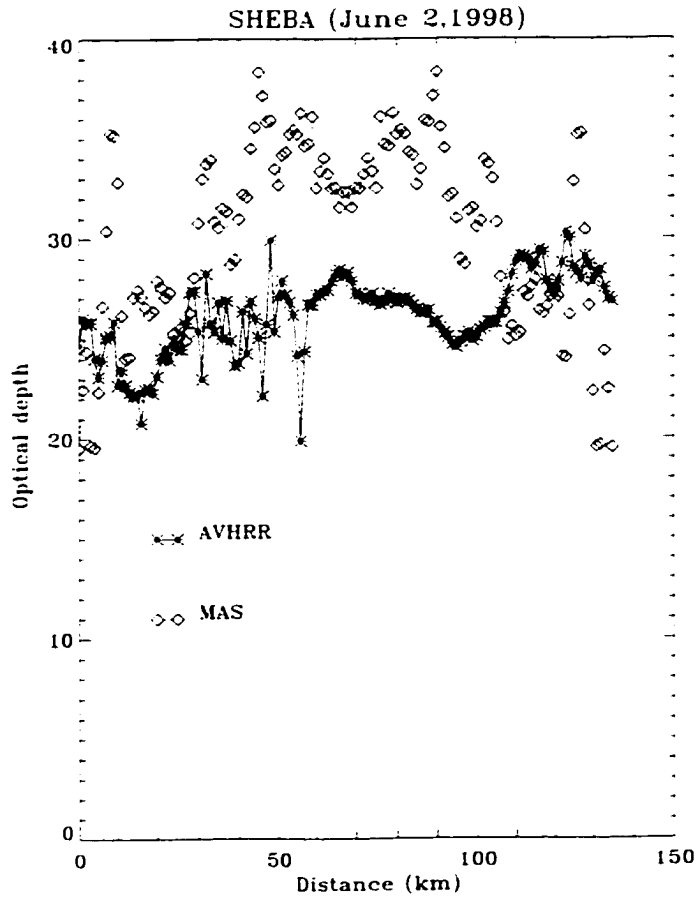


**Figure 5.23** As in Figure 5.21, but for the retrieved $\tau$ for collocated MAS and AVHRR images from the afternoon of June 2, 1998.

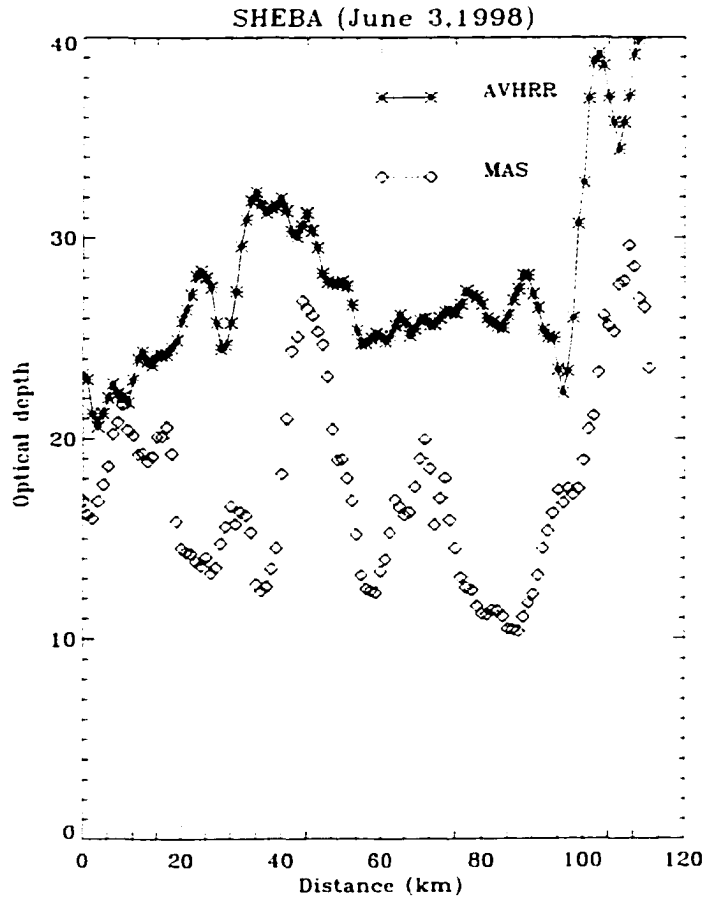


**Figure 5.24** As in Figure 5.23, but for the retrieved $\tau$ for collocated MAS and AVHRR images from the afternoon of June 3, 1998 .

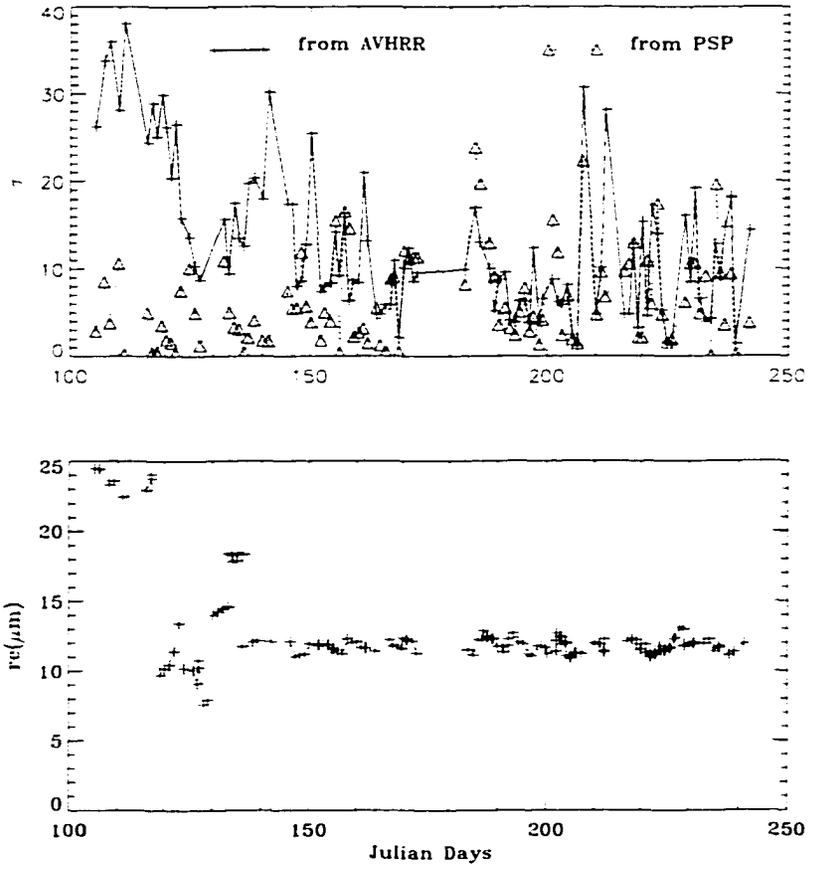


**Figure 5.25** Seasonal variation of mean $\tau$ inferred from AVHRR and downwelling solar irradiance (upper panel) and variation of mean $r_e$ (lower panel) from AVHRR over SHEBA between April and August, 1998 .

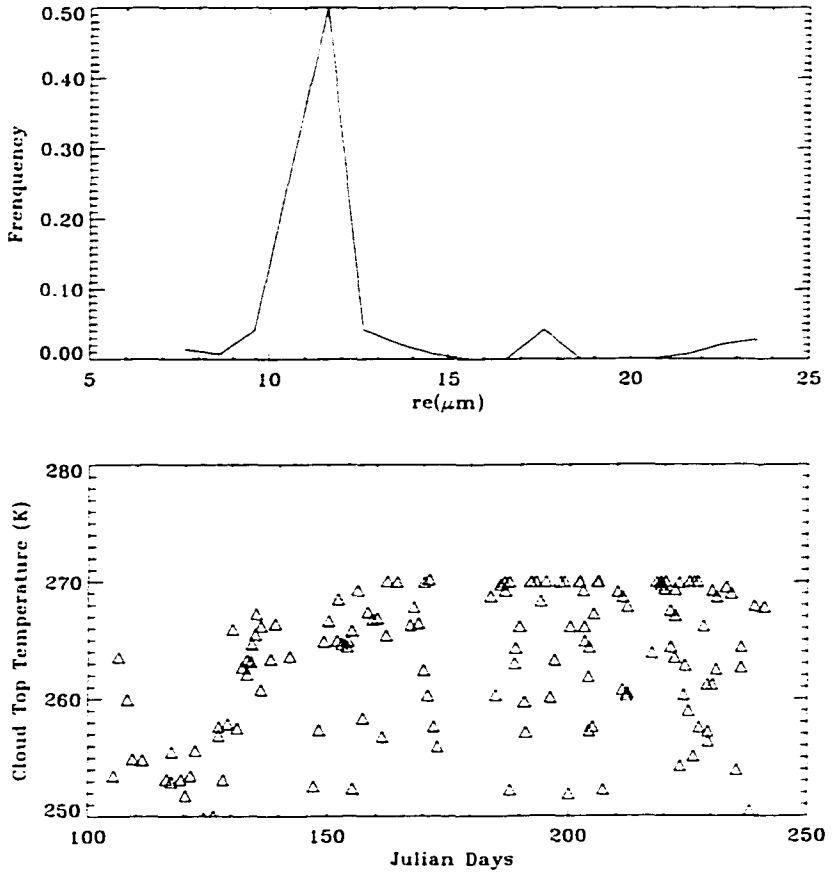


Figure 5.26 Frequency distribution of effective cloud droplet size (upper panel) and the seasonal variation of cloud top temperature (lower panel) derived from AVHRR .

# Chapter 6

# Solar Radiation Budget in the Arctic

## 6.1 Introduction

Studies of the Solar Radiation Budget (SRB) in the Arctic provide a basis for understanding energy exchange and transport in the Arctic earth-atmosphere system. However, the effects of clouds on the radiation are very complex in the Arctic, particularly due to the presence of the highly reflecting snow and ice, the absence of solar radiation for a large portion of the year, low temperature, and the presence of temperature inversions (Curry *et al.*, 1996). The most comprehensive, long-term information on Arctic radiative fluxes is nearly 30 years old (Key et al., 1997) and based on a sparse network of drifting stations, ice islands and coastal stations. In view of the sparse surface measurements of radiation in the Arctic, its monitoring by the use of satellite remote sensing techniques is of particular importance. Unfortunately, polar clouds present unique challenges for satellite remote sensing, and the largest disagreements in the ISCCP (International Satellite Cloud Climatology Project) cloud properties and the ERBE (Earth Radiation Budget Experiment)

cloud-radiative forcing occur in the polar regions (e.g., Rossow *et al.*, 1993; Ramanathan *et al.*, 1989). Therefore, a thorough evaluation of the SRB derivation from satellite data, and its validation with surface measurements from SHEBA and ARM data sets are essential to improve the current algorithms before they are applied to derive a climatological data base of the Arctic SRB.

During the last decade, significant progress has been made in developing methods to derive the SRB parameters from satellite observations. Review of these techniques was provided by Schmetz (1989, 1991), Raschke et al. (1992), Schweiger and Key (1992), Pinker and Laszlo (1992) and Pinker et al. (1995). The precision of Downward Surface Shortwave Radiation (DSSR) fluxes is within 20 $W/m^2$ or better on monthly time scales, or 10% for the daily average. Methods for deriving the Net Surface Shortwave Radiation (NSSR) fluxes from satellite observations are promising, but needs to be further evaluated (Pinker *et al.*, 1995).

The NSSR is defined as the difference between the downward and the upwelling shortwave radiation fluxes at the surface. It describes the energy exchange at the surface. In principle, the NSSR can be estimated directly from satellite measurements, or from the DSSR and the surface albedo ($\alpha_s$):

$$NSSR = DSSR * (1 - \alpha_s). \tag{6.1}$$

Since the knowledge of albedo is a prerequisite for both the determination DSSR fluxes and cloud optical properties, the error in albedo could accumulate to affect the above estimate of NSSR (Cess and Vulis, 1989; Cess et al., 1991; Sellers *et al.*, 1990). Therefore, a possibly better approach is to derive the NSSR directly from satellite observations at the TOA. As reported by many investigators (Ramanathan, 1986; Cess and Vulis, 1989; Cess *et al.*, 1991; Schmetz, 1993; Li *et al.*, 1993), the relationship between NSSR at the TOA and at the surface is almost linear. Based on climate model results, Ramanathan (1986) found a simple

proportionality between the net fluxes at the TOA and at the surface. By using a delta-Eddington model for the radiative transfer calculations. Cess and Vulis (1989) found that the relationship is linear but required an offset under cloudy conditions. Further investigation by Cess and co-workers (1991) shows that the relationship is moderately sensitive to atmospheric water vapor and aerosol content but very sensitive to the nature of the surface and the cloud optical thickness. However, after carrying out extensive radiative modeling for different surface, atmosphere, and cloud conditions with an accurate doubling-adding model, Li and co-workers (1993) found a linear relationship for a fixed solar zenith angle. The relationship depends strongly on solar zenith angle, moderately on precipitable water and cloud type, and is independent of cloud optical thickness and surface albedo. Other factors, such as optical thickness, cloud top altitude (Schmetz, 1993), amount of water vapor and aerosols (Laszlo and Pinker, 1994), may influence the linear relationship and need to be considered for accurate assessment of NSSR from TOA measurements.

All methods available to derive the shortwave radiation budget from space-borne measurements could be categorized into two kinds: (1) empirical/statistical models; and (2) theoretical/physical models. The empirical/statistical models are easy to implement, but they are site specific, and not well suited for global implementation. Use of empirical methods is especially difficult since (1) surface measurements are sparse in the polar regions due to the hostile environment, and we do not have data of radiation components at the TOA collocated with SHEBA surface measurements; and (2) the surface albedo changes significantly during the melt season and the empirical relations should change as snow melt progresses. On the contrary, the theoretical/physical models can treat different atmospheric and surface conditions once all the required input parameters to the radiative transfer model can be derived from satellite data. The theoretical/physical mod-

els consider the complex physical processes in the atmosphere and the feedback of snow/ice albedo. so it can help us understand the effects of different processes and has the predictive capability. In this chapter. we only investigated the use of theoretical/physical models to study the SRB in the Arctic.

Because of the difficulty in using current satellite observations to discriminate cloudy/clear conditions and the difficulty in retrieving cloud and surface optical properties in the polar regions. most methods developed to infer SRB from satellite measurements are not applicable in the Arctic (Li *et al.*, 1993). The error in the inferred fluxes of DSSR or NSSR is much larger at high latitudes than at lower latitudes (Pinker *et al.*, 1995; Li *et al.*, 1993). Using algorithms already developed in previous chapters. we can discriminate clouds. and retrieve the cloud and the surface optical properties. With these results as inputs to the RTM. SRB in the Arctic could be estimated from forward calculations using the theoretical/physical model. However. uncertainties in the cloud mask and in the retrievals of surface and cloud optical properties result in uncertainty in the SRB estimation. Before applying these calculations to estimate the seasonal variation of SRB over SHEBA. we first need to analyze the uncertainty of SRB with regard to uncertainties in all individual input variables. and the combined uncertainty. which can be estimated from error analysis. Finally. the theoretical/physical model is applied to calculate the seasonal variation of SRB over SHEBA. Seasonal variation of the DSSR inferred from satellite data is compared with SHEBA surface measurements.

## 6.2 Method of SRB Estimation from AVHRR

### 6.2.1 Theoretical/Physical Model

Ideally, the radiative transfer described above could be applied to calculate the SRB at the TOA and surface. The same RTM as discussed before is used, which considers radiative interactions with atmospheric gases, such as $CO_2$, $O_3$, $O_2$, and water vapor, and scattering and absorption/emission by stratospheric aerosols, haze particles, and tropospheric aerosols. Radiative transfer calculations are carried out by a discrete-ordinates method applicable for a plane-parallel vertically inhomogeneous atmosphere-Earth system (Stamnes et al., 1988). Water cloud optical properties depend mainly on equivalent radius throughout the solar and terrestrial spectrum and are insensitive to the details of the droplet size distribution. Hu and Stamnes (1993) showed that the optical properties of water clouds can be parameterized as a function of cloud liquid water path and equivalent cloud droplet radius in the range of radii 2.5-12 $\mu m$, 12-30 $\mu m$ and 30-60 $\mu m$ separately. For ice clouds, the optical properties are calculated using the parameterization of Fu and Liou (1993). Thus, if the cloud water content, equivalent radius, mixture of water/ice particle percentage is available, the optical depth, the asymmetry factor, and the single scattering albedo of the cloud could be calculated. The scattering was described by the Henyey and Greenstein (1941) phase function. The solar spectrum from 0.28 to 4 $\mu$m is divided into 24 bands, as defined by Slingo (1989), with unequal spectral widths which vary from 240 to 3040 $cm^{-1}$. The spectral variation of the surface albedo in these 24 bands will be considered.

We will calculate the following components with respect to the SRB: (1) Net Shortwave Radiation at the Top of atmosphere (NSRT); (2) Net Shortwave Surface Radiation NSSR; (3) Downward Surface Shortwave Radiation DSSR; and (4) Net

Irradiance gain (or net absorption) in the atmospheric column ($\delta F_{atm}$), which is defined as follows:

$$\delta F_{atm} = C_0 * \cos(\theta_0) - UPTOA - NSSR. \quad (6.2)$$

where $C_0$ is the solar constant, and $\theta_0$ is the solar zenith angle. $UPTOA$ is the upward solar irradiance at the TOA.

### 6.2.2 Input Variables and Their Uncertainties

Input variables to the theoretical/physical model to calculate the SRB include the surface albedo, absorption trace gases such as water vapor, ozone, aerosol or arctic haze, cloud amount, and cloud microphysical parameters (effective droplet radius and optical depth). Most of these variables can be retrieved directly from satellite measurements as we discussed before, but large uncertainties still exist in the polar regions.

1. Atmospheric Profile, Ozone, Water vapor and Arctic Haze

   The sub-arctic summer model atmosphere (McClatchey et al., 1971), as described above was used while considering the variation of ozone and water vapor content. Total column ozone amounts ($O_3$) is taken from climatological data contained in the ISCCP $C_2$ (monthly) cloud data products for the years 1984-1990. The uncertainties used in the sensitivity tests are the standard deviation for the summer months poleward of 62.5° N latitude (Key et al., 1997). Humidity profiles are taken from the SHEBA radiosonde data. Comparison of humidity profiles from TOVS with radiosonde data from north polar drifting stations provides an uncertainty for Precipitable Water (PW) of 20% (Key et al., 1997).

For aerosols in the layer between 0 and 2 km we adopted the "arctic aerosol" model of Blanchet and List (1983): in the layers between 2 and 9 km and between 10 and 30 km we use the "tropospheric" and "stratospheric background" aerosols, respectively, from Shettle and Fenn (1979). As the Arctic haze is an important feature in the Arctic with a maximum concentration in late spring (Shaw, 1982), Arctic haze is included. The optical depth for Arctic haze is taken to lie between 0.06 and 0.16 at 0.50 $\mu$m for summer and spring, respectively as used by Han et al. (1999). This value is consistent with that provided by Shaw (1985).

2. Surface Albedo

Both field measurements and model simulations indicate that snow exhibits significant bidirectional reflectance properties, which are more pronounced at large solar zenith angles (e.g., Grenfell et al., 1994; Brandt et al., 1991; Sergent et al., 1993; Han et al., 1999). The bidirectional effects over snow is considered in the RTM as the snow is treated as one additional vertical layer when we carry out the radiation transfer calculations. Mie theory is used to get the extinction coefficients and the phase function assuming the snow grains to be spherical particles (Wiscombe and Warren, 1980). As small, highly-absorbing particles, presented in concentrations of only 1 ppmw or less, can lower snow albedo in the visible by 5-15% from the high values (96-99%) predicted for pure snow, soot particles in some concentration of ppmw needs to be considered (Warren and Wiscombe, 1980; Warren, 1982). Mean grain size and the mass-fraction of soot are used to describe the variation of albedo, and the average grain size lies in the range of 40-100 $\mu$m for new snow, 100-300 $\mu$m for finer-grained older snow, and 1000-1500 $\mu$m for old snow near the melting point. The mass-fraction of soot is in the region of 0.02-2.5

ppmw (parts per million by weight). Look-up tables of albedo over snow corresponding to the above range of grain size, soot fraction and variation of solar zenith angle from 30 to 80 degrees were generated through extensive model computations, and the actual albedo of snow for a specific grain size, mass fraction of soot and solar zenith angle will be obtained through linear interpolation.

As discussed in Chapter 3, AVHRR data in channels 1 and 2 were used to derive the snow grain size and soot for snow surfaces. These were used directly in the RTM for the coupled snow-atmosphere system. For other surfaces, AVHRR channels 1 and 2 are used to retrieve the narrowband surface albedo in each channel individually, then through the NTB conversion to derive the broadband albedo. In contrast to the algorithm developed by Lindsay and Rothrock (1994), this method to retrieve the surface albedo depends on the look-up tables and an accurate RTM without any additional atmospheric correction and correction of angular dependence. Thus, the error stems exclusively from the interpolation in the look-up tables and from the uncertainties in the input variables to the RTM. The NTB conversion is one of the largest sources of uncertainty. Uncertainty analyses demonstrate that lack of onboard calibration is another large source of uncertainty, especially for snow surfaces. The uncertainty of albedo retrieval is about 10% on average. Surface albedo before the onset of melting in June is about 0.8, and from July to September before the freeze-up, it is about 0.5.

3. Cloud Parameters

The cloud parameters influencing the solar radiation budget include the cloud cover fraction, cloud particle effective radius and liquid or ice water content. During the summer, low-level stratiform clouds are a prevalent feature in

the Arctic (Tsay et al., 1989). Completely overcast skies exist about 50% of the year, and the cloud cover is maximum between May and November (70% - 90%) (Maykut and Church, 1973). Equivalent droplet radius, $r_e$, of Arctic stratus clouds was observed to lie in the range between 3.3 $\mu$m and 11.4 $\mu$m, as reported by Herman and Curry (1984). The cloud optical depth, estimated from ground-based measurements of incoming solar radiation in Barrow, Alaska during the spring-summer season, is about 8-20, varying by a factor of 4 (Leontyeva and Stamnes, 1994). Model simulations (Leontyeva and Stamnes, 1994; 1996) show that the incoming solar irradiance at the surface during overcast conditions depends primarily on the cloud optical thickness and the surface albedo, and its dependence on $r_e$ is weak.

Cloud discrimination over bright snow or ice surfaces is especially difficult due to small contrast between the surface and clouds in the visible and infrared AVHRR channels. Reflectance of solar radiation in AVHRR channel 3 provides better discrimination of the clouds from the surface in the polar regions as discussed in Chapter 2. The error associated with varying cloud cover fraction is less than 10%.

While cloud water content is not directly retrievable from satellite data, the optical depth $\tau$ can be retrieved (Key et al., 1997). Simultaneous determination of $\tau$, $r_e$ and cloud top temperature $T_c$ were performed from AVHRR channels 2, 3 and 4, as discussed in Chapter 5. Uncertainty in the satellite measured radiance is the largest source of uncertainty for simultaneous determination of $\tau$ and $r_e$. Error in the cloud detection, especially for partly cloudy situations, and the presence of cirrus and vertically inhomogeneous cloud stratification results in an error in $\tau$ of 50% or more, the error in $r_e$ is no more than 30%. The effect of the surface albedo is important only for

thin clouds. The algorithm is reliable for $\tau > 3$ and $r_e > 3$ (Han et al., 1999). The characteristic value of the cloud optical depth is chosen to be 6 in April-May before the onset of snow melt, and 10 in June-August based on the results in Chapter 4. Effective radius is chosen to be 10 $\mu$m. Sensitivity of radiation fluxes over the Arctic ocean to cloud optical depth was discussed by Curry and Ebert (1992).

## 6.3 Uncertainty of SRB from AVHRR

The uncertainty in the SRB resulting from uncertainties in individual variables are evaluated through a series of numerical simulations based on the RTM. In these analyses, the other variables, except the individual variable being examined, are fixed at reference values representing the mean values for a wide range of atmospheric conditions.

Tables 6.1- 6.4 list the reference values for different variables and the corresponding relative error in the calculated NSRT, NSSR and DSSR. In these tables, variables are defined as follows:

$\tau_h$ is aerosol optical depth, PW is precipitable water, $O_3$ is ozone column amount, $r_e$ is cloud droplet effective radius, $\tau_c$ is the cloud optical depth, and $A_c$ is the cloud cover fraction.

Table 6.1 shows the sensitivities of the SRB to individual variables for a cloud-free atmosphere overlying a snow surface. The snow is set as new snow (100 $\mu$m, 0.1 ppmw) with albedo 0.79. This situation corresponds to the April-May time period at SHEBA (the set of soot content may be a little high and albedo is a little low, but it does not influence the simulation results). After the snow starts melting, the surface is composed of melt ponds, leads and ice, so we just treated it as a Lambert surface, and the albedo is assumed to be 0.5 based on the satellite retrievals and

**Table 6.1** Sensitivity of the SRB to Input Variables under Clear Sky Conditions over a Snow Surface.

| Variables | Reference Value ($x_0$) | Error ($\pm$) $\Delta$x | NSRT $\frac{\Delta F}{F}(\%)$ | NSRT $\frac{\Delta F}{\Delta x}$ | NSSR $\frac{\Delta F}{F}(\%)$ | NSSR $\frac{\Delta F}{\Delta x}$ | DSSR $\frac{\Delta F}{F}(\%)$ | DSSR $\frac{\Delta F}{\Delta x}$ |
|---|---|---|---|---|---|---|---|---|
| Snow ($\mu$m, ppmw) (albedo) | 100, 0.1 (0.79) | +100, +0.1 (0.72) | 15.1 | -560.0 | 29.1 | -581.0 | 1.1 | 105.0 |
| $\tau_h$ | 0.08 | +0.08 | 3.1 | 71.3 | 1.1 | -13.0 | 0.9 | -105.0 |
| PW, mm | 2.0 | 0.4 (20%) | 0.7 | 3.5 | 1.3 | -3.8 | 1.1 | -15.3 |
| $O_3$, g $m^{-2}$ | 7.22 | 0.37 | 0.7 | 1.4 | 0.01 | -0.02 | 0.2 | -0.9 |

**Table 6.2** Sensitivity of the SRB to Input Variables under Clear Sky Conditions over a Lambert Surface.

| Variables | Reference Value($x_0$) | Error ($\pm$) $\Delta$x | NSRT $\frac{\Delta F}{F}(\%)$ | NSRT $\frac{\Delta F}{\Delta x}$ | NSSR $\frac{\Delta F}{F}(\%)$ | NSSR $\frac{\Delta F}{\Delta x}$ | DSSR $\frac{\Delta F}{F}(\%)$ | DSSR $\frac{\Delta F}{\Delta x}$ |
|---|---|---|---|---|---|---|---|---|
| albedo | 0.5 | 0.05 | 6.1 | -474.0 | 8.9 | -494.0 | 0.4 | 46.0 |
| $\tau_h$ | 0.08 | +0.08 | 0.2 | 11.3 | 1.6 | -52.5 | 1.6 | -102.5 |
| PW, mm | 11.9 | 2.4 (20%) | 0.4 | 0.7 | 0.7 | -0.7 | 0.6 | -1.4 |
| $O_3$, g $m^{-2}$ | 7.15 | 0.1 | 0.01 | 0.04 | 0.01 | -0.05 | 0.01 | -0.03 |

SHEBA surface measurements between July and August (see Chapter 3). Haze optical depth is in the range of 0.08-0.16, which is consistent with observations (Shaw, 1985). Precipitable water for spring over snow surface is set to 2.0 mm, and during summer after the onset of snow melt, it is set to 11.9 mm (Key et al., 1997).

Table 6.3 shows the sensitivities of the SRB to individual variables for cloudy sky over a snow surface. Both water clouds and ice clouds are considered, and for ice clouds the cloud particle size is set to 40 $\mu$m, the optical depth is set to 6. Table 6.4 shows the sensitivities of the SRB to individual variables for cloudy sky over a Lambert surface, but only water clouds are considered. As the cloud tends

Table 6.3 Sensitivity of the SRB to Input Variables under Cloudy Sky Conditions over a Snow Surface.

| Variables | Reference Value($x_0$) | Error ($\pm$) $\triangle$x | NSRT $\frac{\triangle F}{F}(\%)$ $\frac{\triangle F}{\triangle x}$ | NSSR $\frac{\triangle F}{F}(\%)$ $\frac{\triangle F}{\triangle x}$ | DSSR $\frac{\triangle F}{F}(\%)$ $\frac{\triangle F}{\triangle x}$ |
|---|---|---|---|---|---|
| Snow ($\mu$m, ppmw) (albedo) | 100, 0.1 (0.79) | +100, +0.1 (0.72) | 6.7 -227.0 | 15.4 -237.0 | 4.2 338.0 |
| $A_c$ | 0.6 | 0.06 | 1.0 -34.2 | 3.5 -52.2 | 1.8 -143.3 |
| $\tau_c$ | 6 | 3(50%) | 1.7 -1.1 | 5.9 -1.8 | 4.3 -7.0 |
| $r_e$, $\mu$m | 8.0 | 2.0 | 0.3 0.4 | 0.4 -0.2 | 1.3 -3.2 |
| $\tau_c$ | 6(ice) | 3(50%) | 0.7 0.6 | 8.0 -2.1 | 4.1 -6.2 |
| $r_e$, $\mu$m | 40.0(ice) | 10.0 | 1.5 0.3 | 1.9 -0.1 | 6.0 -0.3 |
| PW, mm | 2.0 | 0.4 (20%) | 0.6 2.9 | 0.4 -0.9 | 1.4 -17.3 |
| $O_3$, g $m^{-2}$ | 7.22 | 0.27 | 0.4 0.5 | 0.05 -0.06 | 1.3 -6.0 |

to be thicker in the summer and autumn as mentioned in Chapter 4, the optical depth is set as 10.

The simulation results show that the uncertainty in the albedo is the largest source of uncertainty for SRB under clear sky conditions, and the second largest source is the aerosol optical depth. Under cloudy sky conditions, the uncertainty in the albedo is the largest source of uncertainty for SRB over snow surfaces, but the uncertainty in the cloud cover fraction and cloud optical depth are also very important. This significant effect of albedo is related with the setting of cloud optical depth as 6, which may be a little low. From these simulations, we found that the improvement on the retrieval of cloud optical depth and surface albedo is urgent for improving SRB estimation from satellites.

If the sensitivities of the SRB to the individual variables and the uncertainties of these variables derived from AVHRR are known, we can estimate the combined uncertainty in the SRB with regards to all these inputs based on error propagation theory. Suppose $f$ is a function of variables $x$ and $y$, and assume their errors $\delta$x

Table 6.4 Sensitivity of the SRB to Input Variables under Cloudy Sky Conditions over a Lambert Surface.

| Variables | Reference Value($x_0$) | Error ($\pm$) $\triangle$x | NSRT $\frac{\triangle F}{F}(\%)$ | NSRT $\frac{\triangle F}{\triangle x}$ | NSSR $\frac{\triangle F}{F}(\%)$ | NSSR $\frac{\triangle F}{\triangle x}$ | DSSR $\frac{\triangle F}{F}(\%)$ | DSSR $\frac{\triangle F}{\triangle x}$ |
|---|---|---|---|---|---|---|---|---|
| albedo | 0.5 | 0.05 | 1.7 | -99.2 | 3.6 | -110.4 | 2.8 | 8.0 |
| $\tau_c$ | 10.0 | 5.0 | 5.5 | -3.2 | 12.0 | -3.7 | 12.0 | -7.4 |
| $A_c$ | 0.8 | 0.08 | 3.2 | -11.5 | 7.1 | -134.9 | 7.1 | -269.6 |
| $r_e$, $\mu$m | 8 | 2 | 0.4 | 0.6 | 0.4 | -0.3 | 0.4 | -0.6 |
| PW, mm | 11.9 | 2.4 (20%) | 0.6 | 0.7 | 0.3 | - 0.2 | 0.4 | -0.5 |
| $O_3$, g $m^{-2}$ | 7.15 | 0.1 | 0.03 | 0.07 | 0.01 | -0.02 | 0.01 | -0.08 |

and $\delta y$ are random. From error propagation theory, the uncertainty in $f$ can be calculated as:

$$\delta f = \sqrt{(\frac{\partial f}{\partial x})^2(\delta x)^2 + (\frac{\partial f}{\partial y})^2(\delta y)^2}. \tag{6.3}$$

The above formula is the standard formula form of the equation for the propagation of errors, and can be expanded to any number of independent variables. However, if the variables $x$ and $y$ are not independent, the covariance between them must be considered. In our calculation of SRB from the radiative transfer equation, the SRB can be taken as a function of the variables listed in Table 6.1 - 6.4. The assumption of independence of these variables may not right, and the covariance among them is difficult to assess. However, we can estimate the maximum error as follows:

$$\delta f = (\frac{\partial f}{\partial x})\delta x + (\frac{\partial f}{\partial y})\delta y. \tag{6.4}$$

If the partial derivatives in the above equation can be approximated as the finite differences ( $\triangle F/\triangle x$), we can obtain the combined uncertainty in the solar

Table 6.5 Combined Uncertainty of the SRB to Inputs Variables Derived from AVHRR in the Arctic.

| Conditions | NSRT | | NSSR | | DSSR | |
|---|---|---|---|---|---|---|
| | Error | Max. | Error | Max. | Error | Max. |
| Clear over snow | 34.11 | 41.22 | 34.91 | 37.43 | 12.16 | 21.55 |
| Clear over Lambert | 23.78 | 26.28 | 25.11 | 30.64 | 9.15 | 13.84 |
| Cloudy over snow (ice) | 13.97 (13.97) | 20.13 (20.73) | 15.34 (15.71) | 23.75 (25.49) | 31.18 (29.00) | 61.39 (55.51) |
| Cloudy over Lambert | 16.90 | 24.54 | 22.02 | 33.77 | 40.66 | 56.69 |

radiation budget from eq. (6.3) and the maximum uncertainty from eq. (6.4). The results are presented in Table 6.5. For cloudy sky conditions over a snow surface, both liquid water clouds and ice clouds are considered.

## 6.4 Effects of Cirrus/Water Clouds and Cloud Phase on SRB

Surface observations show that Arctic clouds often have 2 or 3 layers, and in-situ observations also show that the cloud droplet effective radius increases from the cloud bottom to the cloud top. However, in radiative transfer models used for remote sensing retrieval purposes, the clouds are usually assumed to be a homogeneous layer with a constant cloud effective radius. This assumption is not consistent with observations. To examine the effects of multilayered clouds or cloud phase on the SRB, we performed a series of numerical experiments in which the cloud was assumed to consist of two layers. The upper layer is an ice cloud located between 7 and 8 km, and the lower layer is a water cloud located between 1 and 2 km. Five tests were made:

1. Water cloud with $r_e = 10$ $\mu$m, representing a typical water cloud:

2. Ice cloud with $D_e = 20$ $\mu$m:

3. Ice cloud with $D_e = 40$ $\mu$m:

4. Mixed phase cloud with 50% ice and 50% liquid water, and with an effective particle size of 20 $\mu$m for both phases:

5. Cirrus over low cloud, for cirrus $D_e = 40$ $\mu$m, $\tau = 0.5$, for water cloud $r_e = 10$ $\mu$m and $\tau$ is allowed to vary:

6. Cirrus over a low water cloud, and the cirrus is set as $D_e = 40$ $\mu$m, $\tau = 0.1$: the water cloud is set as $r_e = 10$ $\mu$m and $\tau$ is allowed to vary:

In these calculations, the solar zenith angle is set to 60°, and the surface is assumed to be snow with a grain size of 1000 $\mu$m and a mass-fraction of soot of 0.3 ppmw. The total cloud optical depth for these five tests is taken to be the same.

Figure 6.1 shows the difference between the different cloud types and the water cloud for DSSR and NSSR. The results demonstrate that cirrus overlying a liquid water cloud has only minor influence on the DSSR (1-2 $Wm^{-2}$). The ice cloud or the mixed phase cloud results in a decrease in the DSSR and the NSSR by about 10 $wm^{-2}$ and $5wm^{-2}$, respectively. These influences are only a weak function of the total cloud optical depth, and the smaller the $\tau$ ($\tau < 5$), the smaller the influence of the cloud phase. These results also demonstrate that the DSSR is mainly a function of cloud optical depth, and that its dependence on the effective cloud particle size and cloud phase is weak. In contrast to the DSSR and the NSSR, the NSRT depends primarily on effective cloud droplet size (Figure 6.2). Both ice clouds and cirrus overlying low-level water clouds result in a decrease in NSRT and $\delta F_{atm}$ by as much as 40 $Wm^{-2}$ depending on the cloud optical depth. Mixed phase clouds result in a decrease in NSRT by as much as 20 $Wm^{-2}$ as compared to water clouds. The different dependences of the DSSR and the UPTOA on cloud

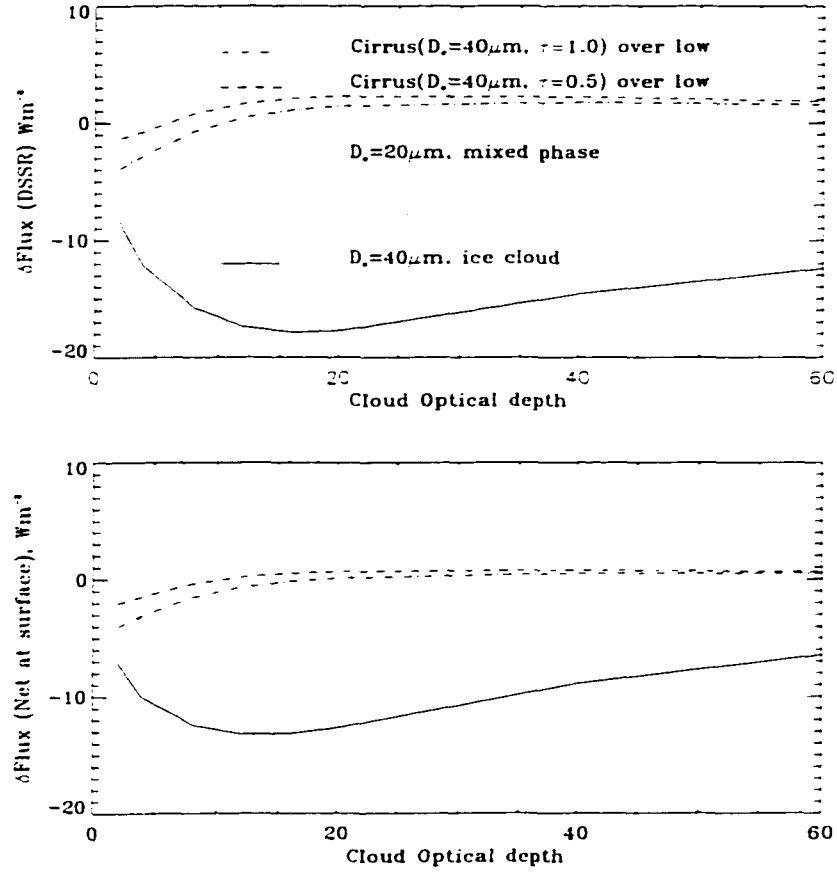


**Figure 6.1** DSSR (upper panel) and NSSR (lower panel) between different clouds and water cloud. Under conditions of $\theta_0 = 60°$, snow grain size 1000 $\mu$m and mass-fraction of soot 0.3 ppmw .

phase and cloud structure also demonstrates that the satellite retrieval based on the reflectance at the TOA and the surface retrieval based on the transmittance will not give exactly the same results.

One surprising result is that the net solar radiation absorbed in the atmospheric column depends strongly on cloud phase and on effective cloud particle size. Compared to liquid water clouds, thick ice clouds can result in an increase of $\delta F_{atm}$ by as much as 50 $Wm^{-2}$, and mixed phase clouds can result in an increase of $\delta F_{atm}$ by 20 $Wm^{-2}$. Even more interesting, thin cirrus overlying low liquid water clouds

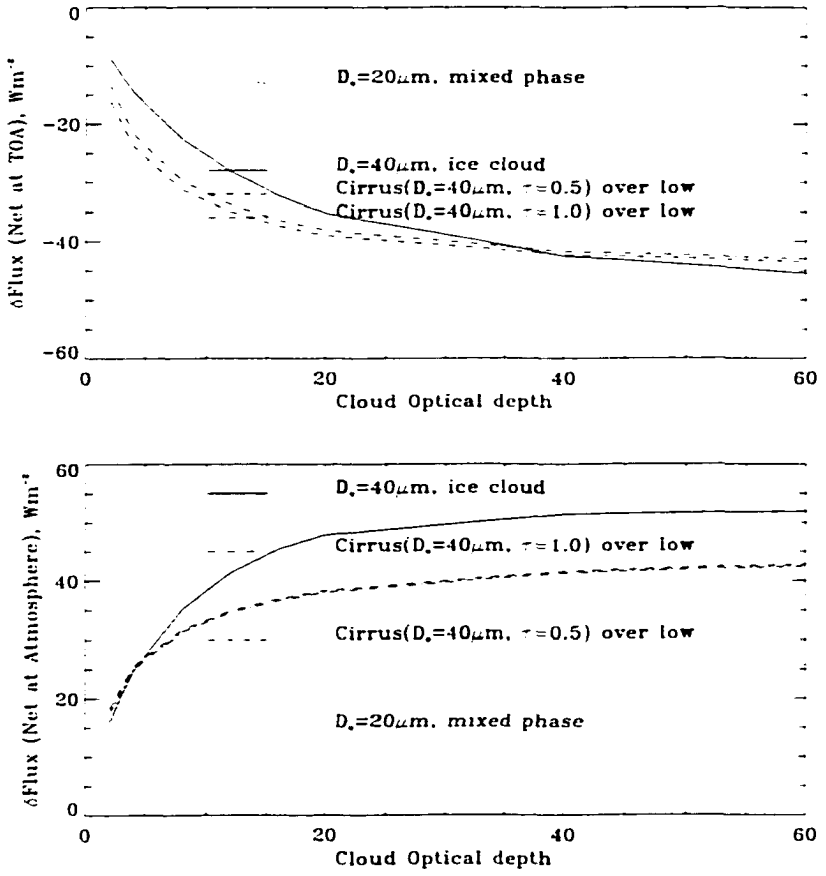


**Figure 6.2** As in Figure 6.1, but for Net Solar Radiation at the TOA (upper panel) and Net Solar Radiation in the atmospheric column (lower panel) .

increases the absorption ($\delta F_{atm}$) by as much as 40 $Wm^{-2}$ as compared to liquid water cloud. This radiative forcing made by cirrus may play an essential role in climate change.

## 6.5 Application and Results

### 6.5.1 Data

Using the algorithms for cloudy/clear discrimination and for retrievals of surface and cloud properties, we can obtain cloud particle size and optical depth under cloudy conditions, and the surface properties under clear sky conditions from AVHRR data obtained over SHEBA. Inserting all these data into the RTM, the DSSR, the NSSR, the UPTOA and the $\delta F_{atm}$ can be obtained via forward calculations (xiong et al., 2000b). For a snow surface, the snow grain size and mass fraction of soot can be used directly in the RTM for the coupled atmosphere-snow system. For other surfaces, albedos retrieved from AVHRR are used. Under cloudy conditions, we will use the surface albedo obtained under clear conditions in the previous or the following day.

### 6.5.2 Seasonal Variation of SRB over SHEBA

Using the retrieved snow grain and soot, or surface albedo (Chapter 3), and the retrieved cloud droplet effective radius and optical depth (Chapter 5), we calculated the DSSR and NSSR (average for 30 by 30 pixels) and compared it with SHEBA measurements (1 hour average during the overpass of the satellite) as shown in Figure 6.3. Both the DSSR and the NSSR increase significantly from April to June, corresponding to the decrease in solar zenith angle from about 69° to 55°. After summer solstice the solar zenith angle increases again and the DSSR and the NSSR decrease. This seasonal variation is mainly controlled by the solar zenith angle: the smaller the solar zenith angle, the larger the DSSR and the NSSR. After snow melt begins in late June, the seasonal trend becomes less obvious because the DSSR and the NSSR are influenced significantly by the surface albedo, which

changes rapidly during this period. Day-by-day change in the SRB is mainly controlled by the cloud optical properties. Note that our analysis follows the track of the SHEBA Ice Camp. so change in solar zenith angle depends on both the relationship between the Sun and Earth. as well as the latitude of the SHEBA Ice Camp. Further comparison between the surface measurements and the model calculations with inputs from AVHRR retrievals is shown in the scatter plot in Figure 6.4. This comparison shows that the mean discrepancies in both the DSSR and the NSSR during April 15-June 14 time period are as large as 32 %. and 7% from the middle of June to the end of August. much less than before the onset of snow melt. The large discrepancy before snow melt is directly related with the large overestimate of cloud optical depth during this period.

## 6.6 Summary

Using a comprehensive RTM. we have analyzed the sensitivity of the SRB to the individual variables. and the combined uncertainty by using the AVHRR retrieval of surface and cloud properties as inputs to the computations. Sensitivity tests show that under clear sky conditions. the surface albedo and the aerosol optical depth are the main sources of uncertainty. and under cloudy sky conditions. the surface albedo. the cloud optical depth and the cloud fraction cover are the main sources of uncertainty for the SRB estimation. Calibration uncertainties in AVHRR channels 1 and 2 are still one of the largest sources of uncertainty because they affect all surface and cloud retrievals. These results demonstrate that improvements in satellite calibration. cloud discrimination and cloud retrievals over snow and ice surface are required. Use of in-situ humidity profiles will improve the SRB estimation. Uncertainty in ozone amount on the total SRB is small. but its effect on UV is significant. The combined uncertainty of the SRB shows that under clear

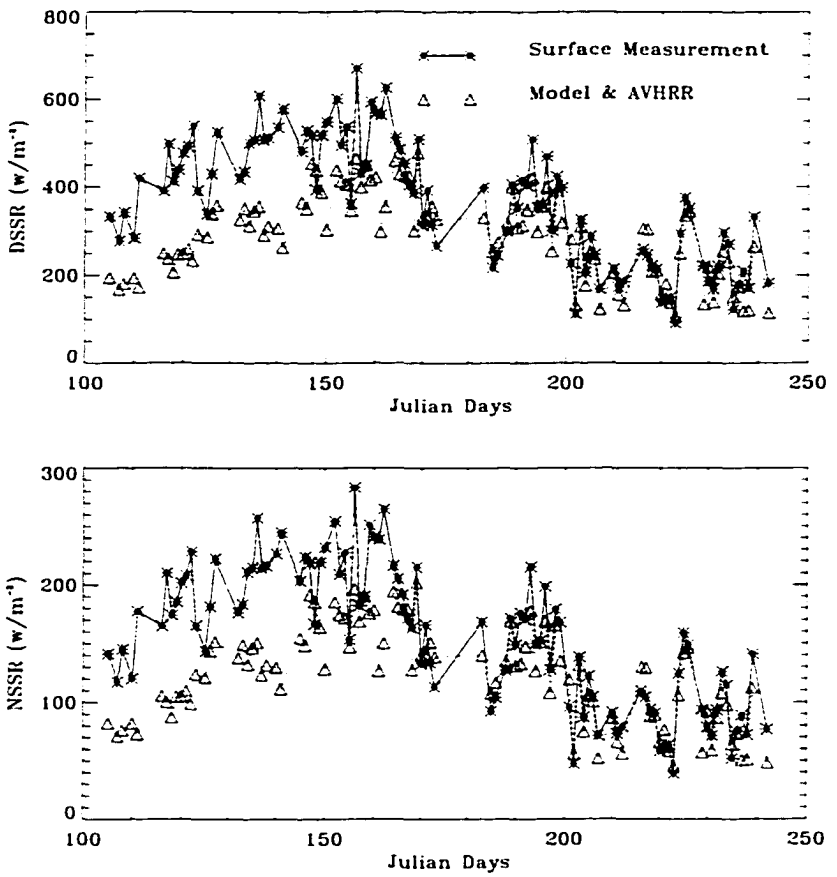


**Figure 6.3** Seasonal variation of DSSR (upper panel) and NSSR (lower panel) from SHEBA surface measurements and satellite retrieval .

sky conditions, the uncertainty in the DSSR is about $\pm 10\ Wm^{-2}$. This value is similar to that obtained by other methods (Pinker et al., 1995). Under cloudy sky conditions, the error in the retrieved DSSR could be as high as $\pm 30 \sim 40 Wm^{-2}$, because of the uncertainty in cloud cover fraction and cloud optical depth retrieved over snow or ice surfaces. The uncertainty of NSSR is about $\pm 15 \sim 20 Wm^{-2}$.

Model simulations demonstrate that the effect of the inhomogeneity of the cloud layer and the cloud phase on the estimated DSSR and NSSR is small, but its effect on the cloud radiative forcing in the atmospheric column is very large, especially

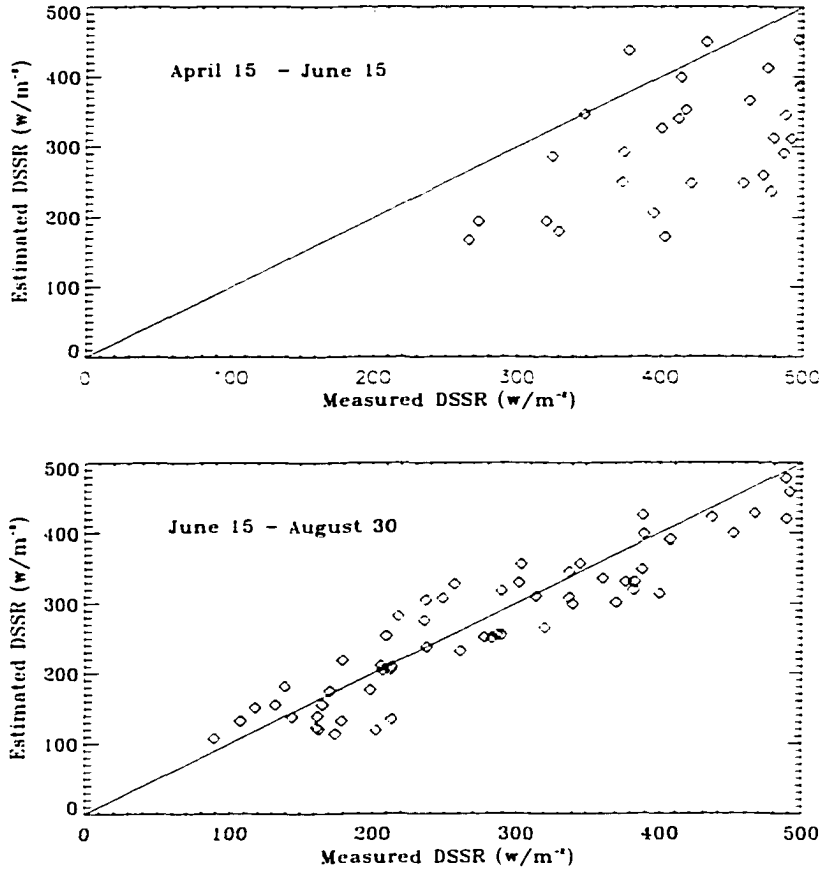


Figure 6.4 Comparison of DSSR between SHEBA surface measurements and satellite retrieval for the periods of April 1 - June 14 (upper panel) and June 16 - August 30, 1998 (lower panel) .

when thin cirrus is overlying low liquid water clouds. This implies that accurate detection of cirrus and its retrieval are very important for correct assessment of cloud radiative forcing in climate models.

Using the surface albedo, snow grain size, surface temperature, cloud optical depth and effective cloud droplet size retrieved from the AVHRR data in a comprehensive RTM, we estimated the seasonal variation of DSSR and NSSR. Seasonal variations of DSSR and NSSR are obvious before the melting begins in June, and this variation is mainly controlled by the solar illumination angle. However, the

seasonal variations after the onset of snow melt are less obvious because the DSSR and the NSSR are influenced significantly by both the rapidly changing surface albedo and the solar illumination angle. The decrease in the albedo with the melting of the snow/surface tends to increase the NSSR, whereas the decrease in the solar illumination angle tends to decrease the DSSR. These two opposite effects result in a small variation in the DSSR.

Daily variation of the SRB are mainly controlled by the cloud optical properties. Comparison of SHEBA surface measurements and model calculations with inputs from the AVHRR retrievals show that before the snow melt begins, the error is more than 30%, but a good agreement with a mean error of about 7% is obtained after the onset of snow melt considering the difference in spatial coverage between the satellite and the surface measurements. With regard to the plane-parallel RTM, the influence of the cloud horizontal heterogeneity on the SRB is not clear (Pinker *et al.*, 1995; Hartmann *et al.*, 1986). An assessment of the uncertainties associated with horizontal heterogeneity requires the use of a 3-D radiative transfer model.

# Chapter 7

# Summary and Discussion

Because surface measurements are sparse and difficult in the Arctic and our knowledge of the Arctic cloud and sea-ice albedo feedback is poor, use of satellite remote sensing to monitor the surface and cloud properties and to infer solar radiation budget is of particular importance in the polar regions. However, large uncertainties in cloud cover fraction and cloud optical depth between ISCCP and surface observation occurred for the Arctic clouds (Curry et al., 1996). The primary goal of this work has been to investigate the use of satellite measurements to study the Arctic surface and cloud properties and the solar shortwave radiation budget. Use of satellite data for this remote sensing application requires accurate calibration of the satellite data, discrimination between clear and cloudy sky, and retrievals of surface and cloud properties. Based on these requirements, this thesis was divided into five chapters, except for the background provided in Chapter 1 and this conclusion. A comprehensive plane-parallel RTM based on the DISORT code provides the theoretical basis. Using this model we first performed a series of theoretical sensitivity and uncertainty analyses, then we designed several algorithms. The algorithms are validated against the composite surface measurements from the SHEBA, and in-situ aircraft measurements from FIRE-ACE. We chose

to use AVHRR sensors deployed on the NOAA polar orbiting satellites for our study because this data has more than 20 years of history and is widely used for environmental research. However, the AVHRR only has 5 channels, much less than that available on newly launched or planned satellites, like MODIS and GLI. We therefore do not have too many options for choosing the most appropriate channels for our research purposes. This paucity of spectral information is one of the difficulties we have in discriminating clouds from snow/ice surfaces and retrieving surface snow grain size and mass-fraction of soot. A large uncertainty in the retrieval of cloud optical depth is also related with the paucity of channels. Lack of onboard calibration of AVHRR channels 1 and 2 is one of the most significant sources of uncertainty.

In this thesis, we first developed an automatic cloud discrimination algorithm over snow/ice surfaces primarily using the solar reflectance in AVHRR channel 3. After improving the estimation of solar reflectance in channel 3 by removing the undesired thermal component, and making an appropriate anisotropic correction based on a RTM, we obtained the albedo at the TOA. An easily calculated threshold function was found. We also examined thresholds using the spectral information in AVHRR channels 1 to 5 from model simulations. From this work, it is found that the brightness temperature difference between channels 4 and 5 can be used to detect cirrus but cannot discriminate cirrus from thin warm clouds. For this reason BT4 needs to be used. Application of this cloud discrimination scheme to AVHRR data taken during overpasses over the SHEBA Ice Camp during the melting season between April and August, 1998 demonstrates that the cloud cover fraction from AVHRR is in good agreement with surface weather observations over SHEBA.

Algorithms were developed to derive snow grain size and mass-fraction of soot, and to derive surface albedo for clear sky conditions. It was expected that use

of the derived snow optical properties in a RTM for the coupled atmosphere - snow system would yield precise estimate of the bidirectional effects of the snow surface. This in turn was expected to improve the accuracy of the cloud retrieval as well as the SRB. However, this expectation has not been satisfactorily resolved because there are no in-situ snow data available for validation. Uncertainty in satellite radiometric measurements, effects of aerosol in channel 1 and strong water absorption in channel 2 result in significant uncertainty in the retrieved snow grain size and mass-fraction of soot. For a $\pm$ 5% error in the satellite radiometric measurements, the error in the snow grain size and mass fraction of soot is about 200% for $s_t < 0.05$ ppmw, and for $s_t > 0.1$ ppmw the error is more than 50%. Use of subarctic summer instead of winter atmospheric constituent profiles could lead to a difference in channel 2 reflectance of 40% over a snow surface. Therefore, additional channels available on instruments such as GLI and MODIS, or the 1.6 $\mu$m channel available on NOAA-15 will provide opportunities to get more reliable results on snow grain size and mass fraction of soot.

On the other hand, albedo retrieval from AVHRR is more promising. The relatively broad AVHRR channels 1 and 2 provide good representation of the visible and near visible parts of solar radiation, where the reflectance is large. The spectral albedo in channels 1 and 2 can be retrieved separately. The uncertainty in albedo with regard to the uncertainty in the satellite radiometric measurement is of the same magnitude, but the effect of aerosols in channel 1 and the effect of water vapor in channel 2 is relatively significant. NTB conversion is one of the main sources of uncertainty. This research suggests that different NTB conversion coefficients should be used for different surface conditions. Application of our algorithm to more than 100 images from April to August yields a good agreement with SHEBA surface measurements of albedo. Minor differences between them are due to the difference in spatial coverage, and the large spatial variations of

the surface albedo due to the occurrence of melt ponds and leads. Failure to discriminate thin/cirrus clouds from snow surfaces may lead to an error in albedo retrieval. The deployment of new sensors, such as GLI and MODIS, is expected to improve the discrimination of ice cloud using the 1.38 $\mu$m channel, which will be helpful for improving the albedo retrieval over a snow surface.

Retrieval of cloud properties in the polar regions from AVHRR data is investigated in Chapter 5. Since channel 2 is more sensitive to cloud optical depth than channel 1 over high albedo surfaces, channel 2 together with channels 3 and 4 are used to retrieve the cloud optical depth, cloud droplet size and cloud top temperature simultaneously. Considering the bidirectional effect of the snow/ice surface, two algorithms for cloud retrieval corresponding to snow surface and Lambert surface are developed. As satellite remote sensing almost always assumes clouds to be one homogeneous layer, we first examined the uncertainties of cloud retrievals with regard to partly cloudy cover, multi-layer structure, cloud phase and vertically inhomogeneous stratification. It is found that cloud inhomogeneity causes the retrieved cloud effective droplet size to be about 80-90% of $r_e$ at the cloud top, while the error in $\tau$ is only 5-10%. The presence of partly cloudy cover leads to an overestimate of $r_e$ and an underestimate of $\tau$. Retrieval of $r_e$ and $\tau$ for cirrus overlying water clouds is possible when $\tau_{ci} < 0.2$, but the retrieved $r_e$ is 20-30% larger than the $r_e$ of lower warm clouds. Uncertainty in the radiometric measurement in AVHRR channel 2 represents the main source of uncertainty for the retrieval of cloud optical depth. The algorithm is more reliable for relatively thick clouds, but for thin clouds ($\tau < 2$), the retrieval error is large.

These algorithms are tested against (1) the NCAR C-130 in-situ measurements of cloud effective droplet size, (2) the retrieval of optical depths using surface incoming solar radiation, and (3) the MAS data collected on the NASA ER-2. Overall, the retrieved cloud droplet effective radius is in good agreement with the

actual cloud droplet size, but the cloud optical depth tends to be overestimated over snow/ice surfaces. A much better agreement of the cloud optical depth derived from AVHRR with that derived from surface measurements is obtained after snow melt. Overlap of cirrus overlying the lower warm cloud or the existence of mixed phase clouds is one of most important reasons for the disagreement between satellite retrieved $\tau$ and that derived from surface measurements due to the inaccurate representation of the phase function.

Cloud optical depth was also retrieved using the downward solar radiation. Because the downward solar radiation is insensitive to cloud droplet size, we may use a constant value of $r_e$=$\bar{7}$ $\mu$m while deriving the cloud optical depth. A 5% uncertainty in the surface radiometric measurement results in an uncertainty in $\tau$ of almost 3-4 for high albedo surfaces. From the SHEBA surface measurements during April to August, 1998, the mean optical depth is found to be about 10, and it tends to increase after the onset of melt. The error in cloud retrieval is larger on April-May as compared to that in June-August.

The surface albedo, snow grain size, surface temperature, cloud optical depth and effective droplet size are used as inputs to the RTM to compute the SRB. In Chapter 6 we evaluated the uncertainty in the SRB to the individual input variables retrieved from satellite remote sensing data and the combined uncertainties. We found that the effect of cloud inhomogeneity and cloud phase on DSSR and NSSR is small, but their effect on the radiative forcing of the atmospheric column is very large, particularly for the situation with thin cirrus over liquid water clouds significantly enhances the cloud radiative forcing. The combined uncertainty is about $\pm 10$ $Wm^{-2}$ under clear sky conditions for DSSR. But under cloudy sky conditions, the DSSR uncertainty could be as high as $\pm 30 \sim 40 Wm^{-2}$. This is due to the large uncertainty in cloud cover and cloud optical depth retrived over snow or ice surfaces. The uncertainty in the net radiation at the surface

is $\pm 15 \sim 20 Wm^{-2}$, and is even larger for clear sky over snow surfaces. From the surface and cloud properties retrieved from AVHRR overpasses over SHEBA between April and August, the DSSR and NSSR are estimated and compared with those derived from surface measurements at SHEBA. The results show that before the snow melt, the error is more than 30%, but a good agreement is found after the onset of snow melt begins, and the mean error is about 7%. Seasonal variation of DSSR and NSSR depends not only on variation of solar zenith angle, but also on the variation of cloud properties and surface albedo.

In this work more than 100 AVHRR images were examined and the results compared with SHEBA surface measurements and aircraft FIRE-ACE data sets. Most results are promising. However, further tests with more data will be helpful. With many more satellites sensors already launched, or soon to be launched, more data with more suitable channels will become available on these satellite instruments. These new data will provide the opportunity to calibrate the AVHRR data, and thus provide better retrievals of surface and cloud properties. However, only AVHRR provides the opportunity to use data collected over the past 20 years to study possible long term changes in cloud and surface properties related to climate change. In the future, we plan to use data from the ARM measurements over the North Slope of Alaska, Barrow in conjunction with collocated AVHRR and MODIS data to conduct additional tests of these algorithms. The retrieval algorithms developed in this thesis can be utilized to study cloud and surface properties and the radiation budget in the Arctic region as well as the entire globe. Following the same philosophy but with suitable changes, these algorithms can be extended for application to other satellite sensors.

# Appendix A

# Acronyms

| | |
|---|---|
| APPLLO | AVHRR Processing scheme Over Land, cLoud and Ocean |
| ARF | Anisotropic Reflectance Factor |
| ARM/NSA | Atmospheric Radiation Measurement at North Slope of Alaska (Barrow) |
| ATSR | Along Track Scanning Radiometer |
| AVHRR | Advanced Very High Resolution Radiometer |
| BTD | Brightness Temperature Difference |
| BRDF | Bidirectional Reflectance Distribution Function |
| CERES | The Clouds and the Earth's Radiant Energy System |
| CLAVR | NOAA Cloud Advanced Very High Resolution Radiometer |
| CRAS | Cloud Retrieval Algorithm over Snow surface |
| CRAL | Cloud Retrieval Algorithm over a Lambert surface |
| DISORT | DIScrete Ordinate Radiative Transfer |
| DSSR | Downwelling Surface Shortwave Radiation |
| EOS | Earth Observing System |
| ERBE | Earth Radiation Budget Experiment |
| ERBS | Earth Radiation Budget Satellite |
| ESFT | Exponential-Sum Fitting of Transmissions |
| FIRE-ACE | The First ISCCP Regional Experiment-Arctic Cloud Experiment |
| FSSP | Forward Scattering Spectrometer Probe |
| GAC | Global Area Coverage |
| GLI | Global Imager |
| HRPT | High Resolution Picture Transmission |
| IFOV | Instantaneous Field of View |
| ISCCP | International Satellite Cloud Climatology Project |
| LAC | Local Area Coverage |
| LWP | Liquid Water Path |
| MAS | MODIS Airborne Simulator |
| MODIS | Moderate Resolution Imaging Spectroradiometer |
| MODTRAN | Moderate Resolution Model |
| MWR | Microwave Radiometer |
| NOAA | National Oceanic and Atmospheric Administration |
| NSSR | Net Surface Shortwave Radiation |
| NSRT | Net Shortwave Radiation at the Top of atmosphere |
| NTB | Narrow-to-Broadband conversion |
| PSP | Precision Spectral Pyranometer |
| RTM | Radiative Transfer Model |
| SHEBA | Surface Heat Budget of the Arctic Ocean |
| SRB | Solar Radiation Budget |
| TM4 | Thematic Mapper band 4 |
| TOA | Top Of Atmosphere |
| TRMM | Tropical Rainfall Measuring Mission |

# Bibliography

[1] Ackerman S. A., W. L. Smith, A. D. Collard, X. L. Ma, H. E. Revercomb and R. O. Knuteson, 1995: Cirrus cloud properties derived from high spectral resolution infrared spectrometry during FIRE II. Part II: Aircraft HIS results. *J. Atmos. Sci.*, **52**, 4246-4263.

[2] Ackerman S., K. Strabala, P. Menzel, R. Frey, C. Moeller, L. Gumley, B. Baum, C. Schaaf, and G. Riggs, 1997: Discriminating clear-sky from cloud with MODIS algorithm theoretical basis document (MOD35).

[3] Akoi, T., A. Tadao, M. Fukabori, Y. Tachibana, Y. Zaizen, F. Nishio, and T. Oishi, 1998: Spectral albedo observation on the snow field at Barrow, Alaska. *Polar Meteor. Galciol.*, **12**, 1-9.

[4] Albrecht, B. A., 1989: Aerosols, cloud microphysics and fractional cloudiness. *Science*, **245**, 1227-1230.

[5] Albrecht, B. A., D. A. Randall and S. Nicholls, 1988: Observation of marine stratoscumulus clouds during FIRE. *Bull. Amer. Meteror. Soc.*, **69**, 618-626.

[6] Allison, I., R. E. Brandt, and S. G. Warren, 1993: East Antarctic sea ice: Albedo, thickness distribution, and snow cover. *J. Geophys. Res.*, **98**, 12417-12429.

[7] Arking, A., 1985: Retrieval of cloud cover parameters from multispectral satellite images. *J. Climate Appl. Meteor.*, **24**, 322-333.

[8] Barker H. W., T. J. Curtis, E. Leontyeva, and K. Stamnes, 1998: Optical depth of overcast cloud across Canada: Estimates based on surface pyranometer and satellite measurements. *J. Climate*, **11**, 2980-2994.

[9] Baum B. A., V. Tovinkere, J. Titlow, and R. M. Welch, 1997: Automated cloud classification of global AVHRR data using Fuzzy Logic approach. *J. Appl. Meteor.*, **36**, 1519-1539.

[10] Blanchet, J., and R. List, 1983: Estimation of optical properties of arctic haze using a numerical model. *Atmos. Ocean.*, **21**, 444-465.

[11] Brandt, R. E., T. C. Grenfell, and S. G. Warren, 1991: Optical properties of snow. *Antarct. J. U. S.*, **26**(5), 272-275.

[12] Brest, C. L., and W. B. Rossow, 1992: Radiometric calibration and monitoring of NOAA AVHRR data for ISCCP. *Int. J. Remote Sensing*, **13**, 235-273.

[13] Bretherton C. S., S. R. de Roode, C. Jakob, E. L. Andreas, J. Intrieri, R. E. Moritz, and P. Ola G. Persson, 2000: A comparison of the ECMWF forecast model with observation over the annual cycle at SHEBA. *J. Geophys. Res.*, submitted 5/00.

[14] Bourdelles, B., and M. Fily, 1993: Snow grain-size determination from Landsat imagery over Terre Adelie, Antarctica. *Annals of Glaciology*, **17**, 86-92.

[15] Briegleb, B. P., P. Minnis, V. Ramanathan, and E. Harrison, 1986: Comparison of regional clear-sky albedos inferred from satellite observations and model calculations. *J. Climate App. Meteor.*, **25**, 214-226.

[16] Bunting. J. T., and R. P. d'Entremont. 1982: Improved cloud detection utilizing defense meteorological satellite program near infrared measurements. Air Force Geophysics Laboratory. Hanscom AFB. MA. *AFGL-TR-82-0027. Environmental Research Papers.* No. 765. 91pp.

[17] Cess. R. D., and I. L. Vulis. 1989: Inferring surface solar absorption from broadband satellite measurements. *J. Climate.* **2.** 974-985.

[18] Cess. R. D., J. J. DeLuisi. and F. Jiang. 1991: Determining surface solar absorption from broadband satellite measurements for clear skies: Comparison with surface measurements. *J. Climate.* **4.** 236-247.

[19] Clarke. A. D., and K. J. Noone. 1985: Soot in the Arctic snowpack: A cause for perturbations in radiative transfer. *Atmos. Environ.*, **19.** 2045-2053.

[20] Cracknell P. A., 1997 : *The Advanced very high resolution radiometer. Tylor & Francis.* 534pp.

[21] Csiszar C., and G. Gutman. 1999: Mapping global land surface albedo from NOAA AVHRR. *J. Geophys. Res.*, **104.** 6215-6228.

[22] Curran. R. J., and M. L. C. Wu. 1982: Skylab near infrared observations of clouds indicating supercooled liquid water droplets. *J. Atmos. Sci.*, **39.** 635-647.

[23] Curry. J. A., E. E. Ebert. and G. F. Herman. 1988: Mean and turbulent structure on the summertime Arctic vloudy boundary layer. *Quart. J. Roy. Metero. Soc.*, **114.** 715-746.

[24] Curry J. A., F. G. Meyer. L. F. Radke. C. A. Brock and E. E. Ebert. 1990: Occurance and characteristics of lower tropospheric ice crystal in the Arctic. *Int. J. Climatol.*, **10.** 749-764.

[25] Curry. J. A.. and E. E. Ebert. 1992: Annual cycle of radiation fluxes over the Arctic ocean: Sensitivity to cloud optical properties. *J. Climate.* **5**.1267-1280.

[26] Curry J. A.. W. B. Rossow. D. Randall. and J. L. Schramm. 1996: Overview of Arctic cloud and radiation characteristics. *J. of Climate.* **9**. 1731-1764.

[27] Curry. J. A.. and 26 coauthors. 2000: FIRE Arctic clouds experiment. *Bull. Amer. Meteor. Soc..* **81**. 5-29.

[28] Curtis J.. G. Wendler. R. Stone. and E. Dutton. 1998: Precipitaion devrease in the western Arctic. with special emphsis on Barrow and Barter Island. Alaska. *Int. J. Climatol..* **18**. 1687-1707. 1998.

[29] Davis. P. A.. 1993: Spectral radiance-temperature conversion for measurements by AVHRR thermal channels 3. 4. 5. Washington. D.C.. U.S. Dept. of Commerce. National Oceanic and Atmospheric Administration. National Environmental Satellite. Data. and Information Service. *NOAA Technical REPORT. NESDIS 71.*

[30] De Abreu. R. A.. J. Key. J. A. Maslanik. M. C. Serreze. and E. F. LeDrew. 1994: Comparison of in situ and AVHRR-derived broadband albedo over arctic sea ice. *Arctic.* **47**. 288-297.

[31] Dong X.. G. G. Mace. P. Minnis. and D. F. Yong. 2000: Arctic stratus cloud properties and their effects on the surface radiation budget: Selected cases from FIRE ACE. *J. Geophys. Res..* submitted 5/00.

[32] Dozier. J.. and S. G. Warren. 1982: Effect of viewing angle on the infrared brightness temperature of snow. *Water Resour. Res..* **18**. 1424-1434.

[33] Ebert. E.. 1987: A pattern recognition technique for distinguishing surface and cloud types in the polar regions. *J. Climate Appl. Meteor..* **26**. 1412-1427.

[34] Ebert, E. E., 1989: Analysis of polar clouds from satellite imagery using pattern recognition and a statistical cloud analysis scheme. *J. Appl. Meteor.*, **28**, 382-399.

[35] Ebert, E. E., 1992: Recognition analysis of polar clouds during summer and winter. *Int. J. Remote Sensing*, **13**, 97-109.

[36] Ebert, E. E. and J. A. Curry, 1993: An intermediate one-dimensional thermodynamic sea ice model for investigating ice-atmosphere interactions. *J. Geophys. Res.*, **98**, 10085-10109.

[37] Ellrod G., and J. P. Nelson, 1997: An experimental GOES image product to identify conditions favorable for aircraft icing. *7th Conf. on Aviation, Range and Aerospace Meteor., 2-7, Febuary, Long Beach, California, Amer. Meteor. Soc., Boston, 112-115.*

[38] Fily M., B. Bourdelles, J. P. Dedieu, and C. Sergent, 1997: Comparison of in situ and Landsat Thematic Mapper derived snow grain characteristics in the Alps. *Remote Sens. Environ.*, **59**, 452-460.

[39] Foot, J. S., 1988: Some observations of the optical properties of clouds. I: Stratocumulus. *Quart. J. Roy. Meteor. Soc.*, **114**, 129-144.

[40] Fu, Q., and K. N. Liou, 1993: Parameterization of the radiative properties of cirrus clouds. *J. Atmos. Sci.*, **50**, 2009-2025.

[41] Garand L., and S. Nadon, 1998: High-resolution satellite analysis and model evaluation of clouds and radiation over the Mackenzie basin using AVHRR data. *J. Climate*, **11**, 1976-1996.

[42] Gao, B.-C., A. F. H. Goetz, and W. J. Wiscombe, 1993: Cirrus cloud detection from airborne imaging spectrometer data using the 1.38 micron water vapor band. *Geophys. Res. Lett.*, **20**, 301-304.

[43] Gesell, G., 1989: An algorithm for snow and ice detection using AVHRR data: An extension to the APOLLO software package. *Int. J. Remote Sens.*, **10**, 897-905.

[44] Grenfell, T. C., and G. A. Maykut, 1977: The optical properties of ice and snow in the Arctic Basin. *J. Glaciol.*, **18**, 445-463.

[45] Grenfell, T. C., and D. K. Perovich, 1984: Spectral albedos of sea ice and incident solar irradiance in the southern Beaufort Sea. *J. Geophys. Res.*, **89**, 3573-3580.

[46] Grenfell, T. C., S. G. Warren, and P. C. Mullen, 1994: Reflection of solar radiation by the Antarctic snow at ultraviolet, visible, and near-infrared wavelengths. *J. Geophys. Res.*, **99**, 18669-18684.

[47] Hahn, C. J., S. G. Warren and J. London, 1995: The effect of moonlight on observation of cloud cover at night, and application to cloud climatology. *J. Climate*, **8**, 1429-1446.

[48] Hall, D. K., G. A. Riggs, and V. V. Salomonson, 1995: Development of methods for mapping global snow cover using Moderate Resolution Imaging Spectroradiometer data. *Remote Sens. Env.*, **54**, 127-140.

[49] Han, Q., W. B. Rossow, and A. A. Lacis, 1994: Near-global survey of effective droplet radius in liquid water clouds using ISCCP data. *J. Climate*, **7**, 465-497.

[50] Han, W., K. Stamnes, and D. Lubin, 1999: Retrieval of surface and cloud properties in the Arctic from NOAA AVHRR measurements. *J. Appl. Meteor.*, **38**, 989-1012.

[51] Harrington J. Y., T. Reisin, W. R. Cotton, and S. M. Kreidenweis, 1999: Cloud resolving simulations of Arctic stratus. Part II: Transition-season clouds. *Atmos. Res.*, **51**, 45-75.

[52] Hartmann D. L., V. Ramanathan, A. Berroir and G. E. Hunt, 1986: Earth Radiation budget data and climate research. *Review of Geophy.*, **24**, No. 2, 439-468.

[53] Herman and Goody, 1976: Formation and persistence of summertime Arctic strtus clouds. *J. Atmos. Sci.*, **33**, 5-55.

[54] Herman, G. F, 1977: Solar radiation in the summer stratus clouds. *J. Atmos. Sci.*, **34**, 1425-1432.

[55] Herman G. F., and J. A. Curry, 1984: Observational and theoretical studies of solar radiation in Arctic stratus clouds. *J. Climate Appl. Meteor.*, **23**, 5-24.

[56] Henyey, L. C., and J. L. Greenstein, 1941: Diffuse radiation in the galaxy. *Astrophys. J.*, **93**, 70-83.

[57] Hu, Y. X., and K. Stamnes, 1993: An accurate parameterization of the radiative properties of water clouds suitable for use in climate models. *J. Climate*, **6**, 728-742.

[58] Hu, Y. X., and K. Stamnes, 2000: Climate sensitivity to cloud optical properties. *Tellus*, 5213, 81-93.

[59] Hutchison K. D., and K. R. Hardy, 1995: Threshold functions for automated cloud analyses of global meteorological satellite imagery. *Int. J. Remote Sensing.* **16**, 18, 3665-3680.

[60] Hutchison K. D., and J. K. Locke, 1997: Snow cover identification through cirrus-cloudy atmospheres using daytime AVHRR imagery. *Geophy. Res. Lett.*, **24**, 1791-1794.

[61] Inoue T., 1985: On the temperature and effective emissivity determination of semi-transparent cirrus clouds by bi-spectral measurements in the 10 $\mu$m window region. *J. Meteor. Soc. Jpn.* **63**(1), 88-98.

[62] Inoue T., 1987: A cloud type classification with NOAA-7 split-window measurements. *J. Geophy. Res.*, **92**, 3991-4000.

[63] Intrieri, J. M., M. D. Shupe, B. J. McCarty, and T. Uttal, 2000: Annual cycle of Arctic cloud statistics from Lidar and Radar at SHEBA. *J. Geophys. Res.*, submitted 5/00.

[64] IPCC, 1990: Climate Change: *The IPCC Scientific Assessment*, J. T. Houghton, G. J. Jenkins, and J. J. Ephraums, Eds., Cambridge University Press, 365pp.

[65] Jayaweera K. O. L. F., and T. Ohtake, 1973: Concentration of ice crystals in the Arctic Stratus Clouds. *J. Rech. Atmos.*, **7**, 199-207

[66] Jin, Z., and K. Stamnes, 1994: Radiative transfer in nonuniformly refracting media such as the atmosphere/ocean system. *Appl. Opt.*, **33**, 431-442.

[67] Jin, Z., K. Stamnes, W. F. Weeks, and S. C. Tsay, 1994: The effect of sea ice on the solar energy budget in the atmosphere-sea ice-ocean system: A model study. *J. Geophys. Res.*, **99**, 25281-25294.

[68] Kaufman, Y. J., and B. N. Holben, 1993: Calibration of the AVHRR visible and near-IR bands by atmospheric scattering, ocean glint, and desert reflection. *Int. J. Remote Sensing*, **14**, 21-52.

[69] Kaufman, Y. J., and T. Nakajima, 1993: Effect of Amazon smoke on cloud microphysics and albedo analysis from satellite imagery. *J. Appl. Meteor.*, **32**, 729-744.

[70] Kato, S., T. P. Ackerman, E. E. Clothiaux, J. H. Mather, G. G. Mace, M. L. Wesely, F. Murcray, and J. Michalsky, 1997: Uncertainties in modeled and measured clear-sky surface shortwave irradiances. *J. Geophy. Res.*, **102**, 25881-25898.

[71] Key J., and R. G. Barry, 1989: Cloud cover analysis with Arctic AVHRR data, 1. Cloud detection. *J. Geophys. Res.*, **94**, 18521-18535.

[72] Key, J., and M. Haefliger, 1991: Retrieval of ice surface temperature, outgoing longwave radiation, and cloud cover from AVHRR data. *World Climate Research Program, Sea Ice and Climate*, edited by E. Raschke, H. Cattle, P. Lemke, and W. Rossow, Appendix C, p. 22.

[73] Key, J., 1996: *The Cloud and Surface Parameter Retrieval (CASPR) System for Polar AVHRR, Version 1.0: User's Guide*, Department of Geography, Boston University, Boston, 73pp.

[74] Key, J., and M. Haefliger, 1992: Arctic ice surface temperature retrieval from AVHRR thermal channels. *J. Geophys. Res.*, **97**, 5885-5893.

[75] Key, J., 1995: Retrieval of cloud optical depth and particle effective radius at high latitudes using visible and thermal satellite data. *Passive Infrared Remote Sensing of Clouds and the Atmosphere 3*.

[76] Key J. R., A. J. Schweiger, and R. S. Stone, 1997 : Expected uncertainty in satellite-derived estimateds of the surface radiation budget at high latitudes. *J. Geophy. Res.*, **102**, 15837-15847.

[77] Key J. R., J.B. Collins, C. Fowler, and R. S. Stone, 1997: High-latitude surface temperature estimates from thermal satellite data. *Remote Sens. Environ.*, **61**, 302-309.

[78] Kidwell, K. B., 1995: *NOAA polar orbiter data user's guide*. NOAA/NESDIS/NCDC, Washington, D.C., 20233, U.S.A.

[79] King, M. D., 1987: Determination of the scaled optical thickness of clouds from reflected solar radiation measurements. *J. Atmos. Sci.*, **44**, 1734-1751.

[80] King, M. D., S. Tsay, S. E. Platnick, M. Wang, K. Liou, 1997: Cloud retrieval algorithms for MODIS: Optical thickness, effective particle radius, and thermodynamic phase. *ATBD-MOD-05, NASA Goddard Space Flight Center*.

[81] Knollenberg, R. G., 1981 : *Techniques for probing cloud microstructure. Clouds: Their formation, Optical properties, and Effects*. P. V. Hobbs and A. Deepak, Eds., Academic Press, 15-91.

[82] Konvalin C., A. Logar, D. Lloyd, E. Corwin, M. Panaloza, R. Feind and R. Welch, 1998: *SPIE: The International Society for Optical Engineering*. V.3220, 0277-786x.

[83] Kimes, D. S., and P. J. Sellers, 1985: Inferring hemispherical reflectance of the earth's surface for global energy budgets from remotely-sensed nadir or directional radiance values. *Remote Sensing of Environment*, **18**, 205.

[84] Kriebel, K. T., and R. W. Saunders, 1988: An improved method for detecting clear sky and cloudy radiances from AVHRR data. *Int. J. Remote Sens.*, **9**, 123-150.

[85] Kriebel, K. T., R. W. Saunders, and G. Gesell, 1989: Optical properties of clouds derived from fully clouds pixels. *Contr. Phys. Atmos.*, **62**, 165-171.

[86] Kyle, H. L., R. J. Curran, W. L. Barnes, and D. Escoe, 1978: A cloud physics radiometer. *Third Conference on Atmospheric Radiation*, Davis, CA, 107-109.

[87] Langleben, M. P, 1971: Albedo of melting sea ice in the southern Beaufort Sea. *J. Glaciol.*, **10**, 101-104.

[88] Laszlo, I., and R. T. Pinker, 1994: On the relationship between shortwave net radiative fluxes at the top of the atmosphere and at the surface, *8th Conference on Atmospheric Radiation*, Nashville, TN.

[89] Leontyeva, E., and K. Stamnes, 1994: Estimaes of cloud optical thickness from ground-based measurements of incoming solar radiation in the Arctic. *J. Climate*, **7**, 566-578.

[90] Leontyeva, E., and K. Stamnes, 1996: Remote sensing of cloud optical properties from ground-based measurements of transmittance: A feasibility study. *J. Appl. Metero.*, **35**, No. 11, 2011-2022.

[91] Li, W., X. Xiong, Knut Stamnes and B. Chen, 2000: Snow grain size determination from AVIRIS data over Arctic ocean. *10th conference on satellite meteorology and oceanography*, 9-14 January 2000, Long Beach, CA, Amer. Meteor. Soc., Boston, MA.

[92] Li Z., and H. G. Leighton. 1992: Narrowband to broadband conversion with spatially autocorrelated reflectance measurement. *J. Appl. Meteor.*, **31**. 421-433.

[93] Li, Z., H. Leighton, K. Masuda and T. Takashima. 1993: Estimate of SW flux absorbed at the surface from TOA reflected flux. *J. Climate*. **6**. 317-330.

[94] Lindsay R. W., and D. A. Rothrock. 1994: Arctic sea ice albedo from AVHRR. *J. Climate*. **7**. 1737-1749.

[95] Loeb, N. G., 1997: In-flight calibration of NOAA AVHRR visible and near-IR bands over Greenland and Antarctica. *Int. J. Remote Sensing*. **18**. 477-490.

[96] Lubin, D., P. Ricchiazzi, C. Gautier, and R. H. Whritner. 1994: A method for mapping Antarctic surface ultraviolet radiation using multispectral satellite imagery. *Amer. Geophys. Union Antarct. Res. Ser.*, **62**. 53-81.

[97] Lubin, D., and P. J. Weber. 1995: The use of cloud reflectance functions with satellite data for surface radiation budget estimation. *J. Appl. Meteor.*, **34**. 1333-1347.

[98] Lubin, D., and E. Morrow. 1998: Evaluation of an AVHRR cloud detectoin and classification method over the central Arctic Ocean. *J. Appl. Meteor.*, **37**. 166-183.

[99] Marshall J. F. L. J. J. Simpson and Z. Jin. 1999: Satellite calibration using a collocated nadir observation technique: Theoretical basis and application to GMS-5 pathfinder Benchmark period. *IEEE Trans. Geosci. Remote Sensing*. **37**. 499-507.

[100] Matveev, L. T., 1984: *Cloud Dynamics*. D. Reidel. 340pp.

[101] Maykut, G. A., and P. E. Church, 1973: Radiation climate of Barrow, Alaska, 1962-1966. *J. Appl. Meteor.*, **12**, 620-628.

[102] McClatchey, R. A., R. W. Fenn, J. E. A. Selby, F. E. Volz, and J. S. Garing, 1971: *Optical properties of the atmosphere*. Air Force Cambridge Rep. AFCRL-71-0279, 85 pp.

[103] McInnes, K.L., and J. A. Curry, 1995: Modeling the mean and turbulent structure of the summertime Arctic cloudy boundary layer. *Bound.-Layer Meteor.*, **73**, 125-143.

[104] Menzel, P., and K. Strabala, 1997: Cloud top properties and cloud phase algorithm theoretical basis document. *ATBD-MOD-04, NASA Goddard Space Flight Center.*

[105] Min, Q., and L. C. Harrison, 1996: Cloud properties derived from surface MFRSR measurements and comparison with GOES results at ARM SGP site. *Geophys. Res. Lett.*, **23**, 1641-1644.

[106] Minnis, P., K.-N. Liou, and Y. Takano, 1993: Inferrence of cirrus cloud properties using satellite-observed the visible and infrared radiances. Part II: Verification of theoretical cirrus radiative properties. *J. Atmos. Sci.*, **50**, 1305-1322.

[107] Minnis P., W. L. Smith Jr., D. P. Garber, J. K. Ayers, and D. R. Doelling, 1995: Cloud properties derived from GOES-7 for the Spring 1994 ARM Intensive Observing Period using version 1.0.0 of the ARM satellite data analysis program. *NASA Rep.* 1366, 59pp.

[108] Minnis P., D. P. Garber, D. F. Young, R. F. Arduini, and Y. Takano, 1998: Parameterization of reflectance and effective emittance for satellite remote sensing of clouds properties. *J. Atmos. Sci.*, **55**, 3313-3339.

[109] Minnis, P., D. Doelling, C. Venkatesan, D. C. Spangenberg, L. Nguyen, R. Palikonda, T. Uttal, M. Shuoe, and R. F. Arduini, 1999, Arctic cloud coverage during FIRE-ACE derived from AVHRR data. *J. Geophys. Res.*, submitted 5/00.

[110] Moritz R. E., and D. K. Perovich (eds), 1996, Surface Heat Budget of the Arctic Ocean Science Plan. *ARCSS/OAII Report Number 5*, University of Washington, Seattle, 64pp.

[111] Moritz, R. W., J. A. Curry, A. S. Thorndike, and N. Untersteiner,1993: Surface Heat Budget of the Arctic Ocean. *NSF-ARCSS OAII Report number 3*, University of Washington, Seattle, 34 pp.

[112] Nakajima, T., M. D. King, J. D. Spinhirne and L. F. Radke, 1991: Determination of the optical thickness and effective particle radius of clouds from reflected solar radiation measurements. Part II, Marine stratocumulus observations. *J. Atmos. Sci.*, **48**, 728-750.

[113] Nakajima, T., and M. D. King, 1990: Determination of the optical thickness and effective particle radius of clouds from reflected solar radiation measurements. Part I: Theory. *J. Atmos. Sci.*, **47**, 1878-1893.

[114] Nakajima, T. Y., and T. Nakajima, 1995: Wide-area determination of cloud microphysical properties from NOAA AVHRR measurements for FIRE and ASTEX regions. *J. Atmos. Sci.*, **52**, 4043-4059.

[115] Nolin, A. W., and J. Dozier, 1993: Estimating snow grain size using AVIRIS data. *Remote Sens. Environ.*, **44**, 231-238.

[116] Olsson P. Q., Harrinton J. Y., G. Feingold, W. R. Cotton, S. M. Kreidenweis, 1998: Exploratory cloud-resolving simulations of boundary-layer Arctic stratus clouds. Part I: Warm-season clouds. *Atmos. Res.*, 47-48, 573-597.

[117] Ou S. C., K. N. Liou, W. M. Gooch, and Y. Takano, 1993: Remote sensing of cirrus cloud parameters using advanced very-high resolution radiometer 3.7 and 10.9 $\mu$m channels. *Appl. Opt.*, **32**, 2171-2180.

[118] Ou S. C., K. L. Liou and B. A. Baum, 1996: Detection of multilayer cirrus cloud systems using AVHRR data: Verification based on FIRE II IFO composite measurements. *J. Appl. Meteor.*, **35**, 178-191.

[119] Penndorf, R., 1957: Tables of the refractive index for standard air and the Rayleigh scattering coefficient for the spectral region between 0.2-20 $\mu$ m and their application to atmospheric optics. *J. Opt. Soc. Am.*, **47**, 176-182.

[120] Perovich, D. K., T. C. Grenfell, B. Light, J. A. Richter-Menge, M. Sturm, W. B. Tucker III, H. Eicken, G. A. Mayhut, and B. Elder, 1999: SHEBA: *Snow and Ice Studies CD-ROM*. Obtainable from D. Perovich, CRREL, 72 Lyme Road, Hanover, NH, USA 03755.

[121] Perovich D. K., C. Roesler and W. S. Pegau, 1998: Variability in Arctic sea ice optical properties. *J. Geophys. Res.*, **103**, 1193-1208, 1998.

[122] Pinker R. T., R. Frouin and Z. Li, 1995: A review of satellite methods to drive surface shortwave irradiance. *Remote Sens. Environ.*, **51**, 108-124.

[123] Pinker, R. T., and I. Laszlo, 1992: Modeling surface solar irradiance for satellite applications on a global scale. *J. Appl. Meteor.*, **31**, 194-211.

[124] Platnick, S., and S. Twomey, 1994: Determining the susceptibility of cloud albedo to change in droplet concentration with the Advanced Very High Resolution Radiometer. *J. Appl. Meteor.*, **3**, 334-345.

[125] Platnick, S., and F. P. J. Valero, 1995: A validation of a satellite cloud retrieval during ASTEX. *J. Atmos. Sci.*, **52**, 2985-3001.

[126] Ramanathan, V., 1986: Scientific use of surface radiation budget data for climate studies. *Report of the workshop on Surface Radiation Budget for Climate Applications.*

[127] Ramanathan, V., R. D. Cess, E. F. Harisson, P. Minis, B. R. Barkstrom, E. Ahmad, and D. Hartman, 1989: Cloud-radiative forcing and climate: Results from the Earth Radiation Budget Experiment. *Science*, **243**, 57-63.

[128] Rao, C. R. N., and J. Chen, 1995: Inter-satellite calibration linkages for the visible and near-infrared channels of the Advanced Very High Resolution Radiometer on the NOAA-7, -9, and -11 spacecraft. *Int. J. Remote Sensing*, **16**, 1931-1942.

[129] Rao, C. R. N., and J. Chen, 1996: Post-launch calibration of the visible and near-infrared channels of the Advanced Very High Resolution Radiometer on the NOAA-14 sspacescraft. *Int. J. Remote Sensing*, **17**, 2743-2747.

[130] Rao, C. R. N., and J. Chen, 1999: Post-launch calibration of the visible and near-infrared channels of the Advanced Very High Resolution Radiometer (AVHRR) on the NOAA-14 sspacescraft. *Int. J. Remote Sensing*, **20**, 3485-3491.

[131] Raschke. E.. 1987: Report of the International Satellite Cloud Climatology Project (ISCCP). *Workshop on cloud algorithms on the polar regions. WCP-131. WMO/TD-No.170. WMO. Geneva.*

[132] Raschke. E.. P. Baur. and H. J. Lutz. 1992: Remote sensing of clouds and surface radiation budget over polar regions. *Int. J. Remote Sensing.* **13.** 13-22.

[133] Rawlins. F.. and J. S. Foot. 1990: Remotely sensed measurements of stratocumulus properties during FIRE using the C130 aircraft multichannel radiometer. *J. Atmos. Sci..* **47.** 2488.

[134] Riggs. G. A.. D. K. Hall. and S. A. Ackerman. 1998: Sea ice extent and classification mapping with the Moderate Resolution Imaging Spectroradiometer Airborne Simulator (MAS). *Remote Sens. of Environ..* **68.** 152-163.

[135] Rogers. R. R.. and M. K. Yau. 1989: *A short course in cloud physics.* 3d ed. Pergamon Press. 292pp.

[136] Rosenthal. C. W.. 1993: Mapping montane snow cover at subpixel resolution from the Landsat thematic mapper. *M. A. Thesis. Department of Geophysics. University of California at Santa Barbara. 70pp.*

[137] Rossow. W. B.. L. C. Gardner. and A. A. Lacis. 1989: Global seasonal cloud variations from satellite radiation measurements. Part I. Sensitivity of analysis. *J. Climate.* **2.** 419-458.

[138] Rossow. W. B.. A. W. Walker and L. C. Garder. 1993: Comparison of ISCCP and other cloud amounts. *J. Climate.* **6.** 2394-2418.

[139] Rossow. W. B.. and R. A. Schiffer. 1991: ISCCP cloud data products. *Bull. Amer. Meteor. Soc..* **72.** 2-20.

[140] Rossow, W. B., L. C. Garder, P. J. Lu, and A. W. Walker, 1991: International Satellite Climatology Project(ISCCP) Documentation of cloud data. *WMO/TD-No. 226 (revised)*. *WMO*, Geneva, 76pp + three appendices.

[141] Rossow, W. B., 1989: Measuring cloud properties from space: A review. *J. Climate*, **2**, 201-213.

[142] Rossow, W. B., and L. C. Garder, 1993a: Validation of ISCCP cloud detection. *J. Climate*, **6**, 2370-2393.

[143] Rossow, W. B., and L. C. Garder, 1993b: Cloud detection using satellite measurements of infrared and the visible radiances for ISCCP. *J. Climate*, **6**, 2341-2369.

[144] Rossow, W. B., L. C. Gardner, and A. A. Lacis, 1989: Global seasonal cloud variations from satellite radiance measurements. Part I: Sensitivity of analysis. *J. Climate*., **2**, 419-458.

[145] Sassen, K., 1991: The polarization lidar technique for cloud research: A review and current assessment. *Bull. Amer. Meteor. Soc*., **72**, 1848-1866.

[146] Saunders, R. W., and K. T. Kriebel, 1988: An improved method for detecting clear sky and cloudy radiances from AVHRR data. *International Journal of Remote Sensing*, **42**, 83-106.

[147] Saunders, R. W., 1990: The determination of broad band surface albedo from AVHRR visible and near-infrared radiances. *Int. J. Remote Sensing*, **11**, 49-67.

[148] Schmetz, J., 1991: Retrieval of surface radiation fluxes from satellite data. *Dynamics Atmos. Ocean*, **16**, 61-72.

[149] Schmetz. J.. 1993: On the relationship between solar net radiative fluxes at the top of atmosphere and at surface. *J. Atmos. Sci.*. **50**. 1122-1132.

[150] Schweiger. J. A.. and J. R. Key. 1992: Arctic cloudiness: Comparison of ISCCP-C2 and Nimbus-7 satellite-derived cloud products with a surface-based cloud climatology. *J. Climate*. **5**. 1514-1527.

[151] Sellers. W. D.. 1969: A climate model based on the energy balance of the earth-atmosphere system. *J. of Appl. Meteor.*. **8**. 392-400.

[152] Sellers. P. J.. S. I. Rasool. and H. J. Bolle. 1990: A review of satellite data algorithms for studies of the land surface. *Bull. Amer. Meteor. Soc.*. **71**. 1429-1447.

[153] Sergent. C.. E. Pougatch. and M. Sudul. 1993: Experimental investigation of optical snow properties. *Annals of Glaciology*. **17**. 281-287.

[154] Shaw. G.. 1982: Atmospheric turbidity in the polar regions. *J. Appl. Meteor.*. **21**. 1080-1088.

[155] Shettle E. P.. and R. W. Fenn. 1976: Models of atmospheric aerosols and their optical properties. in Agard Conference Proceedings No. 183. *Optical Propagation in the Atmosphere*. AGARD-CP-183. NTIS. ADA 028615.

[156] Simpson J. J.. and R. H. Keller. 1995: An improved Fuzzy Logic Segmentation of sea ice. clouds. and ocean in remotely sensed imagery. *Remote Sens. Environ.*. **54**. 290-312.

[157] Singer. F. S.. and R. W. Popham. 1963: Non-meteorological observations from weather satellites. *Astronautics and Aerospace Engineering*. **1** (3). 89-92.

[158] Slingo, A., S. Nichools and J. Schmetz.1982 : Aircraft observation of marine stratoscumulus during JASIN. *Quart. J. Roy. Meteor. Soc.*, **108**, 833-856.

[159] Slingo, A., 1989: A GCM parameterization for shortwave radiative properties of water clouds. *J. Atmos. Sci.*, **46**, 1419-1427.

[160] Song J., and W. Gao, 1999: An improved method to derive surface albedo from narrowband AVHRR satellite data: Narrowband to Broadband Conversion. *J. Appl. Meteo.*, **38**, 239-249.

[161] Spinhire, J. D., R. Boers and W. D. Hart, 1989: Cloud top liquid water from lidar observations of marine stratocumulus. *J. Appl. Meteor.*, **28**, 81-90.

[162] Stamnes, K., 1982: Reflection and transmission by a vertically inhomogeneous planetary atmosphere. *Planet. Space Sci.*, **30**, 727-732.

[163] Stamnes, K., and S. C. Tsay, 1990: Optimum spectral resolution for computing atmospheric heating and photodissociation rates. *Planet. Space Sci.*, **38**, 807-820.

[164] Stamnes K., S. C. Tsay, W. Wiscombe, and K. Jayaweera, 1988: Numerically stable algorithm for discrete-ordinate-method radiative transfer in multiple scattering and emitting layered media. *Appl. Opt.*, **27**, 2502-2509.

[165] Stamnes, K., R. G., Ellingson, J. A. Curry , J. E. Walsh, and B. D. Zak, 1999: Review of science issues and deployment strategies for the North Slope of Alaska/Adjacent Arctic Ocean (NSA/AAO) ARM site. *J. Climate*, 29, 1413-1423 .

[166] Steffen, K., R. Bindschadler, G. Casassa, J. Comiso, D. Eppler, F. Fetterer, J. Hawkins, J. Key, D. Rothrock, R. Thomas, R. Weaver, R. Welch, 1993:

Snow and ice applications of AVHRR in polar regions: *report of a workshop held in Boulder, Colorado, 20 May 1992.*

[167] Stephens, G. L., and C. M. R. Platt, 1987: Aricraft observations of the radiative and microphysical properties of stratocumulus and cumulus clouds fields. *J. Climate Appl. Meteor.*, **26**, 1243-1269.

[168] Stowe, L. L., S. K. Vemury, and A. V. Rao, 1994: AVHRR clear sky radiation data sets at NOAA/NESDIS. *Adv. Space Res.*, **14**, 113-116.

[169] Stuhlmann, R., and P. Bauer, 1990: Retrievals of radiation from satellite data and aircraft measurements, in *Workshop on Polar Radiation Fluxes and Sea-Ice Modeling, November 5-8, Bremerhaven, Germany*, 29-40. Appendix C.

[170] Taylor, V. R., and L. L. Stowe, 1984: *Atlas of reflectance patterns for uniform earth and cloud surfaces (NIMBUS-7ERB-61 days). NOAA Technical Report NESDIS 10, 66pp.*

[171] Teillet, P. M., P. N. Slater, Y. Ding, R. P. Santer, R. D. Jackson, and M. S. Moran, 1990: Three methods for the absolute calibration of the NOAA AVHRR sensors in-flight. *Remote Sens. Environ.*, **31**, 105-120.

[172] Thompson, G., T. F. Lee and J. Vivekanandan, 1997: Comparison of satellit-based aircraft icing diagnoses, *7th Conf. on Aviation, Range and Aerospace Meteor.*, 2-7, Febuary, Long Beach, California, Amer. Meteor. Soc., Boston, 132-137.

[173] Toll D. L., D. Shirey, and D. S. Kimes, 1997: NOAA AVHRR land surface albedo algorithm development. *Int. J. Remote Sensing*, **18**, 3761-3796.

[174] Tsay, S. C., and K. Jayaweera, 1984: Physical characteristics of arctic stratus clouds. *J. Climate Appl. Meteor.*, **23**, 584-596.

[175] Tsay S. C., K. Stamnes and K. Jayaweera, 1989: Radiative energy budget in the cloudy and hazy Arctic. *J. Atmos. Sci.*, **46**, 1002-1017.

[176] Tsay, S. C., K. Stamnes and K. Jayaweera, 1990: Radiative transfer in stratified atmospheres: development and verification of a unified model. *J. Quant. Spectrosc. Radiat. Transfer*, **43**, 133-148.

[177] Twomey, S., and T. Cocks, 1982: Spectral reflectance of clouds in the near-infrared: Comparison of measurements and calculations. *J. Meteor. Soc. Japan*, **60**, 583.

[178] Twomey, S., and T. Cocks, 1989: Remote sensing of cloud parameters from spectral reflectance in the near-infrared. *Beitr. Phys. Atmos.*, **62**, 172.

Valero, F. R. J., T. P. Ackerman and W. J. Y. Gore, 1983: Radiative effects of the arctic haze. *Geophys. Res. Lett.*, **10**, 1184-1187.

[179] Wang M., and M. D. King, 1997: Correction of Rayleigh scattering effects in cloud optical thickness retrievals. *J. Geophy. Res.*, **102**, 25915-25926.

[180] Warren, S. G., 1982: Optical properties of snow. *Rev. Geophy. Space Phys.*, **20**, 67-89.

[181] Warren, S. G., and W. J. Wiscombe, 1980: A model for the spectral albedo of snow. II. Snow containing atmospheric aerosols. *J. Atmos. Sci.*, **37**, 2734-2745.

[182] Warren, S. G., T. C. Grenfell, and P. C. Mullen, 1986: Optical properties of Antartic snow. *Antarct. J. U. S.*, **21**, 247-248.

[183] Welch R. M., S. K. Sengupta and K. S. Kuo. 1988: Marine Stratocumulus cloud fields off the coast of southern california observed using LANDSAT imagery. Part II: Textual Analysis. *J. Appl. Meteor.*, **27**, 363-378.

[184] Welch R. M., S. K. Sengupta, A. K. Goroch, P. Rabindra, N. Rangaraj and M. S. Navar, 1992: Polar cloud and surface classification using AVHRR imagery: An intercomparison of methods. *J. Appl. Meteor.*, **31**, 405-420.

[185] Welch, R. M., and B. A. Weilicki, 1989: Reflected fluxes for broken clouds over a Lambertian surface. *J. Atmos. Sci.*, **46**, 1384-1395.

[186] Wielicki, B. A., and B. R. Barkstrom, 1991: Clouds and the Earth's radiant energy system (CERES): An Earth observing system experiment. *2nd Symposium on Global Change Studies, January 14-18, 1991, New Orleans, LA, American Meteorological Society, Boston, MA, 11-16.*

[187] Wielicki B. A., B. R. Barkstrom, E. F. Harrison, R. B. Lee, G. L. Smith and J. E. Cooper, 1996: Clouds and the Earth's Radiant Energy System (CERES): An earth observing experiment. *Bull. Amer. Meteor. Soc.*, **77**, 853-868.

[188] Wiscombe, W. J., and S. G. Warren, 1980: A model for the spectral albedo of snow. I. Pure Snow. *J. Atmos. Sci.*, **37**, 2712-2733.

[189] Wu, X., J. J. Bates, and S. Singh Khalsa, 1993: A climateology of the water vapor band brightness temperature for NOAA operational satellite. *J. Climate*, **7**, 1282-1300.

[190] Xiong X., W. Li, D. Lubin, and K. Stamnes, 2000a: Evaluating the principles of cloud remote sensing with AVHRR and MAS imagery over SHEBA. *J. Geophys. Res.*, submitted 5/00.

[191] Xiong, X., K. Stamnes, and D. Lubin, 2000b: Arctic Solar Radiation Budget Derived from AVHRR/SHEBA data. *EOS Transactions, American Geophysical Union*, Volume 81, A52A-01, S149, 2000.

[192] Xiong,X, R. Storvold R., D. Lubin, W. Li and K. Stamnes, 2000c: Validation of AVHRR Cloud Retrieval with ARM NSA and SHEBA data. *ARM Science Team Meeting*, San Antonio, Texas, March 13-17, 2000.

[193] Yamanouchi, T., K. Suzuki, and S. Kawaguci, 1987 : Detection of clouds in Antarctic from infrared multispectral data of AVHRR. *J. Meteor. Soc. Japan*, **65**, 949-962.

[194] Yamanouchi, T., and S. Kawaguci, 1992: Cloud distribution in the Antarctic from AVHRR data and radiation measurements at the surface. *Int. J. Remote Sens.*, **13**, 111-127.